SFB 837
Interaktionsmodelle für den
maschinellen Tunnelbau

RUHR
UNIVERSITÄT
BOCHUM

# Steel Fiber Reinforced Concrete Under Concentrated Load

by

**M.Sc. Fanbing Song**

**Dissertation**

for the degree

**Doctor of Engineering (Dr.-Ing.)**

**Department of Civil and Environmental Engineering**
**Ruhr University Bochum**
**Germany**

Bochum 2017

| | |
|---|---|
| Date of submission: | $14^{th}$ October 2016 |
| Date of oral examination: | $08^{th}$ February 2017 |

| | |
|---|---|
| Referees: | Prof. Dr.-Ing. Rolf Breitenbücher<br>Lehrstuhl für Baustofftechnik<br>Fakultät für Bau- und Umweltingenieurwissenschaften<br>Ruhr-Universität Bochum |
| | Prof. Dr.-Ing. habil. Peter Mark<br>Lehrstuhl für Massivbau<br>Fakultät für Bau- und Umweltingenieurwissenschaften<br>Ruhr-Universität Bochum |

# Acknowledgement

This thesis is the result of a research project "SFB 837 B1: Optimized Structural for Durable and Robust Tunnel Lining Systems", carried out from 2010 to 2014 during my activity as research associate in the Institute of Building Materials at Ruhr University Bochum (RUB). This research project is a part of the Collaborative Research Center SFB 837 "Interaction Modeling in Mechanized Tunneling", which is funded by the German Science Foundation (DFG). The main purpose of the research conducted in this subproject (SFB 837 B1) was hence to improve the robustness and ductility of concrete by addition of steel fibers against impact und concentrated loads, whereby the mechanical properties of SFRC have been extensively investigated by experimental approach especially under various situations of concentrated loading.

I would first of all want to sincerely thank my supervisor Prof. Dr.-Ing. Rolf Breitenbücher for giving me the opportunity to work on this research project and for his innovative views, professional advices, critical comments and enormous support throughout the entire period.

I would gratefully appreciate Prof. Dr.-Ing. Peter Mark for his willingness to assume the second supervisor and for his friendly support and efforts.

An essential part of this research project was to perform experiments, which would not have been realized so straightforwardly without the support and experience of the colleagues in the Structural Testing Laboratory (KIB-KON) of RUB. I want to thank Dr.-Ing. Hussein Alawieh and Dipl.-Ing. Heiko Rahm for their help and support on the organization of the test execution. Thanks also to Dipl.-Ing. (FH) Michael Plohberger, Ruben Sewald for their technical support and expert execution of the tests.

I also wish to express my gratitude to the rest of the technical staff in KIBKON as well as all my colleagues and the student assistants in the Institute of Building Materials of RUB for their help.

I owe special thanks to my friend Dr.-Ing. Yijian Zhang, who also worked on one of the research projects of the Collaborative Research Center SFB 837, for the close cooperation, the productive discussions and the patience for the proofreading of the preliminary version of this thesis.

Finally, and with all my heart, I would like to thank my parents, my sisters and other family members for their love, support and patience.

Bochum, March 2017 Fanbing Song

# Abstract

The situation of high compressive load transmitted onto limited area of concrete member occurs frequently in a variety of industrial and engineering structures. Hence, numerous investigations have been conducted in the past to study the behavior of concrete under such loading, but mostly of plain and conventionally reinforced concretes. With the increasingly widespread use of steel fibers in the field of structural application, it is therefore of great interest to investigate the performance of steel fiber reinforced concrete (SFRC) subjected to concentrated load.

The objective of the present PhD thesis was to characterize the load-bearing and fracture behavior of SFRC under concentrated loading (i.e. point loading) by means of experimental approach. Based on an extensive literature survey, a comprehensive experimental program containing both non-fiber-related and fiber-related parameters has been proposed and performed under laboratory conditions. The non-fiber-related variables commonly influencing the structural behavior of plain concrete included concrete compressive strength, specimen dimension, area ratio and eccentricity of load. The fiber-related factors specifically affecting the mechanical properties of SFRC included fiber properties (e.g. strength, dimension, geometry and aspect ratio), fiber content and orientation, combination of different fiber types (i.e. hybrid fiber reinforcement). In addition, hybrid concrete systems consisting of both plain and fiber concretes have been produced and tested under the same conditions. The effect of these parameters on the maximum local compressive stress, the stress versus displacement (or deformation) response as well as the failure and crack characteristics of concrete specimens have been presented and evaluated.

Based on the experimental results, it can be concluded that the presence of steel fibers substantially improved the load-bearing behavior of concrete under concentrated load and changed the failure mode of concrete from a brittle to a ductile one. Such improvements could be attained even by incorporating a thin layer of fiber reinforcement as observed in the case of hybrid concrete system. The positive effect of steel fiber on the maximum load-bearing capacity and the post-cracking ductility increased notably with the increase of tensile strength, dimension and content of steel fiber, and thickness of fiber reinforcement layer as well as by using optimized hybrid fiber reinforcement. Generally, the reinforcing effectiveness of steel fibers tended to reduce progressively with decreasing area ratio or with increasing eccentricity of load and specimen dimension. A higher concrete strength led to higher maximum load-bearing capacity, but less ductile post-cracking behavior. The aforementioned benefits provided by steel fiber could, however, only be guaranteed on the condition that a favorable and uniform fiber orientation towards the directions of the acting tensile stresses existed in the SFRC specimen. Moreover, the fiber orientation could be most significantly affected by the casting direction.

The findings acquired here can be used as fundamental information for the composition and optimization of SFRC mixtures, the production of SFRC concrete elements as well as for the constructive design and practical application of SFRC structural members exposed to concentrated load.

# Table of contents

**1 Introduction** ........ 1

1.1 Background and motivation ........ 1

1.2 Objective and strategy ........ 2

**2 State of the Art** ........ 3

2.1 Steel fiber reinforced concrete (SFRC) ........ 3

2.1.1 Introduction ........ 3

2.1.2 Classification of steel fibers ........ 3

2.1.3 Pullout behavior of single steel fiber ........ 5

2.1.4 Fiber distribution and orientation ........ 13

2.1.5 Design and production of SFRC mixture ........ 16

2.1.6 Properties of steel fiber reinforced concrete ........ 18

2.1.6.1 Properties of fresh SFRC ........ 18

2.1.6.2 Properties of hardened SFRC ........ 19

2.2 Concrete under concentrated load ........ 24

2.2.1 Introduction ........ 24

2.2.2 Analysis of tensile stresses ........ 26

2.2.2.1 Plane case of concentrated loading ........ 26

2.2.2.2 Spatial case of concentrated loading ........ 30

2.2.3 Investigation of load-bearing capacity ........ 35

2.2.3.1 Experimental investigations ........ 35

2.2.3.2 Analytical and numerical investigations ........ 46

2.3 SFRC under concentrated load ........ 48

**3 Experimental research** ........ 51

3.1 Scope of experimental research ........ 51

3.2 Materials and specimens ........ 52

3.3 Experimental tests ..... 56
3.3.1 Standard tests ..... 56
3.3.2 Fiber concentration and orientation ..... 56
3.3.3 Concentrated loading tests ..... 58
3.4 Hybrid concrete system ..... 60
3.5 Experimental program ..... 62

**4 Results of experimental investigations ..... 68**
4.1 Properties of fresh and hardened concretes ..... 68
4.2 Concentrated loading tests ..... 70
4.2.1 Influence of area ratio and concrete strength ..... 70
4.2.2 Influence of specimen dimension ..... 80
4.2.3 Influence of fiber property ..... 87
4.2.4 Influence of fiber concentration and combination ..... 94
4.2.5 Influence of fiber orientation ..... 104
4.2.6 Influence of eccentricity of load ..... 114
4.2.7 Hybrid concrete system ..... 124

**5 Conclusions and future perspectives ..... 137**
5.1 Conclusions ..... 137
5.2 Future perspectives and practical recommendations ..... 142

**References ..... 144**

**Appendix A ..... 153**

**Appendix B ..... 164**

# Notations and symbols

**Geometric parameters**

| | |
|---|---|
| a | Width of bearing plate |
| b | Breadth of bearing plate |
| c | Breadth of loaded surface of specimen |
| d | Width of loaded surface of specimen |
| h | Height of specimen |
| $A_{c0}$ | Loaded area (i.e. area of bearing plate) |
| $A_{c1}$ | Cross-sectional area of specimen |
| $A_c$ | Arithmetic distribution area in specimen |
| $R = A_{c1}/ A_{c0}$ | Ratio of areas of specimen cross-section and bearing plate |

**Forces and stresses**

| | |
|---|---|
| P | Concentrated load |
| T | Bursting tensile force |
| $T_y$, $T_z$ | Bursting tensile force in y or z axial direction |
| $\sigma_y$, $\sigma_z$ | Bursting tensile stress in y or z axial direction |
| $\sigma_0$ | Uniform compressive stress |
| q | Allowable bearing stress under loaded area |
| $F_{Ru}$ | Allowable local force |
| $F_{Rdu}$ | Design value of allowable local force |
| $\sigma_{Rdu}$ | Design value of allowable bearing stress |

**Concrete properties**

| | |
|---|---|
| $f_{c,uniaxial}$ | Uniaxial compressive strength of concrete |
| $f_{c,cube}$ | Compressive strength of concrete cube |
| $f_{c,cyl}$ | Compressive strength of concrete cylinder |
| $f_{c,pr}$ | Compressive strength of concrete prism |
| $f_{ct}$ | Concrete tensile strength |
| $f_{cd}$ | Design value of compressive strength of concrete cylinder |

**Others**

| | |
|---|---|
| $f_{s,pr}$ | Compressive strength of sandstone prism |
| $f_t$ | Ultimate tensile strength of steel |

**Experimental symbols**

| | |
|---|---|
| $q_{max}$ | Maximal local compressive stress (i.e. bearing stress) |
| n | Ratio of maximal local compressive stress $q_{max}$ and concrete compressive stress $f_{c,cube}$ |
| | |
| NS | Normal-strength base concrete mixture |
| | |
| d150, d300 | Dimension of specimen: 150 x 150 x 300-mm, 300 x 300 x 600-mm |
| | |
| L | Long, hook-ended normal-strength macrofiber: RC-80/60-BN |
| Lt | Long, thick hook-ended normal-strength macrofiber: RC-65/60-BN |
| Lh | Long, high-strength hook-ended macrofiber: RC-80/60-BP |
| M | Medium, hook-ended normal-strength mesofiber: ZP 305 |
| S | Short, straight high-strength microfiber: FM 13/0.19 |
| | |
| l | Lying wooden mold: 150 x 150 x 300-mm |
| i | Compaction with internal vibrator |
| p | Sampling parallel to casting direction from large concrete beam (300 x 300 x 800-mm) |
| v | Sampling direction perpendicular to casting direction from large concrete beam (300 x 300 x 800-mm) |
| | |
| e | Eccentric load introduction |
| e15, e30 | Uniaxial eccentricity of load: e = 15 mm, e = 30 mm |
| E | Edge loading |
| C | Corner loading |
| | |
| z | Fiber reinforcement layer |
| z50, z100, z150 | Thickness of fiber reinforcement layer: 50 mm, 100 mm, 150 mm |

# 1 Introduction

## 1.1 Background and motivation

In the field of civil engineering, the situation of concentration of load, in which large compressive force is transmitted onto concrete structural member through limited contact area, takes place frequently. Common examples of structural elements subjected to concentrated load are anchorages in post-tensioned concrete members, bearings over piers in bridge structures, stanchions over concrete footings and tunnel lining segments under pressing forces from tunnel boring machine.

Under such concentrated loading situation, a multi-axial stress state containing both longitudinal high compressive stresses and lateral tensile stresses develops immediately under the limited loaded area. If the tensile stresses exceed the concrete tensile strength, concrete damages in the form of cracking and spalling occur and probably lead to the failure of structural members. In order to properly maintain the serviceability, load-bearing capacity and durability of concrete structure within the designed service life, it is of great importance to get a better understanding of the magnitude and distribution of the stresses generated under localized compression.

To this end, a great number of studies on this topic have been conducted in the last decades using theoretical, numerical and experimental approaches. The researches focused either on the analyses of the tensile stresses developed in a concrete member or on the investigations of the load-bearing capacity of concrete. These results have been partially adopted in some design specifications or standards to predict the allowable stresses and further to configure the splitting tensile reinforcement. It should be noted that the studies performed previously dealt mostly with the structural behavior of plain concrete or conventional reinforced concrete, since in practice concrete elements exposed to localized force are usually strengthened with transverse steel rebars (e.g. hoops or stirrups).

Since the 1970s, steel fibers have been increasingly used in diverse concrete structures worldwide. The principal effects of steel fiber in concrete are to transfer the stresses across the cracks after cracking and to retard the growth and propagation of these cracks. Consequently, the load-bearing capacity and the ductility (i.e. toughness) of the quasi-brittle material in the post-cracking stage can be substantially improved. Compared to the conventional reinforcement, fiber reinforcement exhibits distinct advantages as reported in the pertinent literature. For instance, owing to a randomly discrete distribution of fibers in concrete matrix, even concrete in the surface-near regions can be effectively strengthened, which can hardly be reinforced by conventional rebars due to the requirement of a minimum concrete cover.

From the original purpose of crack control, with the development of new fiber types and modern concrete technologies, steel fibers have been nowadays widely applied with load-bearing function in a variety of structural applications, such as in the structural members listed in the first paragraph. Hence, the problem associated with the transmission of localized force emerges inevitably in concrete structural elements partially or fully strengthened with steel fibers. As mentioned above, despite a large number of already existing works on this issue, few attentions have been paid to the performance of steel fiber reinforced concrete (SFRC). Therefore, it is absolutely necessary to systematically investigate the structural behavior of SFRC under concentrated load.

## 1.2 Objective and strategy

The objective of this research project was to characterize the load-bearing and fracture behavior of steel fiber reinforced concrete (SFRC) under concentrated loading (i.e. point loading) through experimental investigation. The results obtained in this work can be used as a basis for the formulation and optimization of SFRC mixtures, the production of SFRC concrete elements as well as for the constructive design and practical application of SFRC structural members subjected to concentrated load.

To obtain an insight into this topic, an extensive literature survey has been conducted in the first place. The first part of the literature review focused primarily on the introduction of the fiber-matrix interfacial bond characteristics, the typical single fiber pullout responses, and the mechanical properties of SFRC under various loading situations. The second part concentrated mainly on the description of the features of two or three dimensional stress distribution in a concrete member subjected to concentrated load, the approaches to estimate the compressive and tensile stresses, and the findings of experimental investigations on the load-bearing behavior of different types of concrete.

On the basis of literature study, a comprehensive experimental program considering various testing parameters has been proposed and implemented (Figure 1.1). In combination with the common factors (non-fiber-related) affecting the structural behavior of plain concrete under concentrated load, the specific variables (fiber-related) influencing the mechanical properties of SFRC have been taken into account. In addition, hybrid concrete systems consisting of both plain and fiber concretes have been produced and tested under the same conditions. The experimental parameters were partially overlapped in some test series in order to study their joint effects. The test results of SFRC specimens have been evaluated and compared with those of plain and hybrid concrete samples so as to provide more solid conclusions and more rational recommendations for the practical application and the future research in this field.

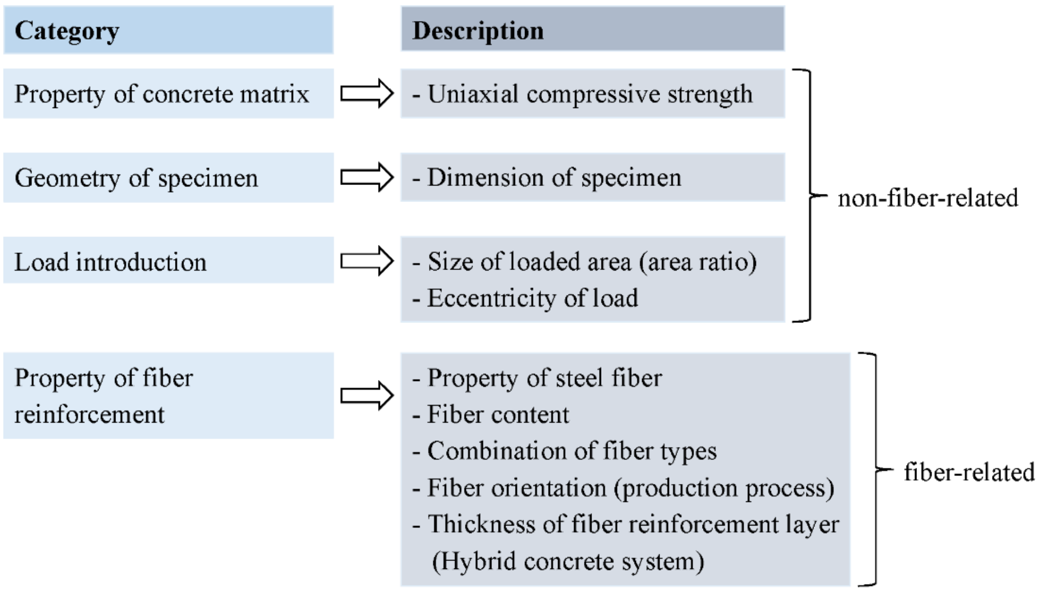


*Figure 1.1: Parameters of the experimental tests under concentrated loading (point-loading)*

# 2 State of the Art

## 2.1 Steel fiber reinforced concrete (SFRC)

### 2.1.1 Introduction

In the last decades, steel fiber reinforced concrete (SFRC) has been widely used throughout the world to partially or completely replace the conventional reinforcing bars in various applications, such as flat slabs, sewer pipes, industry floors and tunnel structures (shotcrete, precast tunnel lining segments). The principal effect of adding steel fibers is to improve the load-bearing capacity of concrete beyond the peak load, i.e. to increase the ductility or toughness of the quasi-brittle material. This is mainly due to the fact that fibers bridging the cracks transfer the stresses across these cracks and thus retard the growth and propagation of the cracks. Originally, SFRC was extensively used for crack control (non-structural application). With the development of new fiber types and modern concrete technologies, SFRC (normally with high performance) has been increasingly applied for the total substitution of the conventional reinforcement in concrete structures (structural application).

This chapter is aimed to provide an overview of the current scientific and technological state of SFRC. It starts with the introduction of the types and properties of the commonly-used steel fibers for the building industries and their corresponding production processes. In the following section, the fiber-matrix interfacial bond characteristics as well as the typical single fiber pullout behavior will be presented at a micro level with the purpose to give a better understanding of the mechanical behavior of SFRC at a macro level. Parameters influencing the pullout behavior of an individual fiber will be discussed, as they may further affect the mechanical properties of SFRC. To achieve a good quality and economic construction with SFRC, specific attentions should be made in the design and production procedures of SFRC mixtures and will be outlined in the next section. In the final section, the mechanical behavior of SFRC will be described for diverse loading situations concerning various key parameters.

### 2.1.2 Classification of steel fibers

Steel fibers commonly used for the building industries vary widely in geometric and mechanical properties. The variation or classification of steel fibers depends largely on the manufacturing process and the raw material. In ASTM 820/ A820M-11 (2011), five types of steel fiber are defined with specific requirements on the application for SFRC: the fibers shall be straight or deformed, and of types I (cold-drawn wire), II (cut sheet), III (melt-extracted), IV (mill cut), and V (modified cold-drawn wire). Similar classifications of steel fibers can also be found in other international standards, for example in DIN EN 14889-1 (2006). The steels used for producing fibers are usually carbon steels or alloy steels. Steel fibers frequently used for SFRC are primarily manufactured from cold-drawn steel wire, cut from thin steel sheet, and milled from steel block. In the following, the common manufacturing processes and the properties of the corresponding fibers will be presented.

**Mill cut fibers**
This kind of steel fibers is cut from a rolling steel block through a rotating milling cutter (Figure 2.1). They typically have a sickle-shaped cross-section and are twisted in the longitudinal axis, as shown in Figure 2.4-a. These fibers have a smooth external surface and a rough internal surface. With this geometric deformation and surface roughness, a better bond with the matrix can be achieved. Through

variations of cutter shape and feed rate, it is possible to produce fibers with different thickness and width. The mill-cut fibers have normally a length of 32 mm and a thickness of about 0.4 mm; the tensile strength is around 800 MPa (König et al. 2001).

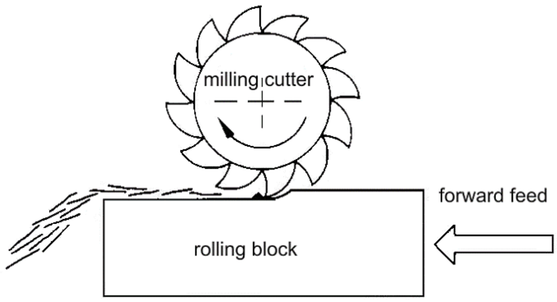


*Figure 2.1: Manufacturing of mill cut steel fibers (Maidl 1991)*

**Sheet cut fibers**

In this manner of production, thin steel sheet is first deformed under compression, and then cut into single fibers (Figure 2.2). By means of the applied compressive pressure, fibers of this kind can be produced either with embossing or with end hook (Figure 2.4-b and -c) in order to improve the fiber-matrix bond. These fibers usually have a length of 25-45 mm and the rectangular cross-sectional dimensions are typically in the range of 0.5-1.0 mm thick and 1.5-2.5 mm wide; the tensile strength is relatively low and varies from 400-800 MPa, depending on the raw material used (König et al. 2001).

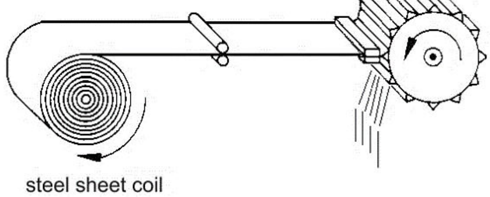


*Figure 2.2: Manufacturing of sheet cut steel fibers (Maidl 1991)*

**Cold drawn fibers**

In the production of cold-drawn steel fibers, steel wire is first drawn to a requested diameter, and then deformed and cut by two rollers rotating in opposite directions (Figure 2.3). Using this production technique, fibers can be produced in a variety of geometries and dimensions. This kind of fibers has usually a round cross-section, typically with diameters from 0.15 to 1.0 mm and length from 6 to 60 mm; the tensile strength normally ranges from 1000 to 1400 MPa, or over 2000 MPa when produced with high-strength steel wire (König et al. 2001).

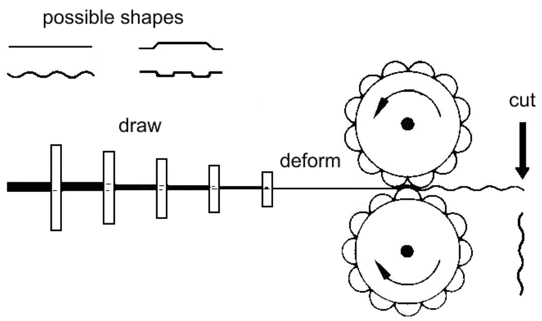


*Figure 2.3: Manufacturing of cold drawn steel fibers (Maidl 1991)*

To ensure a sufficient bond with the matrix, modern cold drawn fibers are solely manufactured with mechanical deformations. As demonstrated in Figure 2.4-d and -e, the deformations may extend along the full length of fiber (e.g. crimped, indented or twisted), or be restricted to the end portions (e.g. end-hooked or end-buttoned), or even in a combined manner. Aside from the mechanical deformation, the aspect ratio, defined as the ratio of the fiber length to diameter, also exerts great influence on the bond strength of fiber in the matrix. The typical values of aspect ratio are in the range of 30 to 100. Generally, the higher the aspect ratio is, the higher the bond strength is, in particular for smooth straight fibers. However, with increasing aspect ratio and/or degree of geometric deformation (e.g. crimped fibers), fibers tend more easily to agglomerate during the mixing process. For an easier handling and mixing during the production of SFRC, some fibers (mostly hook-ended fibers) are collated into bundles of around 30 pieces using a water-soluble glue, which dissolves during the mixing process (Figure 2.4-f).

*a) mill cut fibers* *b) embossed sheet cut fibers* *c) hooked sheet cut fibers*

*d) hooked cold drawn fibers* *e) hooked and indented cold drawn fibers* *f) hooked cold drawn fibers in bundle*

*Figure 2.4: Different types of steel fibers with various geometries and dimensions (Rümmelin 2005)*

Among the different types of steel fiber, fibers made of cold drawn wire distinguish themselves in their high tensile strength, good ductility, diverse geometric shapes and mechanical deformations, which contribute to a much stronger bond with the concrete matrix (see discussions in Section 2.13). Thus, cold drawn fibers, in particular hook-ended fibers, are more widespreadly used in the production of SFRC for various structural applications.

### 2.1.3 Pullout behavior of single steel fiber

As is well known, the primary benefit of adding steel fibers into concrete is to improve the post-cracking behavior (i.e. toughness or energy absorption) of the quasi-brittle material especially under tension. This is because fibers bridging the cracks transfer the stresses across these cracks and thus retard the crack opening and propagation, which is essentially achieved by deforming and/or pulling out of the fiber (Alwan et al. 1991). The bridging efficiency or capacity of stress transfer of a single fiber depends highly on the fiber-matrix bond characteristics (Mandel et al. 1987), which are principally governed by the properties of fiber (e.g. geometry, strength and dimension) and matrix (e.g. strength), the properties of the fiber-matrix interface zone and the fiber orientation with respect to the loading direction.

It is generally agreed that the mechanical behavior of SFRC in the post-cracking stage is to a large extent influenced by the pullout behavior of the fibers. Therefore, it is of great importance to first investigate the fiber-matrix bond mechanisms at a micro level in order to get a qualitative estimation of the mechanical behavior of SFRC at a structural (i.e. macro) level as well as to develop rational design procedures for SFRC with good performance. To assess the effectiveness of a given fiber as a medium of stress transfer, the single fiber pullout tests have been frequently conducted, whereby the fiber slip is monitored as a function of the applied fiber load (Banthia & Trottier 1994).

**Characteristics of fiber-matrix interface**

Since the pullout behavior of a single fiber is strongly influenced by the properties of the fiber-matrix bond characteristics, it is necessary to look into the microstructure of the fiber-matrix interface zone, also known as Interfacial Transition Zone (ITZ). The microstructure of the ITZ around the fibers in a mature composite is qualitatively similar to that of the aggregate-matrix interface zone, however, considerably distinct from that of the matrix paste away from the interface. The formation of this ITZ is closely related to the particulate nature of the fresh matrix, resulting in the formation of water-filled spaces around the fibers through bleeding and entrapment of water as well as inefficient packing of finest cement particles around the fiber surface (Bentur & Mindess 2007). Thus, the matrix in the vicinity of the fiber is partially filled with hydration products and much more porous than the bulk matrix paste.

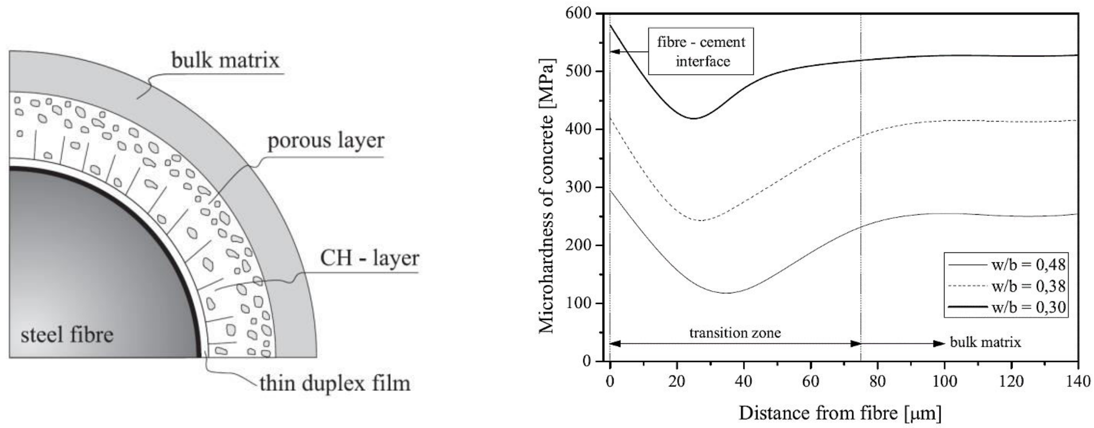


*Figure 2.5: Left, interfacial transition zone in steel fiber reinforced concrete, adapted from Cunha (2010) according to Bentur and Mindess (1990); right, results of microhardness tests of cement matrix paste around steel fibers, adapted from Cunha (2010) according to Wei et al. (1986)*

As illustrated in Figure 2.5-left, the fiber surface is directly surrounded by a dense layer of CH (Calcium-Hydroxide), backed up with a porous layer consisting of CSH (Calcium-Silicate-Hydrate) and some ettringite. The CH layer can be as thin as 1 μm (duplex film), or over several μm (Bentur et al. 1985). The width of the ITZ (duplex film, CH layer and porous layer of CSH and ettringite) determined by SE Microscope typically ranges from 20 to 70 μm (Bentur & Mindess 1990, Li & Stang 1997). The higher porosity and lower strength of the ITZ have been experimentally proved by microhardness tests (Figure 2.5-right), indicating the lowest values of the tests in a zone at a certain distance from the fiber surface (Wei et al. 1986). It can also be seen that the lower the w/b-ratio is, the higher the hardness and the smaller the ITZ is. Additionally, the density of the ITZ can be enhanced through adding micro-fillers, such as micro-silica fume (Bentur & Mindess 2007, Cunha 2010).

**Components of fiber-matrix bond**

The bond between the fiber and the surrounding matrix is very complex and consists of several components that interact with each other during the pullout process. According to Naaman and Najm (1991) and Naaman (2000), these include:

a) physical and/or chemical adhesion

In SFRC, the adhesive bond between fiber and matrix is controlled by the properties of ITZ and is comparatively weak or even nonexistent. This elastic bond exists, as long as the interfacial shear stresses due to loading do not exceed the fiber-matrix shear strength.

b) friction

For straight (smooth) fibers, after the adhesive bond is fully destroyed, the interfacial frictional stresses resist the pullout load. These stresses are generated by the abrasion and compaction processes inside and long the interfacial zone through slipping of a fiber along its channel (Markovic 2006). The frictional resistance remains effective until the complete pullout of fiber.

c) mechanical bond

The mechanical bond can only be induced by fibers with surficial or geometric deformations. After the breakdown of the adhesive bond, the mechanical bond is activated through the plastic deformation of fiber. However, the mechanical bond remains effective only up to a certain fiber slip determined by fiber geometry. Afterwards, the frictional resistance prevails the pullout process.

d) fiber-to-fiber interlock

Bond of this kind exists normally in SFRC with very high fiber concentrations, for instance SIFCON (Slurry Infiltrated Fiber Concrete) or SIMCON (Slurry Infiltrated Mat Concrete), where fibers are in direct contact with each other even before the addition of concrete. For SFRC with modest fiber contents, bond of this kind shall not be considered when analyzing the pullout process.

**Typical pullout responses of straight and end-hooked fibers**

As mentioned above, the mechanisms of bond for straight and end-hooked fibers are quite different, resulting in distinct pullout behavior. A qualitative overview of the total pullout responses for straight and end-hooked fibers aligned to the loading direction is given in Figure 2.6.

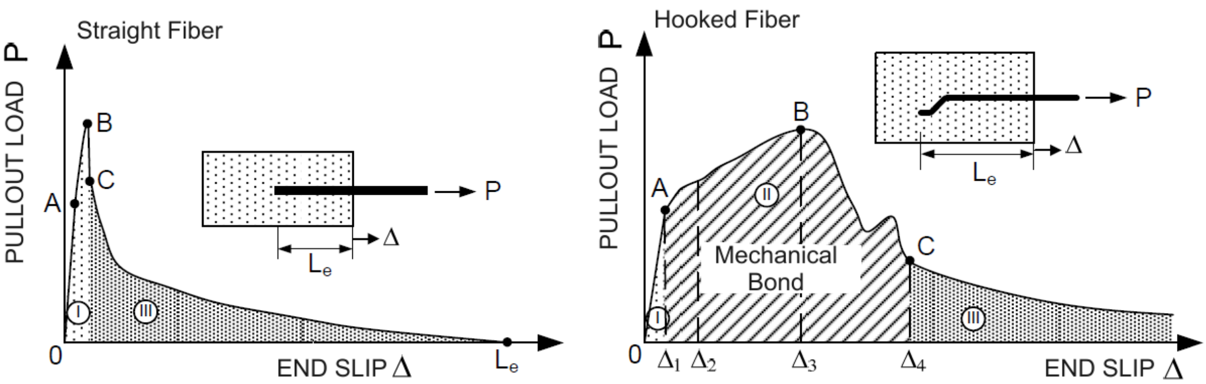


*Figure 2.6: Typical pullout responses of straight fiber (left) and end-hooked fiber (right), adapted from Strack (2007) according to Naaman (2004)*

For a straight fiber, the total pullout resistance is basically constituted of two components: I) adhesive and III) frictional bond. As shown in Figure 2.6-left, the pullout curve is characterized by a steep ascending branch up to a peak load, followed by a sudden drop up to a load level at which the load stabilizes and declines gradually with increasing slip, as a result of the decreasing embedded fiber length $L_e$ (Naaman 2004). Observed more closely, prior to the critical load at point A, the adhesive bond still exists over the entire embedded length. After exceeding the interfacial bond strength at point A, the debonding process is initiated, starting from the outer edge of the fiber channel. From a micromechanical point of view, the debonding can be regarded as a micro-cracking process inside and along the interfacial transition zone and propagates with the ongoing process of fiber pullout. The debonding occurs in the weakest region of the ITZ, which is located at a certain distance from the fiber surface (Wei et al. 1986). In this stage (from point A through B to C), the pullout load is resisted by combined adhesion and static friction. Beyond point C, at which the full debonding is attained, the pullout load is then exclusively counteracted by the dynamic friction.

The pullout behavior of an end-hooked fiber is similar to that of a straight fiber before the full debonding at point A (Figure 2.6-right). Afterwards, the pullout process is, however, supplemented by the mechanical anchorage (II, here induced by the two hinges of the hook). After the complete debonding beyond point A, the two hinges tend to progressively deform, associated with a considerable increase in pullout load. At the peak load (point B), the both hinges are deformed, accompanied by a decrease in load with increasing slip under further pullout. From point C, at which the two hinges have been straightened, the pullout process is controlled by the frictional resistance, similar to that of straight fiber. Since the hook is normally not completely straightened, the frictional resistance of hooked fiber is higher than that of straight fiber. To explicitly describe the successive processes of the plastic deformation of hook under pullout, Alwan et al. (1999) developed a theoretical model (Figure 2.7).

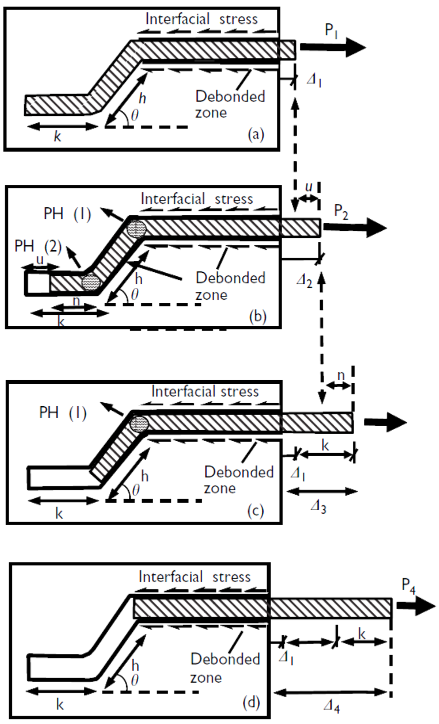


*Figure 2.7:*
*a) hooked steel fiber at onset of complete debonding;*

*b) hooked steel fiber during mechanical anchorage with two plastic hinges; PH is plastic hinge.*

*c) mechanical anchorage with one plastic hinge (corresponding to the maximum pullout load);*

*d) hooked steel fiber at onset of frictional pullout, adapted from Bentur and Mindness (2007) according to Alwan et al. (1999)*

It must be noted that Figure 2.6 only presents a qualitative comparison of the different pullout behavior of aligned straight and end-hooked fibers. Generally, deformed fibers exhibit drastically higher pullout load and energy absorption than straight fibers, as will be presented in the next section based on the results obtained from various experimental investigations. Meanwhile, effects of various parameters influencing the pullout behavior of steel fiber will also be discussed there.

**Influential factors on the pullout behavior**

***Properties of steel fiber***

Since the pullout resistance of straight (smooth) fibers is relatively low, attempts have been made to manufacture diverse deformed fibers to effectively increase the bond strength. Although in general the pullout resistance can be significantly improved through the mechanical anchorage provided by deformed fibers, their pullout responses are quite different among each other due to the various types of geometrical deformations.

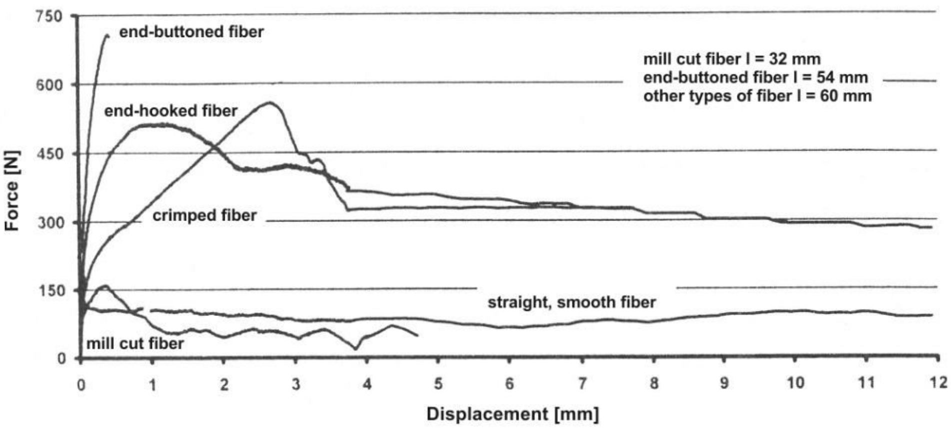


*Figure 2.8: Typical bond-slip curves of various types of steel fibers embedded with respect to the pullout load direction (Feyerabend 1995)*

It can be clearly seen in Figure 2.8 that due to the extremely strong anchorage fibers with end buttons exhibited the highest pullout load, however, failed without exception under pullout. This is consistent with the observations of Banthia & Trottier (1994) and Breitenbücher et al. (2014). Compared to hooked fibers, crimped fibers can either be completely pulled out with higher pullout load and toughness (Naaman & Najm 1991, Banthia & Trottier 1994 and Feyerabend 1995) or ruptured prematurely in the first pullout phase (Breitenbücher et al. 2014), largely depending on the amplitude of the wave and the matrix strength. To obtain a ductile post-cracking behavior of concrete, instead of fiber fracture at small fiber slip (i.e. crack width), fibers should rather be pulled out of the matrix with a high utilization of its tensile capacity. Therefore, more concerns should be given when choosing the type of deformed fibers for a given concrete matrix.

In addition, a new type of high-strength steel fibers with a polygonal cross section resulted from twisting mechanical treatment has been developed and used in structural applications (Naaman 2003). Fibers of this kind exhibit a successive increase in pullout load up to very large slip, indicating a slip-hardening response provided by the untwisting process under pullout, whereas common deformed fibers mentioned above show slip-softening pullout behavior. Generally, fibers with larger diameter exhibit higher pullout resistance primarily due to the fact that more energy is required for the plastic deformation, as reported by Groth (2000) and Breitenbücher and Song (2014); and this is also valid for fibers made of steels with higher yield strength (Breitenbücher & Song 2014). Roughing the surface of fibers increases the fiber-matrix bond strength through enlarging the interfacial contact area, thus leading to higher peak pullout load (Stengel 2009, Breitenbücher & Song 2014); however, it is rather more pronounced for straight fibers (Breitenbücher & Song 2014).

***Properties of concrete***
As was pointed out above, the strength of the fiber-matrix bond is strongly affected by the quality of the ITZ, in other words, by the quality of the concrete matrix. The latter can be influenced by a variety of factors, such as w/b-ratio (i.e. strength), additives (e.g. fly ash, silica fume, metakaoline), type of cement, maximum grain size and packing density of aggregates as well as the presence of secondary fibers in the pullout medium.

Reducing the w/b-ratio results in a marked increase in the density and strength of the bulk matrix as well as the matrix in the ITZ (Wei et al. 1986), and consequently enhances the pullout resistance of steel fibers (Naaman & Najm 1991, Banthia & Trottier 1994 and Alwan et al.1999). For instance, an increase in the peak load of about 30-40% was observed by hooked fibers when decreasing the w/b-ratio from 0.45 to 0.29 (Markovic 2006). Compared to normal-strength hooked steel fibers, the variation of concrete strength had larger influence on the pullout responses of high-strength fibers (Breitenbücher et al. 2014). Additionally, extremely high strength of concrete matrix may increase the probability of fiber fracture, especially for fibers with high degree of geometric deformation (e.g. crimped or end-buttoned).

Another common technology to increase the density and strength of concrete is to incorporate fine filler materials, such as fly ash, silica fume, metakaoline and limestone filler, into the matrix. In comparison with cement particles, particles of some of these materials exhibit a considerably smaller grain size. For instance, the average grain size of microsilica is in the range of 0.1-0.5 µm compared to that of cement with 10-25 µm (Maibaum & Hüttl 2004). Thus, the empty spaces between cement particles and fibers in the ITZ can be effectively filled. In addition to the filling effect, materials like silica fume and metakaoline show pozzolanic reactivity, which results in partial substitution of CH crystals with much stronger CSH crystals during the hydration reaction. A further improvement in fiber-matrix interfacial bond could be provided by the 2-3 times increased shrinkage through adding silica fume, leading to a higher clamping pressure on the fiber (Li & Stang 1997).

Results from single fiber pullout tests have been shown that increases in peak pullout load and toughness of hooked fibers were up to approximately 50% by adding about 10% by weight of silica fume for conventional concrete (Robins et al. 2002). For modern reactive powder concrete, through adding 30% by weight of silica fume, increases in pullout load of 14% and in toughness of approximately 100% were observed for straight fibers (Chan & Chu 2004). Mixing fly ash into concrete matrix can also improve the total pullout resistance similarly due to the pozzolanic reaction (Naaman & Najm 1991, Guererro & Naaman 2000).

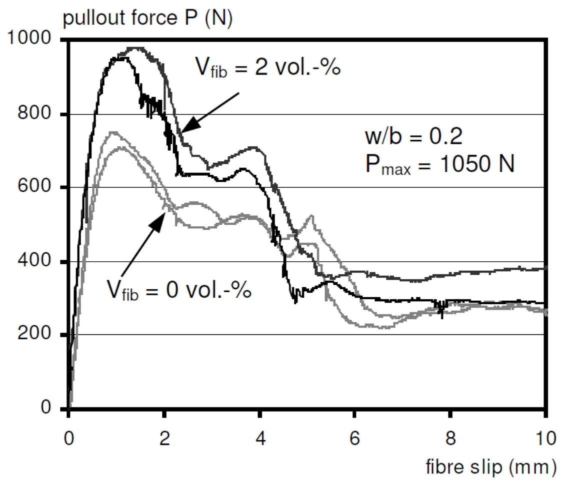


*Figure 2.9: Influence of addition of short straight fibers in the pullout medium on the pullout behavior of long hooked fiber (Markovic 2006)*

Adding secondary short fibers, either steel or polypropylene, in the pullout medium does improve the total pullout resistance of primary long fibers. This beneficial effect is mainly attributed to the interaction between short and long fibers by crack control. According to Markovic (2006), after the initiation of microcracks around the long fibers, the short fibers bridge those microcracks and retard their further opening and propagation, which increases the energy (i.e. pullout force) needed to deform the hook of the long fibers in the first pullout stage. As shown in Figure 2.9, an increase in the peak force of about 40% for long hooked fibers (Dramix RC-80/60-BP) was observed in an pullout medium with 2% by volume of short straight fibers (Dramix OL 13/0.20, 13 mm in length and 0.2 mm in diameter).

***Embedded length***

For fibers with same perimeter, higher pullout resistance regarding peak load and total work can be expected with the increase of embedded length due to enlarged interfacial contact area between the fiber and the surrounding matrix. However, this holds mostly true for straight, smooth fibers (Li & Stang 1997). For fibers with end deformation (e.g. hooked, buttoned or flattened fibers), the geometric deformation at the fiber ends exerts more predominant influence on the pullout behavior than the embedded length, as experimentally confirmed by several investigators (Naaman & Najm 1991, Hamoush et al. 2010 and Breitenbücher & Song 2014). Figure 2.10 shows the pullout responses of aligned straight and hooked fibers with an identical diameter as a function of embedded length.

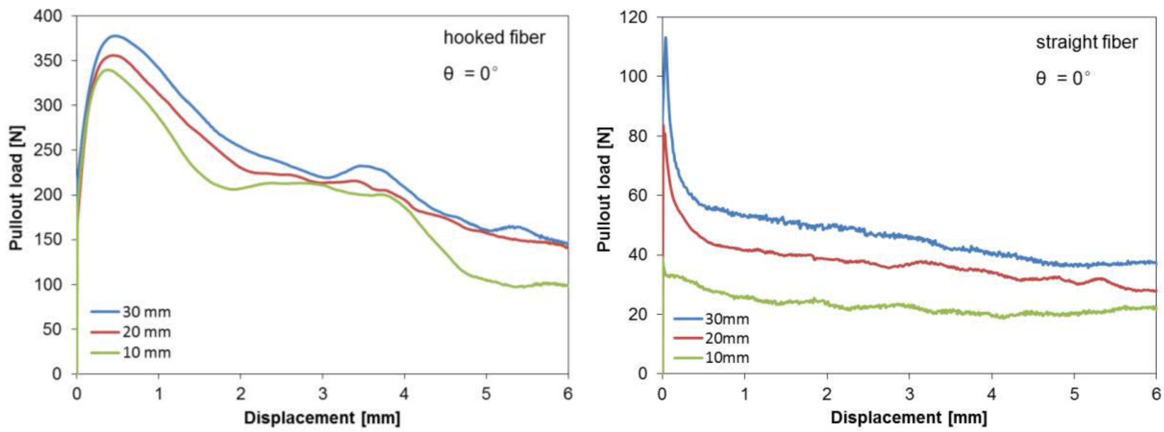


*Figure 2.10: Influence of various embedded length (10 mm, 20 mm and 30 mm) on the pullout responses of aligned straight and hooked fibers with the same diameter (Breitenbücher & Song 2014)*

To fully utilize the mechanical anchorage, a minimum embedment length of hooked fibers in the matrix is required, as pointed out by Robins et al. (2002) and Naaman (2004). The minimum embedment length depends largely on the dimension of the hook and the matrix strength, which should be greater than the length of the hook. Otherwise, it may result in marked reduction of maximum pullout load in conjunction with inferior pullout work due to the fracture of the matrix wedge behind the hook. For fibers deformed along the entire length (e.g. crimped or indented fibers), the pullout performance also improves with increasing embedment length, however, rather due to the correspondingly increased number of mechanical deformations (Naaman & Najm 1991).

***Embedded angle***

In a SFRC structure element, steel fibers disperse randomly in the matrix because of the inherent discontinuity of the fibers and the current production technology of fiber concrete. This implies that most of the fibers in the concrete orient with a certain angle with respect to the loading direction. After the crack initiation, inclined fiber bridging a crack is subjected to local flexure at the crack surface due to geometrical constraints; consequently, a complex state of stress will be developed, that is to say, flexural stresses will be induced in the fiber associated with compressive stresses in the matrix (Bentur

& Mindess 2007). This generally results in an increase in the total pullout resistance consisting of the bending resistance of the fiber itself and the frictional resistance along the fiber channel. Thus, the pullout behavior of inclined fibers differs from that of aligned fibers, and depends largely on the interactions between the rigidity and ductility of the fiber and matrix with the inclination angle, as shown in Figure 2.11 for hooked steel fibers with similar dimension, but different tensile strength under complete pullout (Breitenbücher et al. 2014).

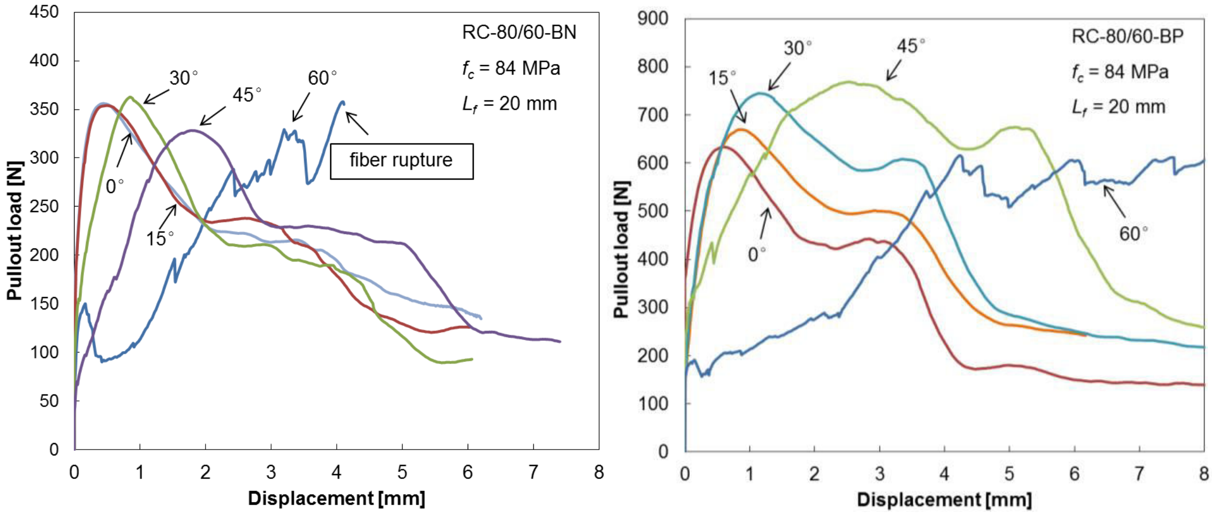


*Figure 2.11: Influence of fiber inclination angles (0º, 15º, 30º, 45º and 60º) on the pullout responses of normal-strength hooked fibers ($f_t$ = 1225 MPa, left) and high-strength hooked fibers ($f_t$ = 2600 MPa, right) with an embedded length of 20 mm in high-strength concrete*

Due to the additional pullout resistance, the peak pullout load of inclined fibers, not only hooked and crimped (Banthia & Trottier 1994, Robins et al. 2002 and Breitenbücher & Song 2014) but also straight fibers (Naaman & Shah 1976, Ouyang et al. 1994), is generally higher than that of aligned fibers even at a very large inclination angle of 60º. This phenomenon is more pronounced for high-strength fibers (Figure 2.11-right).

With increasing fiber inclination, the pullout displacement corresponding to the peak load increases drastically, ranging from 0.45 to 4.95 mm (Figure 2.11). In terms of serviceability and durability, the maximum allowable crack width is designed (by code) smaller than 0.4 mm in most concrete structures (Naaman 2004). Since the maximum pullout load achieved by large fiber displacement or slip does not reflect the real performance of fibers in the SFRC structures, one should observe the pullout response of fiber at an appropriate slip or crack width (It is commonly assumed that the crack width is similar to the fiber slip). In order to compare the fiber efficiency between inclined and aligned hooked fibers at a certain inclination, the tensile stress ratio $\sigma_{inclined}/\sigma_{aligned}$ was determined and compared at fiber slips of 0.1 mm, 0.25 mm, 0.5 mm and 1.0 mm (Breitenbücher & Song 2014). It has been established that except for the large fiber slip of 1.0 mm, fibers with inclination angles up to about 15º showed the highest stress ratio or fiber efficiency. A significant decrease was observed for larger values of inclination angle, independent of fiber tensile strength. The observation made here confirmed the previous findings of Banthia and Trottier (1994) and Robins et al. (2002).

During the pullout process of inclined fibers, other phenomena in the form of matrix spalling and/or fiber rupture may arise. For inclined fibers, additional compressive stresses derived from the pullout force are exerted on the concrete matrix wedge, where the fiber enters the matrix. With increasing embedment angles, the effect of this stress concentration magnifies significantly, resulting in an increase of localized matrix crushing and spalling at the fiber exit point in conjunction with larger fiber slip. This effect was particularly pronounced in the case of high-strength steel fibers, as experimentally confirmed by Breitenbücher et al. (2014). Meanwhile, due to high stress concentration in the fiber at the exit point, fiber rupture is more likely to occur in the case of hooked fibers, especially for large angles beyond 45º (Banthia & Trottier 1994, Breitenbücher & Song 2014), or for fibers with normal tensile strength (Breitenbücher & Song 2014).

***Pullout rate***

Banthia and Trottier (1991) observed an increase in peak pullout load of about 10-40% for hooked fibers when increasing the loading rate from 0.0085 to 2.12 mm/s. Similar observations have been made by Abu-Lebdeh et al. (2010) on the basis of a number of single fiber pullout tests in VHSC (Very High-Strength Concrete, 133-196 MPa). They revealed that the increase in loading rate (from quasi-static 0.021 to seismic 25.4 mm/s) substantially increased both the peak load and total pullout work of hooked fibers with high and normal strengths, but had no noticeable effect on smooth fibers. All highly deformed steel fibers such as flattened-end or twisted fibers ruptured in high pullout rate, although they exhibited remarkably high peak load. Contradictory results reported by Kim et al. (2008) implied that high-strength hooked fiber showed no appreciable rate sensitivity at seismic loading rate, compared to high-strength twisted fiber. Additionally, no fiber fracture was observed for both types of fiber.

***Temperature***

Based on results of single fiber pullout tests at 22 ºC and -50 ºC, Banthia (1991) concluded that the pullout occurring at -50 ºC always registered high values of peak loads than the pullout at 22 ºC for both crimped and hooked steel fibers. The latter exhibited even a more substantial increase in energy absorption. This may be attributed to the fact that both cement paste and carbon steel are stronger at -50 ºC than at 22 ºC. The addition of microsilica led to a considerable reduction in peak load and absorbed energy at -50 ºC, possibly due to matrix fracture or splitting during the pullout process caused by the extreme brittleness of matrix with microsilica at -50 ºC.

### 2.1.4 Fiber distribution and orientation

One of the advantages of fiber reinforcement, compared to conventional reinforcement, is its ability to withstand tensile loads from any direction based on the assumption that fibers are uniformly distributed and randomly oriented throughout the concrete matrix (Holschemacher et al. 2011). Unfortunately, the assumed uniform distribution and three-dimensional orientation of fibers can hardly be guaranteed in practice due to a variety of factors, such as fiber geometry and content, manner of fiber addition, rheological properties of concrete, casting procedure, vibration procedure, geometry and size of mold, and existence of reinforcing bars. More information about the variables influencing the fiber distribution and orientation can be found in the works of Strack (2007), Bentur & Mindess (2007) and Cunha (2010).

Consequently, the mechanical properties of SFRC can be considerably affected. As shown in Figure 2.12, the stress-displacement responses of drilled SFRC cylinders under uniaxial tensile loading are strongly influenced by the geometry of specimen (mold) and sampling direction (fiber orientation) with respect to the casting direction.

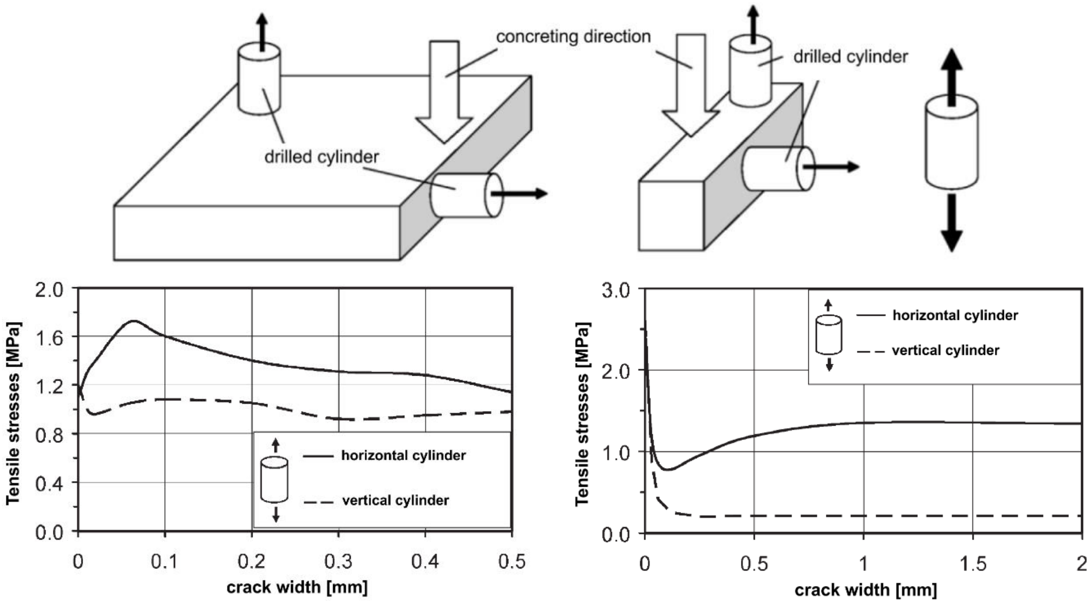


*Figure 2.12: Influence of specimen geometry and sampling direction on the tensile behavior of SFRC cylinders, adapted from Rosenbusch (2004) according to Lin (1999) (left) and Barragan (2003) (right)*

As is well-known, the efficiency of a given fiber (i.e. resistance of the fiber against pullout) is strongly affected by the embedment angle with respect to the pullout load, in other words, its orientation towards the direction of the principal tensile stresses. Therefore, when evaluating the performance of the fibers in a SFRC structural member, the distribution and orientation of the fibers must be taken into consideration. More specifically, the bridging or reinforcing effect of the steel fibers (i.e. effectiveness of fiber reinforcement) in a SFRC cross-section is governed by the interactions of the number of fibers intersecting an active crack and their orientation towards the crack surface. In the literature (Fanella & Krajcinovic 1985, Soroushian & Lee 1990), the following equation is commonly proposed to predict the number of fibers per unit cross-sectional area of concrete:

$$N_f = \eta \cdot \frac{V_f}{A_f} \qquad \textit{Eq. 2.1}$$

where
$N_f$ = number of fibers per unit area
$V_f$ = volume fraction of steel fibers in concrete
$A_f$ = cross-sectional area of steel fibers
$\eta$ = fiber orientation factor

To obtain a homogeneous fiber distribution and a notably efficient fiber reinforcing effect, according to Vodicka et al. (2004), a sufficient minimum fiber content is required, which is estimated to be in the range from 30 to 40 kg/m³. This is due to the fact that with a relatively low fiber content the probability or number of fibers crossing an active crack becomes low. For a well-designed SFRC mixture, an acceptably low variability in the fiber distribution can be possibly achieved through proper production technology including mixing, handling, placing and finishing procedures (Taerwe et al. 1999).

Depending on the boundary conditions, fibers can orient three, two and even one-dimensionally (3-D, 2-D and 1-D) in the matrix. In the more common case, the fiber orientation can be expressed by a combination of predominant 3-D and 2-D fiber orientation arrangements (Stroeven 1986). The aforementioned fiber orientation factor is generally used to describe the effects of fiber orientation, which is the average ratio, for all possible fiber orientations, of the projected fiber length in the tensile stress direction to the embedded fiber length. A schematic illustration of determining the orientation factor is presented in Figure 2.13.

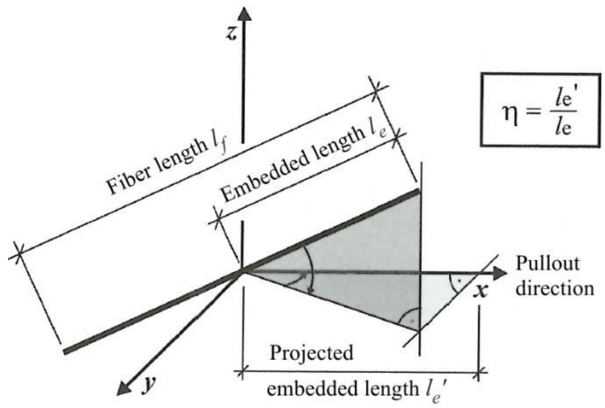


*Figure 2.13: Schema for determining the fiber orientation factor η (Holschemacher et al. 2011)*

*Table 2.1: Typical values of η for three, two and one-dimensional fiber orientation*

| Fiber orientation | Orientation factor η |
|---|---|
| 3-D | 0.200…0.667 |
| 2-D | 0.375…0.785 |
| 1-D | 0.825…1.000 |

The typical values of η given in the literature (Naaman et al. 1973, Fanella & Krajcinovic 1985, Maidl 1991 and Lin 1999) vary with the degrees of fiber orientation, as summarized in Table 2.1. According to Soroushian and Lee (1990), the actual orientation factor would fall between the 2-D and 3-D values and exhibit a tendency from 3-D to 2-D orientation in horizontal planes with the increase of mold height and/or fiber length as well as vibration energy.

The values of orientation factor imply that 3-D oriented fibers exhibit relatively lower capacity of stress transfer compared to fibers with 2-D or 1-D orientation. This is principally based on the fact that for the 1-D orientation all fibers are aligned to the direction of load and develop their full fiber efficiency, whereas in the 3-D case fewer fractions of the fibers contribute to the stress transfer. However, it cannot simply assert that a 2-D or 1-D orientation of fibers in the matrix is more advantageous for a concrete structure. Apart from other factors, the effectiveness of fiber reinforcement depends strongly on the main acting direction of the loads applied on a concrete structural member and the orientation of the fibers in the loaded areas with respect to the direction of the principal tensile stresses. For example, for structural members primarily subjected to flexure a preferential 2-D or 1-D orientation towards the direction of the tensile stresses in the bending zone is undoubtedly beneficial, whereas for structural elements subjected to loads from unpredictable directions a 3-D fiber orientation is much more advantageous.

Furthermore, for a given concrete structural member, it is possible to purposefully influence the fiber orientation in the matrix by means of e.g. varying casting procedures and/or rheological properties of concrete, and thus to optimize the effect of fibers on the mechanical behavior of concrete, as reported by Stähli et al. (2008) and Barnett et al. (2010).

As the fiber distribution and orientation have strong impact on the mechanical behavior of SFRC, it is of great importance to develop feasible techniques to effectively monitor the quality of SFRC. Recently, various experimental methods based on different measuring principles have been developed and adopted to qualitatively or quantitatively determine the fiber distribution (or content in a unit volume) and/or orientation in fresh and/or hardened SFRC (Table 2.2). Note that, each method has its inherent advantages and disadvantages in terms of cost, measuring accuracy, practicability and reproducibility etc., which should be evaluated for the selection and application in practice.

*Table 2.2: Some experimental methods to determine the fiber distribution and orientation*

| Methods | FD[1)] | FO[2)] | F-SFRC[3)] | H-SFRC[4)] | Quotations |
|---|---|---|---|---|---|
| Wash-out/<br>Manual counting | yes | no | yes | yes | DIN EN 14721<br>Soroushian & Lee (1990) |
| Optical section/<br>Image analysis | yes | yes | no | yes | Grünewald (2004)<br>Bernasconi et al. (2012) |
| Ferro-magnetic induction | yes | yes | yes | yes | Breitenbücher & Rahm (2007)<br>Torrents et al. (2012) |
| AC-IS<br>(Alternating current-impedance spectroscopy) | yes | yes | no | yes | Woo et al. (2005)<br>Ozyurt et al. (2006) |
| X-Ray scan | yes | yes | no | yes | Robbins et al. (2003)<br>Vandewalle et al. (2008) |
| 3D-CT scan<br>(computerized tomography) | yes | yes | no | yes | Stähli et al. (2008)<br>Schuler & Sych (2009) |

[1)] Fiber Distribution; [2)] Fiber Orientation; [3)] Fresh-SFRC; [4)] Hardened-SFRC

### 2.1.5 Design and production of SFRC mixture

**Design of SFRC mixture**

Since steel fiber is basically regarded as a sort of concrete additives, the volume-based design procedure for plain concrete is still applicable in the design of SFRC mixtures. For relatively low fiber content (< 40 $kg/m^3$), no further modifications on the mix composition of plain concrete are necessary (Schulz 2000, Bentur & Mindess 2007 and Breitenbücher 2012). For high fiber content, some aspects with emphasis on the workability should be taken into account in the mix design procedure of SFRC.

In general, incorporating steel fibers into concrete matrix results in a stiffer mixture. To ensure adequate workability of SFRC mixtures, it is commonly recommended to increase the cement weight by approximately 10% (Kooiman 2000) and the percentage of fine aggregate (ACI 1996). This is essentially due to the enlarged internal surface caused by adding fibers, which needs to be wrapped by fine particles. It is also recommended to adjust the ratio of fine to total aggregate volume between 40 to 60% to attain an optimum packing density (Kooiman 2000). Limiting the amount of coarse aggregate and the maximum grain size $d_{g,max}$ leads to a more random and uniform dispersion of fibers in the matrix (Figure 2.14) and thus significantly reduces the probability of fiber balling.

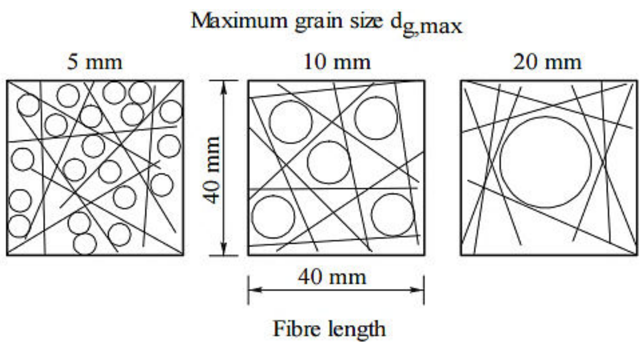


*Figure 2.14: Effect of maximum grain size on the fiber distribution and orientation (Johnston 1996)*

In addition, the workability of SFRC mixture depends significantly on the concentration and aspect ratio of fiber. With increasing fiber content and/or aspect ratio, the workability decreases remarkably, as demonstrated in Figure 2.15. Moreover, the potential of fiber balling increases as well. The typical fiber concentrations for SFRC range from around 30 to 160 kg/m³, depending on the properties of fibers and specific requirements of applications. Therefore, when composing the SFRC mixture, the content and aspect ratio of fiber need to be properly selected and proportioned in conjunction with other concrete components for a given project.

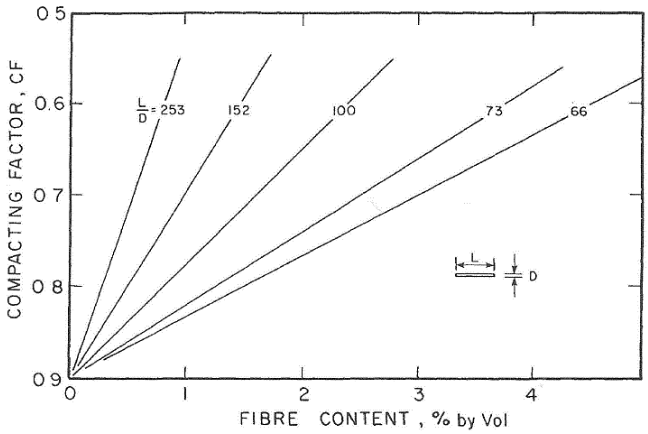


*Figure 2.15: Effect of fiber content and aspect ratio on the workability of concrete, as measured by the compacting factor (Edgington et al. 1974)*

Fly ash is commonly used to partially replace the cement and to enhance the workability owning to its pozzolanic reactivity and spherical shape. High dosage of water reducing admixture may be required to provide better workability of SFRC mixtures.

The American Concrete Institute recommended a guideline containing the range of proportions of the relevant concrete components (Table 2.3). However, it must be noted here that the values listed in Table 2.3 should only be used as reference values. In other words, the design procedure of a SFRC mixture for a given project should be processed individually based on the specific requirements on the type and content of fibers, workability, concrete strength and durability.

*Table 2.3: ACI guideline for normal weight SFRC mix design (ACI 1996)*

| **Mix parameters** | **$d_{max}$ = 10 mm** | **$d_{max}$ = 19 mm** | **$d_{max}$ = 38 mm** |
|---|---|---|---|
| Cement (kg/m³) | 355-600 | 300-355 | 280-415 |
| w/c-ratio | 0.35-0.45 | 0.35-0.50 | 0.35-0.55 |
| Percent of fine to coarse aggregate | 45-60 | 45-55 | 40-55 |
| Entrained air content, percent | 4-8 | 4-6 | 4-5 |
| Fiber content, vol. percent | | | |
| Deformed fiber | 0.4-1.0 | 0.3-0.8 | 0.2-0.7 |
| Smooth fiber | 0.8-2.0 | 0.6-1.6 | 0.4-1.4 |

**Production of SFRC mixture**
SFRC can usually be produced with technology and equipment currently used for conventional concrete. However, to ensure a random and uniform dispersion of fibers, special attentions should be given to the mixing, transporting, placing, compacting and finishing procedures of SFRC. In the mixing stage, fibers should be gradually added free of clumps either manually or automatically (i.e. by conveyor belt or compressed air) to a fluid mix (wet concrete with a softer consistency as desired). Afterwards, additional

mix time is required to properly disperse the fibers. For instance, the extra mix time is in the range of 1-2 min for common concrete mixers (Breitenbücher 2012). Alternatively, for mass production, fibers can be added simultaneously with the fine aggregate through a conveyor belt to the concrete mix and mixed in the normal manner (ACI 1993).

Generally, transporting and placing of SFRC can be accomplished with most conventional equipment. As stated previously, incorporating steel fibers into a plain concrete mixture adversely affects the workability of the fresh mix. Certainly, the workability can be improved by adjusting the mix composition or adding a superplasticizer. Yet, the improved workability of the fresh SFRC in combination with the pouring and flowing direction greatly affects the fiber orientation (Kooiman 2000).

Use of vibrator allows easy placing of the relatively stiff and unworkable SFRC. However, vibration, in particular external vibration, can initiate a material flow in the mold possibly resulting in a preferential fiber orientation perpendicular to the direction of vibration. In the case of excessive vibration, the probability of fiber segregation increases.

The finishing operations of SFRC are essentially the same as for ordinary concrete, unless high demands on the surface quality in terms of evenness and smoothness are made. Since fibers tend to protrude at corners and edges, more care must be taken regarding techniques and workmanship (ACI 1993).

### 2.1.6 Properties of steel fiber reinforced concrete

#### 2.1.6.1 Properties of fresh SFRC

The main detrimental effect of steel fibers on the properties of the freshly mixed concrete is the reduction of its workability including the flow capacity (or mobility) and compactability. For a given mix composition, the flow capacity of a SFRC mixture is the function of the volume percentage $V_f$ and aspect ratio l/d of the fiber (Eq. 2.2). Obviously, the flow capacity proportionally decreases with the increase of fiber concentration and aspect ratio (Hemmy 2003):

$$\text{Flow capacity} = (l/d)^2 . V_f \qquad \textit{Eq. 2.2}$$

Although vibration facilitates the placing and handling work of the fresh SFRC mixture, in some extreme cases an adequate compaction or consolidation may still hardly be insured even with extra vibration energy and time. This leads to a less dense matrix with higher air avoids and a less bond with reinforcing bars. Additionally, excessive vibration causes other problems, as previously pointed out. This may further adversely affect the strength and other material properties of the hardened SFRC.

Nonetheless, the cohesive capacity and the green strength of the fresh concrete mix can be improved by adding steel fibers. For shotcrete mixed with steel fibers, lower dosage of accelerator is thus needed (Schulz 2000). Moreover, the early concrete strength increases dramatically up to 300% due to the addition of fibers (Maidl 1991), however, this effect declines with ongoing hydration process.

The workability or consistency of SFRC with low or intermediate fiber contents can be determined by flow spread method; from a fiber content of 60 kg/m³, slump test is suggested to evaluate the workability (Holschemacher et al. 2011). In USA and UK, either the VeBe test or the Inverted Slump-Cone test is recommended rather than the conventional slump measurement for assessing the workability of a stiff fresh SFRC mixture (ACI 1996).

#### 2.1.6.2 Properties of hardened SFRC

Besides the factors controlling the mechanical behavior of non-fibrous concrete (e.g. mix composition, maximum aggregate size, geometry and size of specimen, method of preparation and loading rate), the properties of hardened SFRC are essentially governed by the properties of fiber (e.g. type, geometry, strength and aspect ratio), fiber content as well as distribution and orientation of fibers in the matrix. Although steel fibers affect the mechanical properties of hardened SFRC under all modes of loading, their effectiveness in improving strength and toughness varies quite widely. This is basically attributed to the inherent bonding mechanisms of steel fibers in the concrete matrix, as extensively discussed in Section 2.1.3. Hence, fibers are especially effective in direct tension, and in flexure, shear, impact and fatigue, however, less effective in compression (Bentur & Mindess 2007). In the following, the effects of adding steel fibers on some relevant mechanical properties of hardened SFRC will be presented for the cases of static and dynamic loading, respectively.

**Static mechanical properties**

***Compression***

In the normal range of fiber concentrations up to 1.5% by volume, the static compressive strength of concrete is only slightly influenced by the addition of steel fibers. In the pertinent literature (Johnston 1974, Bonzel & Dahms 1981 and Fanella & Naaman 1985), the observed increases in strength are in the range of 0 to 15%, compared to plain concrete. Even very high fiber contents do not enhance the compressive strength dramatically as expected. Strangenberg (1986) reported an increase in strength up to 22% with a fiber volume fraction of 3%. Sun et al. (1999) observed a maximum 50% increase in strength by SFICON with fiber contents of up to 10% by volume. This modest increment may be due to the difficulties in achieving full compaction by very high fiber concentrations.

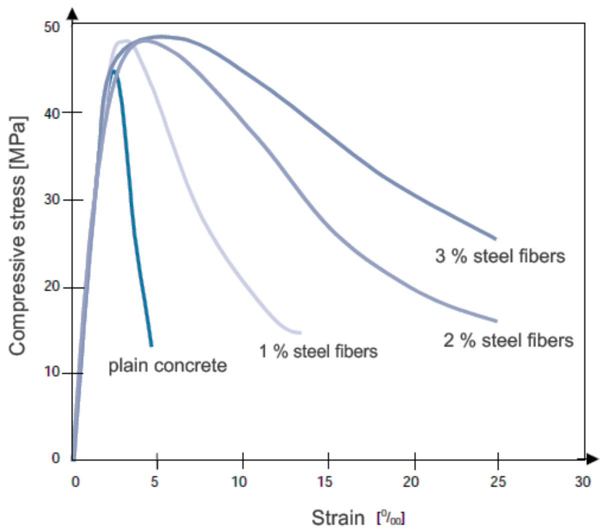


*Figure 2.16: Effect of volume percentage of steel fibers on the stress-strain behavior of concrete under compression (Strangenberg 1986)*

Apparently, the improvement in compressive strength is marginally affected by adding steel fibers with normal contents and uneconomically with high concentrations. As demonstrated in Figure 2.16, the major effect of steel fibers is to increase the post-cracking ductility (or energy absorption) through crack-bridging and stress transfer. This effect is more distinct for a preferred fiber orientation perpendicular to the compressive loading (Lin 1999). The failure of SFRC is hence characterized by a more ductile mode instead of a brittle one. Varying the fiber properties, e.g. increasing the aspect ratio of fiber, increases rather the roughness than the strength (Fanella & Naaman 1985).

***Direct Tension***

The direct tensile strength of SFRC with common fiber concentrations is of great dependence on the inherent tensile strength of base plain concrete (König et al. 2001, Holschemacher et al. 2011). The corresponding values are generally of the same order as those of plain concrete, typically ranging from 2 to 4 MPa for normal-strength plain concrete (Papworth 1997). After the formation of cracks with a crack width > 50 µm (Kützing 2000), fibers are then activated and contribute to stress transfer, resulting in a ductile post-cracking behavior. If the fibers are geometrically deformed or orient preferentially in the direction of the tensile stresses, this effect is much more considerable. From a fiber concentration of 2% by volume, the tensile strength of SFRC tends to increase steadily with increasing aspect ratio, however, indicating only intermediate percentage values (Johnston & Coleman 1974).

Depending on the fiber-matrix interactions under pullout, the stress-strain curves of SFRC after cracking exhibit either a strain-softening or a strain-hardening characteristic. Once the fiber content in a SFRC mixture is greater than the critical fiber content, a strain-hardening post-cracking behavior associated with multiple-cracking of the matrix can be expected. In this case, the ultimate tensile strength is much greater than the first-crack tensile strength even at large values of crack width. SFRC of this kind is technically termed as (Ultra) High Performance SFRC. The critical fiber content is a function of fiber-matrix bond, aspect ratio of fiber and fiber orientation; the typical values are in the range of 1-3% by volume for short fibers (Bentur & Mindess 2007). Meanwhile, the composition of the SFRC mixture should also be carefully formulated. Additionally, a strain-hardening behavior of SFRC beyond peak load can be achieved by using twisted steel fibers (Naaman 2003). SFRC produced with twisted fibers distinguishes itself by its superior post-cracking behavior with a post-cracking tensile strength of about 13 MPa from SFRCs strengthened by fibers with other shapes (Figure 2.17).

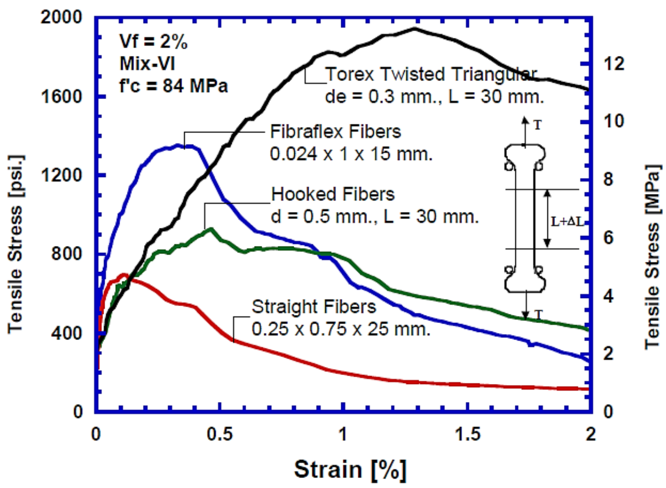


*Figure 2.17: Typical responses in tension of dog-bone specimen reinforced with different shapes of steel fiber (Naaman 2003)*

***Flexure***

Due to the complexity of specimen preparation for the direct tension test, the flexural or bending test is more frequently conducted in practice to characterize the post-cracking behavior of SFRC. The magnitude of the flexural strength of SFRC is of the same order as that of plain concrete at low fiber fractions (Papworth 1997, ACI 1996). However, once the critical fiber content has been reached, the ultimate flexural strength tends to increase remarkably associated with a deflection-hardening post-cracking behavior. For some high-performance SFRCs with fiber volume ≥ 2%, the increases in flexural strength have been reported more than 100% (Bentur & Mindess 2007), and exceeded the value of 45 MPa or even higher (Richard & Cheyrezy 1994, Chavillard & Rigaud 2003).

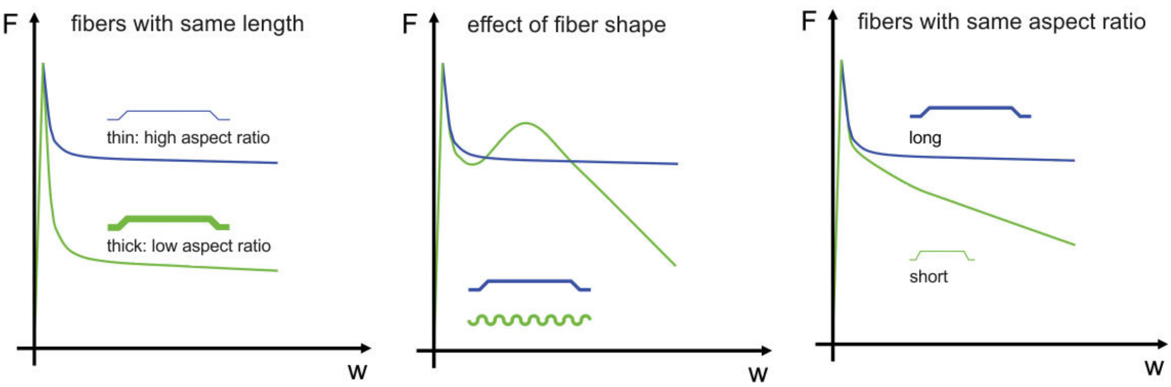


*Figure 2.18: Influence of fiber types on the load-deflection response of SFRC (Vitt et al. 2009)*

In addition to fiber content, factors that control the fiber pullout or tensile behavior exert significant influence on the load-deflection response as well, as illustrated in Figure 2.18. It can be observed that fibers with better bond characteristics, such as high aspect ratio, high strength and proper mechanical anchorage (i.e. end-hook) exhibit better post-cracking behavior or higher post-crack strength at high deflections under otherwise identical conditions. Certainly, a preferential orientation of fibers with respect to the direction of the tensile stresses in the flexure zone is beneficial.

As has been stated previously, the main purpose of adding steel fibers to concrete is to improve the toughness rather than the strength. Hence, flexural tests are commonly used to evaluate the toughness of SFRC. Generally, the flexural toughness is defined as the area under the load-deflection or load-displacement curve out to some particular deflections or displacements, or out to some points where the load has fallen back to certain predefined percentages of the peak load. However, the procedures of defining and determining the toughness of SFRC are quite different per code or guideline. A detailed comparison on this issue was summarized by Bentur and Mindess (2007).

***Shear***

Steel fibers are widely used as secondary shear reinforcement in conjunction with conventional reinforcing bars (Schulz 2000, Bentur & Mindess 2007). Limited test data dealing strictly with the shear behavior of SFRC indicate that steel fibers generally improve the shear resistance of concrete. Barr (1987) reported the increases in shear strength varying from negligible to 30% for a fiber volume fraction of 1%, whereas other investigators (Valle & Buyukozturk 1993, Sun et al. 1999) observed higher increases in strength or roughness with similar fiber contents. The scatter of the test results depends strongly on the properties and orientation of the fibers in the shear failure zone as well as the “non-standardized” shear testing technique. Nonetheless, steel fibers in sufficient quantity and with high fiber efficiency can impart residual shear strength and distributed cracking with reduced crack width to concrete and prevent catastrophic diagonal tension failure of concrete structural members.

***Modulus of elasticity and Poisson´s ratio***

For fiber concentrations less than 2% by volume, the modulus of elasticity and Poisson´s ratio of SFRC are insignificantly affected by the fibers. For the common fiber volume less than 1%, the increases in elastic modulus are only up to 5%, compared to plain concrete (Edgington 1974, König et al. 2001). In practice, these two physical quantities are generally taken as equal to those of a non-fibrous concrete or mortar with similar mix proportions (ACI 1996).

***Shrinkage***

The beneficial effect of steel fibers is to control the amount of cracks and the crack width rather than to reduce the drying shrinkage. For instance, the drying shrinkage was reduced by about 15-20% with 1%

by volume of steel fibers (Swamy & Stavrides 1979). With 0.5% by volume of steel fibers, the maximum crack width was reduced by 80% and the average crack width by 90% (Malmberg & Skarendahl 1978). Regarding the influence of fiber properties, fibers with higher aspect ratio are more capable of reducing the drying shrinkage (Chern & Young 1990).

***Creep***

Generally, the creep behavior of concrete is marginally affected by the addition of steel fibers with volume content less than 1% (ACI 1996). This is essentially due to the fact that no macrocracking is initiated during the creep process (Bentur & Mindess 2007). However, test results indicating either slight increase in creep (Balaguru & Ramakrishnan 1988) or even significant increase up to 40% (Houde et al. 1987) have been reported. The differences in the test procedures may be a possible reason for the large scatter of the obtained test results.

**Dynamic mechanical properties**

***Fatigue behavior***

Analogous to the performance in the static loading, steel fibers improve the fatigue properties of concrete more significantly in direct tensile or flexural fatigue loading than in compressive fatigue loading. It should be noted that the flexural fatigue strength of SFRC is usually lower than the static strength, typically in the range of 65-90% at 2 million cycles of loading (Baston et al. 1972, Ramakrishnan et al. 1987). For a given concrete composition, high fiber concentration or fibers with geometric deformations lead to better performance in flexural fatigue tests (in terms of higher endurance limits, finer cracks and much more energy absorption to failure) than fibers with high aspect ratio. To ensure a positive effect of steel fibers, a minimum critical fiber volume between 0.5 and 0.75% was proposed by Johnston and Zemp (1991). Papworth (1997) has reported the influence of fiber content and shape on the flexural fatigue strength of concrete, as illustrated in Figure 2.19. A comprehensive overview of the fatigue behavior of plain and fiber reinforced concretes was given by Lee and Barr (2004).

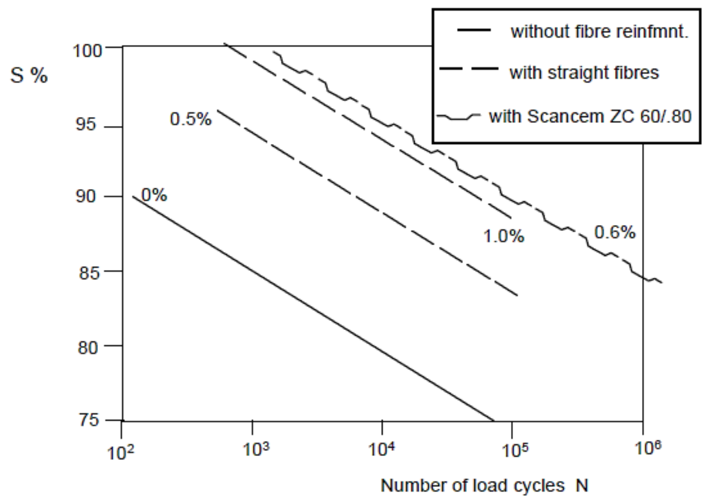


*Figure 2.19: Effect of fiber content and shape on the flexural fatigue behavior of concrete (Papworth 1997)*

***Behavior under impact loading***

Compared to plain concrete, SFRC shows remarkably better impact resistance in terms of strength and fracture energy under impact loading induced by e.g. explosive charges, drop-weight impact machines or modified Charpy machines. Generally, increasing the fiber volume results in higher impact strength and fracture energy to some extent (Bindiganavile et al. 2002). Aside from that, the impact behavior of SFRC appears to be strongly dependent on the details of the specimen geometry and the test arrangement

(Bentur & Mindess 2007). Hence, it seems to be quite difficult to compare the obtained results from the various experiments. Nonetheless, a general description on the impact responses of SFRC can still be given (ACI 1996): For normal-strength concrete under flexural impact loading, the peak loads for SFRC were about 40% higher than those obtained for plain concrete. For high-strength concrete, a similar improvement was also observed. The fracture energy can be increased through adding fibers by a factor of about 2.5 for normal-strength concrete and by a factor of about 3.5 for high-strength concrete. Additionally, the resistance of SFRC under impact loading is much higher than that under static loading. For instance, the increases in peak loads were in the range of 2 to 3 times for normal-strength concrete and about 1.5 times for high-strength concrete. Regarding the fracture energy, the increases were about 5 and 4 times, respectively.

**Durability of SFRC**

Factors affecting the durability of conventionally reinforced concrete influence the durability performance of SFRC as well. Note that, the addition of fibers does bring some benefits. For instance, steel fibers increase the water impermeability of concrete due to their capability of reducing crack width (Hemmy 2003). Air-entrained SFRC exhibits significantly higher freeze-thaw resistance than air-entrained non-fibrous concrete due to the sufficient fiber-matrix bond (Schnell & Ackermann 2009).

Regarding the durability of SFRC, more attentions have been paid to the corrosion resistance not only in uncracked but also in cracked state of SFRC. In the first case, the corrosion of steel fibers is only confined to the surface-near layer of concrete, mostly resulting in discoloration of the surface, but no any loss of strength or toughness. In carbonated SFRC, the corrosion of fibers does not propagate into the concrete more than 2 mm, and for concrete highly saturated with chloride ions, no more than 5 mm (Böhme et al. 2009). This is consistent with the earlier observations of Schupack (1986) and Mangat and Gurusamy (1988). In addition to the conditions of the aggressive environment, the extent of corrosion of steel fibers in cracked SFRC depends largely upon the crack width. For a crack width less than 0.2 mm, only limited corrosion of steel fibers occurs (Hannant 1975, Granju & Baluch 2005). However, from a crack width of 0.2 mm, both the strength and roughness of SFRC can be considerably impaired due to the reduced cross-section of fibers induced by corrosion and the increasing fiber fracture under pullout, as has been experimentally confirmed by Hannant (1978) and Mangat and Gurusamy (1987). Alternatively, it is recommended to use galvanized steel fibers or fibers made of alloyed or stainless steel to reduce the probability of (severe) corrosion in aggressive environment.

Compared to reinforcing bars, steel fibers show considerably lower sensitivity to corrosion in concrete. This insensitivity is governed by several mechanisms concluded by Bentur (1998):

- lower tendency to cracking and increased tendency for self-healing of cracks in fiber reinforced concrete composites;
- small diameter of fiber which does not lead to the formation of sufficient rust for scaling of the concrete;
- lack of electrical conductivity because of the discrete nature of the steel fiber;
- improved matrix microstructure and denser interfacial transition zone in the fibers compared with conventional steel.

## 2.2 Concrete under concentrated load

### 2.2.1 Introduction

When introducing concentrated load into a structure, large compressive force is transmitted onto limited contact area of concrete. The force can be introduced in the form of either strip-loading (plane case, 2-D) or point-loading (spatial case, 3-D) into the structure. The situation of concentrations of load occurs frequently in concrete elements of diverse building and engineering structures, such as anchorages in post-tensioned concrete members, bearings over piers in bridge structures, stanchions over concrete footings and tunnel lining segments under pressing forces from tunnel boring machine.

Under such concentrations of load, a multi-axial stress state develops immediately under the limited loaded area, as illustrated in Figure 2.20. The region directly beneath the load is subjected to high compressive stresses (i.e. bearing stresses). Due to the diffusion of the longitudinal compressive stresses, lateral tensile stresses (i.e. bursting stresses), along directions perpendicular to the load, are induced over some distance to the load, and they tend to gradually diminish. Meanwhile, local tensile stresses, known as spalling stresses, may occur along the loaded edge of concrete member, despite the fact that they normally do not cause any spalling of the concrete (Breen et al. 1994).

In the case of strip-loading, the width of the loaded area is equal to one of the member width and thus the longitudinal compressive stresses spread only in one axial direction into the structural member, whereas for point-loading the compressive stresses propagate in a radial direction. From a distance approximately equal to the width of cross-section, the state of stresses in the structure exhibits a uniform stress distribution. Due to the disturbance of the ordinarily assumed linear strain distribution, the stresses within this distance cannot be determined by the ordinary bending theory (Leonhardt & Mönnig 1986). This region is referred to as “St. Venant disturbance zone”.

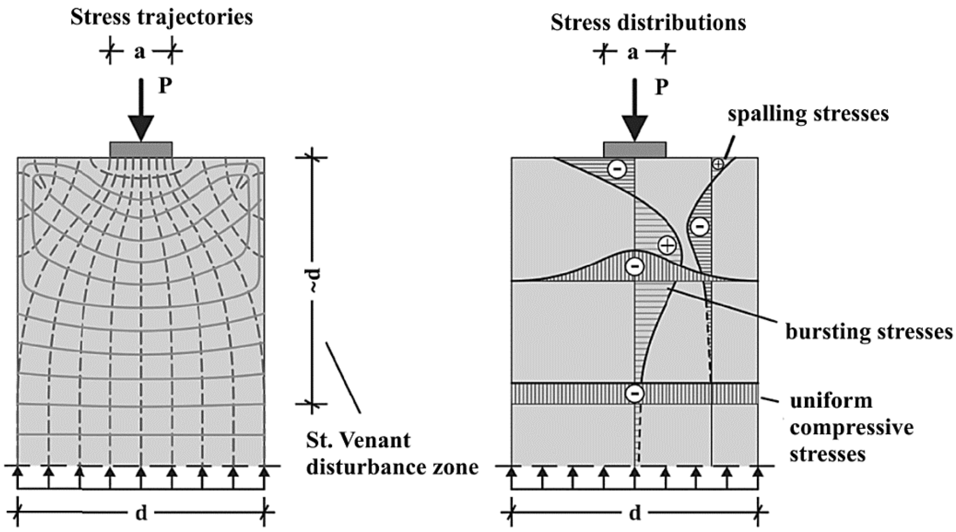


*Figure 2.20: Flow of stresses in concrete member under localized force: a) stress trajectories; b) stress distributions (Wichers 2013)*

Owing to the confinement effect of the surrounding non-loaded concrete, the allowable compressive stresses generated in the multi-axial stress state are much higher than those in the uniaxial loading situation (Leonhardt & Mönnig 1986). The magnitude of the compressive stresses is highest directly beneath the load and decreases rapidly with the increasing distance to the load (Breen et al. 1994). The magnitude and distribution of the lateral tensile stresses depend largely on the extent of the concentrations of load, in other words, the ratio of unloaded area to loaded area. If the bursting stresses exceed the concrete tensile strength, concrete damages in the form of cracking and spalling occur.

In practice, concrete structural members under concentrated load are commonly reinforced with steel reinforcement (e.g. hoops or stirrups) to withstand the tensile stresses. An alternative approach is to incorporate steel fibers into the concrete matrix, since fibers intersecting the cracks transfer the stresses across these cracks and inhibit the crack opening and propagation. Furthermore, the structure can be effectively strengthened even in the concrete cover, which can hardly be reinforced by conventional reinforcement due to the adherence to a minimum concrete cover.

The load-bearing behavior of concrete structural member under concentrated load can be affected by a great number of factors, as summarized in Table 2.4.

*Table 2.4: Influential parameters on the load-bearing behavior of concrete structural member under concentrated load (Wichers 2013)*

| **Category** | **Factor** |
|---|---|
| Geometry of structure element, load introduction | ▪ Geometry of structure element, slenderness<br>▪ Shape and size of loaded area<br>▪ Eccentricity, inclination of compressive force<br>▪ Recess under load surface<br>▪ Number of load introduction points |
| Constructive boundary conditions | ▪ Stiffness of bearing plate<br>▪ Restraint of lateral strain<br>▪ Elastic interlayer<br>▪ Thickness of concrete cover |
| Properties of concrete | ▪ Uniaxial compressive and tensile strength<br>▪ Young´s modulus, Poisson´s ratio<br>▪ Multi-axial material behavior<br>▪ Post-cracking behavior and tensile strength<br>▪ Pre-damage |
| Splitting tensile reinforcement | ▪ Mechanical parameters of rebar<br>▪ Type of rebar (ribbed/ smooth)<br>▪ Bending shape/ formation<br>▪ Ratio of reinforcement<br>▪ Constructive design |

The problems associated with the transmission of localized force into a structure member have been investigated intensively in the last several decades. Based on a comprehensive literature research, it was found that the previous studies on this issue focused either on the analysis of the tensile stresses or forces developed in the concrete or on the investigation of the load-bearing capacity of concrete. The results of the theoretical or experimental studies have been partially adopted in some design specifications or codes to predict the allowable stresses and to configure the splitting tensile reinforcement. In the next sections, highlights of the previous works concerning these two aspects will be discussed.

### 2.2.2 Analysis of tensile stresses

To analyze the tensile stresses (i.e. bursting and spalling stresses) in a structure member subjected to concentrated load, enormous studies have been carried out in the past by means of diverse methods:

- Linear elastic studies, such as theory of elasticity
- Photoelastic investigations
- Non-linear analyses
- Finite element analyses
- Experimental studies

In the following paragraphs, some relevant findings of these studies will be presented in detail for plain and reinforced concretes in plane and spatial cases, respectively. Influences of various parameters on the magnitude and distribution of the tensile stresses will be discussed as well.

#### 2.2.2.1 Plane case of concentrated loading

**Concentric loading situation**

Mörsch (1924) presented an equilibrium-based model to illustrate the load path in a concentrically loaded member. He simply assumed a parabolic distribution of the lateral tensile stresses and summarized the longitudinal compressive stresses as a resulting stress (Figure 2.21). Under this assumption the bursting force T can be determined approximately by using the strut-and-tie model:

$$T = 0.25 \cdot P \cdot (1 - \frac{a}{d}) \qquad \textit{Eq. 2.3}$$

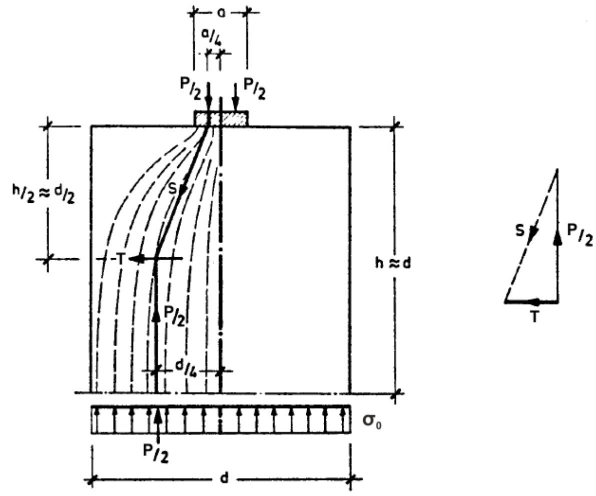


*Figure 2.21: Strut-and-tie model after Mörsch (Mörsch 1924)*

Guyon (1953) initially applied the 2-D theory of elasticity to theoretically investigate the anchorage zone stresses for members with rectangular cross-section. He determined the distribution of the bursting stresses ahead of a concentric end anchor for various concentration ratios. The values of the integrated bursting stresses showed a good agreement with those obtained from Mörsch´s simple truss solution (Figure 2.22). Since then, a number of linear elastic studies have been carried out for the 2-D problem (Magnel 1954, Iyengar 1960, Hiltscher & Florin 1968 and Leonhardt & Mönnig 1986).

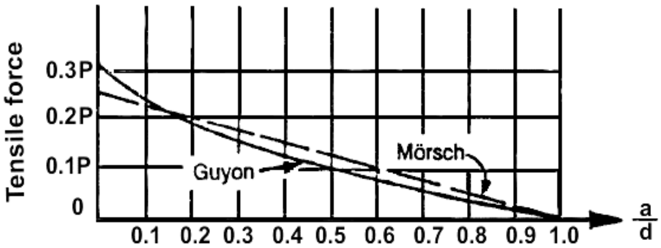


*Figure 2.22: Magnitude of the bursting force after Guyon (Guyon 1953)*

An exact solution to describe the stress state in an elastic half-strip with infinite length was introduced by Iyengar (1960) using the Fourier series. This half-strip was loaded on its narrow side with different ratios of member width d to plate width a. As shown in Figure 2.23, the magnitude of the bursting stresses $\sigma_y$ increased steadily with increasing concentration ratio d/a and it reached the maximum value at d/a = ∞. The bursting force T can be computed as the Integral of the tensile stresses $\sigma_y$.

Based on the Iyengar´s solution, Leonhardt and Mönnig (1986) applied a simplified approach to approximately calculate the bursting force T with:

$$T \approx 0.3 \cdot P \cdot (1 - \frac{a}{d}) \qquad \textit{Eq. 2.4}$$

The maximum bursting force T is approximately equal to 0.25 P under the assumption that d/a > 10 occurs very rarely. They also recommended approaches to configure the splitting tensile reinforcement.

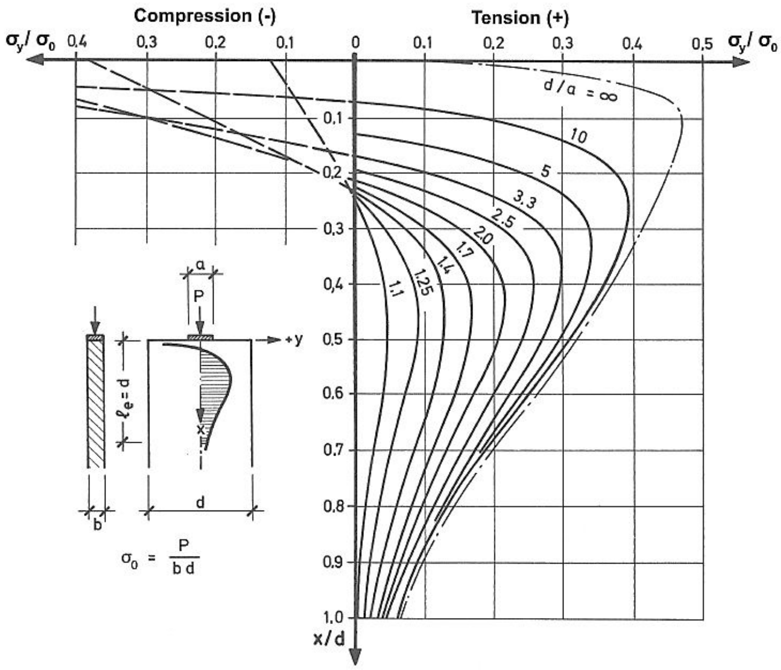


*Figure 2.23: Bursting tensile stresses $\sigma_y$ relative to the uniform stress $\sigma_o$ for different concentration ratios d/a (Iyengar 1960)*

For h/d > 2, Leonhardt and Mönnig (1986) also gave the correlation between the concentration ratio d/a and the magnitude of bursting force T relative to the load P, and the positions of the maximum $\sigma_y$ and $\sigma_y = 0$ relative to the member width d, as shown in Figure 2.24. Using the curves in this diagram, one can design the reinforcement in rectangular-section prism for various concentration ratios.

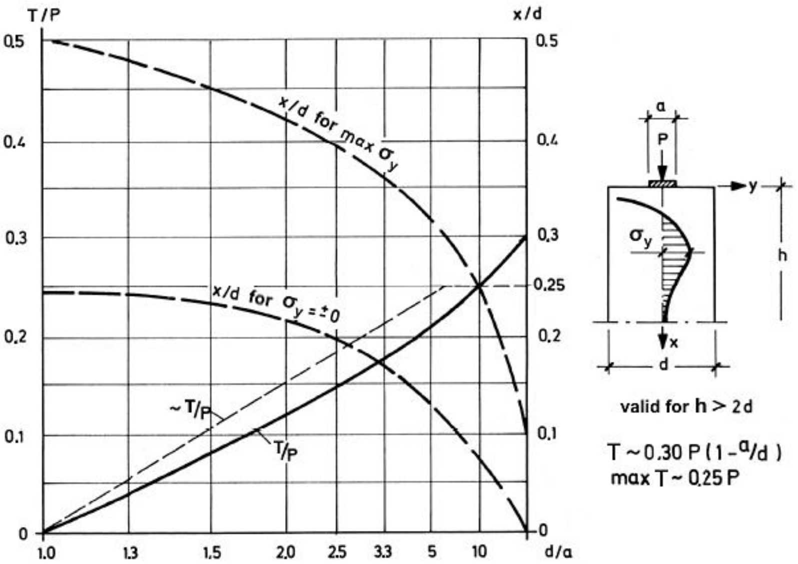


*Figure 2.24: Magnitude of the bursting force T relative to the load P, and the positions of the maximum bursting stress $\sigma_y$ and $\sigma_y = 0$ relative to the member width d for h/d > 2 (Leonhardt & Mönnig 1986)*

Hiltscher and Florin (1968) studied the effect of specimen slenderness for h/d ≤ 2 on the magnitude of the bursting force T. They found a marked reduction in the bursting force with decreasing slenderness h/d due to the increasing restraint of lateral strain caused by the bearing support (Figure 2.25).

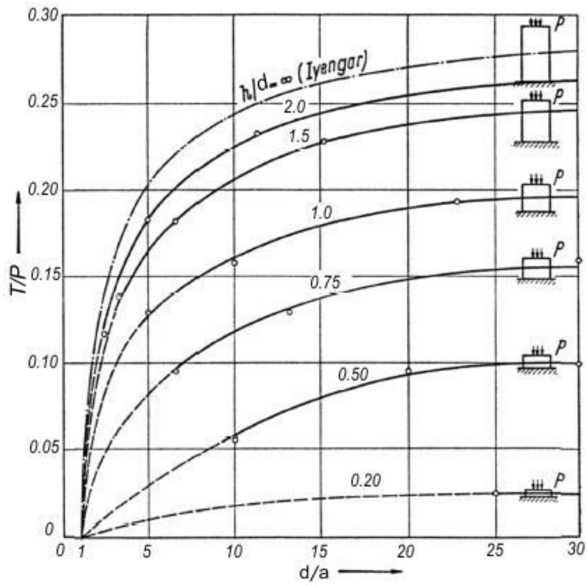


*Figure 2.25: Influence of specimen slenderness h/d on the magnitude of the bursting force T (Hiltscher & Florin 1968)*

Due to the great complexity of obtaining the exact solution based on the theory of elasticity, photoelastic approach was considered. Results of the investigations conducted by Christodoulides (1956) and Hiltscher and Florin (1962) found a good agreement with those obtained from the theoretical studies discussed previously.

The aforementioned studies described the stress state in the region of linear elastic material behavior. In the nonlinear stage, the magnitude and distribution of the stresses appeared to be quite different. Spitz (1977) conducted a nonlinear finite element study, and he found that the bursting force considerably decreased immediately after the initial cracking and it tended to further reduce with increasing crack growth. Using the same method, Adeghe (1986) observed a significant redistribution of stresses after cracking, resulting in a steeper spreading angle of the compressive stresses. Fenwicke and Lee (1986) confirmed the above observations numerically and experimentally. They further pointed out that the bursting force depended heavily on the ratio of cross axial stiffness of the structure member before and after cracking. And they suggested the following expression to compute the bursting force:

$$T \approx 0.13{\sim}0.30 \cdot P \cdot (1 - \frac{a}{d}) \qquad \textit{Eq. 2.5}$$

Other researchers (Samkari 1987, Ukhagbe 1990) basically made the similar observations on the nonlinear behavior of concentrically loaded concrete members and they used some variations of Mörsch´s equation (Eq. 2.3) to determine the bursting force.

A comprehensive experimental study on the 2-D problem was conducted by Wurm and Daschner (1983). They tested a large number of concrete strips with various strengths and reinforcement configurations to determine the bursting forces in the tensile reinforcement through measuring the lateral deformations on the specimen surfaces. As plotted in Figure 2.26, the bursting forces were considerably affected by the crack formation and the reinforcement configuration. Prior to the initial cracking, the reinforcement contributed slightly to resist the tensile stresses and even after cracking. Up a load level of 80% of ultimate load, the stresses in the reinforcement increased disproportionately. Depending on the reinforcement rate, the maximum values of bursting force were either far over (for high rate) or almost equal to (for moderate rate) the values predicted by Mörsch´s equation (Eq. 2.3).

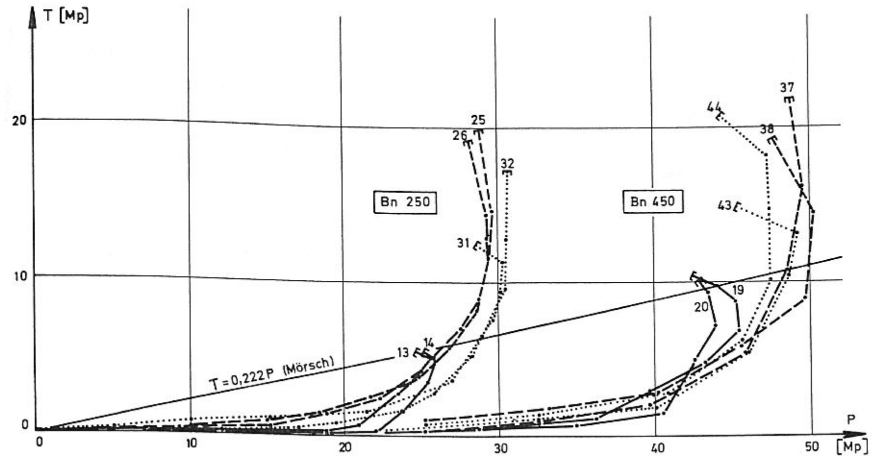


*Figure 2.26: Bursting force T in the tensile reinforcement: Test series 1 and 2 for a concentration ratio d/a = 9 (Wurm & Daschner 1983)*

**Eccentric loading situation**

Under eccentric introduction of concentrated load, the stresses along the specimen axis exhibit a trapezoidal or triangular-shaped distribution beyond the “St. Venant disturbance zone”. Furthermore, the stress trajectories are asymmetric. In this case, one can apply the “symmetrical prism” approach, which was first proposed by Guyon (1953), to estimate the bursting force as well as the distribution of the tensile stresses by replacing the member width d with $d_1$ (Figure 2.27).

On the basis of experimental results, Sargious (1960) found that with increasing eccentricity the bursting stresses decreased in the interior of the structure member, however, increased in edge zones adjacent to the load in conjunction with the growth of the spalling stresses in the zones away from the load. Through photoelastic investigations, Hiltscher and Florin (1963) observed that in the case of extremely eccentric loading the spalling force can be as high as the bursting force developed under concentric loading. In this case, in addition to the splitting tensile reinforcement, the arrangement of extra reinforcement in these edge zones should also be taken into consideration.

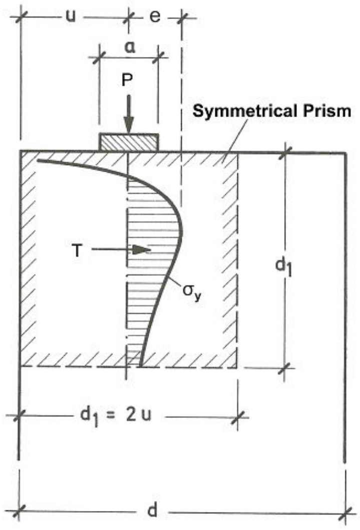


*Figure 2.27: Symmetrical prism approach to predict the bursting force for eccentric load (Guyon 1953)*

### 2.2.2.2 Spatial case of concentrated loading

**Concentric loading situation**

For the estimation of the stress state in a 3-D rectangular prism, Guyon (1958) firstly introduced an analytical approximate solution on the basis of linear-elasticity theory. Yettram and Robbins (1969) performed a series of elasticity finite element studies on a square-section prism. They observed high surface bursting stresses in the prism, which could not be revealed by Guyon´s solution. As depicted in Figure 2.28, for high concentration ratio d/a ≥ 9, the centroidal stresses are higher than the surface stresses; however, for low ratio d/a ≤ 2, a reverse tendency has been observed. Additionally, the position of the maximum bursting forces is slightly closer to the loaded surface as in the plane case.

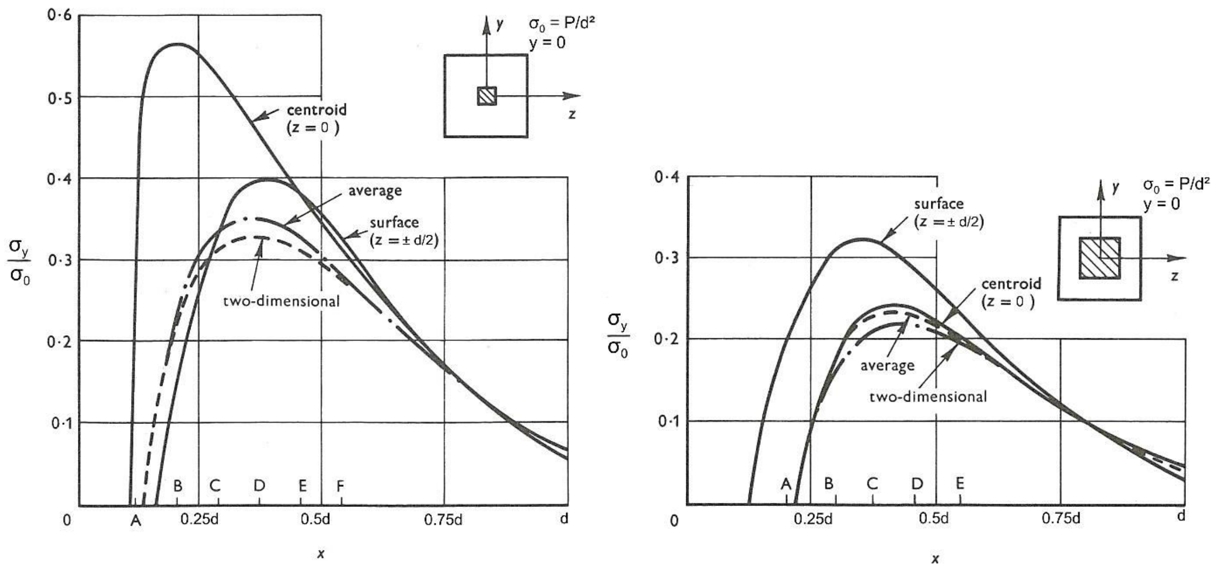


*Figure 2.28: Distribution of bursting stress $\sigma_y$ for different concentration ratios d/a: left, d/a = 9; right, d/a = 2 (Yettram & Robbins 1969)*

Similarly, by using finite element approach Buchhardt (1978) investigated the 3-D stress state in a rectangular block under concentric and eccentric loading. In the case of concentric loading, the numerically determined bursting forces exhibited nearly identical magnitudes compared to those calculated by the theoretical approach of Mörsch (1924). For eccentric loading, the spalling stresses were more critical, however, their values were partially conservatively predicted by finite element method compared to those given by the analytical solution (Grasser & Thielen 1976).

More recently, Leung and Cheung (2009) conducted a numerical study based on elastic finite element analysis to obtain the distribution of the principal stresses in a plain concrete prism (Figure 2.29). According to the computational results, they concluded that the high tensile stresses below the edges of the loaded area decrease rapidly from the loaded surface and thus there may not be sufficient energy to induce significant cracking resulting in member failure for an area ratio of 2.77. The lateral tensile stresses on the external surface are much higher than that around the center of the member, so tensile splitting should start at the surface and propagate inwards. This assumption of failure mode was later experimentally confirmed by the crack pattern of concrete members subjected to localized compression.

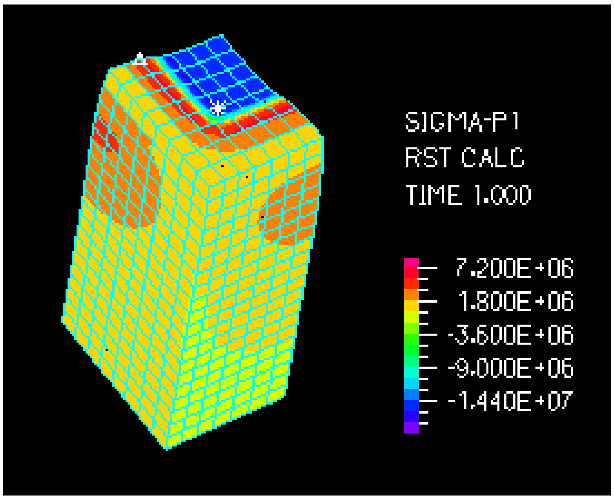


*Figure 2.29: Principal stress distribution of 3-D elastic FEM model with an area ratio $A_{c1}/A_{c0}$= 2.77 (Leung & Cheung 2009)*

Based upon the research data of Yettram and Robbins (1969), Leonhardt and Mönnig (1986) derived an approximate solution, similar to Mörsch´s approach for the plane case (Eq. 2.3), to determine the bursting force T in each axial direction (Eq. 2.6). Grasser and Thielen (1976 and 1991) also suggested the same equation to calculate the bursting force for the spatial case.

$$T_y = T_z \approx 0.25 \cdot P \cdot (1 - \frac{a}{d}) \qquad \textit{Eq. 2.6}$$

Using the curves in Figure 2.30, one can design the reinforcement in 3-D square-section prism for various concentration ratios. For prism with rectangular section, the maximum bursting stresses $\sigma_y$ and $\sigma_z$ do not possess the same magnitude and they exist at different positions. The bursting forces should be determined in each axial direction depending on the ratio of member width d to plate width a using the solution for the 2-D case.

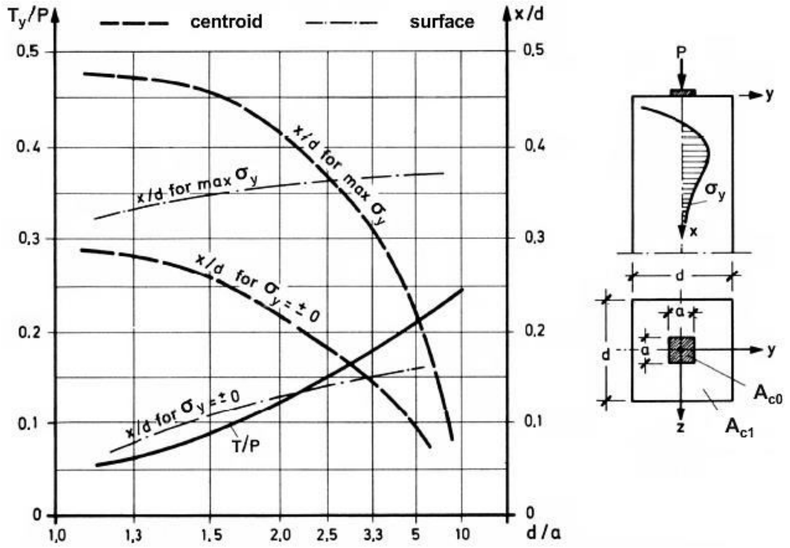


*Figure 2.30: Magnitude of the bursting force $T_y$ relative to the load P, and the positions of the maximum $\sigma_y$ and $\sigma_y = 0$ relative to the member width d for the spatial case (Leonhard & Mönnig 1986)*

For 3-D cylindrical specimens, Iyengar and Yogananda (1966) and Hiltscher and Florin (1972) conducted linear elastic studies to analytically estimate the bursting stresses. They both compared the magnitude of the bursting stresses in plane and spatial cases and came to the same conclusions that the bursting stresses in spatial case were considerably smaller than those in plane case. Hiltscher and Florin (1972) illustrated this variation in Figure 2.31 by comparing the maximum bursting stresses relative to the uniform stresses in both plane and spatial cases for different concentration ratios.

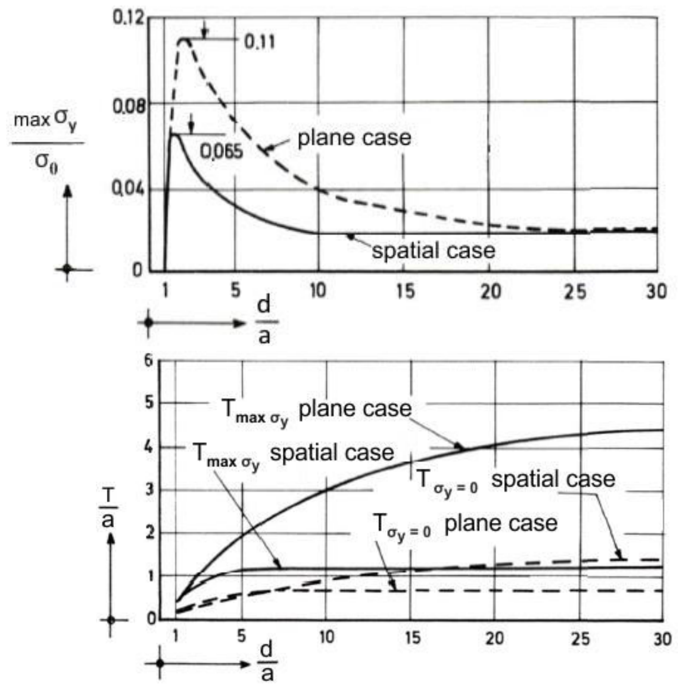


*Figure 2.31: Comparison of the magnitude and position of bursting stresses for the plane and spatial cases: Upper, maximum bursting stresses; lower, position of bursting stresses (Hiltscher & Florin 1972)*

Moreover, they revealed that the bursting stresses in spatial case concentrated more intensively in the region adjacent to the loaded surface and located more closely to the central axis of specimen. Spiral reinforcement was then recommended for such circular cylindrical prisms. For rectangular or square structural members, reinforcement should be dimensioned and layered in each individual direction.

The bursting stresses in spatial case can also be determined by using modified 3-D strut-and-tie models introduced by Nguyen (2002), as shown in Figure 2.32. For square-section prisms, the 3-D solution complied with the Mörsch´s solution (Eq. 2.3) for the plane case. It should be clearly noted that the formation of the strut-and-tie model considerably affected the evaluation of the bursting forces.

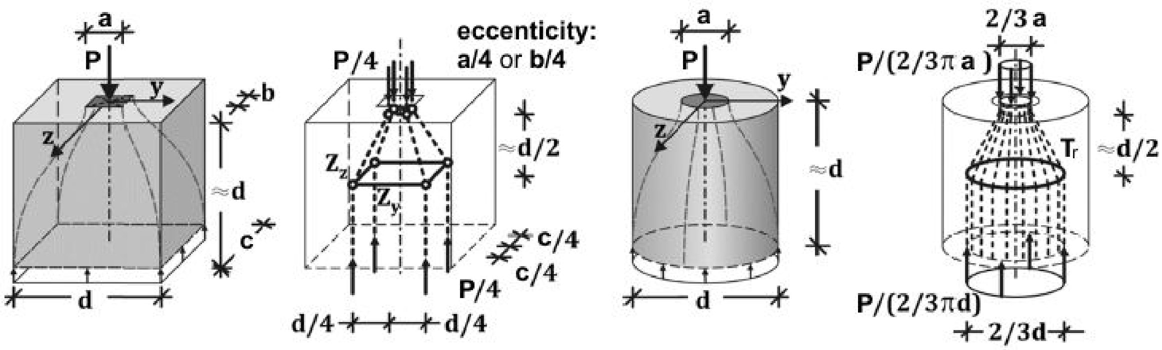


*Figure 2.32: 3-D strut-and-tie models (Nguyen 2002)*

Several experimental attempts have been made to study the 3-D stress state. One of the most extensive investigations was carried out by Zielinski and Rowe (1960) through testing a great number of concrete prisms with various reinforcement configurations. The bursting stresses or forces were determined through the strain measurement on the lateral surfaces of the prisms. It has been observed that the area ratio was the most important factor influencing the transverse stress distribution. The higher the ratio is, the higher the stress is. The maximum bursting stresses occurred on the axis of the load. However, due to the distinctly different stress distributions over the specimen thickness revealed by Yettram and Robbins (1969), the magnitude of the obtained bursting stresses was overestimated, as demonstrated in Figure 2.33. In terms of reinforcement configuration, spiral reinforcement was proved to be more efficient in resisting the bursting stresses than the orthogonal mats.

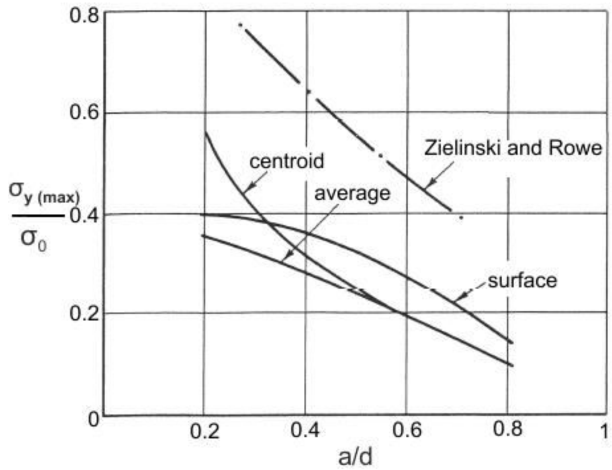


*Figure 2.33: Comparison of maximum bursting stresses as a function of a/d ratio (Yettram & Robbins 1969)*

Wurm and Daschner (1977) also experimentally investigated the bursting stresses in the reinforcement of centrally loaded concrete prisms produced with diverse concrete strengths and reinforcement configurations. Before the initial cracking, the surrounding concrete withstood primarily the bursting stresses. In contrast to the observations in the plane case, the stresses in the reinforcement grew significantly after cracking and the maximum values exceeded those determined by Mörsch´s equation (Eq. 2.3), as shown in Figure 2.34. This phenomenon was more pronounced in the case of specimens reinforced with high reinforcement rate.

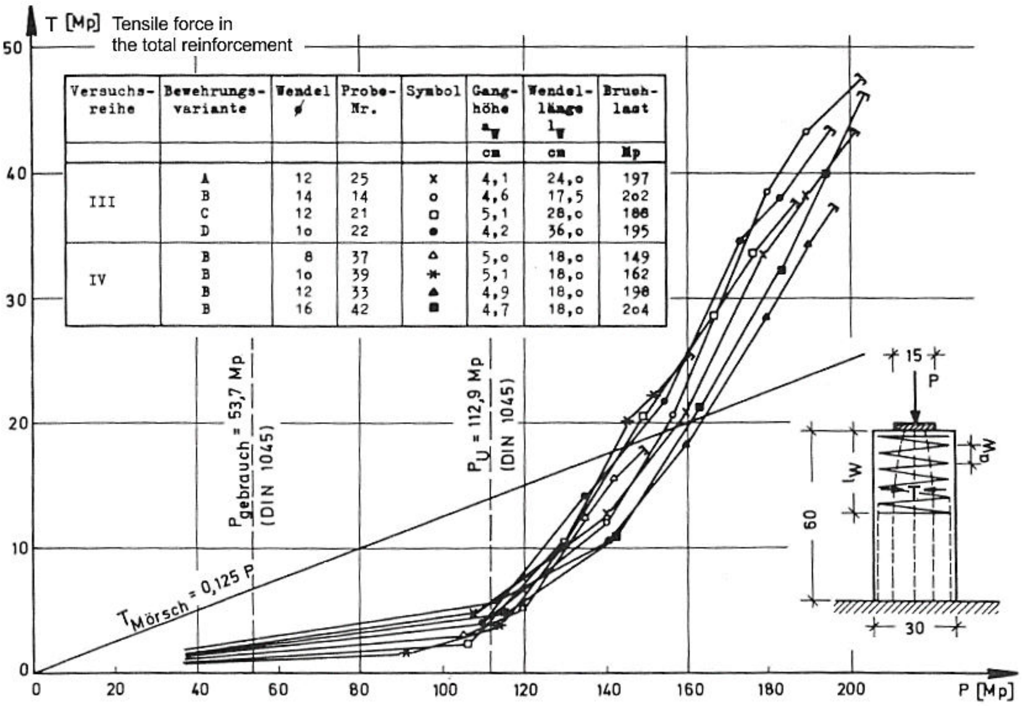


*Figure 2.34: Magnitude of the bursting force T in the spiral reinforcement: Test series III and IV for an area ratio $A_{c1}/A_{c0}$ = 4 (Wurm & Daschner 1977)*

**Eccentric loading situation**

In the case of eccentric loading, as suggested by Leonhardt and Mönnig (1986), one can alternatively apply the above-mentioned approaches by using the values for the 2-D case.

**Summary**

Since the failure of concrete under concentrated load was primarily induced by the tensile stresses (i.e. bursting stresses), enormous studies based on various methods have been carried out. Theoretical or empirical equations have been suggested to estimate the bursting stresses for specific design purposes. Some of these expressions have been adopted in the national and international standards or guidelines. An overview of recommendations in various standards and guidelines on the determination of the allowable tensile stresses and on the constructive design of the splitting tensile reinforcement was summarized by Wichers (2013). Despite the diversity of the methods used and the loading situations applied, general conclusions can still be drawn from the results of the theoretical and experimental investigations for the plane and spatial cases.

- The area ratio $A_{c1}/A_{c0}$ or concentration ratio d/a has significant influence on the magnitude and distribution of the bursting stresses. With increasing area ratio or concentration ratio, the magnitude of the bursting stresses increases remarkably.
- The bursting stresses in spatial case are considerably smaller than those in plane case and they are locate slightly closer to the loaded surface.
- With increasing eccentricity of load, the bursting stresses decrease in the interior of the structure member, however, increase in edge zones adjacent to the load. The spalling stresses in the edge zones become critical under extreme eccentricity.
- The magnitude and distribution of the bursting stresses can be considerably affected by initial crack formation and reinforcement configuration.

### 2.2.3 Investigation of load-bearing capacity

The bearing capacity of structural concrete members under concentrated load has been extensively studied in the last several decades, mostly through experimental approaches and additionally through analytical or numerical methods. Effects of various parameters (see Table 2.4) on the load-bearing capacity of concrete have been intensively investigated and discussed. However, these researches focused primarily on individual aspects of the problem and thus their results have application limits practical design due to the specific boundary conditions or assumptions used in the experimental or theoretical investigations. In this section, some relevant findings in the literature will be presented for plain concrete and conventionally reinforced concrete under strip-loading (i.e. plane case, 2-D) and point-loading (i.e. spatial case, 3-D), respectively.

#### 2.2.3.1 Experimental investigations

**Plane case of concentrated loading**

In 1876, Bauschniger (1876) investigated the bearing capacity of sandstone cubes under strip-loading and introduced the well-known cube-root formula to estimate the allowable bearing strength of this building material. The following equation was then also widely proposed for the design of concrete structural members for a long time:

$$q = f_{s,pr} \cdot \sqrt[3]{\frac{A_{c1}}{A_{c0}}} \qquad \textit{Eq. 2.7}$$

Kriz and Raths (1963) carried out an extensive study on the bearing capacity of plain and reinforced concrete column heads under strip-loading. A revised cube-root formula was suggested to predict the permissible bearing strength, which was later reaffirmed by Hawkins (1970) on his plain and reinforced concrete prisms under symmetric and eccentric strip-loading. Hawkins stated that properly proportioned and positioned reinforcement can increase the bearing capacity, however, the effect of reinforcement wasn´t taken into account in his equation (Eq. 2.8):

$$q = C \cdot \sqrt{f_{c,cyl}} \cdot \sqrt[3]{D/W} \qquad \textit{Eq. 2.8}$$

where
C = 18.5
D = distance from edge of block to center-line of bearing plate
W = width of bearing plate

Based on a great number of tests on plain concrete specimens under concentric strip-loading through rigid plate, Niyogi (1973) observed that the cube-root formula somewhat overestimated the ultimate bearing strength of his samples. Consequently, he recommended a square-root equation (Eq. 2.9) to estimate the bearing capacity. The primary parameters investigated for strip-loading were size of bearing plate, geometry and size of specimen. In general, it was concluded that the bearing strength increases with increasing area ratio $R = A_{c1}/ A_{c0}$, however, decreases with increasing height of specimen h and the effect being more evident for smaller R. For shallow specimens ($h/d < 1$ and $R > 8$), the bearing strength decreases with decreasing height, as showed in Figure 2.35.

$$n = \frac{q}{f_{c,cube}} = 0.42 \cdot (\frac{d}{a} + 2) - 0.29 \cdot \sqrt{(\frac{d}{a} - 2)^2 + 5.06} \qquad Eq.\ 2.9$$

In a subsequent study (Niyogi 1974), the influences of concrete strength, specimen size etc. were investigated. The results have shown that the higher the compressive strength of concrete is, the lower the value of relative ultimate bearing stress ratio n is for a given R. Furthermore, the bearing strength ratio n decreases with the increase in size of specimens with similar shape.

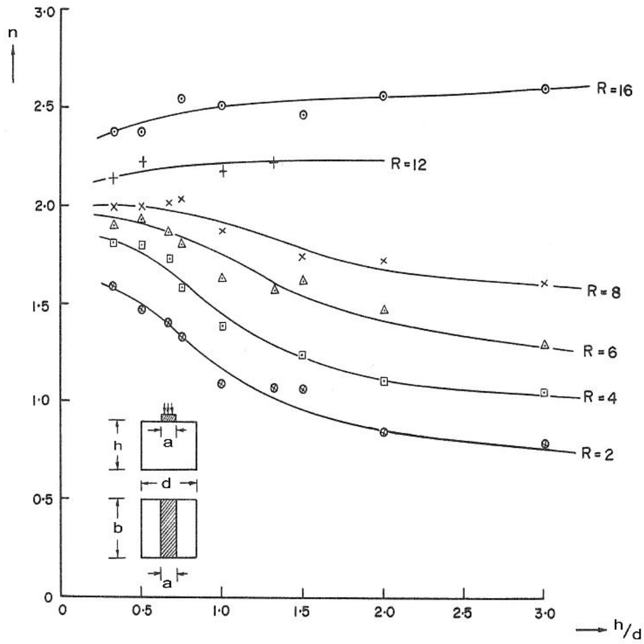


*Figure 2.35: Strip-loading on concrete prisms: Influence of h/d on n (Niyogi 1973)*

Wurm and Daschner (1983) confirmed Bauschniger´s cube-root formula (Eq. 2.7) on the test data of plain concrete prisms under concentric strip-loading, and a good agreement was found. Nonetheless, they introduced a linear equation to approximately predict the ultimate bearing stress for area ratio ≤ 9:

$$\frac{q}{f_{c,pr}} = 0.15 \cdot \left(\frac{A_{c1}}{A_{c0}}\right) + 0.85 \qquad Eq.\ 2.10$$

For reinforced concrete prisms, they also proposed a linear equation considering the contribution of the stirrup reinforcement with various amounts and positions (Figure 2.36) to the bearing capacity:

$$\frac{q_{reinf,m}}{f_{c,pr}} = \frac{q}{f_{c,pr}} + k \cdot \mu \qquad Eq.\ 2.11$$

where

$q_{reinf,m}$ = mean allowable bearing stress of reinforced concrete

k = $0.0625 \cdot \frac{A_{c1}}{A_{c0}} + 0.29$

μ = relative reinforcement rate in the St. Venant disturbance zone

They reported that when exceeding a reinforcement rate of μ = 0.8%, no further increase in the ultimate bearing strength was observed (Figure 2.37). And no noticeable difference in the bearing strength was found in terms of various reinforcement positions for μ = 1.8% (Figure 2.36, right). Moreover, they revealed the application limits of the above two equations, which are only valid for concrete strength class C20/25 (Bn 250) and C35/45(Bn 450), area ratio $A_{c1}/A_{c0} \leq 9$ and steel strength BSt 420/500 (BSt 42/50).

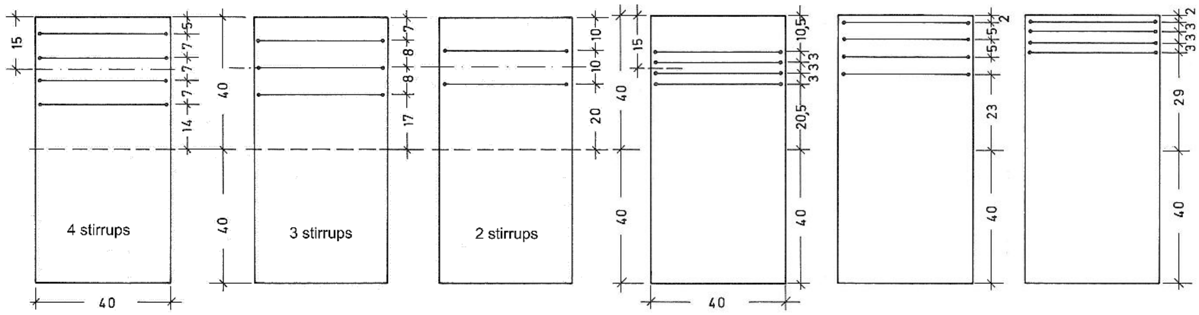


*Figure 2.36: Concrete prisms reinforced with stirrup reinforcement: Left, testing series 1 - various amount of reinforcement; right, test series 3 - different positions of reinforcement (Wurm & Daschner 1983)*

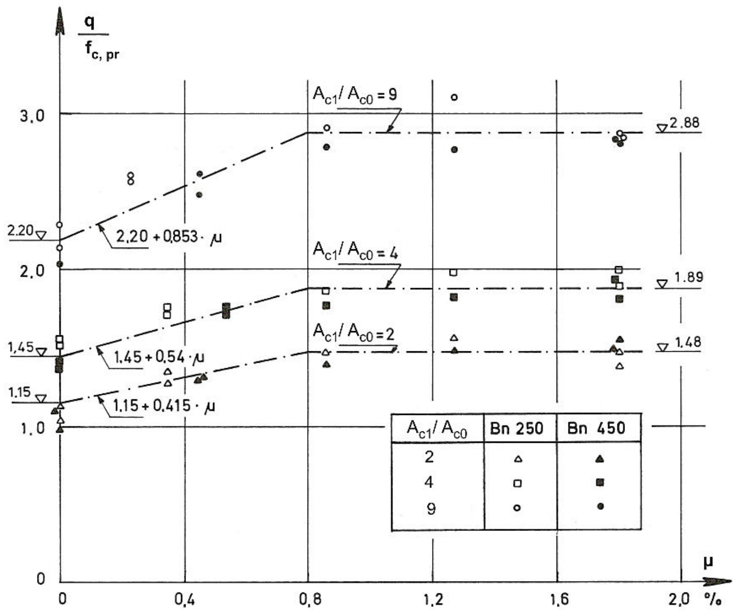


*Figure 2.37: Influence of relative reinforcement rate $\mu$ on the bearing strength ratio $q/f_{c,pr}$ (Wurm & Daschner 1983)*

The influence of surface-near reinforcement was recently investigated by Empelmann and Wichers (2008). They observed that prisms strengthened with conventional reinforcement according to the recommendations of Grasser and Thielen (1976) exhibited the highest bearing strength, whereas the additional surface-near reinforcement did not lead to an increase in the bearing capacity. In another paper, Empelmann and Wichers (2009) found a good agreement (Figure 2.38-left) between the obtained test data and the values calculated by the cube-root equation below:

$$F_{Ru} = A_{c0} \cdot f_{c,uniaxial} \cdot \sqrt[3]{\frac{A_c}{A_{c0}}} \qquad \textit{Eq. 2.12}$$

After comparing the factor of strength increase $\alpha^*$ determined by the design approaches in DIN 1045-1 (2008) and Eurocode 2 (2004) with that computed by the above cube-root formula, they concluded that the design proposal for allowable bearing stress $\sigma_{Rdu,max} = 1.1 \cdot f_{cd}$ in both codes is rather conservative for the design of structural concrete members under strip-loading (Figure 2.38-right).

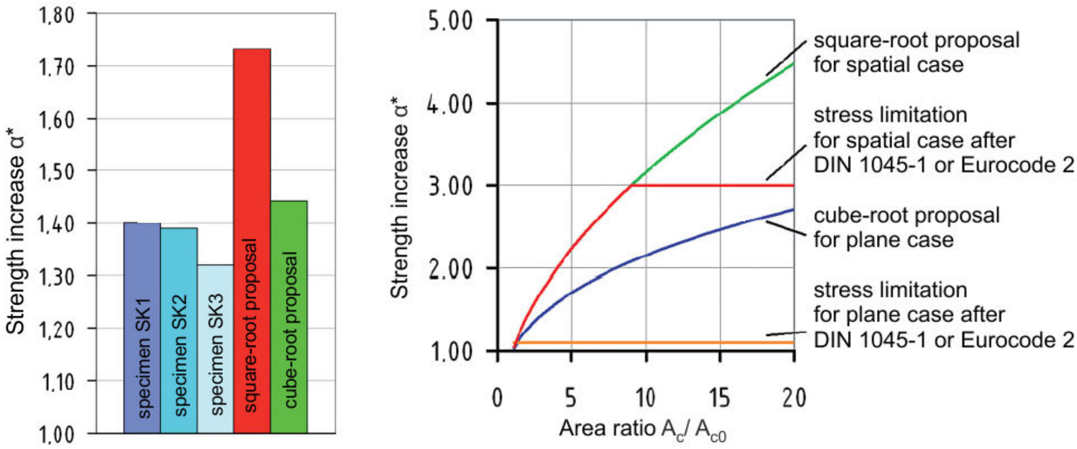


*Figure 2.38: Left, comparison of strength increase factor α* ($A_c/A_{c0} = 3$); right, strength increase factor α* for concentrated loading according to different proposals (Empelmann & Wichers 2009)*

**Spatial case of concentrated loading**

Based upon a number of tests on plain concrete cylinders, Billig (1948) recommended a cube-root formula to estimate the permissible bearing stresses for point-loading:

$$q = 0.6 \cdot f_{c,cyl} \cdot \sqrt[3]{\frac{A_{c1}}{A_{co}}} \leq f_{c,cyl} \qquad \text{Eq. 2.13}$$

Later, the cube-root equation was proved to be inappropriate for an accurate prediction of the bearing stresses in a 3-D stress state through extensive experiments conducted by other investigators (Komendant 1952, Meyerhof 1953, Shelson 1957, Spieth 1959 and 1961, Au & Baird 1960, and Middendorf 1960 and 1963). In the 3-D case, the actual bearing stresses increase more rapidly with growing area ratio $A_{c1}/ A_{c0}$ due to the confinement effect of the surrounding non-loaded concrete. Therefore, it can be underestimated by using the cube-root formula. Based on a number of tests on plain and reinforced concrete cylinders, Komendant (1952) initially proposed a square-root equation:

$$q = 0.6 \cdot f_{c,cyl} \cdot \sqrt{\frac{A_{c1}}{A_{co}}} \leq f_{c,cyl} \qquad \text{Eq. 2.14}$$

Through substantial tests on rectangular blocks and cylinders of plain concrete, Middendorf (1960 and 1963) reaffirmed the recommendations of Komendant. He further suggested that the restriction $q \leq f_{c,cyl}$ should be increased to some multiple of $f_{c,cyl}$ - probably 3. Meanwhile, he pointed out that the recommendations are applicable for concrete with $f_{c,cyl}$ ranging from 4000 to 6000 psi (i.e. approximately from 27.6 to 41.4 MPa).

Due to the fact that the bearing behavior or capacity of concrete under concentrated load is not simply affected by the compressive strength of concrete or the area ratio, numerous experimental researches have been conducted with the focus on the effects of some other influential variables (Table 2.4)

Hawkins (1968a) investigated the effects of concentric and eccentric load introduction, geometry of specimen and bearing plate as well as type and strength of concrete on the bearing strength of plain concrete blocks loaded through rigid plate. A correct or conservative expression to estimate the ultimate bearing strength was developed on the basis of the failure modes observed in the tests for R′ < 40 (R′ is defined as the ratio of effective unloaded area to loaded area):

$$\frac{q}{f_{c,cyl}} = 1 + \frac{K}{\sqrt{f_{c,cyl}}}(\sqrt{R'} - 1) \qquad \textit{Eq. 2.15}$$

where the factor K depends largely on the tensile strength $f_{ct}$ and angle of internal friction φ, for practical purposes K can be taken as 50; R′ should be chosen with due consideration of the loading eccentricity and the shape of the loaded area.

Additionally, he reported that the bearing strength is directly dependent upon the concrete quality (i.e. angle of internal friction φ) in the bearing zone. The bearing stress ratio $q/f_{c,cyl}$ decreases with increasing concrete strength and increases with increasing R′, as plotted in Figure 2.39. The depth of the block has no theoretical effect unless the proximity of the base restricts the formation of the failure wedge or the loading plate is made progressively rectangular leading to a 2-D problem.

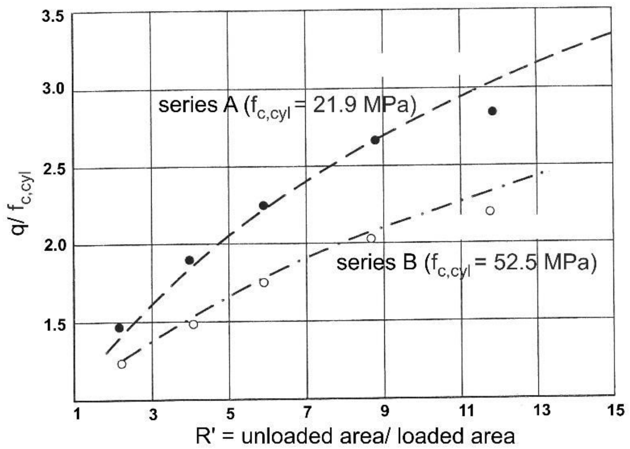


*Figure 2.39: Effect of concrete strength on bearing capacity (Hawkins 1968a)*

In a subsequent paper (Hawkins 1968b), he further studied the bearing strength of concrete loaded through flexible plate. It was concluded that for flexible plate the bearing capacity increases linearly with the plate thickness and the effect of the increase in the area of plate is almost negligible. Approximate solutions were also proposed for the bearing strength of concrete.

Niyogi (1973, 1974 and 1975) carried out one of the most comprehensive investigations on this subject in his time. In the first paper (Niyogi 1973), he mainly discussed the effects of geometrical and dimensional variations of specimen and plate on the bearing strength of concrete as well as the probable mechanism of failure. For concentric loading, a general expression for plain concrete specimens was represented by the following equation, embodying d/a, d/b as the principal:

$$n = \frac{q}{f_{c,cube}} = 0.42 \cdot (\frac{d}{a} + \frac{d}{b}) - 0.29 \cdot \sqrt{(\frac{d}{a} - \frac{d}{b})^2 + 5.06} \qquad \textit{Eq. 2.16}$$

It was concluded that the relative depth or height of specimen influences the bearing strength that generally decreases with increasing height. And the eccentricity of load tends to reduce the load-bearing capacity (Figure 2.40). The equation for eccentric loading is given as for square bearing plate:

$$\frac{n_e}{n} = 2.36 \cdot \sqrt{0.83 - \left(\frac{e}{d} - \frac{e'}{d}\right)^2 - 0.94\left(\frac{e}{d} + \frac{e'}{d}\right)} - 1.15 \qquad \textit{Eq. 2.17}$$

where

$n_e$ = ultimate bearing stress ratio under eccentric loading

e, e′= eccentricities of concentrated load with reference to centroid of loaded surface of specimen in two principal directions

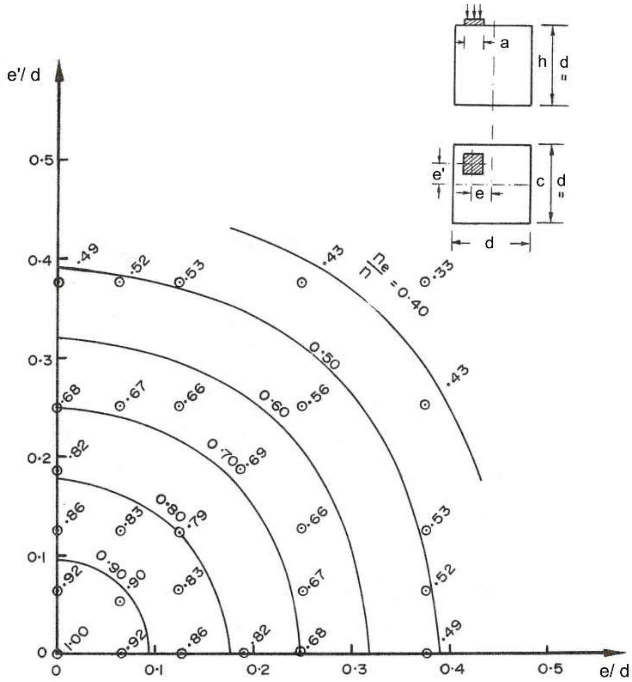

*Figure 2.40: Relationship of $n_e/n$ versus e/d and e′/d (Niyogi 1973)*

In the second paper (Niyogi 1974), lower bearing strength was observed by specimens supported on a compressible bed for h/d < 2 or loaded on both ends. However, the reduction is largely dependent on the specimen height and the supported area. Variations in mix proportion and strength of concrete affect the bearing strength to some extent. For a given area ratio R, the bearing strength ratio n decreases with the increase in compressive strength and size of specimens with similar shape (Figure 2.41).

In the third paper (Niyogi 1975), the effects of the amount and form of reinforcement on the bearing strength and cracking resistance were investigated. In general, the greater the percentage of lateral steel p is, the higher the bearing strength ratio n is for a given area ratio R. And the effect is more pronounced for smaller bearing plates than for larger plates. Spiral reinforcement, in particular with single large diameter, appeared to be more effective than grid reinforcement due to lateral confinement of the concrete over. It was revealed that reinforcement nearer to the load end was more effective than further down. The bearing strength ratio of spirally reinforced concrete $n_{reinf}$ relative to that of plain concrete $n_{plain}$ was proposed by a linear relationship with the steel percentage p and a constant K = 55:

$$\frac{n_{reinf}}{n_{plain}} = 1 + K.p \qquad \textit{Eq. 2.18}$$

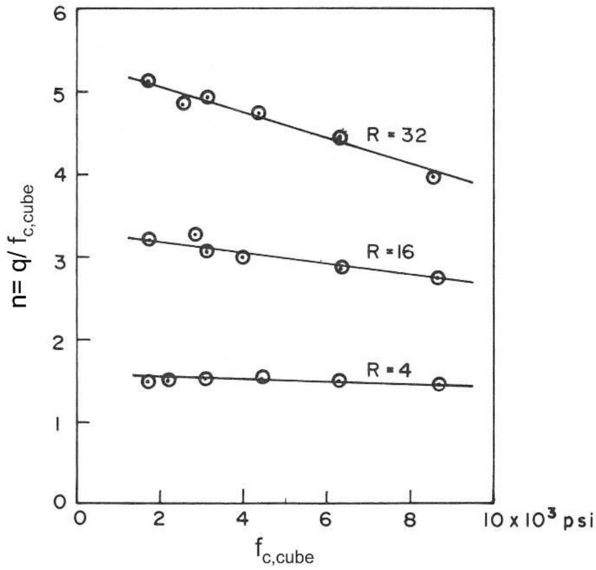


*Figure 2.41: Influence of concrete strength on ultimate bearing strength ratio (Niyogi 1974)*

Wurm and Dascher (1977) also studied the influence of various forms of steel reinforcement on the bearing capacity of concrete. They concluded that spiral reinforcement distinguished itself as the most effective reinforcing form among other forms of reinforcement such as stirrup, grid and loop; and it should be extended into the entire St. Venant disturbance zone. For more critical loading situations near-surface reinforcement was recommended. The positive effect of additional near-surface reinforcement was later confirmed by Empelmann and Wichers (2009) for the 3-D loading situation. They found that prisms strengthened with additional near-surface reinforcement showed an increase in bearing strength of up to 20%, compared to specimens reinforced only with single type of reinforcement (Figure 2.42).

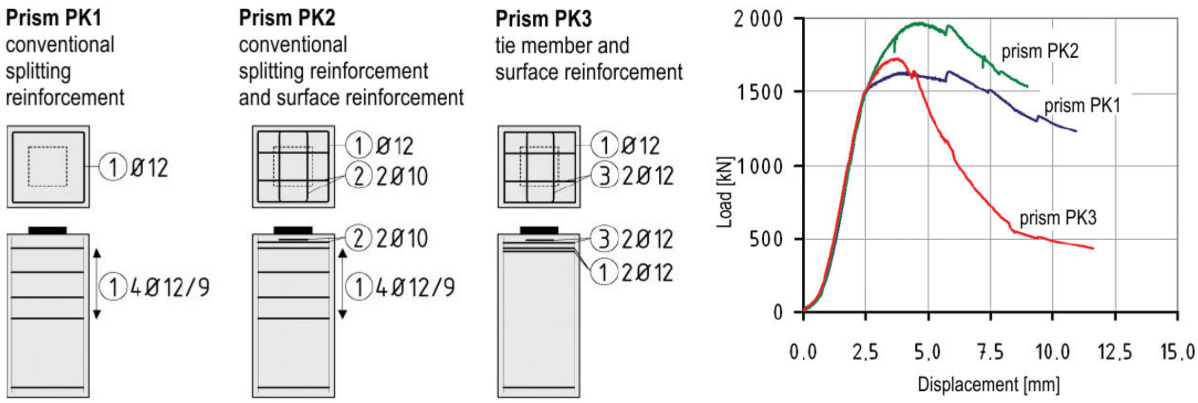


*Figure 2.42: Left, reinforcement configuration; right, its influence on the load-displacement response (Empelmann & Wichers 2009)*

Lieberum and his colleagues (1987 and 1989) investigated the influence of concrete composition (concrete compressive strength: 29-58 MPa and maximum grain size $d_k = 8$, 16 and 32 mm) on the load deformation behavior of reinforced concrete under extreme large concentrations of load. They employed area ratios ranging from 156 to 947, which were considerably greater than those chosen by other investigators. It was revealed that the ratio of $q/ f_{c,\,cube}$ decreases with increasing concrete strength due to the disproportionate increase of the concrete tensile strength. With growing grain size, a reduction in the deformation of concrete under concentric loading was observed, indicating a stress relocation into the deeper region due to the size effect of the large grain (Figure 2.43).

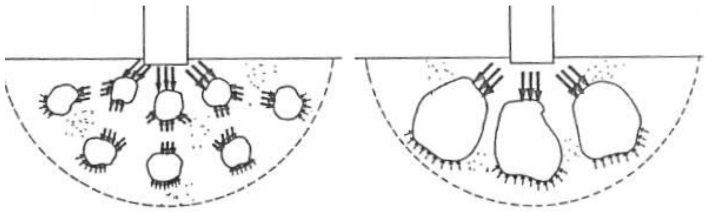

*Figure 2.43: Influence of grain size on the stress distribution (Lieberum 1987)*

The failure pattern basically depended on the area ratio. For area ratio $A_{c1}/A_{c0} \leq 320$, the fracture was characterized by splitting, while for area ratio $A_{c1}/A_{c0} > 320$, the failure was caused by local concrete breakout in the loaded area (Figure 2.44). Design proposals were made depending on the area ratio:

for $A_{c1}/A_{c0} \leq 320$: $q = 0.7 \cdot \frac{f_{c,cube}}{3} \cdot \sqrt{\frac{A_{c1}}{A_{c0}}} \cdot \sqrt{\frac{40}{f_{c,cube}}}$ *Eq. 2.19*

for $A_{c1}/A_{c0} > 320$: $q = 12.5 \cdot \frac{f_{c,cube}}{3} \cdot \sqrt{\frac{40}{f_{c,cube}}}$ *Eq. 2.20*

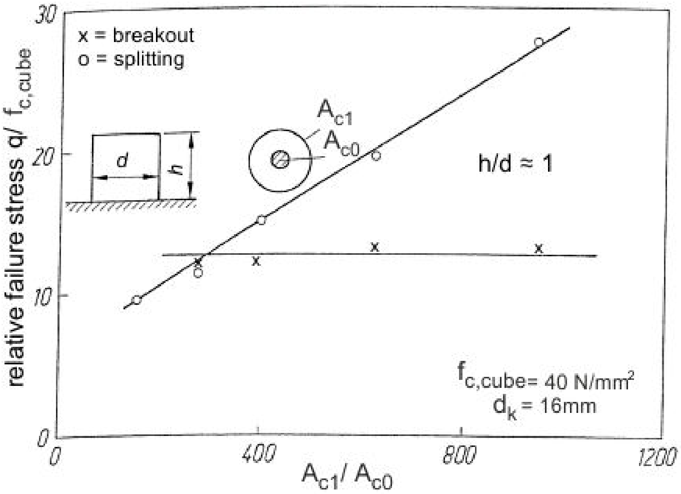


*Figure 2.44: Effect of area ratio on the bearing strength and failure pattern (Lieberum et al. 1989)*

The bearing behavior of high-strength concrete under concentrated loading was reported by Schön and Reinhardt (1994). Concrete cylinders with three different strengths (C40/50, C70/85 and C100/115) were tested with various area ratios. In the case of plain concrete, compared to normal-strength concrete, high-strength concrete exhibited a stiffer pre-cracking ascending branch and a higher ultimate bearing strength, however, a more brittle failure behavior for a given area ratio (Figure 2.45).

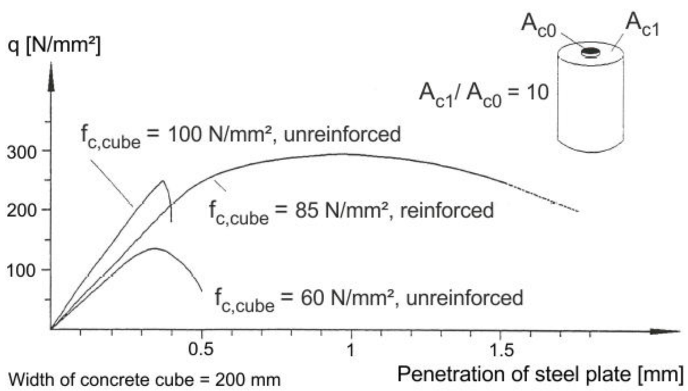


*Figure 2.45: Effect of concrete strength on the load-displacement behavior (Schön & Reinhardt 1994)*

Based on the test results, they introduced an equation with a reduction factor of 0.79 according to the proposal in DIN 1045 (1988) to estimate the permissible bearing strength of high-strength concrete:

$$q = 0.79 \cdot \frac{1}{2.1} \cdot f_{cd} \cdot \sqrt{\frac{A_{c1}}{A_{c0}}} \qquad \textit{Eq. 2.21}$$

They also attributed the reduced bearing capacity of high-strength concrete to the disproportionate increase in tensile strength with increasing compressive strength. For reinforced high-strength concrete, they addressed that the use of the above-mentioned reduction factor is not necessary; only when calculating the service load (i.e. limitation of crack width), one should consider the reduction factor.

In a subsequent study (Reinhardt & Koch 1997), the influence of specimen size as principal variable on the bearing capacity was investigated. It was observed that with growing size of specimen the bearing capacity decreases and the tendency can be expressed using nonlinear regression:

$$r_{0.200} = 0.794 \cdot d_b^{-0.143} \qquad \textit{Eq. 2.22}$$

where
$r_{0.200}$ = reduction factor of the bearing capacity (relative to a cylinder diameter of 200 mm)
$d_b$ = dimension of specimen

Based upon the test results obtained, Reinhardt and Koch (1998) proposed a modified equation with a size reduction factor ζ for high-strength concrete with various member thicknesses d, considering a minimum reinforcement rate of 1.0% according to DAfStb-Guideline (1995):

$$q = 0.8 \cdot \zeta \cdot \frac{1}{2.1} \cdot f_{cd} \cdot \sqrt{\frac{A_{c1}}{A_{c0}}} \leq 1.4 \cdot f_{cd} \qquad \textit{Eq. 2.23}$$

where
$\zeta = 1.0$ for $d \leq 300$ mm
$\zeta = 0.85$ for $300 \text{ mm} < d \leq 600$ mm
$\zeta = 0.8$ for $d > 600$ mm

Figure 2.46 illustrates the correlation between cylinder diameter $d_b$ and size reduction factor ζ.

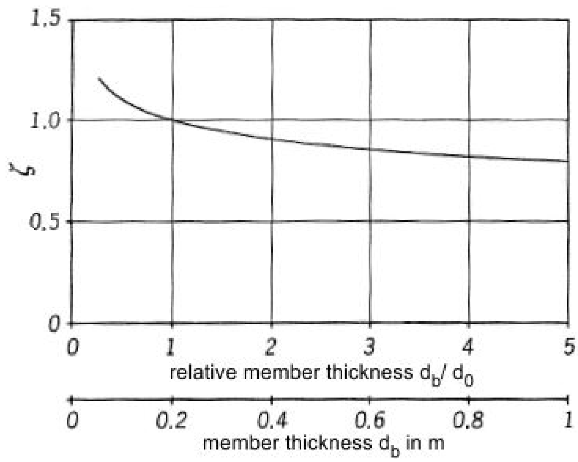


*Figure 2.46: Effect of specimen size on the bearing capacity of concrete (Reinhardt & Koch 1998)*

In the current DIN 1045-1 (2008) and Eurocode 2 (2011) a square-root expression (Eq. 2.24) with specific boundary conditions is prescribed to determine the ultimate load-bearing capacity $F_{Rdu}$ of concrete structural member up to a compressive strength of C100/115. However, no recommendation is given for concrete strength over C 100/115. Furthermore, the positive influence of reinforcement is not taken into consideration in the approach.

$$F_{Rdu} = A_{c0} \cdot f_{cd} \cdot \sqrt{\frac{A_c}{A_{c0}}} \leq 3.0 \cdot A_{c0} \cdot f_{cd} \qquad \textit{Eq. 2.24}$$

The load-bearing behavior of ultra-high-strength concrete was recently investigated by Klotz (2008). Based on the results of an extensive study, Klotz found that the composition of ultra-high-strength concrete had marked influence on the ultimate bearing capacity of this very brittle material. As depicted in Figure 2.47, plain concrete prisms containing coarse basalt chips (UHFB2-U-04), due to better interlocking and inherent strength of the coarse aggregates, exhibited higher values of ultimate bearing stress than plain concrete specimens with fine grains (UHFB1-U-06). As earlier stated, due to the disproportionate increase in tensile strength, the both ultra-high-strength concretes did not exhibit a remarkable increase in the ultimate bearing strength ratio, compared to the high-strength concrete (HF-U-Korr). In the case of reinforced concrete, provision of spiral reinforcement led to a better resistance against crack formation and growth as well as a higher bearing strength.

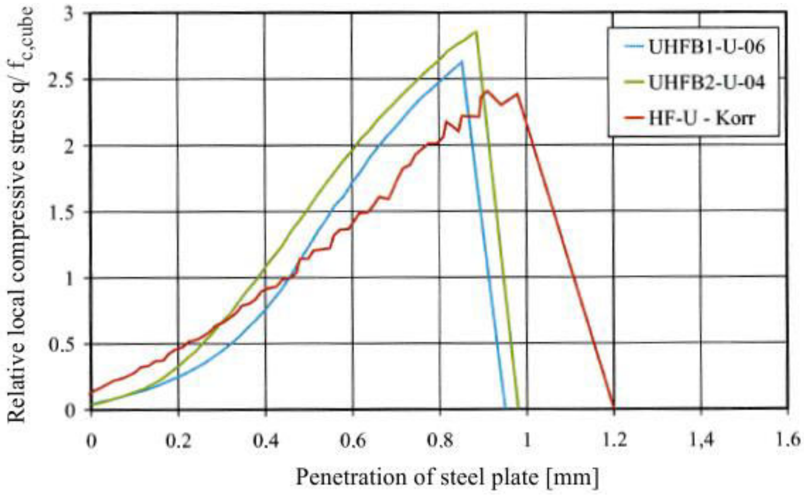


*Figure 2.47: Effect of concrete composition and strength on the bearing strength ratio (Klotz 2008)*

Considering the effect of aggregates, he recommended two expressions to predict the permissible bearing strength of ultra-high-concrete, respectively:

for concrete with fine grains:

$$F_{Rdu} = 0.60 \cdot A_{c0} \cdot f_{cd} \cdot \sqrt{\frac{A_c}{A_{c0}} - 1} \qquad \textit{Eq. 2.25}$$

for concrete with coarse basalt chips:

$$F_{Rdu} = 0.75 \cdot A_{c0} \cdot f_{cd} \cdot \sqrt{\frac{A_c}{A_{c0}} - 1} \qquad \textit{Eq. 2.26}$$

**Summary**

In the pertinent literature, numerous experiments concerning various influential parameters have been carried out to investigate the load-bearing behavior or capacity of concrete structural members under concentrated load. Based on the experimental results, diverse empirical formulae have been proposed to predict the allowable bearing strength. In these formulae, the allowable bearing strength is generally expressed as a function of the uniaxial concrete compressive strength to the cube or square root of the ratio of the total area ($A_{c1}$) to the loaded area ($A_{c0}$). Due to the specific boundary conditions used, these formulae inevitably have inherent application limits for the practical design. In the present national and international codes, the square-root approach is primarily used for the design of concrete structural members subjected to concentrically localized compression (3-D case). A comprehensive literature study on the various design approaches on this issue was conducted by Klotz (2008).

Nonetheless, general conclusions regarding the problem of concrete subjected to concentrated load can still be drawn from the experimental results reported in the literature, which are valid for both 2-D and 3-D cases.

- The bearing strength increases with increasing area ratio, decreases with increasing height of specimen and eccentricity of load.
- The ratio of ultimate bearing stress and concrete compressive strength decreases with increasing concrete strength and size of specimen with similar shape.
- The composition of concrete in terms of maximum grain size or type of aggregate affects the bearing strength of concrete to some extent.
- Properly proportioned and positioned reinforcement increases the bearing capacity, in particular combined with additional surface-near reinforcement under point-loading (i.e. a 3-D case).

### 2.2.3.2 Analytical and numerical investigations

By using modified Mohr-Coulomb yield criterion, several investigators (Chen & Drucker 1969, Ibell & Burgoyne 1994a, and Kupfer 2005) attempted to analytically estimate the load-bearing behavior of concrete. Based on the limit theorems (Drucker et al. 1952) of perfect plasticity, Chen and Drucker (1969) proposed analytical solutions to predict the bearing capacity of concrete blocks subjected to strip or point loading (Figure 2.48). The analysis assumed a modified Mohr-Coulomb yield criterion with a small tension cut off. The analytical approach was later examined experimentally on plain concrete (Hayland & Chen 1970) as well as on fiber concrete (Chen & Carson 1974). The theoretical estimations were consistent well with the experimental results.

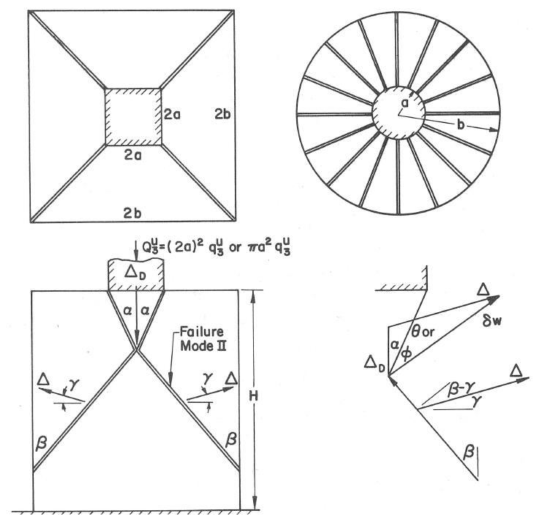


*Figure 2.48: Bearing capacity of concrete under concentric point-loading (Chen & Drucker 1969)*

Based upon the obtained test results (Ibell & Burgoyne 1993) and previous work of Chen and Drucker (1969), Ibell and Burgoyne (1994a) introduced a plasticity solution for the analytical analysis of the 2-D ultimate strength, considering the effect of reinforcement using a modified Mohr-Coulomb failure criterion with non-zero tension cut-off (Figure 2.49). A good correlation was obtained between the results of the analytical model and the experimental investigation. Later, they extended the plasticity solution using linear FEM analyses for the 3-D case (Ibell & Burgoyne 1994b). More recently, Kupfer (2005) proposed an analytical approach based on the increment of compressive strength through rotationally symmetrical transverse compressive stress after the Mohr-Coulomb failure hypothesis.

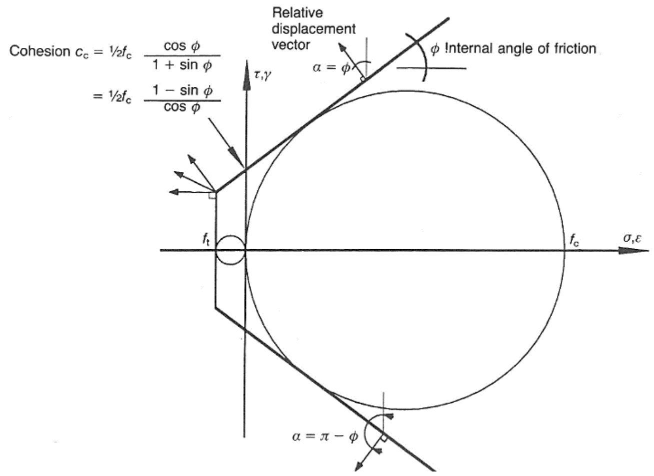


*Figure 2.49: Modified Mohr-Coulomb failure criterion with non-zero tension cut-off (Ibell & Burgoyne 1994a)*

The bearing capacity of concrete members subjected to localized force can also be determined by the strut-and-tie model. Investigations on the application of the 2-D and 3-D strut-and-tie models have already been conducted by Schlaich and Schäfer (2001) and Nguyen (2002). By means of the strut-and-tie model, both concrete compressive failure and steel tensile failure can be described in a discontinuity region such as the force application zone. The ultimate bearing capacity as a result of the failure of the tension tie is considered as achieved, when the reinforcement assigned by the tension tie cannot withstand the bursting force T determined by the strut-and-tie model. However, the bursting force derives exclusively from the redirecting of the compressive strut and its magnitude is largely dependent upon the selected strut-and-tie model. The ultimate bearing capacity $F_{Ru}$ can then be computed as follows:

$$F_{Ru} = \frac{A_s \cdot f_y}{T/P} \qquad \textit{Eq. 2.27}$$

where
$A_s$ = cross-sectional area of steel reinforcement
$f_y$ = yield strength of steel rebar

Kotsovos and Newman (1981) initially applied a computer-based nonlinear finite element technique incorporating a constitutive model of concrete behavior to analyze plain concrete structural forms under concentrations of load. The structural forms used were prisms (under strip-loading) and cylinders (under point-loading) loaded concentrically on both ends. The influence of boundary conditions upon strength and deformational behavior of concrete and fracture process was investigated. It was shown that the predicted bearing strength was consistent well with the experimental values if the boundary conditions assumed by the analysis simulated closely those imposed by the testing techniques. In another paper, Kotsovos (1981) pointed out that nonlinear finite element analysis based on a linear description of stress-strain relationships of concrete considerably underestimated the strength and deformational characteristics of the structure.

Since then, numerous investigations based on finite element analysis have been conducted by Jähring (2004), Empelmann and Wichers (2008), Wichers (2013) and Breitenbücher et al. (2014). In closing this section, the recent work of Wichers (2013) deserves mention. By using nonlinear finite element approach, he investigated the influence of initial cracking and reinforcement configuration on the splitting tensile stresses and the load-bearing capacity of centrally loaded reinforced normal-strength concrete prisms. Within the analysis, various stiffness states and reinforcement arrangements in the force transmission zone were considered and analyzed. Based on the numerical results, proposals for the design calculation as well as the amount and arrangement of reinforcement were recommended for the plane and spatial cases, respectively.

**Summary**

As discussed above, in addition to experimental approach, the bearing capacity of concrete under concentrated load can be predicted by applying various analytical or numerical methods, such as modified Mohr-Coulomb yield criterion with non-zero or small tension cut-off, strut-and-tie model and nonlinear finite element analysis. Generally, it has been established that the theoretically estimated results were consistent well with those obtained experimentally.

Basically, both experimental and analytical or numerical approaches may provide realistic estimations to certain extent. The analytical or numerical approach is considerably advantageous as it can analyze various structure forms under different loading situations and boundary conditions through simply modifying the basic procedure, in particular in the case of computer-based techniques of analysis.

## 2.3 SFRC under concentrated load

Although a great number of investigations on the problem of concrete under concentrated load have been conducted previously, few attempts were made to study the load-bearing behavior of concrete strengthened with steel fibers or combined reinforcement. In this section, the limited well-known findings on the steel fiber reinforced or strengthened concretes will be presented for the 3-D case.

In 1974, Chen and Carson (1974) studied the influence of adding straight fiber wires (25 mm in length, 0.4 mm in diameter, with volume fractions of 0.75% and 1.5%) on the bearing capacity and ductility of 150 mm diameter concrete cylinders with various heights. The load was introduced concentrically through double circular metal punches with 38 mm diameter at both ends. It was found that the bearing capacity of reinforced material was significantly higher than that of unreinforced material, and it increased with growing height of specimen, as shown in Figure 2.50.

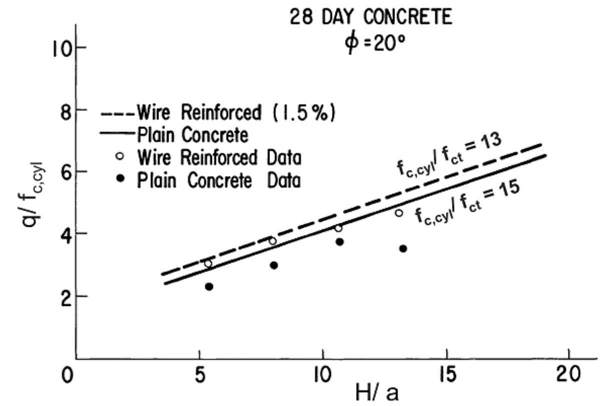


*Figure 2.50: Effect of steel wires and specimen height on the bearing strength (Chen & Carson 1974)*

Schmidt and Fiedler (1993) studied the effect of steel fibers as secondary reinforcement on the bearing and fracture behavior of normal-strength concrete prisms (320 x 320 x 640-mm) loaded centrally through a steel plate with a cross-section of 160 x 160-mm. The steel fibers were added into the upper half of the conventionally reinforced prisms. The fiber content varied from 0.5% to 2.0% by volume. It was observed that prisms additionally strengthened with fibers exhibited a much more ductile material behavior than prisms solely reinforced with conventional reinforcement (Figure 2.51). For a given reinforcement rate, the ultimate bearing strength increased steadily with increasing fiber content.

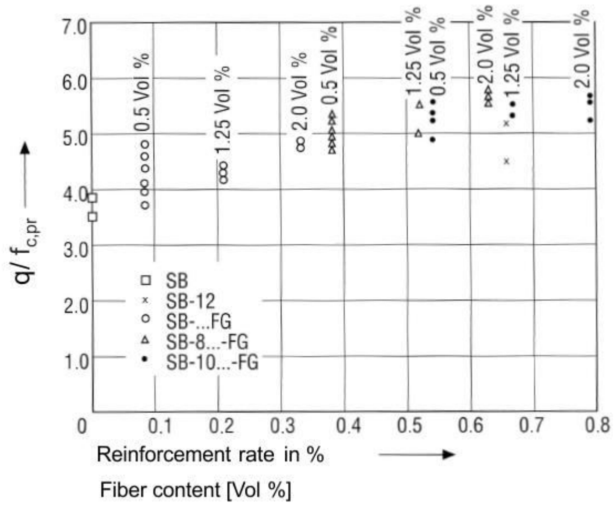


*Figure 2.51: Effect of fiber content on the relative ultimate bearing strength of reinforced concrete prisms (Schmidt & Fiedler 1993)*

Al-Taan and Al-Hamdony (2005) investigated the effect of aspect ratio of steel fiber and fiber content on the bearing capacity of 150 mm square concrete blocks centrally loaded through various sizes of steel plate. The fiber lengths were 16 and 32 mm with equivalent aspect ratio of 21.8 and 32, respectively. Three fiber percentages by volume were employed: 0.4%, 0.8% and 1.2%. The results have shown that the bearing capacity increased with growing volume percentage and aspect ratio of fiber, as showed in Figure 2.52. Fibers with an aspect ratio of 32 exhibited a 10-20% higher maximum bearing strength than fibers with a value of 21.8. All fiber concrete samples showed a ductile failure behavior.

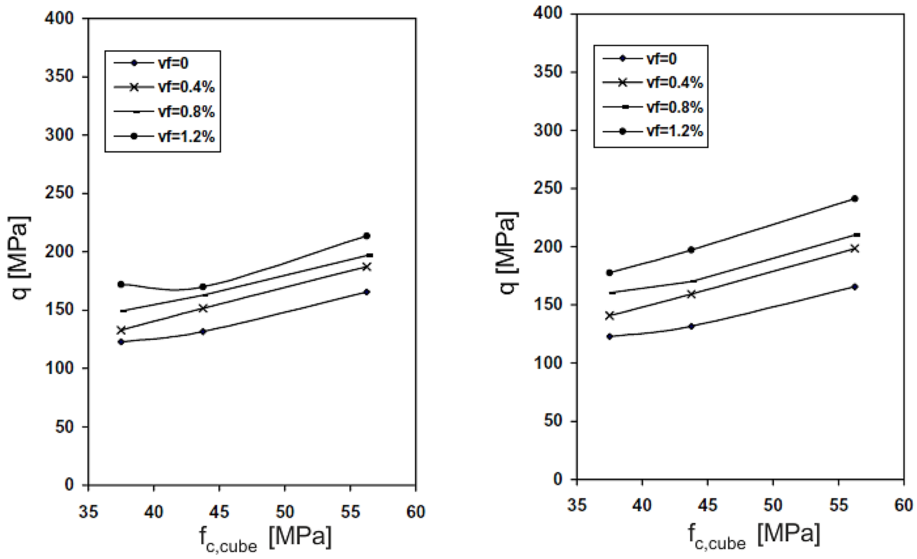


*Figure 2.52: Effect of fiber content and aspect ratio on the bearing strength at the area ratio of 9: Left, aspect ratio = 21.8; right, aspect ratio = 32 (Al-Taan & Al-Hamdony 2005)*

A comprehensive study on the bearing capacity of ultra-high-strength concrete under concentrated load was performed by Klotz (2008), in which the effect of fiber type, volume percentage, hybrid fiber reinforcement and combined reinforcement were investigated. In his work, two kinds of steel fiber (straight microfiber MF: 13 mm/ 0.5 mm and hooked macrofiber DF: 35 mm/ 0.55 mm) were used to produce the concrete prisms (200 x 200 x 400-mm). Four area ratios were employed: 4.0, 8.0, 16.0 and 44.4. In the first series of the tests, the microfiber content was steadily increased from 0.5% up to 2% by volume. Beyond a fiber content of 1.5%, no further increase in the bearing stress was observed, as shown in Figure 2.53. Klotz attributed it to the diminishing workability associated with adverse influence on the properties of hardened concrete.

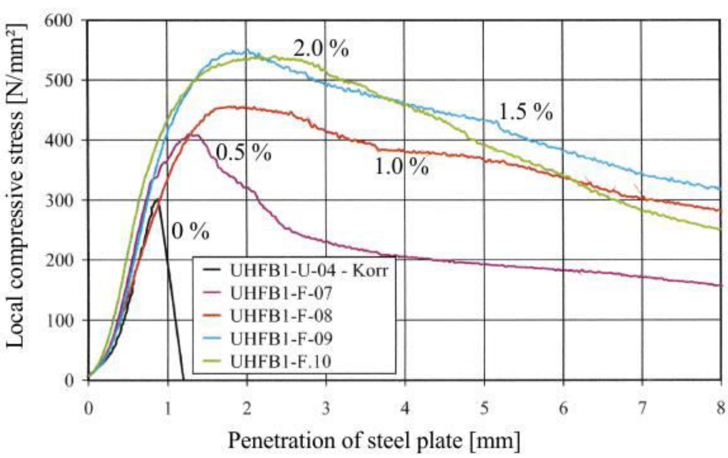


*Figure 2.53: Influence of microfiber concentrations (from 0.5% to 2.0%) on the bearing capacity of ultra-high-strength concrete (Klotz 2008)*

Through tests on prisms reinforced with two different kinds of steel fiber, Klotz observed a synergistic effect. He pointed out that the macrofiber contributed primarily to a higher maximum bearing strength, whereas the microfiber affected the post-cracking behavior (i.e. ductility) more beneficially. In the case of combined reinforcement, it was found that an increase in the microfiber fraction has more positive influence on the maximum bearing strength than the reinforcement rate.

For the prediction of the allowable bearing stress of steel fiber reinforced ultra-high-strength concrete, Klotz recommended the following equation:

$$F_{Rdu} = 0.8 \cdot A_{c0} \cdot f_{cd} \cdot \sqrt{\frac{A_c}{A_{c0}}} \qquad \text{Eq. 2.28}$$

**Summary**

Although a certain number of experiments have been conducted to investigate the positive effect of steel fibers on the load-bearing and fracture behavior of concrete, extremely few design approaches were proposed for SFRC structural members in the pertinent literature. Based on the limited experimental results presented by the aforementioned investigators, the primary influences of steel fibers on the load-bearing and fracture behavior of concrete centrally loaded with local force can be summarized as follows:

- The load-bearing capacity of concrete is significantly improved through incorporating of steel fibers.
- The ultimate bearing strength of concrete increases steadily with increasing fiber content and aspect ratio.
- Concrete reinforced or additionally strengthened with steel fibers exhibits a much more ductile failure behavior.
- A positive synergistic effect can be achieved by using hybrid fiber reinforcement.

# 3 Experimental research

## 3.1 Scope of experimental research

The experiments conducted here were intended to systematically investigate the influences of various parameters on the load-bearing and fracture behavior of SFRC under concentrated loading. The parameters studied included not only the common non-fiber-related variables affecting the structural behaviors of plain concrete but also the specific fiber-related factors influencing the mechanical properties of SFRC (Figure 1.1). For comparison purposes, specimens made of plain concrete were also tested under the same testing conditions. Depending upon the focus and sequence of the research work, the tests performed within the experimental research can be divided into 7 series, as described briefly below:

1. **Area ratio and concrete strength**: Normal-strength and high-strength concrete prisms with or without fiber reinforcement were tested with four different area ratios.

2. **Specimen dimension**: In addition to small prisms, large prisms with identical height to width ratio were produced with high-strength plain and fiber concretes.

3. **Fiber property**: Steel fibers with diverse properties in terms of strength, dimension, geometry and aspect ratio were incorporated into the high-strength concrete mix.

4. **Fiber concentration and combination**: Various fiber concentrations consisting of one or two, or even three different types of steel fiber were adopted to produce high-strength SFRC.

5. **Fiber orientation**: Different production methods of specimen regarding mold type, vibrating type and sampling direction were used to intentionally affect the fiber orientation in high-strength SFRC matrix.

6. **Eccentricity of load**: Four different eccentricities were applied to introduce concentrated load onto high-strength plain and fiber concrete prisms.

7. **Hybrid concrete system**: Hybrid concrete prisms containing both high-strength plain and fiber concretes were produced in a “fresh in fresh” concreting technique and loaded either concentrically or eccentrically.

It should be noted that in some test series the parameters were investigated in a combined way to study their joint effects on the structural and fracture behavior of concrete. More detailed information on the individual test series is given in Section 3.5.

## 3.2 Materials and specimens

For the production of various SFRCs, two kinds of base concrete mixture were composed and their compositions are summarized in Table 3.1. The first mixture was designed as a high-strength plain concrete using an ordinary Portland cement CEM I 52.5 R; the second one was a normal-strength plain concrete produced with a Portland slag cement CEM II B-S 42.5 N. The aggregates consisting of Rhine river sand and gravel with a maximum grain size of 16 mm exhibited a grading curve of A/B 16 (DIN 1045-2, 2008). Fly ash was used to partially substitute the cement and to improve the workability of concrete.

For the purpose of this research project, the term PC is used when referring to the high-strength plain concrete as the most specimens throughout the experiments were made of the high-strength base concrete mixture. And the term NS_PC, additionally with the characters NS, indicates the normal-strength plain concrete. Thus, in default of the characters NS in the code name of test series, it automatically represents concrete with high compressive strength, which is also valid in the case of steel fiber reinforced concrete (e.g. Table 3.8, Section 3.5).

The types and properties of the steel fibers applied are given in Table 3.2. Except for the straight microfiber S, other fibers are all hook-ended fibers with various dimensions and strengths (Figure 3.1). To maintain an adequate workability, the SFRC mixtures were accordingly modified by adding higher dosage of a polycarboxylate-ether-based superplasticizer.

*Table 3.1: Proportions of the plain concretes used for the production of SFRCs*

| Constituents [kg/m³] | PC (high-strength) | NS_PC (normal-strength) |
|---|---|---|
| Cement | CEM I 52.5 R<br>330 | CEM II B-S 42.5 N<br>280 |
| Fly ash | 90 | 60 |
| Aggregate | 1849 | 1856 |
| Superplasticizer | 1.3 | 0.75 |
| Water | 148.5 | 162.8 |
| w/c - ratio | 0.45 | 0.58 |
| 28-day compressive strength $f_{c,cube}$ [MPa] | 84.5 | 45.8 |

*Table 3.2: Types and properties of the steel fibers used*

| Index | Fiber Type | Shape | Length [mm] | Diameter [mm] | Aspect ratio [l/d] | Tensile strength [MPa] |
|---|---|---|---|---|---|---|
| L | RC-80/60-BN | hook-ended | 60 | 0.75 | 80 | 1225 |
| Lt | RC-65/60-BN | | 60 | 0.90 | 67 | 1160 |
| Lh | RC-80/60-BP | | 60 | 0.71 | 85 | 2600 |
| M | ZP 305 | | 30 | 0.55 | 55 | 1345 |
| S | FM 13/0.19 | straight | 13 | 0.19 | 68 | 2000 |

- **L**: **L**ong, hook-ended normal-strength macrofiber
- **Lt**: **L**ong, **t**hick hook-ended normal-strength macrofiber
- **Lh**: **L**ong, **h**igh-strength hook-ended macrofiber
- **M**: **M**edium, hook-ended normal-strength mesofiber
- **S**: **S**hort, straight high-strength microfiber

*RC-80/60-BN (L)* *RC-60/80-BP (Lh)* *ZP 305 (M)* *FM 13/0.19 (S)*

*Figure 3.1: Various types of steel fibers used for the production of SFRCs*

The concentrations of steel fiber investigated varied from 40 to 120 kg/m³ (Table 3.3), whereby the fiber reinforcement consisted of not only one fiber type but also two or even three different fiber types. The type of fiber reinforcement was named in an alphanumeric way. The alphabetic character indicates the type of steel fiber and the numeric character indicates the fiber content in kg/m³. For instance, L40M20S40 represents a fiber reinforcement containing L type of fiber with a content of 40 kg/m³, M type of fiber with a content of 20 kg/m³ and S type of fiber with a content of 40 kg/m³ (i.e. a total fiber content of 100 kg/m³).

For a fiber content of 80 kg/m³ with end-hooked macrofiber L, it has been observed that during the mixing process the steel fibers did not tend to homogeneously disperse in the mixture. Therefore, hybrid fiber reinforcement combining both long and short fibers was primarily considered for the production of SFRCs with the same or even higher fiber concentrations. In spite of relatively low mobility, these freshly mixed SFRCs with hybrid fiber reinforcement exhibited adequate compactability.

*Table 3.3: Concentrations and combinations of steel fiber for the production of SFRCs*

| **Index** | **Fiber type and content [kg/m³]** | | | | |
|---|---|---|---|---|---|
| | RC-80/60-BN (L) | RC-65/60-BN (Lt) | RC-80/60-BP (Lh) | ZP 305 (M) | FM 13/0.19 (S) |
| L60 | 60 | | | | |
| Lt60 | | 60 | | | |
| Lh60 | | | 60 | | |
| M60 | | | | 60 | |
| S60 | | | | | 60 |
| L40 | 40 | | | | |
| L80 | 80 | | | | |
| L40M20 | 40 | | | 20 | |
| L40S20 | 40 | | | | 20 |
| L40M40 | 40 | | | 40 | |
| L40S40 | 40 | | | | 40 |
| L40M20S20 | 40 | | | 20 | 20 |
| L40M40S20 | 40 | | | 40 | 20 |
| L40M20S40 | 40 | | | 20 | 40 |
| L40M40S40 | 40 | | | 40 | 40 |
| L60S20 | 60 | | | | 20 |
| L60S40 | 60 | | | | 40 |
| L60S60 | 60 | | | | 60 |

In the production of the plain and fiber concretes, the following mixing procedure was performed: The cement, fly ash and aggregates were first dry-mixed either in a 250-l or in a 100-l pan mixer (Figure 3.2) for 30 seconds. Tap water with superplasticizer was then added gradually in the running mixer and the wet mixture was mixed for another 2 minutes. During the next minute, the fibers (if used) were scattered in the running mixer and mixed for 3 further minutes.

*Figure 3.2: Left, 250-l pan mixer (Schwelm ZK250EQ); right, 100-l pan mixer (Pemat 3908 ZK150HE)*

The properties of the freshly mixed concretes were determined for each batch. For every sort of plain and fiber concretes, three 150-mm cubes and three 150 x 300-mm cylinders were cast according to DIN EN 12390-2 (2009) to determine the compressive and splitting tensile strength; additionally, three 150 x 300-mm cylinders were manufactured for the investigation of Young's modulus of the plain concretes and some sorts of SFRC.

For the concentrated loading tests, one test group consisted of at least 3 concrete prisms with dimensions of 150 x 150 x 300-mm or 300 x 300 x 600-mm. The small prisms made of SFRC were produced either in the standing or in the lying wooden molds with the purpose to investigate the influence of the casting direction on the orientation of steel fibers in concrete matrix and further on the load-bearing and fracture behavior of SFRC (Figure 3.3). The large prisms were cast in standing wooden forms and designed to study the size effect of specimen of high-strength plain and fiber concretes.

*Figure 3.3: Wooden molds (150 x 150 x 300-mm) used for the production of concrete prism (left, standing mold; right, lying mold)*

To eliminate the wall effect on the fiber orientation, prisms (150 x 150 x 300-mm, for the concentrated loading tests) and cylinders (150 x 300-mm, for the splitting tensile strength tests) were sawed or drilled out of large high-strength SFRC beams with a cross-section of 300 x 300-mm and a length of 800-mm. These prisms and cylinders were sampled out along direction either perpendicular or parallel to the casting direction. The precise positions and directions of sampling are illustrated in Figure 3.4 for the case of prism.

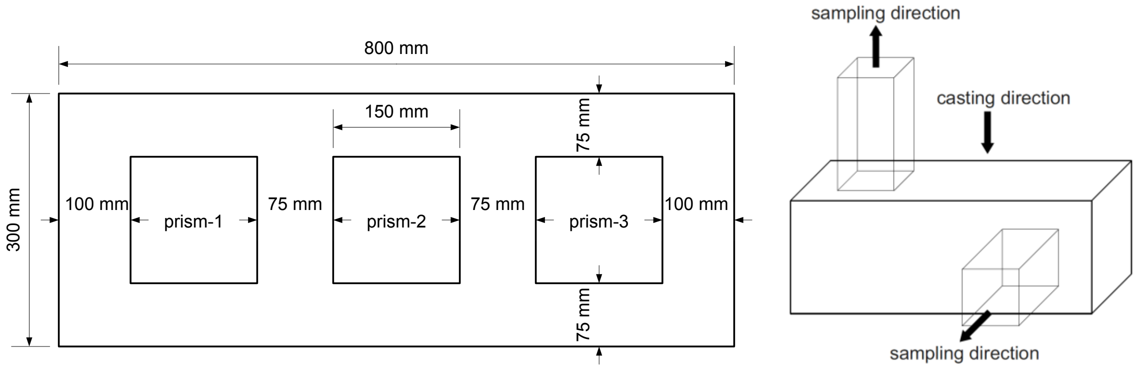


*Figure 3.4: Sampling positions (left) and directions (right) of prisms from large beam produced with high-strength SFRC*

Depending on the size and shape of the forms used, the fresh concrete was placed in two or three layers and properly compacted by either vibrating table or internal vibrator. The placing (i.e. sequence and quantity) and vibrating (i.e. duration, intensity and position) of concrete have been uniformly conducted for a certain production manner. A brief overview of the production manners of prisms for the concentrated loading tests is given in Table 3.4.

*Table 3.4: Overview of the production manners of prisms for the concentrated loading tests*

| Prism dimension | Mold dimension | Mold type | Vibration type | Sampling direction |
|---|---|---|---|---|
| 150 x 150 x 300-mm | 150 x 150 x 300-mm | standing | vibrating table | - |
| | | | internal vibrator | |
| | | lying | vibrating table | - |
| | 300 x 300 x 800-mm | lying | internal vibrator | parallel to casting direction |
| | | | | perpendicular to casting direction |
| 300 x 300 x 600-mm | 300 x 300 x 600-mm | standing | internal vibrator | - |

The concrete samples (cubes, cylinders and small prisms) were cured in accordance with DIN EN 12390-2 (2009): After 24h of storage in the molds, the specimens were demolded and stored in a water curing tank at a temperature of 20 ± 2°C for 6 days. Afterwards, with the exception of the cylinders for the splitting tensile strength tests, the other specimens were taken out of the water tank and restored with a temperature of 20 ± 2°C and a relative humidity of 65 ± 5% (i.e. standard curing condition) for another 21 days.

For the large prisms and beams, the storage in the molds was extended to 48h. After demolding, the prisms and beams were wrapped with plastic film and stored for another 5 days. After removing the plastic membrane, the large prisms were cured under the standard curing condition for the next 21 days. In the case of large beams, after 14 days of storage under the standard curing condition, small prisms and cylinders were sampled out; the cylinders for the splitting tensile strength tests were wrapped with plastic membrane and stored together with the small prisms for the concentrated loading tests under the standard curing condition until the test. The standard tests (i.e. compressive strength, splitting tensile strength and Young´s modulus) and the concentrated loading tests were carried out at an age of 28 days.

## 3.3 Experimental tests

### 3.3.1 Standard tests

The properties of the fresh as well as the hardened plain and fiber concretes were determined in accordance with the German codes listed in Table 3.5. Since the testing procedure of the individual concrete properties is explicitly described in the corresponding code, no specific information regarding the testing methods will be given in this section.

*Table 3.5: Codes for determining the properties of the fresh and hardened plain and fiber concretes*

| Concrete property | Code |
|---|---|
| Flow consistency | DIN EN 12350-5 (2009) |
| Air void content | DIN EN 12350-7 (2009) |
| Bulk density | DIN EN 12350-6 (2011) |
| Compressive strength | DIN EN 12390-3 (2009) |
| Splitting tensile strength | DIN EN 12390-6 (2010) |
| Young's modulus | DIN 1048-5 (1991) |

### 3.3.2 Fiber concentration and orientation

The fiber concentration and orientation in the SFRC samples produced with one type of steel fiber were determined with the BSM100 device based on the magnetic-inductive measuring principle. This device was collaboratively developed by the Technical University of Braunschweig and the company Hertz Systemtechnik (BSM100 2008, Wichmann 2009). As demonstrated in Figure 3.5, the BSM100 device consists of several prime components: one basic unit (yellow case), one steel fiber sensor (black form), one measuring platform (wooden plate) and other accessories (e.g. temperature sensor).

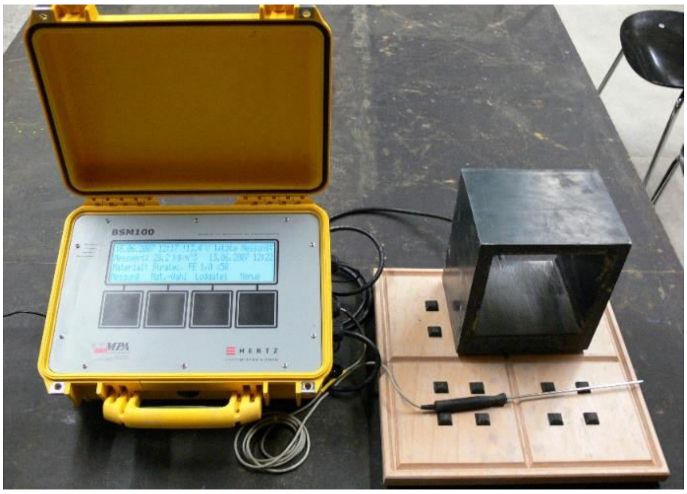


*Figure 3.5: Prime components of the BSM100 device for the measuring of fiber concentration and orientation on SFRC specimen, adopted from Breitenbücher & Rahm (2009)*

Figure 3.6 schematically describes the basic measuring principle of the BSM100 device. During the measuring, a sinusoidal alternating current generated by the generator (basic unit) is fed into the excitation coil (steel fiber sensor). If a cubic or cylindrical SFRC sample is placed in the steel fiber sensor, a magnetic field is generated; meanwhile, a voltage is induced through the built-in induction coil, which is then detected by an integrated voltmeter. Based on the fact that only ferromagnetic materials exhibit inductive properties and SFRC contains no other ferromagnetic materials except steel fibers. Theoretically, the higher the existing steel fibers in a concrete sample is, the higher the induced voltage is. Consequently, a quick quantitative evaluation of the fiber concentration and orientation in three spatial dimensions can be obtained on a either fresh or hardened SFRC sample.

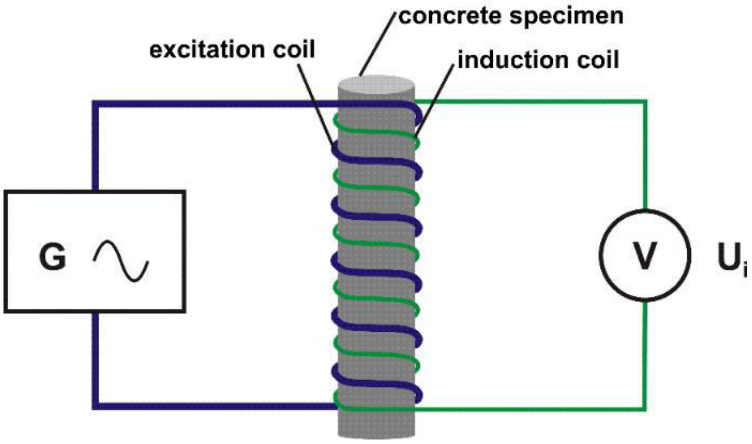


*Figure 3.6: Measuring principle of the BSM100 device (BSM100 2008)*

At the beginning of each measuring, the following basic parameters should be defined and input into the basic unit, such as type of steel fiber, age of concrete (i.e. fresh or hardened) and geometry of specimen (i.e. cube or cylinder). The measuring procedure essentially includes four steps for a hardened cubic SFRC specimen: The first step is a baseline measuring without the sample. The following three steps are then carried out with the concrete cube, whereby the cubic sample is so to turn that it is measured once in each axis direction, as illustrated in Figure 3.7. The measuring procedure for cylindrical specimen is described in detail in the guidebook of the BSM100 device (BSM100 2008). Consequently, the fiber orientation is presented by percentage value in three spatial directions on the display of the basic unit. Each value describes the probability of the orientation of steel fibers in the corresponding spatial direction in the sample. The fiber concentration is described in kg/m³. In this research work, the measuring was uniformly conducted on cubic specimens with a length of 150 mm. These cubes were sampled from the SFRC prisms of dimensions 150 x 150 x 300-mm or 300 x 300 x 600-mm.

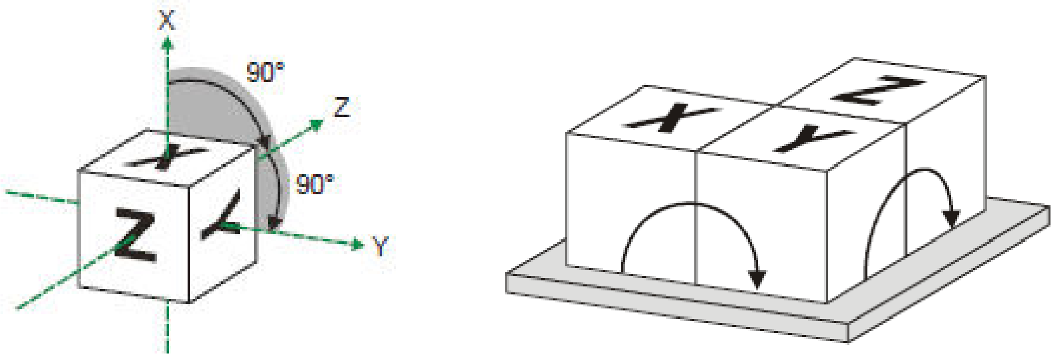


*Figure 3.7: Handling of the cubic specimen during the measuring process (BSM100 2008)*

### 3.3.3 Concentrated loading tests

**Test preparation**

As mentioned above, two sizes of concrete prism were adopted for the tests: 150 x 150 x 300-mm and 300 x 300 x 600-mm, corresponding to a constant ratio of length h to width d of 2. In this case, the influence of the lateral strain restraint caused by the machine platen on the load-bearing capacity can be kept as small as possible (Figure 2.25). In order to avoid any stress concentration induced by surface roughness, the testing surface ($A_{c1}$ = 150 x 150-mm or 300 x 300-mm) was plane parallel ground with grinding machine or smoothened with high-strength grouting mortar shortly prior to the testing.

For the transmission of concentrated load on the small prisms, four area ratios were employed: 16, 9, 4 and 2.25, corresponding to four sizes of square cross-sectional high-strength steel plate with a width of 37.5 mm, 50 mm, 75 mm and 100 mm, respectively. For the testing of the large prisms, two area ratios were chosen: 9 and 4, corresponding to two sizes of square steel plate with a width of 100 mm and 150 mm. The area ratio R is defined as the ratio of the total area ($A_{c1}$ = 150 x 150-mm or 300 x 300-mm) to the loaded area ($A_{c0}$, i.e. area of the steel bearing plate). The dimensions of the steel plates used for the transmission of concentrated load and the corresponding area ratios are listed in Table 3.6.

*Table 3.6: Dimensions of the square steel plates used for the transmission of concentrated load*

| **Width [mm]** | **Thickness [mm]** | **Testing surface $A_{c0}$ [mm²]** | **Cross-sectional area $A_{c1}$ [mm²]** | **Area ratio $R = A_{c1}/A_{c0}$** |
|---|---|---|---|---|
| 37.5 | 40 | 37.5 x 37.5 | 150 x 150 | 16 |
| 50 | | 50 x 50 | | 9 |
| 75 | | 75 x 75 | | 4 |
| 100 | | 100 x 100 | | 2.25 |
| | | | 300 x 300 | 9 |
| 150 | | 150 x 150 | | 4 |

Besides the concentric load introduction, the high-strength plain and fiber concrete prisms with dimensions of 150 x 150 x 300-mm were tested eccentrically with two area ratios of 9 and 4. At the area ratio of 9, four eccentricities of load were employed, as illustrated in Figure 3.8. For the area ratio of 4, only two eccentricities were considered: e15 (e = 15 mm) and E (edge loading). An overview of the eccentricities of load relative to the area ratios is summarized in Table 3.7.

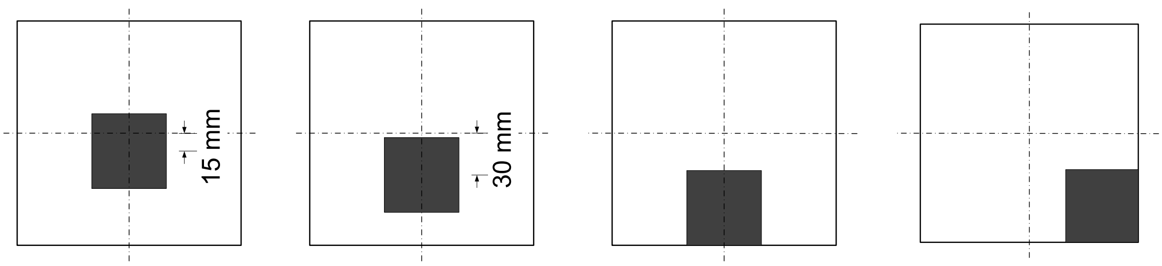


*a) e15 (e = 15 mm)* *b) e30 (e = 30 mm)* *c) E (edge loading)* *d) C (corner loading)*

*Figure 3.8: Eccentricities of load applied for the area ratio R = 9*

*Table 3.7: Overview of the eccentricities of load adopted for the area ratios of 9 and 4*

| **Area ratio $R = A_{c1}/A_{c0}$** | **Eccentricity of load [e]** | | | |
|---|---|---|---|---|
| | e = 15 mm (e15) | e = 30 mm (e30) | edge loading (E) | corner loading (C) |
| 9 | + | + | + | + |
| 4 | + | | + | |

**Testing procedure**

All tests were performed using a servo-hydraulic universal testing machine with a maximum load of 5 MN. The concentrated load was transmitted onto the ground or smoothened surface of prism through the steel plate. The deformations of the specimen as a result of the introduction of concentrated load were measured by the LVDTs (manufacturer: HBM; type: 1-WA/20MM-T). As demonstrated in Figure 3.9, two vertical LVDTs were placed diagonally around the specimen to measure the total longitudinal displacement between the bearing steel plate and the lower platen of the testing machine. The other two vertical LVDTs were attached onto the midpoint of the prism top edges to measure the vertical compressive deformation. Four horizontal LVDTs were positioned around the prism (5 cm from the longitudinal axis of the LVDT to the top edge of specimen) to measure the lateral deformation. The load was continuously applied at a loading rate of 0.5 mm/min. The testing process was automatically terminated by the software under the condition that a load drop by 60% of the maximum load was detected.

For the eccentric load introduction, the specimen was accordingly placed eccentrically on the lower machine platen (Figure 3.10). This can ensure a load introduction along the centroidal axis of the testing machine and the bearing plate into the concrete prism. In the case of extreme eccentricities of load, a possible overturn of the specimen during the test may thus be avoided.


*Figure 3.9: Test set-up for the concentrated loading tests*

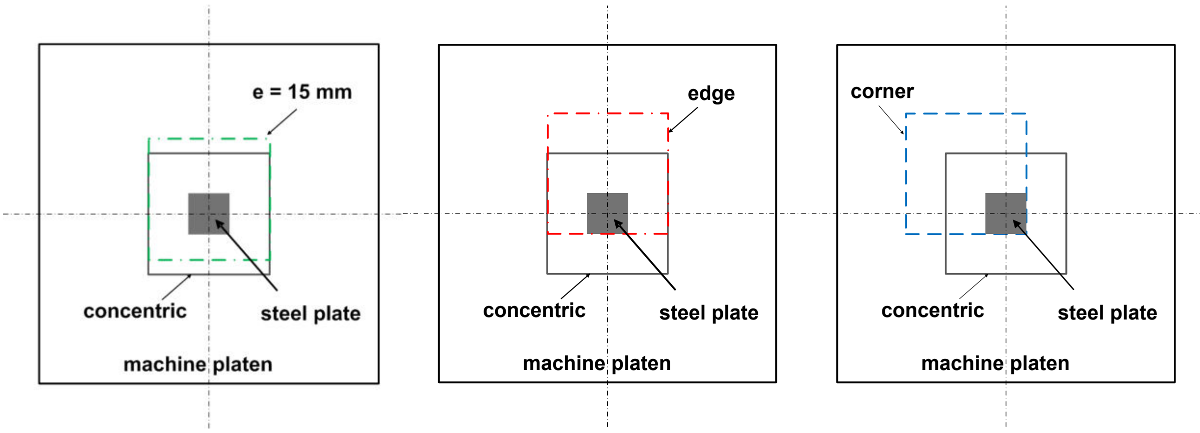


*a) e = 15 mm (e15)* *b) edge loading (E)* *c) corner loading (C)*

*Figure 3.10: Positioning of the specimen under eccentric loading, exemplarily for the area ratio of 9*

## 3.4 Hybrid concrete system

As previously stated in Section 2.2, a multi-axial stress state containing both longitudinal compressive stresses and lateral tensile stresses is generated in a concrete member subjected to concentrated load. And the state of stress exhibits a highly non-uniform distribution in the upper region of concrete member with a depth approximately equal to the width of cross-section (Figure 2.20). In other words, the critical tensile stresses along directions perpendicular to the load exist predominantly in the upper region of the concrete member.

The magnitude and position of the maximum tensile stresses or forces depend essentially upon the extent of the concentrations of load. However, variations in the properties of concrete and the types of reinforcement in this upper zone can also exert large influence on the structural and fracture behavior of concrete member. This effect has been experimentally confirmed by Schmidt and Fiedler (1993) and Empelmann and Wichers (2009) through adding secondary fiber or steel reinforcement into the conventionally reinforced concrete specimens. In both cases, positive effects on the load-bearing and fracture behavior of concrete have been reported.

Hence, in this test series the concrete specimens were partially strengthened with various types and thicknesses of fiber reinforcement only in its upper half, instead of a full range of reinforcement. Under the same testing conditions as applied for the plain and fully reinforced concrete prisms, these partially strengthened prisms were then tested to examine whether comparable performance in terms of load-bearing and fracture behavior would be expected.

Despite a notable saving of material costs and a potential similar structural behavior, special attentions were required in the production of the hybrid concrete prisms. A so-called "fresh in fresh" concreting technique was applied by which the high-strength plain and fiber concretes were placed either in the standing or lying wooden molds (150 x 150 x 300-mm) in their fresh states. Two sorts of fiber reinforcement (L60, L60S60) were used to partially reinforce the concrete specimens.

As the incorporation of fiber reinforcement can alter the distribution of the tensile stresses and further the position of the maximum tensile stresses, three different thicknesses of fiber reinforcement (50 mm, 100 mm and 150 mm) were adopted with the purpose of estimating the optimal reinforcement thickness for a given area ratio. A schematic description of the hybrid concrete prisms with various reinforcement thicknesses is given in Figure 3.11 for the case of standing production.

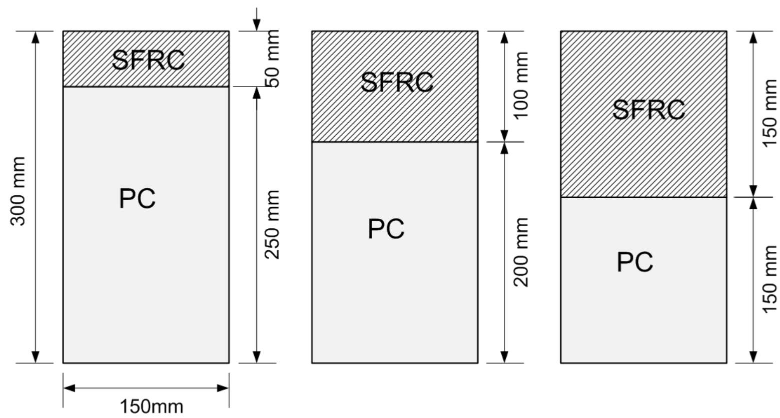


*Figure 3.11: Schematic illustration of the hybrid concrete prisms containing both plain concrete and fiber concrete with various layer thicknesses for the case of standing production*

In the case of standing production, the high-strength plain concrete (PC) was first filled in the form and compacted to a predefined height, then followed by the placing of the high-strength SFRC (L60 or L60S60). In the lying production, the high-strength plain and fiber concretes were simultaneously placed in the mold, however, temporarily separated by a stainless steel plate with a predefined distance to the internal wall of the mold, as shown in Figure 3.12. During the concreting, the steel plate was successively being lifted up and a monolithic combination of the two freshly mixed concretes in the interfacial zone can thus be achieved through vibrating. The concentrated load was later transmitted onto the side of specimen containing SFRC.

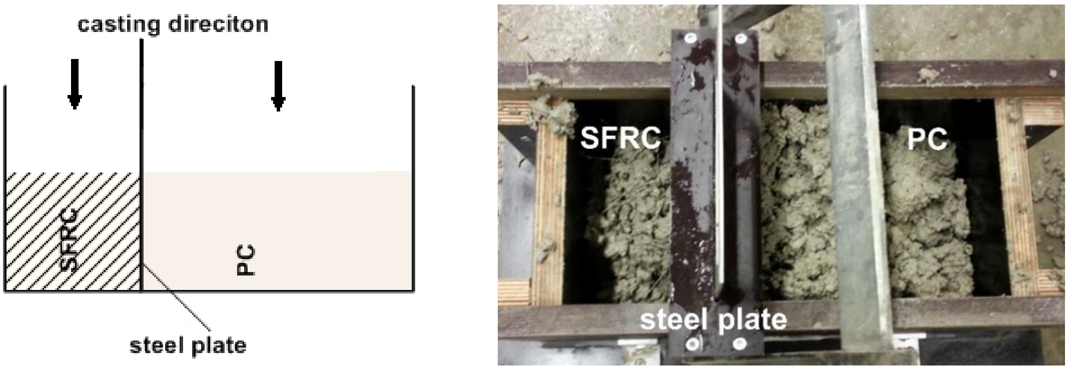


*Figure 3.12: Left, schema of "fresh in fresh" concreting procedure; right, production of hybrid concrete specimen in progress*

The hybrid concrete prisms were cured, prepared and tested in the same manner as used for the plain and fully reinforced specimens. The concentrated load was transmitted either concentrically with two area ratios of 9 and 4 or eccentrically with one area ratio of 9. Thus, the parameters investigated included not only type and thickness of fiber reinforcement layer, casting direction (i.e. fiber orientation) but also area ratio and eccentricity of load. In most cases, the parameters were studied in a combined way (Table 3.14, Section 3.5) and the test results were evaluated in comparison with those obtained from the plain and fully reinforced specimens.

## 3.5 Experimental program

The total experimental program consisted of 7 test series focusing on the diverse parameters that govern the load-bearing and fracture behavior of the non-fibrous and fibrous concretes under concentrated loading. In some test series, the variables were investigated in a combined way with the purpose to study the joint effects. The detailed descriptions of the individual test series are given as follows:

**Test series 1: Influence of area ratio and concrete strength**
In this test series, the 150 x 150 x 300-mm concrete prisms (d150) were manufactured with the standing wooden molds and compacted with vibrating table. The concrete prisms produced in this way were referred to as the standard prisms. For this kind of production, the loading direction was aligned to the casting direction. Two base concrete mixtures (PC: high-strength and NS_PC: normal-strength) were used to manufacture the SFRCs with various compressive strengths (L60: high-strength SFRC and NS_L60: normal-strength SFRC) with an identical fiber concentration of 60 kg/m³. The steel fiber used here was the hook-ended macrofiber L (RC-80/60-BN). The concrete prisms were later concentrically loaded with four different area ratios: 16, 9, 4 and 2.25. The scope of the performed tests within this series is summarized in Table 3.8.

*Table 3.8: Scope of the performed tests in the test series 1*

| Index | Fiber content [kg/m³] | Mold type | Specimen dimension | Area ratio | Load introduction | Code |
|---|---|---|---|---|---|---|
| NS_PC | - | standing | d150 | 16 | concentric | NS_PC_16 |
| | | | | 9 | | NS_PC_9 |
| | | | | 4 | | NS_PC_4 |
| | | | | 2.25 | | NS_PC_2.25 |
| PC | - | | | 16 | | PC_16 |
| | | | | 9 | | PC_9 |
| | | | | 4 | | PC_4 |
| | | | | 2.25 | | PC_2.25 |
| NS_L60 | 60 | | | 16 | | NS_L60_16 |
| | | | | 9 | | NS_L60_9 |
| | | | | 4 | | NS_L60_4 |
| | | | | 2.25 | | NS_L60_2.25 |
| L60 | 60 | | | 16 | | L60_16 |
| | | | | 9 | | L60_9 |
| | | | | 4 | | L60_4 |
| | | | | 2.25 | | L60_2.25 |

**Test series 2: Influence of specimen dimension**

In this test series, the large high-strength plain and fiber concrete prisms with dimensions of 300 x 300 x 600-mm (d300) were produced with the standing wooden molds and compacted with internal vibrator. In this case, the loading direction was aligned to the casting direction. The type and content of steel fiber applied here were identical with those used for the production of the standard prisms in the test series 1. These large prisms were concentrically tested with two area ratios of 9 and 4. For a better comparison, the performed tests on the large prisms (d300) are listed along with those on the standard prisms (d150) from the test series 1 (Table 3.9).

*Table 3.9: Scope of the performed tests in the test series 2*

| Index | Fiber content [kg/m³] | Mold type | Specimen dimension | Area ratio | Load introduction | Code |
|---|---|---|---|---|---|---|
| PC | - | standing | d150 | 9 | concentric | PC_9 |
| | | | | 4 | | PC_4 |
| | | | d300 | 9 | | PC_9_d300 |
| | | | | 4 | | PC_4_d300 |
| L60 | 60 | | d150 | 9 | | L60_9 |
| | | | | 4 | | L60_4 |
| | | | d300 | 9 | | L60_9_d300 |
| | | | | 4 | | L60_4_d300 |

**Test series 3: Influence of fiber property**

In this test series, the high-strength plain concrete (PC) was reinforced with various types of steel fiber. These SFRCs were then cast into the standing wooden molds with dimensions of 150 x 150 x 300-mm and compacted with vibrating table. In all cases, the loading direction was aligned to the casting direction. The amount of steel fiber for each SFRC was uniformly 60 kg/m³. These SFRC prisms were loaded concentrically with three different area ratios of 9, 4 and 2.25. The scope of the performed tests within this series is summarized in Table 3.10, along with the test groups L60_9 and L60_4 from the test series 1 as comparison.

*Table 3.10: Scope of the performed tests in the test series 3*

| Index | Fiber content [kg/m³] | Mold type | Specimen dimension | Area ratio | Load introduction | Code |
|---|---|---|---|---|---|---|
| L60 | 60 | standing | d150 | 9 | concentric | L60_9 |
| | | | | 4 | | L60_4 |
| | | | | 2.25 | | L60_2.25 |
| Lt60 | | | | 9 | | Lt60_9 |
| | | | | 4 | | Lt60_4 |
| Lh60 | | | | 9 | | Lh60_9 |
| | | | | 4 | | Lh60_4 |
| M60 | | | | 9 | | M60_9 |
| | | | | 4 | | M60_4 |
| | | | | 2.25 | | M60_2.25 |
| S60 | | | | 9 | | S60_9 |
| | | | | 4 | | S60_4 |

**Test series 4: Influence of fiber concentration and combination**

In this test series, the high-strength plain concrete (PC) was strengthened with diverse fiber concentrations and combinations. In addition to monofiber reinforcement containing only one fiber type, hybrid fiber reinforcements consisting of two or three different fiber types (different size or shape) were considered. The contents of steel fiber were in the range of 40-120 kg/m³. The SFRCs were cast into the standing wooden molds (d150) and compacted with vibrating table. In all cases, the loading direction was aligned to the casting direction. These SFRC prisms were concentrically loaded with two different area ratios of 9 and 4. The scope of the performed tests within this series is summarized in Table 3.11, along with the test groups L60_9 and L60_4 from the test series 1 as comparison.

*Table 3.11: Scope of the performed tests in the test series 4*

| Index | Fiber content [kg/m³] | Mold type | Specimen dimension | Area ratio | Load introduction | Code |
|---|---|---|---|---|---|---|
| L40 | 40 | standing | d150 | 9 | concentric | L40_9 |
| | | | | 4 | | L40_4 |
| L40S20 | 60 | | | 9 | | L40S20_9 |
| | | | | 4 | | L40S20_4 |
| L40M20 | | | | 9 | | L40M20_9 |
| | | | | 4 | | L40M20_4 |
| L60 | | | | 9 | | L60_9 |
| | | | | 4 | | L60_4 |
| L40S40 | 80 | | | 9 | | L40S40_9 |
| | | | | 4 | | L40S40_4 |
| L40M40 | | | | 9 | | L40M40_9 |
| | | | | 4 | | L40M40_4 |
| L40M20S20 | | | | 9 | | L40M20S20_9 |
| | | | | 4 | | L40M20S20_4 |
| L60S20 | | | | 9 | | L60S20_9 |
| | | | | 4 | | L60S20_4 |
| L80 | | | | 9 | | L80_9 |
| | | | | 4 | | L80_4 |
| L40M20S40 | 100 | | | 9 | | L40M20S40_9 |
| | | | | 4 | | L40M20S40_4 |
| L40M40S20 | | | | 9 | | L40M40S20_9 |
| | | | | 4 | | L40M40S20_4 |
| L60S40 | | | | 9 | | L60S40_9 |
| | | | | 4 | | L60S40_4 |
| L40M40S40 | 120 | | | 9 | | L40M40S40_9 |
| | | | | 4 | | L40M40S40_4 |
| L60S60 | | | | 9 | | L60S60_9 |
| | | | | 4 | | L60S60_4 |

**Test series 5: Influence of fiber orientation**

In this test series, the high-strength plain concrete (PC) was reinforced with two different kinds of fiber reinforcement (L60 and L60S60). As shown in Figure 3.3, these SFRC prisms (d150) were produced with either standing or lying (l) wooden molds and compacted with vibrating table. For the production in the standing molds, the SFRC with fiber reinforcement L60 was additionally compacted with internal vibrator (i). Furthermore, prisms (150 x 150 x 300-mm) were sawed along directions either parallel (p) or vertical (v) to the casting direction out of the large beams (300 x 300 x 800-mm, reinforced with fiber reinforcement L60), as illustrated in Figure 3.4. Hence, the loading direction was along direction either parallel (for the standing production and parallel sampling) or perpendicular (for the lying production and vertical sampling) to the casting direction. These SFRC prisms were concentrically loaded with two different area ratios of 9 and 4. The scope of the performed tests within this series is summarized in Table 3.12, along with the test groups L60_9 and L60_4 from the test series 1 and L60S60_9 and L60S60_4 from the test series 4 as comparison.

*Table 3.12: Scope of the performed tests in the test series 5*

| **Index** | **Fiber content [kg/m³]** | **Variables** | | **Loading direction w. r. t. casting direction** | **Area ratio** | **Code** |
|---|---|---|---|---|---|---|
| L60 | 60 | mold type | standing | parallel | 9 | L60_9 |
| | | | | | 4 | L60_4 |
| | | | lying (l) | perpendicular | 9 | L60_l_9 |
| | | | | | 4 | L60_l_4 |
| | | vibration type | vibrating table | parallel | 9 | L60_9 |
| | | | | | 4 | L60_4 |
| | | | internal vibrator (i) | parallel | 9 | L60_i_9 |
| | | | | | 4 | L60_i_4 |
| | | sampling direction | parallel (p) | parallel | 9 | L60_p_9 |
| | | | | | 4 | L60_p_4 |
| | | | vertical (v) | perpendicular | 9 | L60_v_9 |
| | | | | | 4 | L60_v_4 |
| L60S60 | 120 | mold type | standing | parallel | 9 | L60S60_9 |
| | | | | | 4 | L60S60_4 |
| | | | lying (l) | perpendicular | 9 | L60S60_l_9 |
| | | | | | 4 | L60S60_l_4 |

**Test series 6: Influence of eccentricity of load**

In this test series, not only the high-strength plain concrete prisms but also the high-strength SFRC specimens cast with fiber reinforcement L60, L60S60 and L40M40S40 were loaded eccentrically with two different area ratios of 9 and 4. As demonstrated in Figure 3.8 and Table 3.7, four eccentricities of load were employed: 15 mm (e15), 30 mm (e30), edge (E) and corner (C). These high-strength concrete prisms (d150) were produced with the standing wooden molds and compacted with vibrating table. Thus, the loading direction was aligned to the casting direction. The scope of the performed tests within this series is summarized in Table 3.13.

*Table 3.13: Scope of the performed tests in the test series 6*

| Index | Fiber content [kg/m³] | Mold type | Specimen dimension | Area ratio | Load introduction | Code |
|---|---|---|---|---|---|---|
| PC | - | standing | d150 | 9 | e15 | PC_9_e15 |
| | | | | | e30 | PC_9_e30 |
| | | | | | E | PC_9_E |
| | | | | | C | PC_9_C |
| | | | | 4 | e15 | PC_4_e15 |
| | | | | | E | PC_4_E |
| L60 | 60 | | | 9 | e15 | L60_9_e15 |
| | | | | | e30 | L60_9_e30 |
| | | | | | E | L60_9_E |
| | | | | | C | L60_9_C |
| | | | | 4 | e15 | L60_4_e15 |
| | | | | | E | L60_4_E |
| L60S60 | 120 | | | 9 | e15 | L60S60_9_e15 |
| | | | | | e30 | L60S60_9_e30 |
| | | | | | E | L60S60_9_E |
| | | | | | C | L60S60_9_C |
| | | | | 4 | e15 | L60S60_4_e15 |
| | | | | | E | L60S60_4_E |
| L40M40S40 | 120 | | | 9 | E | L40M40S40_9_E |
| | | | | | C | L40M40S40_9_C |

**Test series 7: Hybrid concrete system**

In this test series, the hybrid concrete prisms (d150) containing both high-strength plain and fiber concretes were produced with either standing or lying (l) wooden molds and compacted with vibrating table. Hence, the loading direction was along direction either parallel (for the standing production) or perpendicular (for the lying production) to the casting direction. Two kinds of fiber reinforcement (L60 and L60S60) were used and incorporated into the form with three different thicknesses (z50: 50 mm, z100: 100 mm and z150: 150 mm). Two different area ratios of 9 and 4 were adopted for the load introduction. In addition to the concentric loading, these hybrid specimens were tested eccentrically under edge and corner loading for a fiber reinforcement thickness of 100 mm (z100). The scope of the performed tests within this series is summarized in Table 3.14.

*Table 3.14: Scope of the performed tests in the test series 7*

| Index | Thickness [mm] | Mold type | Specimen dimension | Area ratio | Load introduction | Code |
|---|---|---|---|---|---|---|
| L60 | 50 | standing | d150 | 9 | concentric | L60_z50_9 |
| | 100 | | | 9 | concentric | L60_z100_9 |
| | | | | | E | L60_z100_9_E |
| | | | | | C | L60_z100_9_C |
| | | | | 4 | concentric | L60_z100_4 |
| | 150 | | | 9 | concentric | L60_z100_9 |
| | 50 | lying (l) | | 9 | concentric | L60_z50_l_9 |
| | 100 | | | | | L60_z100_l_9 |
| | 150 | | | | | L60_z150_l_9 |
| L60S60 | 50 | standing | | 9 | concentric | L60S60_z50_9 |
| | 100 | | | 9 | concentric | L60S60_z100_9 |
| | | | | | E | L60S60_z100_9_E |
| | | | | | C | L60S60_z100_9_C |
| | | | | 4 | concentric | L60S60_z100_4 |
| | 150 | | | 9 | concentric | L60S60_z100_9 |
| | 50 | lying (l) | | 9 | concentric | L60S60_z50_l_9 |
| | 100 | | | | | L60S60_z100_l_9 |
| | 150 | | | | | L60S60_z150_l_9 |

# 4 Results of experimental investigations

## 4.1 Properties of fresh and hardened concretes

The properties of the fresh as well as the hardened plain and fiber concretes were determined in accordance with the corresponding German standards, as listed in Table 3.5. The test results are presented in Table B.1 and Table B.2 (Appendix B) for the fresh and hardened concretes, respectively.

**Properties of fresh concrete**

The properties of the fresh plain and fiber concretes in terms of flow consistency, air void content and bulk density were determined for each batch in order to continuously monitor the quality of the freshly mixed mixtures (Table B.1, Appendix B). The workability of the fresh concretes (i.e. flow consistency) was measured with the Flow Table Test (DIN EN 12350-5, 2009). In order to ensure a flow consistency of about 40 cm, all mixtures were produced with an adequate concentration of superplasticizer based on polycarboxylate-ether. As previously mentioned, the addition of steel fibers, in particular with high amount and/or high aspect ratio, can significantly stiffen the fresh concrete. Thus, for SFRCs with fiber content ≥ 80 kg/m³, the dosage of superplacticizer was so to choose that the fresh mixture exhibited an appropriate compactability in spite of a relatively lower flow consistency. Meanwhile, the mixture did not show any undesirable blending or segregation.

**Properties of hardened concrete**

The properties of the hardened plain and fiber concretes in terms of compressive strength, splitting tensile strength and Young´s modulus were determined for each sort of concrete (Table B.2, Appendix B). The mean values of compressive strength were slightly improved by the fiber addition and generally increased with growing fiber content, as demonstrated in Figure 4.1 for the high-strength concrete. The increments in compressive strength were in the range from essentially nil to about 19%, compared to the values of the plain concrete. A similar tendency was also observed in the case of splitting tensile strength (Figure 4.2). However, the improvement through steel fibers was more appreciable with increases varying from 28% to 140%, especially for SFRCs with hybrid fiber reinforcement with high fiber contents. In both cases, no direct correlation was found between the strengths of concrete and the types of steel fiber. Regarding the influence of concrete strength, the improvement through fiber addition in compressive strength was more evident for the normal-strength concretes ($\Delta_{NS\_L60/\ NS\_PC}$ = 16% vs. $\Delta_{L60/\ PC}$ = 3%); however, the increase in splitting tensile strength was slightly more distinct for the high-strength concretes ($\Delta_{L60/\ PC}$ = 67% vs. $\Delta_{NS\_L60/\ NS\_PC}$ = 59%). Since for a fiber content < 2% by volume the values of Young´s modulus can only be marginally affected by the fibers, no further investigation was conducted on the SFRCs with hybrid fiber reinforcement.

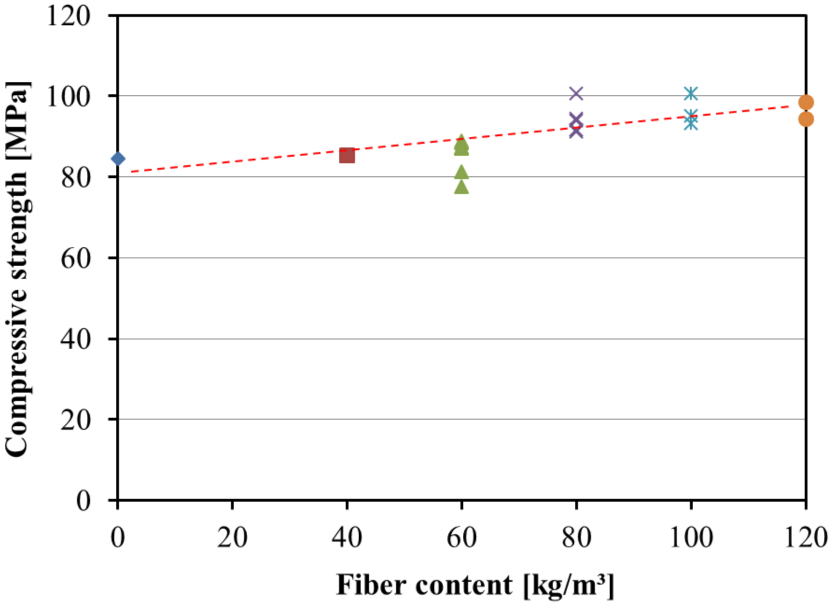


*Figure 4.1: Influence of fiber content on the compressive strength of the high-strength concretes*

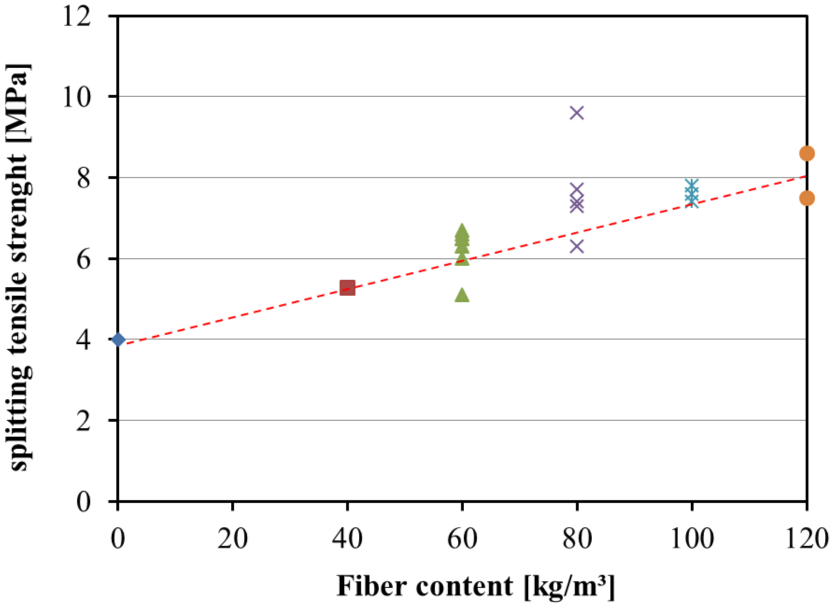


*Figure 4.2: Influence of fiber content on the splitting tensile strength of the high-strength concretes*

## 4.2 Concentrated loading tests

### 4.2.1 Influence of area ratio and concrete strength

As previously stated in Section 2.2, the ratio of total cross-sectional area $A_{c1}$ to loaded area $A_{c0}$ exerts great impact on the magnitude of bearing stresses generated in a concrete member under concentrated load. In this test series, four different area ratios were adopted to study their effects on the load-bearing and fracture behavior of the normal-strength and high-strength concretes with or without fiber addition. The influences of area ratio, concrete strength and fiber addition on the maximum local compressive stress (i.e. bearing stress), the stress versus displacement (or deformation) response as well as the failure mode and crack pattern of the concentrically loaded standard prisms (d150: 150 x 150 x 300-mm) were evaluated.

**Maximum local compressive stress**

The results of this test series are summarized in Table 4.1 and Table 4.2, demonstrating the various effects of area ratio, concrete strength and fiber incorporation on the mean values of the maximum local compressive stress $q_{max}$ (defined as the maximum load divided by the loaded area $A_{c0}$). With decreasing area ratio R, the $q_{max}$ decreased progressively for both plain and fiber concretes tested (Table 4.1), as a result of reducing confinement effect of the surrounding non-loaded concrete. The observations made here confirmed the early findings of Hawkins (1968a), Niyogi (1973) and Klotz (2008). The stress reduction rate due to the decrease of area ratio ($q_{max, R = 16}$/ $q_{max, R}$) corresponded well to the reduction rate of $\sqrt{R}$, independent of concrete strength and fiber addition.

*Table 4.1: Influence of concrete strength and area ratio on the maximum stress $q_{max}$ and stress ratio n of the plain and fiber concretes*

| Index | | Term | Area ratio R | | | |
|---|---|---|---|---|---|---|
| | | | 16 | 9 | 4 | 2.25 |
| | | | Ratio of $\sqrt{R}$ | | | |
| | | | 100% | 75% | 50% | 38% |
| Plain concrete | PC (high-strength: HS) | $q_{max}$ [MPa] | 214 | 152 | 104 | 81 |
| | | $q_{max, R = 16}$/ $q_{max, R}$ | 100% | 71% | 49% | 38% |
| | | n | 2.53 | 1.8 | 1.23 | 0.96 |
| | NS_PC (normal-strength: NS) | $q_{max}$ [MPa] | 136 | 97 | 68 | 52 |
| | | $q_{max, R = 16}$/ $q_{max, R}$ | 100% | 71% | 50% | 38% |
| | | n | 2.97 | 2.12 | 1.48 | 1.14 |
| | | $\Delta(n_{HS}-n_{NS})$ | -0.44 | -0.32 | -0.25 | -0.18 |
| | | $q_{max, HS}$/ $q_{max, NS}$ | 157% | 157% | 153% | 156% |
| Fiber concrete | L60 (high-strength: HS) | $q_{max}$ [MPa] | 298 | 214 | 153 | 113 |
| | | $q_{max, R = 16}$/ $q_{max, R}$ | 100% | 72% | 51% | 38% |
| | | n | 3.41 | 2.45 | 1.75 | 1.29 |
| | NS_L60 (normal-strength: NS) | $q_{max}$ [MPa] | 205 | 142 | 95 | 69 |
| | | $q_{max, R = 16}$/ $q_{max, R}$ | 100% | 69% | 46% | 34% |
| | | n | 3.86 | 2.67 | 1.79 | 1.3 |
| | | $\Delta(n_{HS}-n_{NS})$ | -0.45 | -0.22 | -0.04 | -0.01 |
| | | $q_{max, HS}$/ $q_{max, NS}$ | 145% | 151% | 161% | 164% |

With increasing concrete strength, the $q_{max}$ increased significantly with an average increment of about 55.0% ($q_{max, HS}$/ $q_{max, NS}$) for both plain and fiber concretes. But the percentage values of increase in $q_{max}$ were much lower than those in concrete compressive strength $f_{c,cube}$ (for plain concrete $\Delta$ = 84%, for fiber concrete $\Delta$ = 65%). Thus, in order to better study the influence of concrete strength, the test data were further evaluated by comparing the ratio of the ultimate local compressive stress $q_{max}$ to the concrete compressive strength $f_{c,cube}$. Compared to the normal-strength concretes (NS_PC and NS_L60), the high-strength concretes (PC and L60) exhibited lower values of stress ratio $n = q_{max}/ f_{c,cube}$ at all the area ratios. According to Niyogi (1974) and Reinhardt (1994), it is principally attributed to the disproportionate increase of tensile strength with growing compressive strength for high-strength concrete. Through analyzing the difference of stress ratios between the normal-strength and high-strength concretes $\Delta(n_{HS}$-$n_{NS})$, the reduction effect was found to be more evident at the high area ratios of 16 and 9. At the low area ratios of 4 and 2.25, the difference was even nearly negligible between the SFRCs (Table 4.2 and Figure 4.3).

By incorporating steel fibers (L type: RC-80/60-BN, 60 kg/m³), the load-bearing capacity of the normal-strength and high-strength plain concretes was markedly enhanced with an average increase in $q_{max}$ of about 42% (Table 4.2, $q_{max, fiber}$/ $q_{max, plain}$). This remarkable improvement induced by fiber addition has also been reported by Chen and Carson (1974), Al-Taan and Al-Hamdony (2005) and Klotz (2008). Notably, a slight fall in stress increment with reducing area ratio was only observed between the normal-strength concretes. Moreover, the difference of stress ratios between the fiber and plain concretes $\Delta(n_{fiber}$-$n_{plain})$ tended to reduce with the decrease of area ratio. In other words, the fiber reinforcement was more effective in increasing the load-bearing capacity of concrete at the high area ratios of 16 and 9 (i.e. more severe stress concentrations) and less effective at the low area ratios of 4 and 2.25, especially for the normal-strength SFRCs (NS_L60). This phenomenon is also graphically shown in Figure 4.3.

*Table 4.2: Influence of fiber addition and area ratio on the maximum stress $q_{max}$ and stress ratio n of the normal-strength and high-strength concretes*

| **Index** | **Term** | **Area ratio R** | | | |
|---|---|---|---|---|---|
| | | 16 | 9 | 4 | 2.25 |
| PC | $q_{max}$ [MPa] | 214 | 152 | 104 | 81 |
| | n | 2.53 | 1.8 | 1.23 | 0.96 |
| L60 | $q_{max}$ [MPa] | 298 | 214 | 153 | 113 |
| | n | 3.41 | 2.45 | 1.75 | 1.29 |
| | $q_{max, fiber}$/ $q_{max, plain}$ | 139% | 141% | 147% | 140% |
| | $\Delta(n_{fiber}$-$n_{plain})$ | 0.88 | 0.65 | 0.52 | 0.33 |
| NS_PC | $q_{max}$ [MPa] | 136 | 97 | 68 | 52 |
| | n | 2.97 | 2.12 | 1.48 | 1.14 |
| NS_L60 | $q_{max}$ [MPa] | 205 | 142 | 95 | 69 |
| | n | 3.86 | 2.67 | 1.79 | 1.3 |
| | $q_{max, fiber}$/ $q_{max, plain}$ | 151% | 146% | 140% | 133% |
| | $\Delta(n_{fiber}$-$n_{plain})$ | 0.89 | 0.55 | 0.31 | 0.16 |

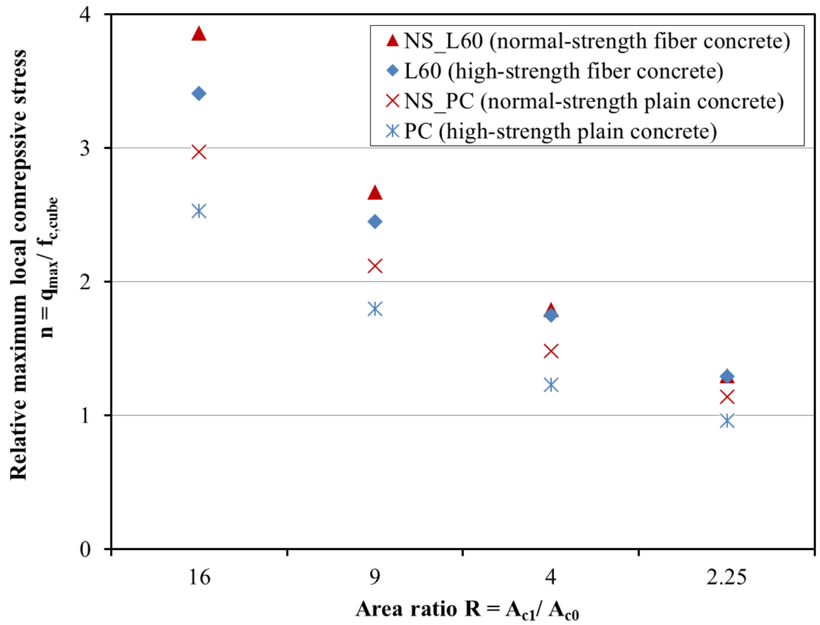


*Figure 4.3: Comparison of the stress ratio n as a function of the area ratio R*

**Stress versus displacement response**

Figure 4.4 and Figure 4.5 depict the effects of area ratio and fiber addition on the local compressive stress versus longitudinal displacement behavior of the normal-strength and high-strength concretes under concentric loading, respectively. As noted before, due to fiber addition and increase of area ratio, the load-bearing capacity of concrete was considerably improved, which can also be clearly observed from the course of the average curves. As shown in Figure 4.4, for a given area ratio, the slope of the curves (i.e. stiffness) of the high-strength plain and fiber concretes (PC and L60) in the pre-peak branch was nearly identical. The stiffness increased with increasing area ratio, mainly due to the reduction of lateral strain restraint effect resulted from the steel bearing plate. Shortly after exceeding the peak stage, a sharp fall of the bearing stress was found on the curves of the PCs, indicating a sudden failure of the specimens during the test. In contrast, the SFRCs exhibited a gradual reduction of stress associated with a continuous increment of displacement, corresponding to a ductile fracture behavior. It is also clear that for the SFRCs the higher the area ratio is, the larger the longitudinal displacement (i.e. mostly the penetration of the steel plate into the concrete) can be attained at the predefined end of the test.

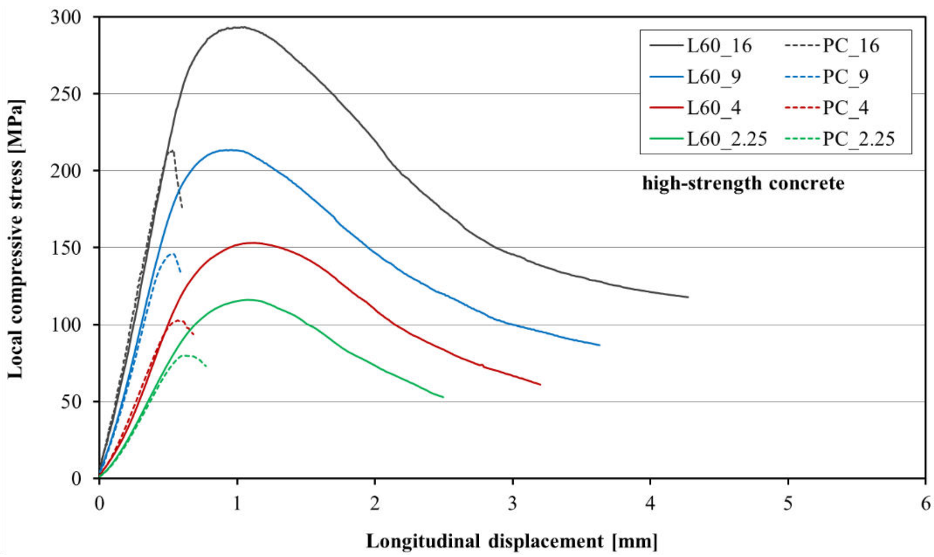


*Figure 4.4: Average local compressive stress versus longitudinal displacement curves of the high-strength concretes (PC and L60) loaded at the area ratios of 16, 9, 4 and 2.25*

A similar tendency was also observed for the normal-strength concretes (NS_PC and NS_L60), as illustrated in Figure 4.5. Expectedly, the stiffness at a given area ratio was relatively smaller than that of the high-strength concretes (PC and L60) due to the lower Young´s modulus of the normal-strength concrete. Noticeably, the normal-strength SFRCs (NS_L60) exhibited a larger plateau state of stress around the peak stage (i.e. more smooth stress transition) and afterwards a significantly slower decline of stress than the high-strength SFRCs (L60), in particular at the high area ratios of 16 and 9. Reinhardt (1994) made the same observations on his normal-strength concrete samples. As reported in Breitenbücher et al. (2014), the change in concrete strength from 84 to 44 MPa (i.e. nearly the same strength variation adopted in this test series) did not noticeably affect the overall pull-out behavior of the normal-strength hook-ended steel fiber (RC-80/60/BN, i.e. the same type of steel fiber used here). The considerably more gradual stress decay of the normal-strength SFRCs (NS_L60) may be accounted for by the much less explosive fracture behavior of the normal-strength concrete matrix, resulting in a more successive crack formation and propagation. In other words, it led to a more lagging pullout process of the fibers from the matrix until reaching a predefined level of stress drop.

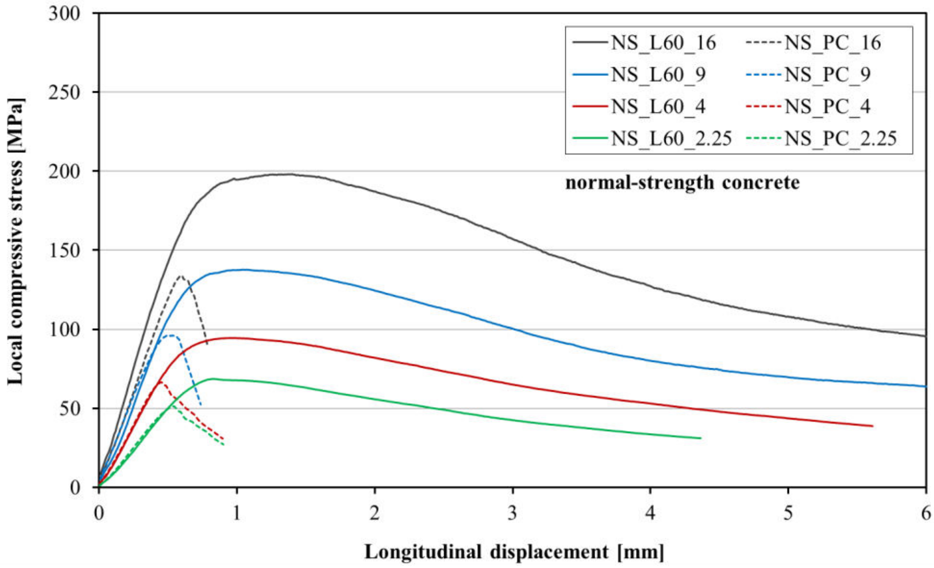


*Figure 4.5: Average local compressive stress versus longitudinal displacement curves of the normal-strength concretes (NS_L60 and NS_PC) loaded at the area ratios of 16, 9, 4 and 2.25*

Figure 4.6 shows the lateral deformation of the high-strength concretes (PC and L60) as a result of the introduction of concentrated load at four different area ratios. Similarly, the improvements in the load-bearing capacity and post-cracking behavior due to fiber addition and increase of area ratio can be clearly observed from the nature of the average curves. More importantly, the stress versus lateral deformation curve reflects to a large extent the relationship between the stress level and the initiation and growth of cracks. As it can be seen that at high area ratio the cracks initiated at a significantly high stress level, however, with growing crack width (i.e. lateral deformation) the stress dropped rapidly, particularly pronounced for the SFRCs loaded at the high area ratios of 16 and 9 (e.g. L60_16 and L60_9). For the normal-strength concretes (NS_PC and NS_L60), the stress reduction due to increasing crack width was considerably gradual especially for the SFRCs (see Figure A.1, Appendix A).

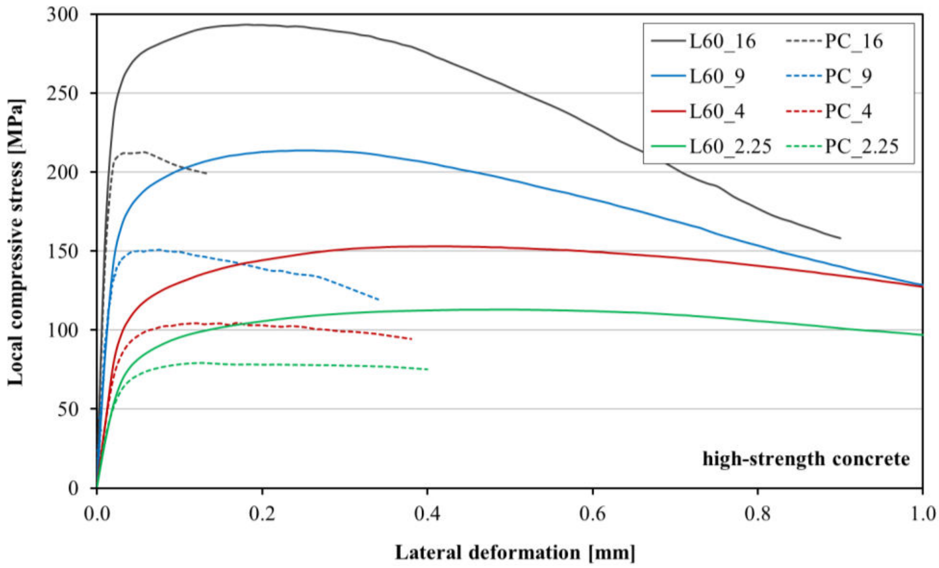


*Figure 4.6: Average local compressive stress versus lateral deformation curves of the high-strength concretes (L60 and PC) loaded at the area ratios of 16, 9, 4 and 2.25*

The mean midpoint longitudinal compressive deformations of the prisms obtained at the maximum local compressive stress $q_{max}$ are illustrated in Figure 4.7 as a function of the area ratio R. As expected, the compressive deformation generally increased with decreasing area ratio, i.e. with increasing size of the steel bearing plate. Due to the ductile post-cracking behavior, the increment was more distinct for the SFRCs, manifesting a better deformability under compression, in particular in the case of normal-strength SFRCs (NS_L60) at the low area ratios of 4 and 2.25.

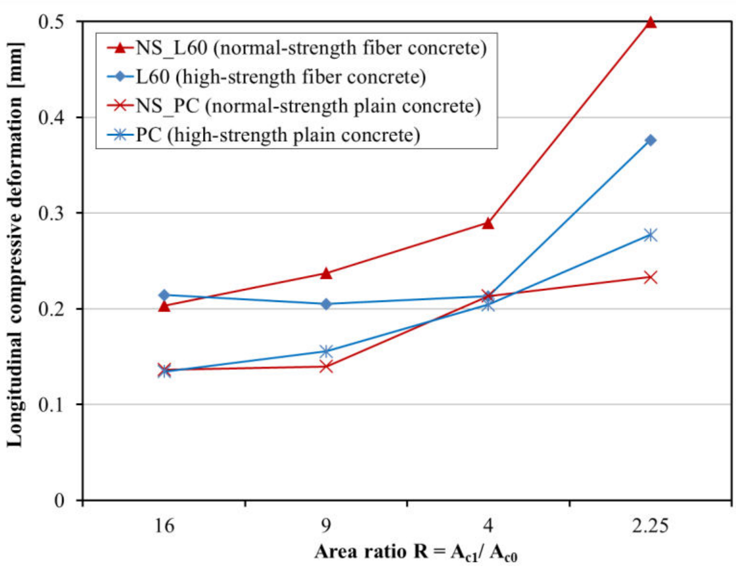


*Figure 4.7: Longitudinal compressive deformations of the specimens as a function of the area ratio R for the normal-strength and high-strength concretes*

**Failure and crack characteristics**

Some representative samples of the failed specimens are shown in Figure 4.8 - Figure 4.13. For both plain and fiber concretes, no visible cracking or spalling was observed until shortly before reaching the peak load. Soon afterwards, all the plain concrete samples failed in a more or less explosive manner, in particular for the prisms produced with high-strength concrete. In contrast, the SFRC samples exhibited a ductile fracture behavior. It should be noted that the failure and crack pattern of concrete prisms depended greatly upon the area ratio and concrete strength.

In the case of high-strength plain concrete prisms tested with the large area ratios of 16 and 9 (Figure 4.8, PC_16 and PC_9), 3-5 major radial cracks developed and spread across the unloaded area of the testing surface, and on some lateral surfaces one longitudinal main crack propagated almost through the total surface. For the prisms loaded with the small area ratios of 4 and 2.25 (Figure 4.8, PC_4 and PC_2.25), the specimens lost their integrity during the test and broke into several parts with an inverted concrete cone beneath the loaded area. Apart from the reduced confinement effect of surrounding non-loaded concrete, this was primarily due to the explosive release of high energy at failure resulted from the joint effect of the large failure load at low area ratio and the inherent brittleness of the high-strength matrix. The width of the concrete cone corresponded to the width of the steel bearing plate and the depth was about 1.5 times of its width (Figure 4.9).

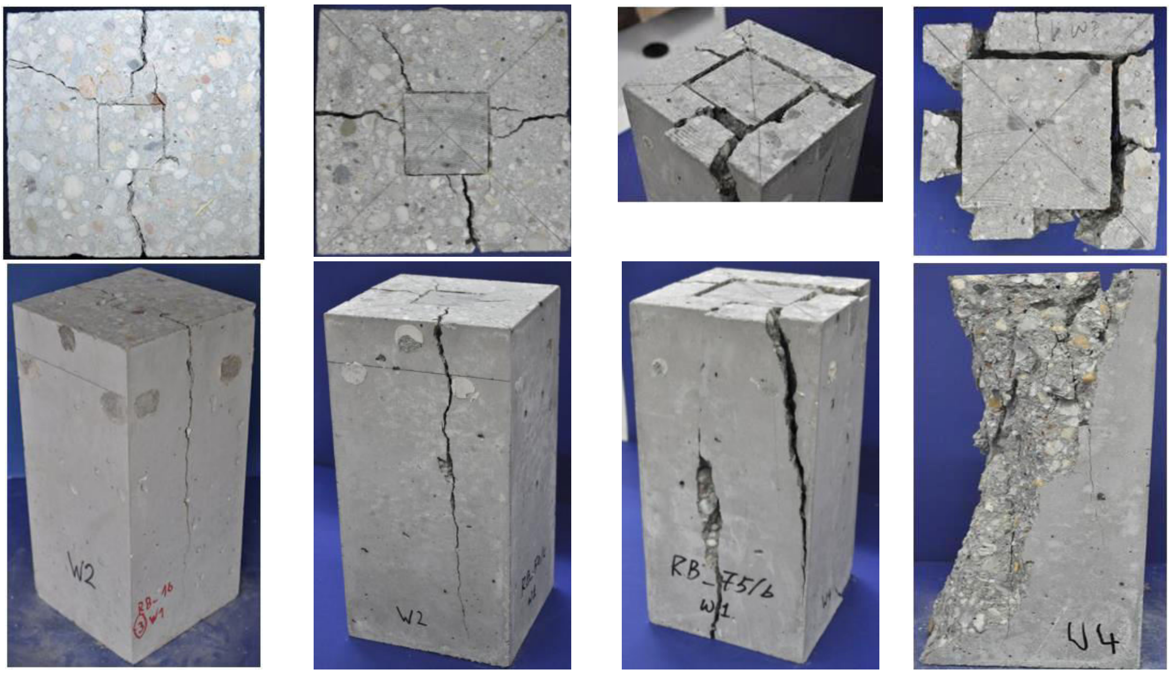


*PC_16 PC_9 PC_4 PC_2.25*

*Figure 4.8: Typical failure patterns of the high-strength plain concrete specimens (PC)*

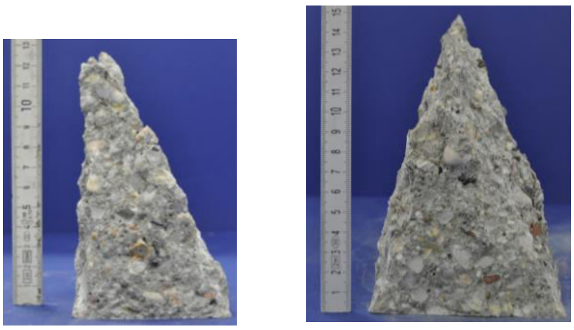

*PC_4 PC_2.25*

*Figure 4.9: Concrete cones of the high-strength plain concrete prisms loaded with low area ratio (PC)*

For the normal-strength plain concrete specimens loaded with the high area ratios of 16 and 9 (Figure 4.10, NS_PC_16 and NS_PC_9), the failure and crack pattern were similar with those of the high-strength plain concrete samples (Figure 4.8, PC_16 and PC_9). Noticeably, even at the low area ratios of 4 and 2.25, the prisms did not lose their integrity at failure (Figure 4.10, NS_PC_4 and NS_PC_2.25). This was essentially attributed to the comparatively low brittleness of the material itself and the relatively small failure load, leading to a much less explosive release of fracture energy, which was not sufficiently strong enough to burst the specimen into parts.

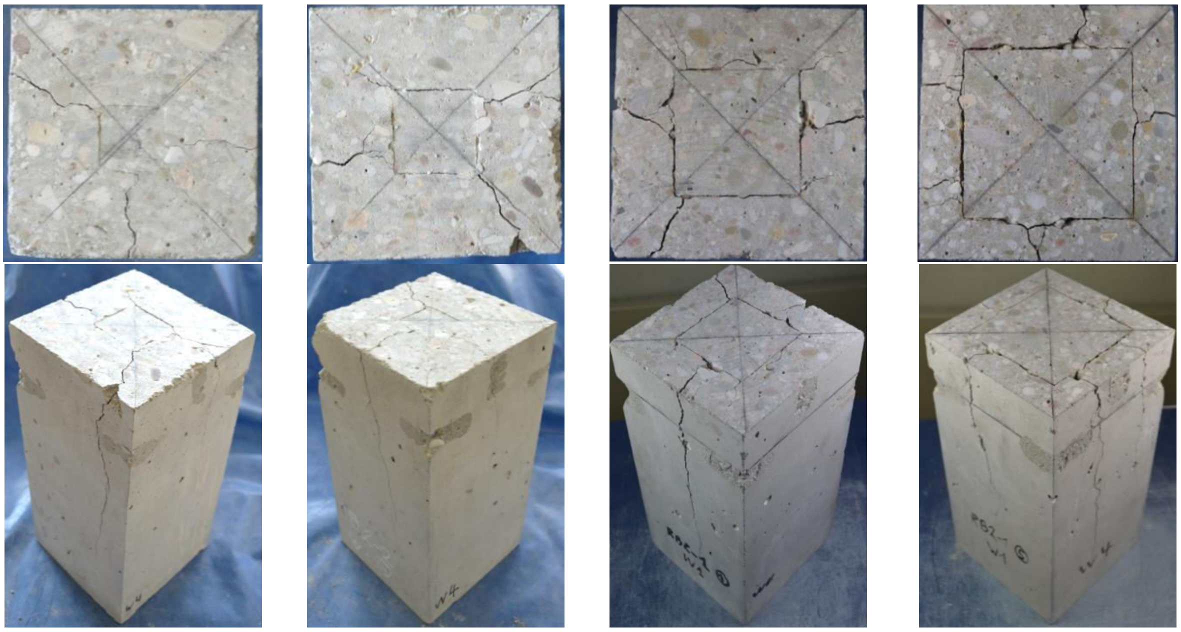

*NS_PC_16:* *NS_PC_9* *NS_PC_4* *NS_PC_2.25*

*Figure 4.10: Typical failure patterns of the normal-strength plain concrete specimens (NS_PC)*

All the SFRC prisms, even the high-strength samples, retained their integrity at the predefined end of the test and exhibited a somewhat multiple-cracking appearance of failure. Depending on the area ratio applied, the failure and crack pattern differed among each other markedly. At the large area ratios of 16 and 9, cracking in conjunction with minor concrete spalling occurred chiefly on the upper half of specimen and on the lateral surfaces the major crack spread downwards only approximately to the half-height of prism (Figure 4.11, L60_16, L60_9 and Figure 4.12, NS_L60_16, NS_L60_9). With decreasing area ratio, concrete spalling along with continuous cracks tended to increasingly develop in the lower half of specimen, in particular at the lowest area ratio of 2.25 (Figure 4.11, L60_2.25 and Figure 4.12, NS_L60_2.25).

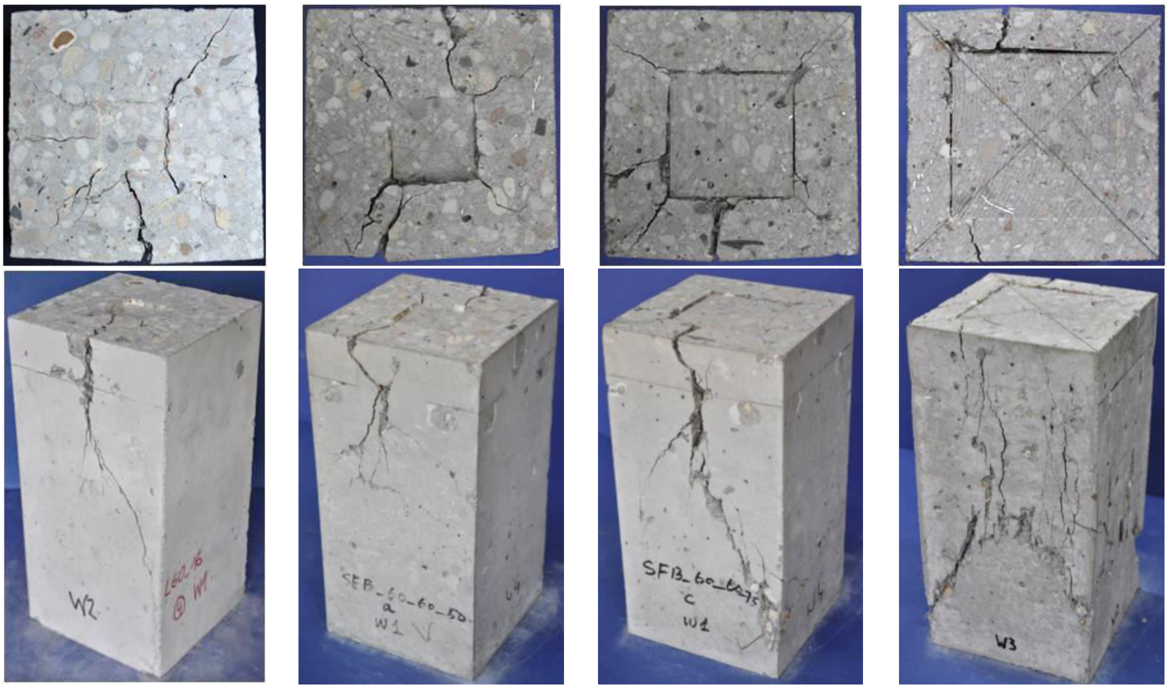

*L60_16* *L60_9* *L60_4* *L60_2.25*

*Figure 4.11: Typical failure patterns of the high-strength fiber concrete specimens (L60)*

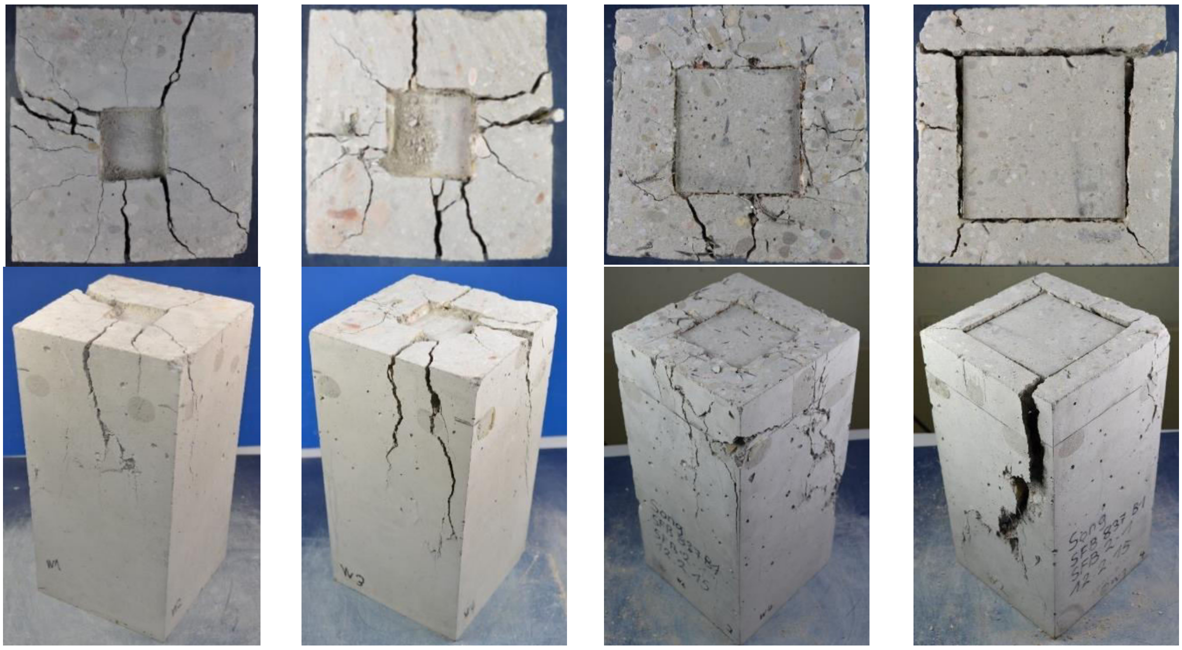

NS_L60_16 NS_L60_9 NS_L60_4 NS_L60_2.25

*Figure 4.12: Typical failure patterns of the normal-strength fiber concrete specimens (NS_L60)*

From the failure and crack patterns of the plain and fiber concrete prisms in Figure 4.8 - Figure 4.12, it is clearly to see that the crack width basically reduced with the distance from the outer surface edge. This implies that the major crack initially formed on the outer surface and then propagated inwards. The above observations were consistent with the experimental and numerical findings of Leung and Cheung (2009). In this test series, this phenomenon was, however, rather more evident for the specimens loaded with the high area ratios of 16 and 9.

Some failed specimens of the high-strength plain and fiber concretes were sawed through along the central axis (Figure 4.13) to closely observe the internal crack propagation.

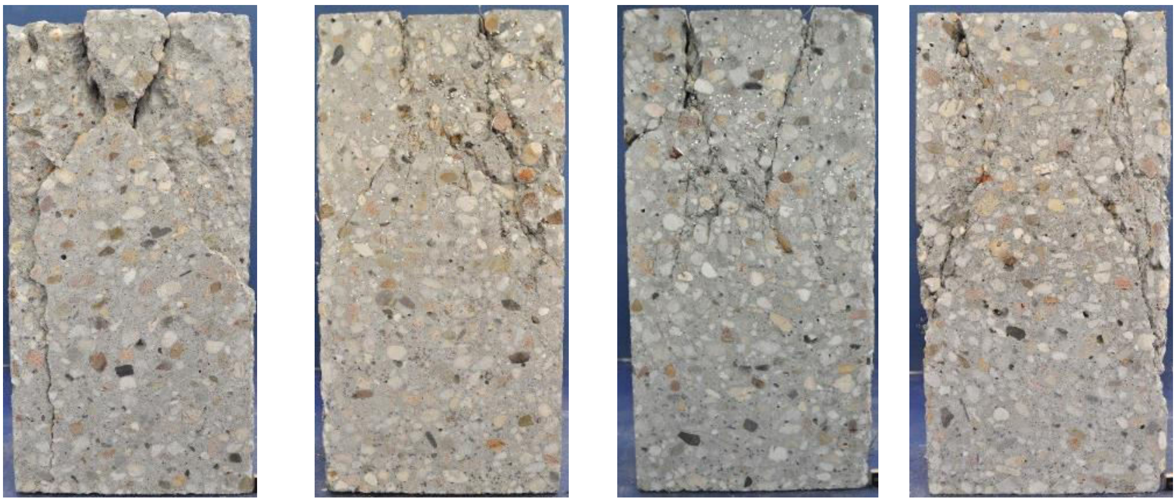

PC_9 L60_9 L60_4 L60_2.25

*Figure 4.13: Sawed samples of the failed high-strength plain and fiber concrete prisms (PC and L60)*

After comparing the crack patterns of the prisms in Figure 4.8, Figure 4.11 and Figure 4.13, it was found that the internal crack pattern reflected basically the external one for the cases studied here. After the formation of initial cracks on the outer surface, the downward crack propagation through the inverted concrete cone occurred as a result of the continuing introduction of concentrated load. For the plain concretes, this process led either to continuous longitudinal cracking or to complete collapse of specimen, depending on the concrete strength and/or the area ratio. For the SFRCs, due to the crack-bridging effect of the fibers, the punch down of the concrete cone caused increased internal cracking and concrete crushing (i.e. external cracking and spalling of concrete), whereby the extent of concrete damages depended largely upon the area ratio employed.

The average values of crack number and maximum crack width on the testing surface were determined at the predefined end of the test (i.e. at a load drop by 60% of the maximum load) for each test group of the plain and fiber concrete prisms (Table B.3, Appendix B). In the case of plain concrete samples, the average values of crack number and maximum crack width increased with decreasing area ratio. This effect was more evident for the normal-strength plain concrete (NS_PC). Compared to the high-strength plain concretes (PC), for a given area ratio (16 or 9), the normal-strength plain concretes (NS_PC) exhibited lower values of crack number and maximum crack width. This may be due to the comparatively less explosive failure of the normal-strength concrete matrix.

For the SFRC prisms, the average values of crack number ranged from 7.0 to 10.7. However, no direct correlations can be established between the crack number and area ratio or between the crack number and concrete strength. In the case of high-strength SFRCs (L60), the average values of maximum crack width decreased with decreasing area ratio. Notably, a reverse tendency was found for the normal-strength SFRCs (NS_L60). Furthermore, except for the area ratio of 16, the NS_L60 series exhibited generally larger crack opening due to the comparatively long test duration (i.e. more gradual stress decline in the post-cracking stage) under the predefined test conditions. Compared to the plain concretes, for a given area ratio the fiber concretes generally had higher values of crack number and maximum crack width due to a much more ductile fracture behavior.

**Summary**

In this sub-section, the results of concentrated loading tests on the normal-strength and high-strength concrete prisms with or without fiber addition have been presented. The plain and fiber concrete prisms (d150: 150 x 150 x 300-mm) were loaded concentrically with four area ratios of 16, 9, 4 and 2.25.

On the basis of the experimental data obtained, the following relevant conclusions can be drawn:

- With reducing area ratio, the maximum local compressive stress and the stress ratio decreased progressively. And the stress reduction rate corresponded well to the square-root of area ratio. These phenomena were independent of concrete strength and fiber addition.

- By adding steel fibers (L type: RC-80/60-BN, 60 kg/m³), the maximum load-bearing capacity of both normal-strength and high-strength concretes was significantly improved with an average increase of the maximum bearing stress by about 42%.

- Compared to the normal-strength concretes (NS_PC and NS_L60), the high-strength concretes (PC and L60) exhibited considerably higher maximum bearing stress at all the area ratios (average stress increment of about 55%), however, modestly lower stress ratio. Between the plain concretes the average reduction in stress ratio was about 16%, while between the fiber concretes the corresponding value was about 10% at the high area ratios of 16 and 9 and almost negligible at the low area ratios of 4 and 2.25.

- Based on the analysis of the difference of stress ratios between the fiber and plain concretes, it has been established that for both concrete strengths investigated the reinforcing effectiveness of steel fibers was markedly more evident at high area ratio (16 or 9, i.e. severe stress concentration) than at low area ratio (4 or 2.25).

- The incorporation of steel fibers had no effect on the stiffness of the stress-longitudinal displacement curves in the pre-peak branch; however, it had great impact on the load-bearing behavior in the post-cracking zone.
  - Generally, the stiffness increased with increasing area ratio or concrete strength.
  - Beyond the peak stress, both plain concretes exhibited a sharp stress fall on the curves, indicating a brittle fracture behavior.
  - Compared to the high-strength SFRCs, the normal-strength SFRCs showed a much more ductile stress-displacement response, particularly pronounced at large area ratio (16 or 9).
- The presence of steel fibers changed the failure mode of concrete from a brittle to a ductile one.
  - For both plain and fiber concretes, no visible cracking or spalling was observed until shortly before reaching the ultimate load.
  - The extent of concrete damages on the plain concrete specimens depended highly on the concrete strength and area ratio. The normal-strength prisms presented a failure pattern of cracking at all the area ratios, while the high-strength samples collapsed completely at low area ratio (4 or 2.25), instead of cracking at high area ratio (16 or 9).
  - All the SFRC prisms retained their integrity with a somewhat multiple-cracking appearance of failure. With reducing area ratio (4 or 2.25), cracking and spalling of concrete tended to noticeably deteriorate and increasingly develop in the lower half of specimen, especially in the case of normal-strength SFRCs.

### 4.2.2 Influence of specimen dimension

The load-bearing capacity of concrete member under concentrated loading can be notably affected by the geometric variations of specimen, as previously reported by Niyogi (1973), Reinhart (1997) and Klotz (2008). In addition to the standard small prisms (d150: 50 x 150 x 300-mm, produced in the test series 1), in this test series large prisms with identical height to width ratio h/ d of 2 (d300: 300 x 300 x 600-mm) were manufactured with the same base high-strength concrete mixture in the standing wooden molds. The fiber type and content used remained uniformly as for the production of the small SFRC prisms (i.e. L type: RC-80/60-BN, 60 kg/m³). These large plain and fiber concrete samples were loaded concentrically with two different area ratios of 9 and 4. The key point of this investigation focused on assessing the influence of specimen size in conjunction with fiber addition and area ratio on the load-bearing and fracture behavior of high-strength plain and fiber concretes.

**Maximum local compressive stress**

As listed in Table 4.3, for both plain and fiber concretes, the mean values of maximum stress $q_{max}$ and stress ratio n decreased with growing specimen dimension for a given area ratio. In terms of the stress reduction rate ($q_{max, d300}$/ $q_{max, d150}$) due to the increase of specimen size, the plain concretes exhibited a modestly lower average value of 10% than the SFRCs with a corresponding value of 14.5%.

Similar results were also observed by Klotz (2008) on his prisms made of ultra-high-strength concrete, indicating an average stress reduction of 8.5% for plain concrete and 8% for fiber concrete. It should be noted that Klotz only doubled the width of his square prisms (from d = 200 to 400 mm) and the height kept constant (h = 400 mm). Based on the test data of the traditionally reinforced high-strength concrete cylinders (h/ d = 2), Reinhardt (1997) reported a more significant reduction in $q_{max}$ of about 28% when enlarging the cylinder diameter from 200 mm to 400 mm. However, no further decrease in stress was found by cylinders with a larger diameter of 800 mm.

The higher mean values of stress reduction of the SFRCs obtained here implied that the load-bearing behavior of SFRC might be more sensitive to the variation of specimen dimension. This phenomenon may be due to the joint effects of fiber orientation and specimen size. A same trend can be also found by comparing the difference of stress ratios $\Delta(n_{d300}-n_{d150})$ in Table 4.3 and in Figure 4.14.

*Table 4.3: Influence of specimen dimension on the maximum stress $q_{max}$ and stress ratio n*

| **Index** | **Term** | **Area ratio R** | |
|---|---|---|---|
| | | 9 | 4 |
| PC (d150) | $q_{max}$ [MPa] | 152 | 104 |
| | n | 1.8 | 1.23 |
| PC_d300 | $q_{max}$ [MPa] | 140 | 92 |
| | n | 1.65 | 1.09 |
| | $q_{max, d300}$/ $q_{max, d150}$ | 92% | 88% |
| | $\Delta(n_{d300}-n_{d150})$ | -0.15 | -0.14 |
| L60 (d150) | $q_{max}$ [MPa] | 214 | 153 |
| | n | 2.54 | 1.81 |
| L60_d300 | $q_{max}$ [MPa] | 177 | 134 |
| | n | 2.1 | 1.59 |
| | $q_{max, d300}$/ $q_{max, d150}$ | 83% | 88% |
| | $\Delta(n_{d300}-n_{d150})$ | -0.44 | -0.22 |

Regarding the contribution of steel fibers to the $q_{max}$ of same-sized specimen (Table 4.4), the mean increase in $q_{max}$ was about 44% for the small samples (d150), and slightly higher than that of the large prisms with a value of 36% (d300). Noticeably, the large specimens loaded with the area ratio of 4 showed a much higher stress increase, while for the small samples the increase was only slightly affected by the area ratio. When comparing the difference of stress ratios $\Delta(n_{fiber}\text{-}n_{plain})$, the large prisms loaded with the small area ratio of 4 exhibited a marginally higher value ($\Delta = 0.5$) than those tested under the large area ratio of 9 ($\Delta = 0.45$). Obviously, this trend was conflicting to that observed by the small prisms.

*Table 4.4: Influence of fiber addition on the maximum stress $q_{max}$ and stress ratio n for same-sized prisms*

| **Index** | **Term** | **Area ratio R** | |
|---|---|---|---|
| | | 9 | 4 |
| PC (d150) | $q_{max}$ [MPa] | 152 | 104 |
| | n | 1.8 | 1.23 |
| L60 (d150) | $q_{max}$ [MPa] | 214 | 153 |
| | n | 2.54 | 1.81 |
| | $q_{max, fiber}/ q_{max, plain}$ | 141% | 147% |
| | $\Delta(n_{fiber}\text{-}n_{plain})$ | 0.74 | 0.58 |
| PC_d300 | $q_{max}$ [MPa] | 140 | 92 |
| | n | 1.65 | 1.09 |
| L60_d300 | $q_{max}$ [MPa] | 177 | 134 |
| | n | 2.1 | 1.59 |
| | $q_{max, fiber}/ q_{max, plain}$ | 126% | 146% |
| | $\Delta(n_{fiber}\text{-}n_{plain})$ | 0.45 | 0.5 |

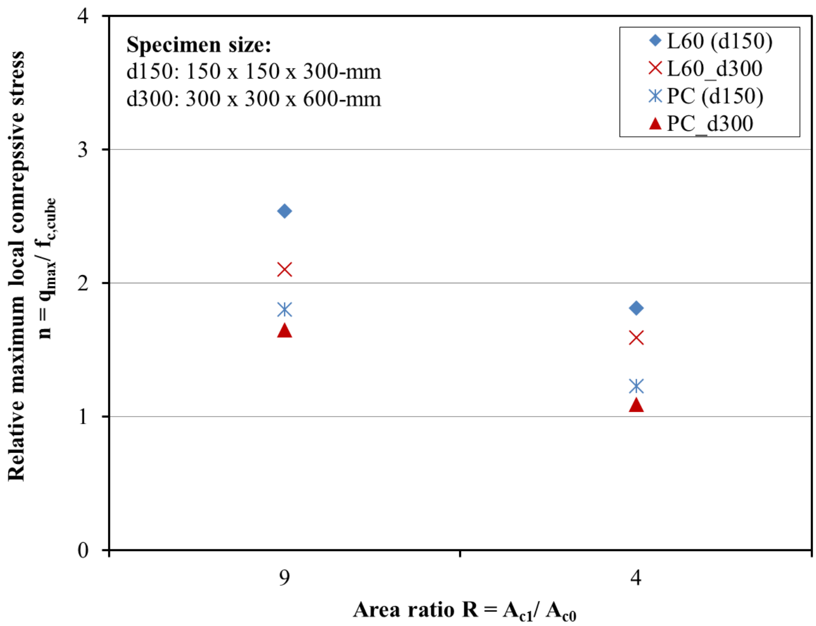


*Figure 4.14: Influence of specimen dimension on the stress ratio n at the area ratios of 9 and 4*

The trends above observed by the large SFRC specimens may be explained by the measuring results of fiber content and orientation determined on the cubes taken from the tested prisms by means of the BSM100 device (Section 3.3.2). Since steel fibers distributed in the St. Venant disturbance zone have predominant influence on the load-bearing capacity of concrete exposed to concentrated load, the measurement was then conducted on the cubes taken from the upper half of prism (at least 2 cubes for one test group). Based on the measuring results, only a slight scatter in the average fiber content was found amongst the small and large SFRC prisms (d150: L60_9 = 62.1 kg/m³, L60_4 = 61.5 kg/m³; d300:

L60_9_d300 = 59.9 kg/m³, L60_4_d300 = 60.3 kg/m³). Regarding the fiber orientation, for the large prisms loaded at the low area ratio of 4 (see Figure A.2, Appendix A, L60_4_d300), only 19.1% of the steel fibers oriented towards the load direction. In other words, more fibers ($\Delta$ = 8.3%) oriented in the directions of the tensile stresses (80.9%) in comparison with the case of L60_9_d300 (72.6%). Between the standard small prisms loaded with the area ratios of 9 and 4, no appreciable difference was found in the fiber orientation (L60_9 vs. L60_4, $\Delta_{max}$ = 1.9% in the loading direction).

As is well known, fibers aligned to the acting direction of tensile stresses have the best crack-bridging capacity. Thus, the somewhat preferable orientation of steel fibers in the directions of tensile stresses as observed in the case of L60_4_d300 might, in conjunction with other factors (e.g. size effect and/or low area ratio), lead to the higher values of $q_{max}$. This slightly preferential fiber orientation may be caused by a softer consistency of the fresh SFRC mixture possibly associated with an excessive vibration during the production process of prism. A more detailed discussion on the effect of fiber orientation on the load-bearing and facture behavior of SFRC will be given in Section 4.2.5.

**Stress versus displacement response**

The effect of specimen dimension on the stress versus longitudinal displacement response of the high-strength plain and fiber concretes under concentric loading is illustrated in Figure 4.15 and Figure 4.16 for the area ratios of 9 and 4, respectively.

As can be seen from the average curves, for a given specimen size, the stiffness of the plain and fiber concretes was almost identical in the pre-peak stage and increased with the growth of area ratio. Compared to the small prisms (d150: PC_9 and L60_9), the large prisms (d300) exhibited considerable lower stiffness for both plain and fiber concretes at the area ratios investigated. The lower stiffness obtained by the large specimens was commonly referred to as size effect in the pertinent literature. More precisely, it ought to be primarily due to the reduced effect of lateral strain restraint with increasing specimen size. Similarly, Reinhardt (1997) also found a reduced stiffness due to the increase of specimen size (with constant h/ d = 2). However, Klotz (2007) did not observe notable change in stiffness on his prisms with various sizes. It may be that for Klotz's large specimens with doubled width and unchanged height (with d = 400 mm and h/ d = 1), the increased lateral strain restraint induced by the supporting machine platen led to higher stiffness, and thus partly compensated the reducing effect caused by the enlarged specimen dimension.

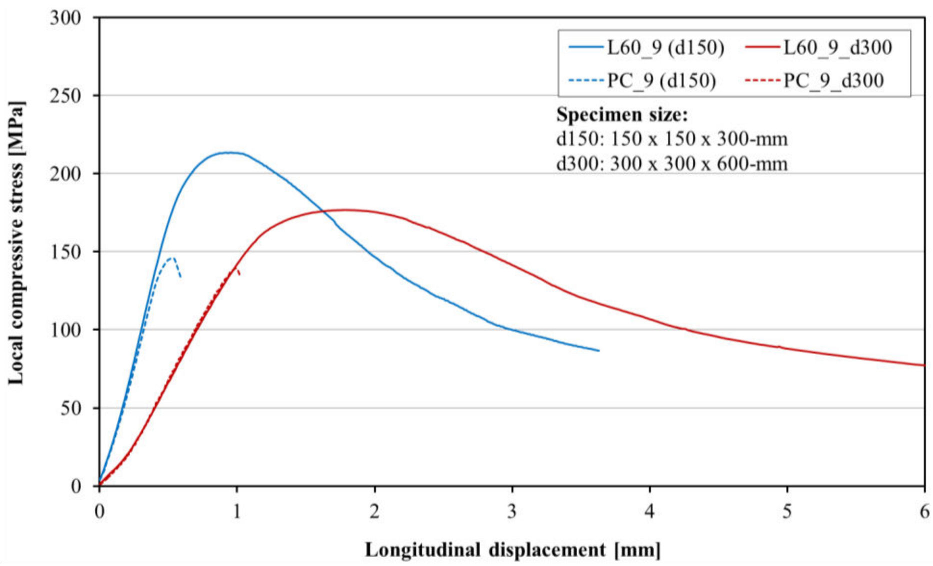


*Figure 4.15: Average local compressive stress versus longitudinal displacement curves of concrete specimens with various sizes loaded at the area ratio of 9*

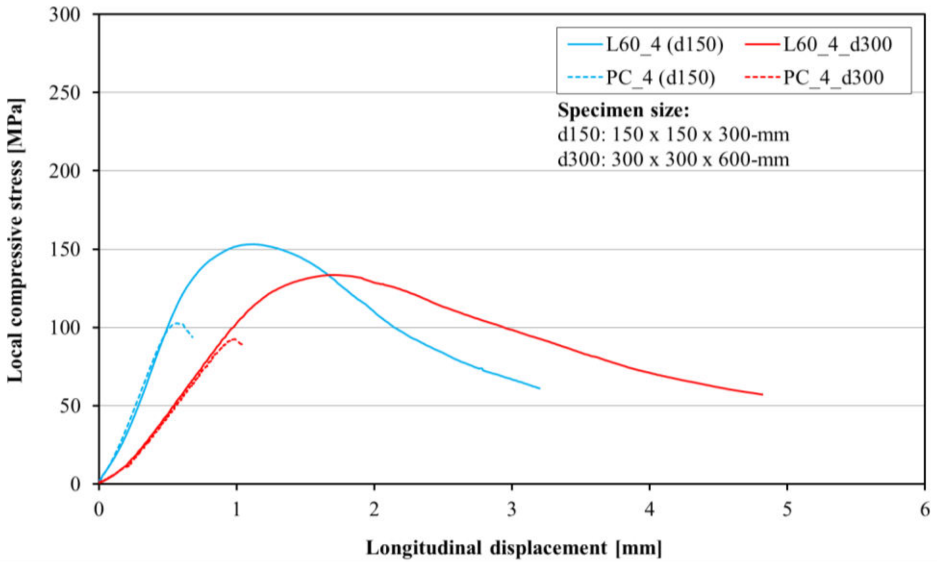


*Figure 4.16: Average local compressive stress versus longitudinal displacement curves of concrete specimens with various sizes loaded at the area ratio of 4*

Despite the relative lower $q_{max}$, the large SFRC prisms showed a larger plateau state of stress around the peak stage (i.e. more smooth stress transition) and afterwards a much slower decline of stress associated with significantly increased displacement than the small SFRC specimens, in particular when loaded at the high area ratio of 9.

Figure 4.17 demonstrates the stress versus lateral deformation behavior of the SFRC specimens with different sizes for the area ratios of 9 and 4. Compared to the small prisms, the cracks on the large samples initiated apparently at much lower stress levels, however, with increasing crack width the stress declined more gradually, particularly pronounced at the area ratio of 9. A similar trend was also observed for the plain concrete specimens (see Figure A.3, Appendix A).

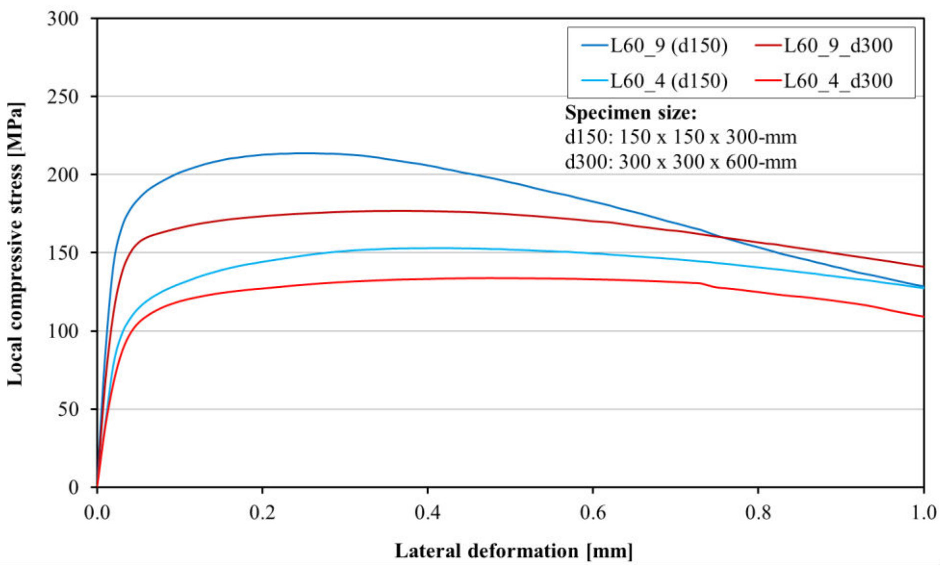


*Figure 4.17: Average local compressive stress versus lateral deformation curves of SFRC prisms with various sizes loaded at the area ratios of 9 and 4*

**Failure and crack characteristics**

Some representative samples of the failed large plain and fiber concrete specimens are demonstrated in Figure 4.18. Similarly, no visible cracking or spalling was observed until shortly before reaching the peak load for both plain and fiber concretes. Soon afterwards, all the large plain concrete prisms exhibited a catastrophic, explosive failure behavior at all the area ratios investigated (R = 9 and 4), whereas for the small prisms a complete collapse only occurred for area ratio ≤ 4 (Figure 4.8).

Failure of this kind observed by the large plain concrete samples was basically due to the enormously high energy release at failure (i.e. due to extremely high failure load). In order to avoid any damage to the test facilities and persons, the prisms were loosely wrapped with several loops of thin steel wire before the testing. Therefore, in appearance the large prisms seemed to remain their integrity at fracture (Figure 4.18). Actually, the specimens have already split into parts and thus the inverted concrete cone beneath the loading plate could be easily taken out (Figure 4.19). Similarly, the width of the concrete cone was equal to the width of the bearing plate and the depth was about 1.5 times of its width.

As expected, the large SFRC prisms exhibited also a ductile fracture behavior as the small SFRC prisms (Figure 4.18). In contrast to the small prisms, it should be noted that for the large specimens the concrete damages in the form of cracking and spalling on the external surfaces did not tend to noticeably deteriorate with reducing area ratio from 9 to 4 (e.g. Figure 4.18, L60_4_d300 vs. Figure 4.11, L60_4). Through observing the internal crack pattern on the surfaces of the sawed large samples, a somewhat more deep crack propagation beyond the loaded area was clearly to see for a given area ratio (Figure 4.20 vs. Figure 4.13).

Compared to the small prisms (Table B.4, Appendix B), the large specimens exhibited expectedly higher values of maximum crack width due to increased specimen dimension, however, slightly lower values of average crack number on the testing surface, in particular at the large area ratio of 9. Furthermore, the reduction in maximum crack width due to decreasing area ratio was rather inappreciable.

*PC_9_d300* *PC_4_d300* *L60_9_d300* *L60_4_d300*

*Figure 4.18: Typical failure patterns of the large concrete specimens (d300: 300 x 300 x 600-mm)*

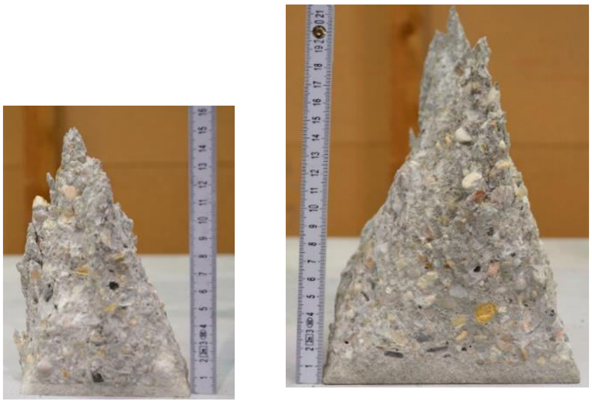

*PC_9_d300* *PC_4_d300*

*Figure 4.19: Concrete cone of the large plain concrete specimens (d300: 300 x 300 x 600-mm)*

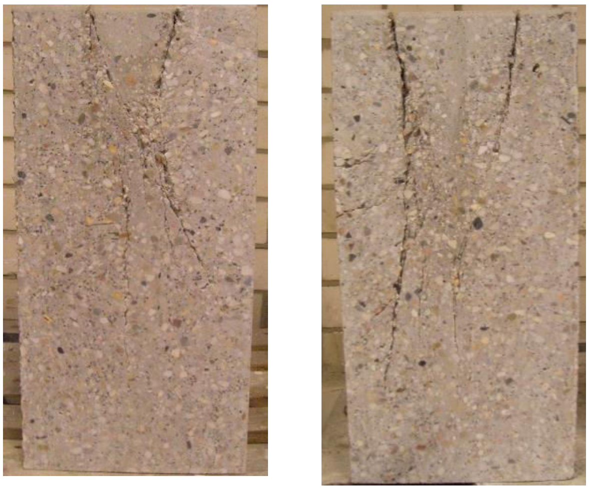

*L60_9_d300* *L60_4_d300*

*Figure 4.20: Sawed samples of the failed large SFRC prisms (d300: 300 x 300 x 600-mm)*

**Summary**

In this sub-section, the large high-strength concrete prisms (d300: 300 x 300 x 600-mm) with or without fiber addition have been loaded concentrically with two area ratios of 9 and 4. The test results have been presented and compared with those obtained from the small high-strength plain and fiber concrete specimens (d150: 150 x 150 x 300-mm) tested under the same conditions.

On the basis of the experimental data obtained, the following relevant conclusions can be drawn:

- With growing specimen size, the maximum local compressive stress $q_{max}$ and the stress ratio n decreased noticeably, independent of fiber addition and area ratio. More specifically, the SFRCs exhibited higher average stress reduction (14.5%) in comparison with the plain concretes (10%), and more pronounced when loaded at the large area ratio of 9 (17%). This indicated a possibly high sensitivity of steel fibers to the variation of specimen size.

- Regarding the contribution of steel fibers (L type: RC-80/60-BN, 60 kg/m³) to the maximum load-bearing capacity of same-sized specimen, the large SFRC specimens showed lower average stress increment (36%) than the small SFRC prisms (44%) for the area ratios of 9 and 4. This implied a possibly low reinforcing effectiveness of steel fibers in large-sized concrete element.

- Based on the measuring results of fiber orientation, it can be assumed that the somewhat preferred fiber alignment towards the directions of the tensile stresses ($\Delta$ = 8.3%) might, in conjunction with other factors (e.g. size effect and/or area ratio), lead to the higher values of maximum stress for the large SFRC specimens loaded at the low area ratio of 4.

- With increasing specimen dimension, the stiffness of the stress-longitudinal displacement curves decreased considerably for both plain and fiber concretes for a given area ratio. Compared to the small SFRC prisms, the large SFRC specimens exhibited a significantly more gradual stress decline in the post-cracking zone of the curves, particularly pronounced at the high area ratio of 9.

- Compared to the plain concrete, the failure behavior of the SFRC was much less sensitive to the variation of specimen size.
  - The large plain concrete prisms showed a much more catastrophic, explosive failure than the small ones, and completely lost their integrity at both area ratios (R = 9 and 4), whereas for the small prisms a complete collapse only occurred at low area ratio (R ≤ 4).

  - For the large SFRC specimens, the external concrete damages (i.e. cracking and spalling) did not tend to noticeably increase with reducing area ratio, in contrast to the small ones; however, the internal cracks propagated somewhat deeper beyond the loaded area.

### 4.2.3 Influence of fiber property

As previously discussed in Section 2.1, the properties of steel fiber itself impact a great number of engineering behaviors of SFRC under various loading situations. Early investigations performed by Al-Taan and Al-Hamdony (2005) have shown that the load-bearing capacity of normal-strength SFRC blocks exposed to concentrated load increased noticeably with increasing aspect ratio of steel fibers. Klotz (2008) revealed that steel fiber with different shapes behaved differently in improving the load-bearing capacity and ductility of ultra-high-strength SFRC prisms under localized compression. In this test series, the effect of steel fibers with diverse properties (tensile strength, aspect ratio, dimension and shape) on the load-bearing and fracture behavior of high-strength concrete was investigated. These standard prisms (d150) made of various SFRCs with an uniform fiber content of 60 kg/m³ were loaded concentrically with three different area ratios (R = 9, 4 and 2.25).

**Maximum local compressive stress**

As listed in Table 4.5, all the SFRCs exhibited significant higher values of $q_{max}$ than the plain concrete. And the increment varied from 28% to 58%, largely depending on the type of steel fiber used. For a given fiber type, the increase in $q_{max}$ ($q_{max,\ fiber}$/ $q_{max,\ plain}$) did not differ notably among the area ratios tested, while the $q_{max}$ decreased markedly with reducing area ratio for all the SFRCs. Expectedly, the high-strength hook-ended macrofiber Lh appeared to be most effective in enhancing the load-bearing capacity of concrete, whereas the hook-ended mesofiber M and the straight microfiber S showed the lowest corresponding values. A same trend was also found by the stress ratio that decreased with reducing area ratio for all the SFRCs.

*Table 4.5: Influence of fiber properties on the maximum stress $q_{max}$ and stress ratio n relative to the high-strength plain concrete (PC)*

| Index | Term | Area ratio R | | |
|---|---|---|---|---|
| | | 9 | 4 | 2.25 |
| PC | $q_{max}$ [MPa] | 152 | 104 | 81 |
| | n | 1.8 | 1.23 | 0.96 |
| L60 | $q_{max}$ [MPa] | 214 | 153 | 113 |
| | $q_{max,\ fiber}$/ $q_{max,\ plain}$ | 141% | 147% | 140% |
| | n | 2.45 | 1.75 | 1.29 |
| | $\Delta(n_{fiber}-n_{plain})$ | 0.65 | 0.52 | 0.33 |
| Lt60 | $q_{max}$ [MPa] | 206 | 146 | |
| | $q_{max,\ fiber}$/ $q_{max,\ plain}$ | 136% | 140% | |
| | n | 2.45 | 1.74 | |
| | $\Delta(n_{fiber}-n_{plain})$ | 0.65 | 0.51 | |
| Lh60 | $q_{max}$ [MPa] | 229 | 164 | |
| | $q_{max,\ fiber}$/ $q_{max,\ plain}$ | 151% | 158% | |
| | n | 2.57 | 1.84 | |
| | $\Delta(n_{fiber}-n_{plain})$ | 0.77 | 0.61 | |
| M60 | $q_{max}$ [MPa] | 196 | 137 | 107 |
| | $q_{max,\ fiber}$/ $q_{max,\ plain}$ | 129% | 132% | 132% |
| | n | 2.4 | 1.68 | 1.31 |
| | $\Delta(n_{fiber}-n_{plain})$ | 0.6 | 0.45 | 0.35 |
| S60 | $q_{max}$ [MPa] | 194 | 141 | |
| | $q_{max,\ fiber}$/ $q_{max,\ plain}$ | 128% | 136% | |
| | n | 2.19 | 1.59 | |
| | $\Delta(n_{fiber}-n_{plain})$ | 0.39 | 0.36 | |

Through taking the values of $q_{max}$ and stress ratio n of the SFRCs produced with L type of steel fiber as reference, the values of $q_{max}/ q_{max, L60}$ and $\Delta(n-n_{L60})$ related to the SFRCs manufactured with other fiber types were assessed and listed in Table 4.6. Compared to the SFRCs with normal-strength hook-ended macrofiber L ($f_t$ = 1225 MPa, l/ d = 60/ 0.75 mm), an average increase in $q_{max}$ of 7% was recorded by the SFRCs with high-strength hook-ended macrofiber Lh with similar dimension (l/ d = 60/ 0.71 mm), however, doubled tensile strength ($f_t$ = 2600 MPa). Increasing the aspect ratio of hook-ended steel fiber from 67 (Lt, l/ d = 60/ 0.90 mm) to 80 (L, l/ d = 60/ 0.75 mm) with similar strength and identical length led to an increment in $q_{max}$ of solely up to 5%. Regarding the fiber size, the SFRC with short hook-ended mesofiber M (l/ d = 30/ 0.55 mm) showed a mean fall in $q_{max}$ of about 7.7%, compared to the SFRC with long hook-ended macrofiber L with similar strength. When using straight microfiber S, a lower load-bearing capacity was observed with a reduction in $q_{max}$ of 8.5%, compared to the hook-ended macrofiber L. In the cases studied here, the variation in maximum stress ($q_{max}/ q_{max, L60}$) due to various types of steel fibers was rather insensitive to the area ratio.

*Table 4.6: Influence of fiber properties on the maximum stress $q_{max}$ and stress ratio n relative to the high-strength SFRC with L type of steel fiber*

| **Index** | **Term** | **Area ratio R** | | |
|---|---|---|---|---|
| | | 9 | 4 | 2.25 |
| L60 | $q_{max}$ [MPa] | 214 | 153 | 113 |
| | n | 2.45 | 1.75 | 1.29 |
| Lt60 | $q_{max}$ [MPa] | 206 | 146 | |
| | n | 2.45 | 1.74 | |
| | $q_{max}/ q_{max, L60}$ | 96% | 95% | |
| | $\Delta(n-n_{L60})$ | 0 | -0.01 | |
| Lh60 | $q_{max}$ [MPa] | 229 | 164 | |
| | n | 2.57 | 1.84 | |
| | $q_{max}/ q_{max, L60}$ | 107% | 107% | |
| | $\Delta(n-n_{L60})$ | 0.12 | 0.09 | |
| M60 | $q_{max}$ [MPa] | 196 | 137 | 107 |
| | n | 2.45 | 1.68 | 1.31 |
| | $q_{max}/ q_{max, L60}$ | 92% | 90% | 95% |
| | $\Delta(n-n_{L60})$ | 0 | -0.07 | 0.02 |
| S60 | $q_{max}$ [MPa] | 194 | 141 | |
| | n | 2.19 | 1.59 | |
| | $q_{max}/ q_{max, L60}$ | 91% | 92% | |
| | $\Delta(n-n_{L60})$ | -0.26 | -0.16 | |

In terms of the difference of stress ratios $\Delta(n-n_{L60})$, an appreciable value was only observed in the case of SFRC with straight microfiber S. Varying the aspect ratio (L vs. Lt) or fiber dimension (L vs. M) did not tend to exert notable influence on the stress ratio n or $\Delta(n-n_{L60})$, as explicitly illustrated in Figure 4.21. Note that, the increase in fiber strength (L vs. Lh) solely resulted in minor improvement in the stress ratio n. This may be accounted for by the effect of various types of steel fibers on the compressive strength of the corresponding SFRCs, since the stress ratio n was determined by dividing the maximum local compressive stress $q_{max}$ through the concrete compressive strength $f_{c,cube}$. Furthermore, for all the SFRCs investigated here the effectiveness of fiber reinforcement reduced progressively with decreasing area ratio, independent of the types of steel fiber used.

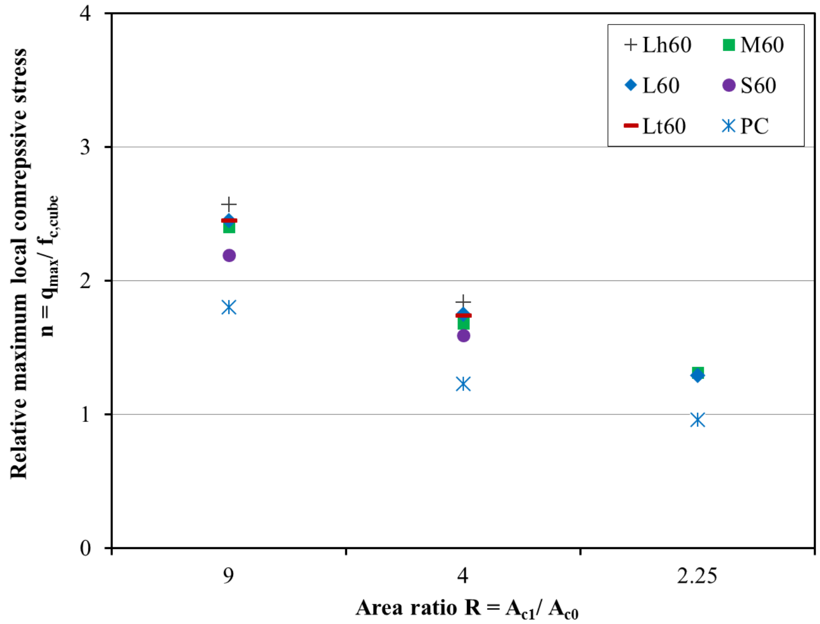


*Figure 4.21: Influence of fiber properties on the stress ratio n at the area ratios of 9, 4 and 2.25*

**Stress versus displacement response**

The stress versus longitudinal displacement relationships of the SFRCs produced with various types of steel fiber are presented in Figure 4.22 and Figure 4.23 for the area ratios of 9 and 4, respectively. For a given area ratio the stress-displacement curves of different SFRCs showed an almost identical stiffness in the pre-peak stage, however, after the peak stage a varying stress decline.

Beyond the peak stage (R = 9), a slightly more steep stress fall was observed by the SFRC with the straight microfiber S (Figure 4.22, S60_9), compared to the SFRCs with other types of steel fiber. A double increase in fiber tensile strength, but with a similar geometry resulted in a considerably better post-cracking ductility characterized by a more gradual stress decay with larger displacement at the predefined test end (L60_9 vs. Lh60_9). Similarly, enlarging the dimension of steel fiber with an identical shape also led to a better load-bearing behavior to some extent (M60_9 vs. L60_9). Increasing the aspect ratio from 67 to 80 had marginal effect on the stress-displacement behavior of SFRC (Lt60_9 vs. L60_9). A similar trend was also observed at the low area ratio of 4 (Figure 4.23).

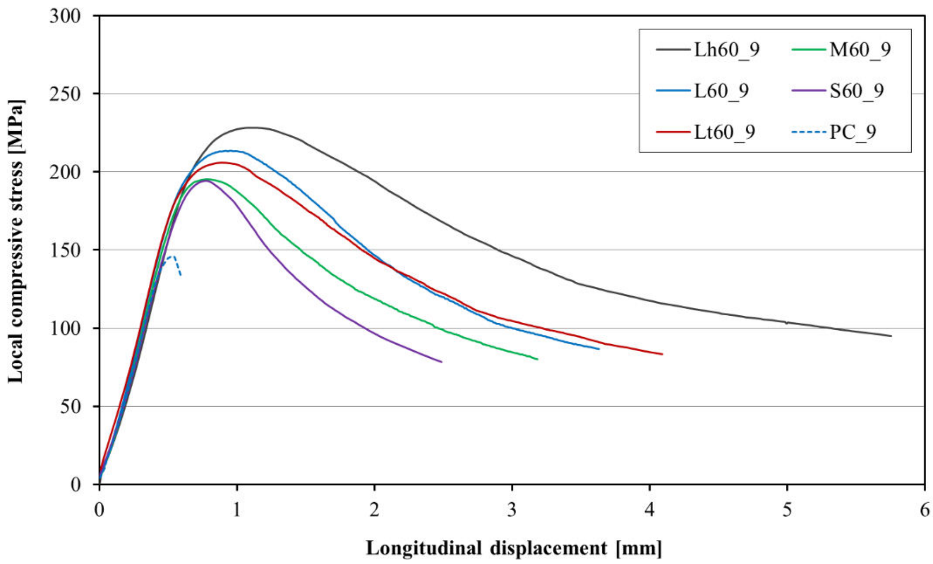


*Figure 4.22: Average local compressive stress versus longitudinal displacement curves of SFRC specimens produced with various types of steel fiber loaded at the area ratio of 9*

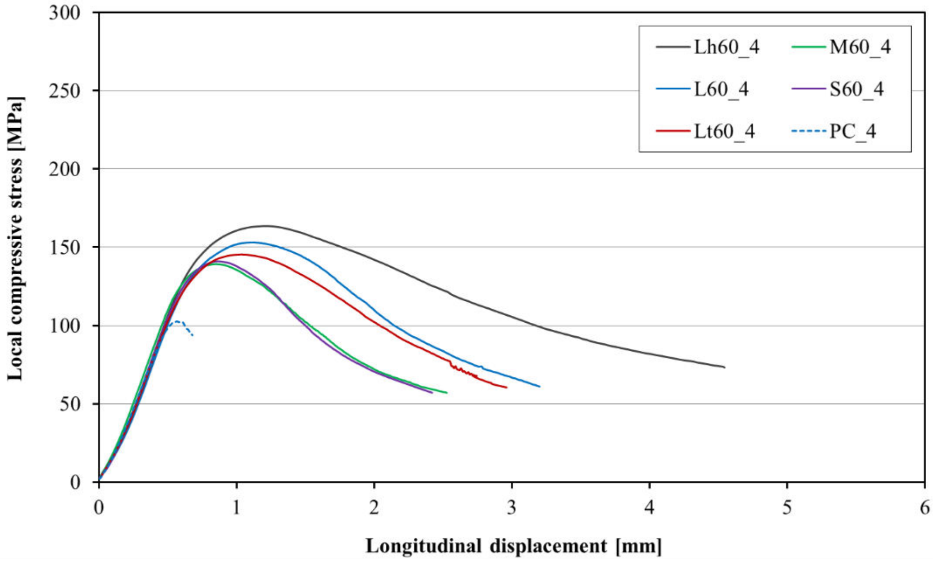


*Figure 4.23: Average local compressive stress versus longitudinal displacement curves of SFRC specimens produced with various types of steel fiber loaded at the area ratio of 4*

Figure 4.24 shows the stress versus lateral deformation responses of the SFRCs with various types of steel fiber at the high area ratio of 9. Although for the SFRC produced with the high-strength hook-ended macrofiber Lh the initial crack developed at the highest stress level, the stress reduction with growing crack opening in the post-cracking zone did not differ noticeably with that of other SFRCs. At the low area ratio of 4, the stress decline of SFRC with the high-strength hook-ended macrofiber Lh was comparatively slower than other SFRCs (Figure A.4, Appendix A).

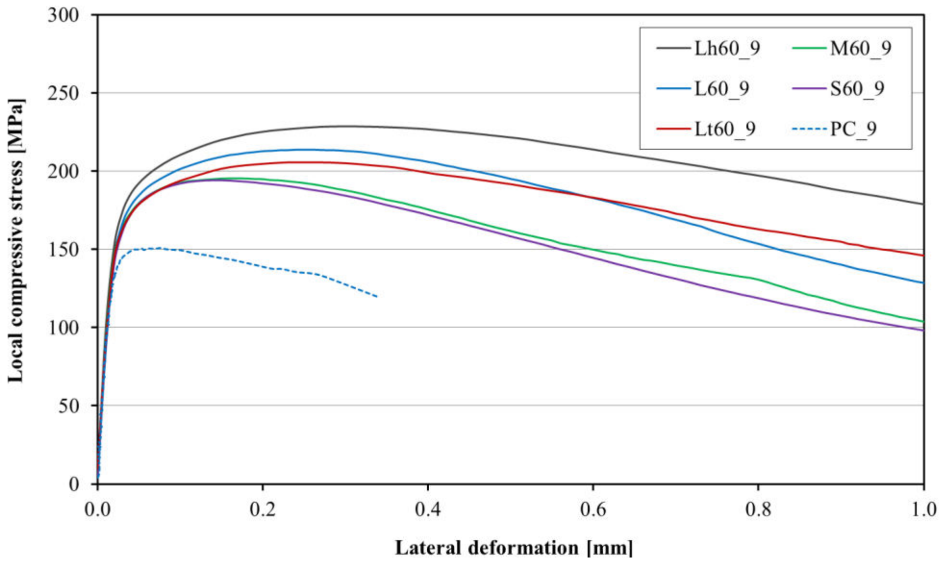


*Figure 4.24: Average local compressive stress versus lateral deformation curves of SFRC specimens reinforced with various fiber types loaded at the area ratio of 9*

The effect of various fiber types on the distribution and orientation of steel fibers in the test samples was determined by the procedure described in Section 4.2.2. The measuring results showed a nearly same fiber content ($\Delta_{max}$ = 2.3 kg/m³) and a similar fiber orientation ($\Delta_{max}$ = 3.9% in one of the three spatial directions) in the upper half of prisms (Figure A.5 and Figure A.6, Appendix A). Therefore, it can be ascertained that for the cases studied here the fiber type exerted insignificant influence on the distribution and orientation of steel fibers in concrete under otherwise identical production conditions.

Thus, the variations in ultimate bearing stress and the stress versus displacement response should only be attributed to the diverse pullout resistance of the individual fibers. The pullout response of the fibers used here was obtained from the uniaxial pullout test on a single fiber embedded in a high-strength concrete matrix ($f_{c,cube}$ = 84 MPa). Some representative results are shown in Figure A.7 (Appendix A). By comparing the results of pullout tests and concentrated loading tests, it has been found that steel fibers with small dimension (i.e. type M or S) showing markedly low pullout resistance, did not necessarily performed accordingly inferiorly under concentrated loading when only considering the peak stress. This effect was mainly due to the drastically increased number of fibers intersecting the cracks. These fibers are more effective in arresting microcracks and retarding their coalescence into macrocracks. This leads to the development of hybrid fiber reinforcement containing both microfibers and macrofibers (primarily bridging over the macrocracks). More details on the hybrid fiber reinforcement are given in Section 4.2.4.

**Failure and crack characteristics**

Some representative samples of the tested concrete prisms produced with various types of steel fibers are demonstrated in Figure 4.25 and Figure 4.26 for the area ratios of 9 and 4, respectively. As one would expect, all the SFRC specimens exhibited a more or less ductile fracture behavior, however, the crack pattern differed remarkably from each other. In general, with reducing area ratio concrete damages such as cracking and spalling tended to deteriorate and propagate downwards to the lower half of specimen.

As reported in Breitenbücher and Song (2014), compared to the normal-strength hook-ended macrofiber L, the high-strength hook-ended macrofiber Lh caused more severe concrete spalling around the fiber exit point during the pullout process, especially for large inclination angles with respect to the loading direction. Thus, in combination with a more ductile post-cracking behavior (i.e. a longer test duration), the failure appearance of the corresponding SFRC prisms was particularly afflicted with increased cracking and spalling on the loading and lateral surfaces (e.g. Figure 4.25, Lh60_9 vs. Figure 4.11, L60_9). Nonetheless, no crack propagation through the lateral surfaces was observed, even at the low area ratio of 4 (Figure 4.26, Lh60_4 vs. Figure 4.11, L60_4).

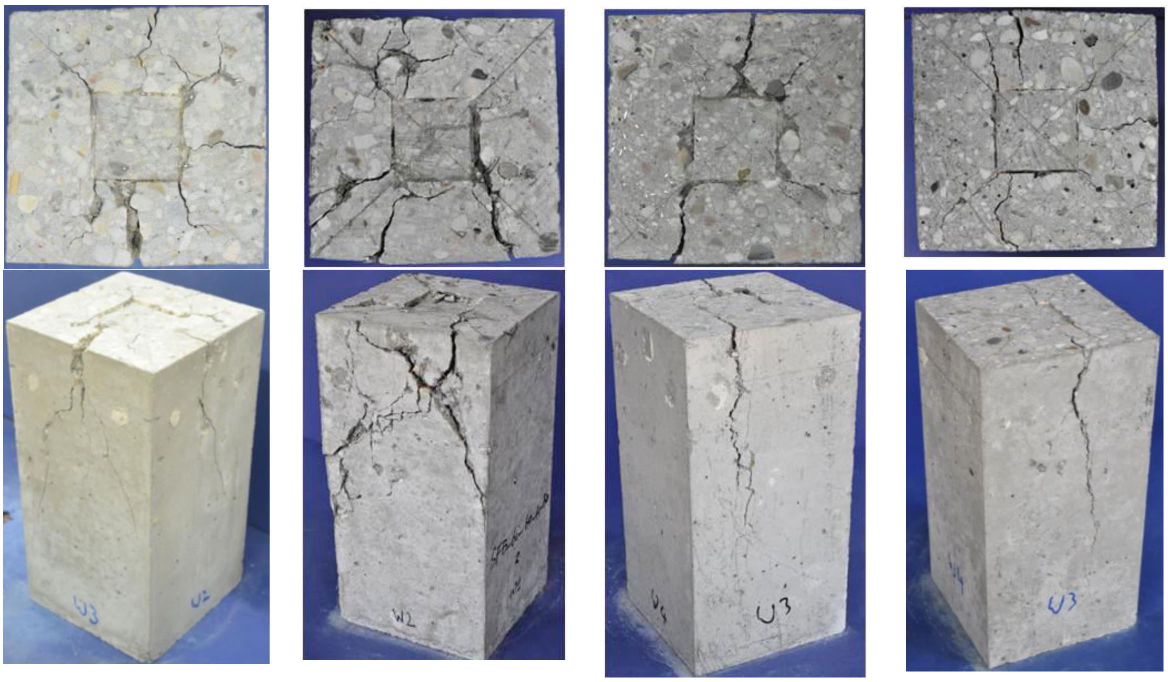

*Lt60_9 Lh60_9 M60_9 S60_9*

*Figure 4.25: Typical failure patterns of SFRC specimens produced with various types of steel fiber tested at the area ratio of 9*

In the case of SFRCs strengthened with macrofiber Lt with lower aspect ratio, no distinct difference was found in the failure pattern at the high area ratio of 9, compared to the prisms cast with macrofiber L (Figure 4.25, Lt60_9 vs. Figure 4.11, L60_9). Noticeably, at the low area ratio of 4, the prisms cast with Lt fiber was less damaged at the predefined test end (Figure 4.26, Lt60_4 vs. Figure 4.11, L60_4). For the prisms reinforced with M or S fiber, major cracks starting from the testing surface spread almost through the lateral surfaces, and particularly pronounced when loaded at the low area ratio of 4 (e.g. Figure 4.26, S60_4). This was mainly due to the insufficient crack-bridging effect of the fibers.

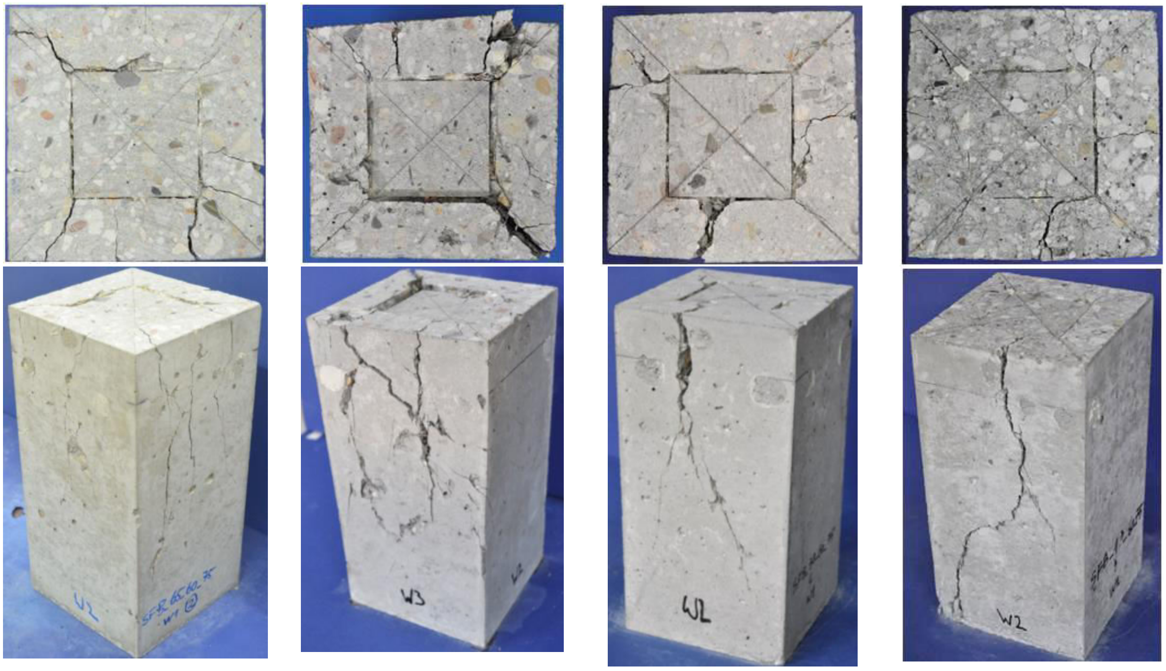

*Lt60_4* *Lh60_4* *M60_4* *S60_4*

*Figure 4.26: Typical failure patterns of SFRC specimens produced with various types of steel fiber tested at the area ratio of 4*

The average crack number of the SFRCs produced with various fiber types differed among each other unnoticeably for a given area ratio (Table B.5, Appendix B). Only a slightly lower value of crack number was found by the SFRC manufactured with microfiber S at the area ratio of 9, compared to other SFRCs. In terms of maximum crack width, the SFRC with high-strength macrofiber Lh exhibited the highest values, primarily due to its superior post-cracking ductility (i.e. long test duration till predefined test end). In spite of a premature failure, the SFRC with straight microfiber S showed nearly the same values of maximum crack width as the SFRC specimens with hook-ended macrofiber L.

**Summary**

In this sub-section, the results of concentrated loading tests on high-strength concrete prisms produced with various types of steel fiber have been presented. These standard SFRC specimens (d150: 150 x 150 x 300-mm) were loaded concentrically with three different area ratios of 9, 4 and 2.25.

On the basis of the experimental data obtained, the following relevant conclusions can be drawn:

- The fiber properties affected the improvement in the maximum load-bearing capacity of concrete to various degrees, showing an increment ranging from 28% (for short straight microfiber, test group S60_9) to 58% (for long hook-ended high-strength macrofiber, test group Lh60_4).

- The difference of stress ratios between the plain and fiber concretes was insignificantly influenced by the fiber properties, except for the case of short straight microfiber S.

- More specifically, increasing the fiber tensile strength (L vs. Lh = 1225 MPa vs. 2600 MPa, hook-ended with similar dimension) or aspect ratio (Lt vs. L = 67 vs. 80, hook-ended with same length and similar strength) led to a slight stress increase (7% or 5%). Reducing the fiber dimension (L vs. M = 60/ 0.75mm vs. 30/ 0.55 mm, hook-ended with similar strength) or changing the fiber shape (L vs. S = hook-ended vs. straight) resulted in a slight stress decrease (7.7% or 8.5%).

- Changing the fiber type exerted no effect on the stiffness of the stress-longitudinal displacement curve, however, great impact on the post-cracking ductility.
  - As expected, the high-strength hook-ended macrofiber (Lh) was most effective in improving the ductility, while the straight microfiber (S) was relatively least effective.

  - Furthermore, enlarging the fiber dimension (M vs. L) enhanced the ductility only to a limited extent. Increasing the aspect ratio (Lt vs. L) had marginal benefit.

  - The effects above-mentioned were found to be independent of the area ratio applied.

- Based on the measuring results of fiber content and orientation, it has been established that the type of steel fiber had essentially inappreciable influence on the concentration and orientation of fibers in the three spatial directions in the SFRC specimens.

- By comparing the results of single fiber pullout tests and concentrated loading tests, it has been observed that steel fibers with small dimension showed markedly low pullout resistance; however, the corresponding specimens did not necessarily demonstrate accordingly inferior performances under concentrated loading especially when only concerning the maximum bearing stress. This effect was primarily due to the considerably increased number of short fibers intersecting the cracks.

- Although all the SFRCs exhibited a more or less ductile fracture behavior, the failure pattern was affected by the fiber type to a large extent.
  - Due to the superior post-cracking ductility, the SFRCs with high-strength hook-ended macrofiber (Lh) presented remarkably increased cracking and spalling of concrete.

  - Varying the aspect ratio of hook-ended steel fiber (Lt vs. L) did not lead to a noticeable change in the failure pattern.

  - Reducing the fiber dimension or change the fiber shape (from hook-ended to straight) led to continuous cracking especially at low area ratio (4 or 2.25), basically due to the insufficient crack-bridging capacity of the fibers (fiber type: M and S).

### 4.2.4 Influence of fiber concentration and combination

One of the principal parameters affecting the load-bearing behavior of SFRC under concentrated load is the amount of steel fibers in concrete. As experimentally confirmed by Schmidt and Fiedler (1993) and Al-Taan and Al-Hamdony (2005), the load-bearing capacity of SFRC increased progressively with growing fiber concentration. More recently, Klotz (2008) varied the proportions of two different types of steel fiber incorporated simultaneously in concrete as hybrid fiber reinforcement. He revealed a synergistic effect of fiber reinforcement of this kind, by which the load-bearing capacity of his ultra-high-strength SFRC prisms was primarily enhanced by the hook-ended macrofibers and the ductility was substantially improved by the straight microfibers.

In this test series, the effect of various fiber concentrations consisting of one or two, or even three different types of steel fibers on the load-bearing and fracture behavior of high-strength SFRC was systematically investigated. These standard prisms (d150) made of various SFRCs were loaded concentrically with two area ratios of 9 and 4.

**Maximum local compressive stress**

As listed in Table 4.7-1 and Table 4.7-2, all the SFRCs exhibited considerably higher $q_{max}$ than the plain concrete, showing a stress increment in the range from 27% up to 80%, depending on the fiber content and the combination of steel fibers (i.e. type of fiber reinforcement). More generally, the $q_{max}$ increased gradually with increasing fiber content, which was consistent with the previous findings of Schmidt and Fiedler (1993) and Al-Taan and Al-Hamdony (2005).

*Table 4.7-1: Influence of fiber concentration and combination on the maximum stress $q_{max}$ and stress ratio n relative to the high-strength plain concrete (PC)*

| Index | Fiber content [kg/m³] | Term | Area ratio R | |
|---|---|---|---|---|
| | | | 9 | 4 |
| PC | 0 | $q_{max}$ [MPa] | 152 | 104 |
| | | n | 1.8 | 1.23 |
| L40 | 40 | $q_{max}$ [MPa] | 194 | 132 |
| | | n | 2.28 | 1.55 |
| | | $q_{max, fiber}$/ $q_{max, plain}$ | 128% | 127% |
| | | $\Delta(n_{fiber}-n_{plain})$ | 0.48 | 0.32 |
| L40S20 | 60 | $q_{max}$ [MPa] | 207 | 148 |
| | | n | 2.38 | 1.7 |
| | | $q_{max, fiber}$/ $q_{max, plain}$ | 136% | 142% |
| | | $\Delta(n_{fiber}-n_{plain})$ | 0.58 | 0.47 |
| L40M20 | | $q_{max}$ [MPa] | 206 | 140 |
| | | n | 2.36 | 1.6 |
| | | $q_{max, fiber}$/ $q_{max, plain}$ | 136% | 135% |
| | | $\Delta(n_{fiber}-n_{plain})$ | 0.56 | 0.37 |
| L60 | | $q_{max}$ [MPa] | 214 | 153 |
| | | n | 2.45 | 1.75 |
| | | $q_{max, fiber}$/ $q_{max, plain}$ | 141% | 147% |
| | | $\Delta(n_{fiber}-n_{plain})$ | 0.65 | 0.52 |

*Table 4.7-2: Influence of fiber concentration and combination on the maximum $q_{max}$ and stress ratio n relative to the high-strength plain concrete (PC)*

| Index | Fiber content [kg/m³] | Term | Area ratio R | |
|---|---|---|---|---|
| | | | 9 | 4 |
| L40S40 | 80 | $q_{max}$ [MPa] | 236 | 162 |
| | | n | 2.58 | 1.77 |
| | | $q_{max, fiber}/q_{max, plain}$ | 155% | 156% |
| | | $\Delta(n_{fiber}-n_{plain})$ | 0.78 | 0.54 |
| L40M40 | | $q_{max}$ [MPa] | 239 | 161 |
| | | n | 2.62 | 1.76 |
| | | $q_{max, fiber}/q_{max, plain}$ | 157% | 155% |
| | | $\Delta(n_{fiber}-n_{plain})$ | 0.82 | 0.53 |
| L40M20S20 | | $q_{max}$ [MPa] | 237 | 165 |
| | | n | 2.52 | 1.76 |
| | | $q_{max, fiber}/q_{max, plain}$ | 156% | 159% |
| | | $\Delta(n_{fiber}-n_{plain})$ | 0.72 | 0.53 |
| L60S20 | | $q_{max}$ [MPa] | 245 | 175 |
| | | n | 2.44 | 1.74 |
| | | $q_{max, fiber}/q_{max, plain}$ | 161% | 168% |
| | | $\Delta(n_{fiber}-n_{plain})$ | 0.64 | 0.51 |
| L80 | | $q_{max}$ [MPa] | 254 | 171 |
| | | n | 2.69 | 1.81 |
| | | $q_{max, fiber}/q_{max, plain}$ | 167% | 164% |
| | | $\Delta(n_{fiber}-n_{plain})$ | 0.89 | 0.58 |
| L40M20S40 | 100 | $q_{max}$ [MPa] | 248 | 174 |
| | | n | 2.47 | 1.73 |
| | | $q_{max, fiber}/q_{max, plain}$ | 163% | 167% |
| | | $\Delta(n_{fiber}-n_{plain})$ | 0.67 | 0.5 |
| L40M40S20 | | $q_{max}$ [MPa] | 239 | 160 |
| | | n | 2.56 | 1.71 |
| | | $q_{max, fiber}/q_{max, plain}$ | 157% | 154% |
| | | $\Delta(n_{fiber}-n_{plain})$ | 0.76 | 0.48 |
| L60S40 | | $q_{max}$ [MPa] | 256 | 169 |
| | | n | 2.69 | 1.78 |
| | | $q_{max, fiber}/q_{max, plain}$ | 168% | 163% |
| | | $\Delta(n_{fiber}-n_{plain})$ | 0.89 | 0.55 |
| L40M40S40 | 120 | $q_{max}$ [MPa] | 273 | 180 |
| | | n | 2.77 | 1.82 |
| | | $q_{max, fiber}/q_{max, plain}$ | 180% | 173% |
| | | $\Delta(n_{fiber}-n_{plain})$ | 0.97 | 0.59 |
| L60S60 | | $q_{max}$ [MPa] | 266 | 184 |
| | | n | 2.82 | 1.95 |
| | | $q_{max, fiber}/q_{max, plain}$ | 175% | 177% |
| | | $\Delta(n_{fiber}-n_{plain})$ | 1.02 | 0.72 |

It should be noted that for a fiber content ≤ 80 kg/m³ the variations in the secondary and/or tertiary fiber type (M and/or S fiber) appeared to have insignificant influence on the $q_{max}$ (e.g. Table 4.7-1, L40S20 vs. L40M20; Table 4.7-2, L40S40 vs. L40M40 vs. L40M20S20). In this range of fiber amount, the SFRCs produced solely with hook-ended macrofiber L or with high proportion of L fiber (primary fiber) exhibited modestly higher values of $q_{max}$ at both area ratios tested. For a fiber concentration ≥ 100 kg/m³, the beneficial effect of the L fiber on the $q_{max}$ was less evident, or even negligible (e.g. Table 4.7-2, L60S40 vs. L40M20S40; L60S60 vs. L40M40S40).

As observed during the production process, a high proportion of short hook-ended mesofiber M and/or straight microfiber S significantly facilitated the mixing of concrete mixtures with high fiber contents ≥ 80 kg/m³. More importantly, as mentioned above, the $q_{max}$ of these SFRCs did not decrease noticeably, in some cases even slightly increased.

Regardless of the improved compressive strength of SFRCs with high fiber contents, a continuously growing trend of the stress ratio n or the difference of stress ratios $\Delta(n_{fiber}-n_{plain})$ with the increase of fiber concentration was observed at both area ratios of 9 and 4. This tendency is summarized in Table 4.7-1 and Table 4.7-2 and graphically presented in Figure 4.27 and Figure 4.28. For a given fiber content, the variations in the fiber type did not exert considerable influence on the stress ratio n.

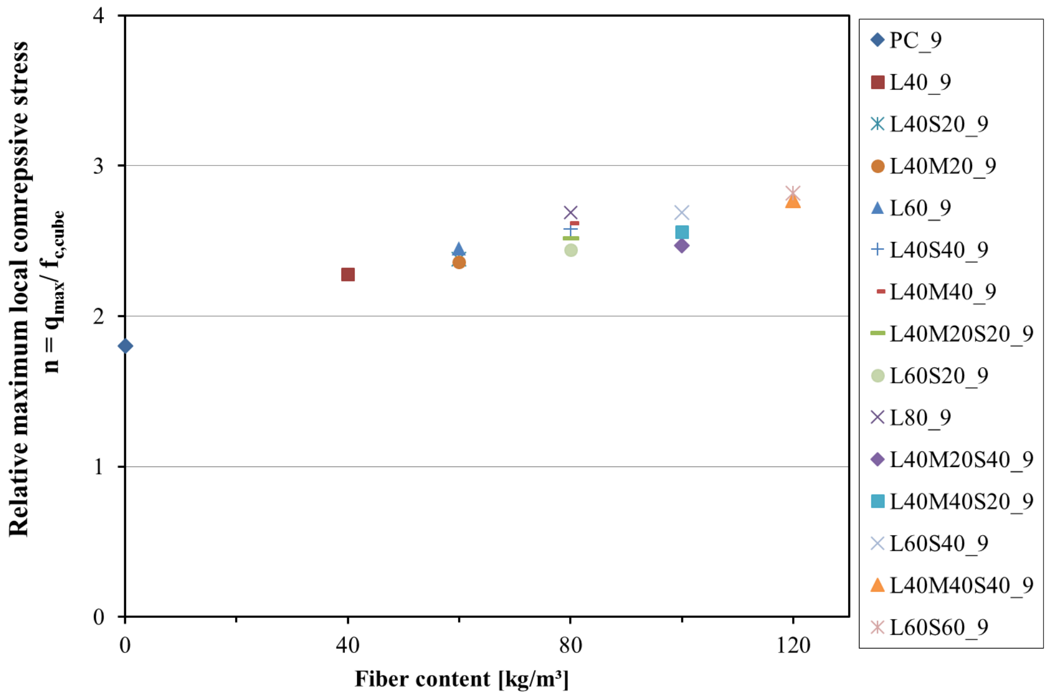


*Figure 4.27: Effect of fiber concentration and combination on the stress ratio n for the area ratio of 9*

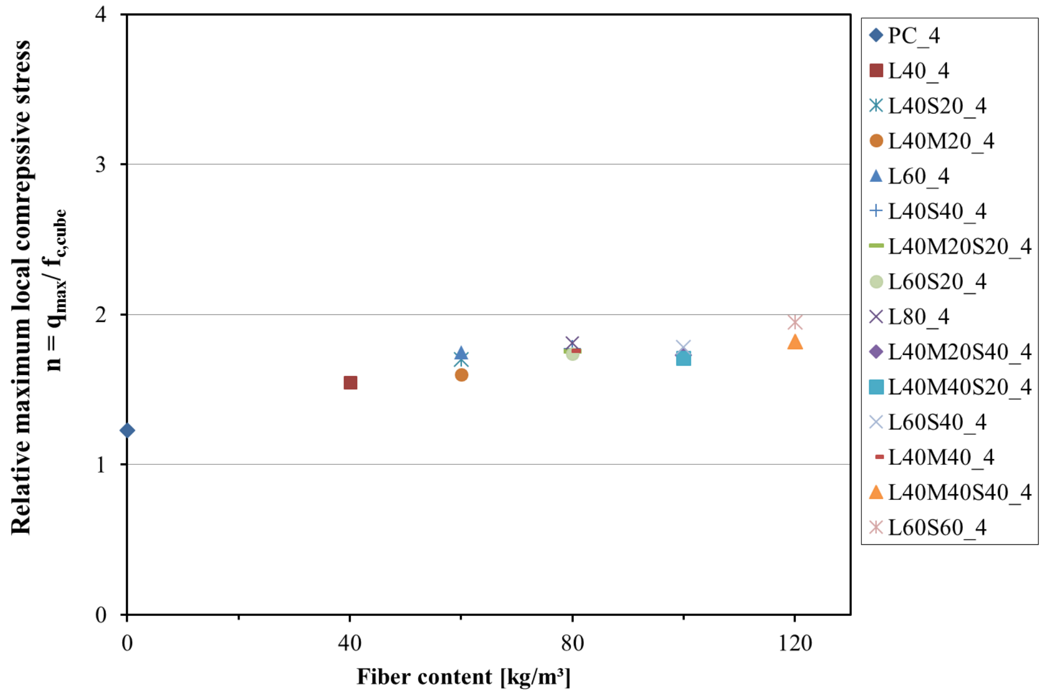


*Figure 4.28: Effect of fiber concentration and combination on the stress ratio n for the area ratio of 4*

**Stress versus displacement response**

The average stress versus longitudinal displacement curves of the SFRCs produced with diverse contents and combinations of steel fibers are depicted in Figure 4.29 - Figure 4.33. In general, for a given area ratio, the stiffness of the stress-displacement curves in the pre-peak branch was nearly identical among the various SFRCs, independent of the type of fiber reinforcement and the fiber amount applied (e.g. Figure 4.29, various fiber reinforcements with a uniform fiber concentration and Figure 4.32, various fiber reinforcements with different fiber concentrations).

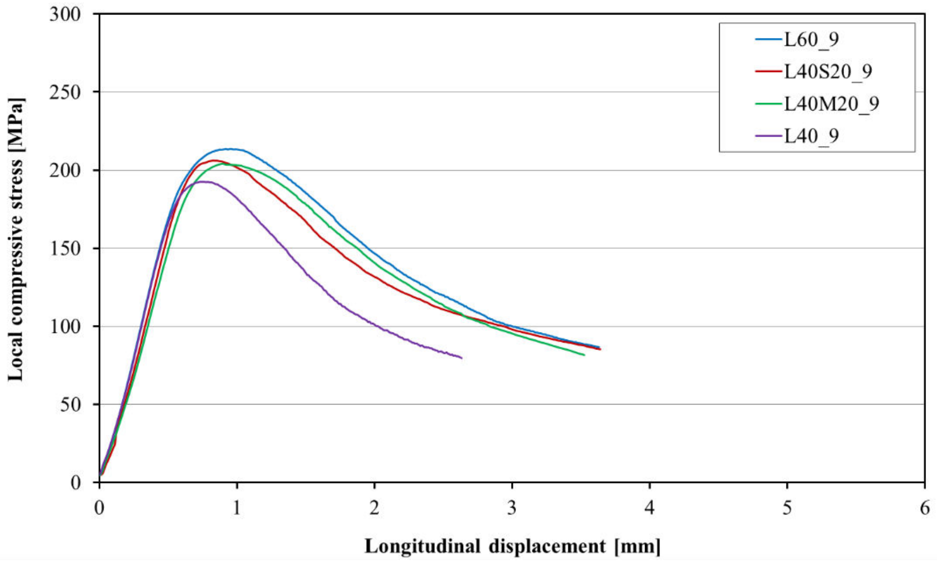


*Figure 4.29: Average local compressive stress versus longitudinal displacement curves of various SFRCs with a fiber content of 60 kg/m³ at the area ratio of 9*

As stated earlier, increasing the fiber content in concrete can substantially enhance the load-bearing capacity of SFRC. As shown in Figure 4.29, starting from a base concentration of 40 kg/m³ of L fibers, the incorporation of additional 20 kg/m³ fibers readily led to a better stress-displacement response characterized by a higher maximum bearing stress $q_{max}$ and a better post-cracking ductility. At the area ratio of 9, the SFRC containing 60 kg/m³ of L fibers (L60_9) exhibited a slightly higher $q_{max}$ than the other two SFRCs with hybrid fiber reinforcement (L40S20_9: 40 kg/m³ of L fibers and 20 kg/m³ of S fibers and L40M20_9: 40 kg/m³ of L fibers and 20 kg/m³ of M fibers). However, the curve shapes beyond the peak stage did not differ markedly among each other and were rather more or less parallel to each other. For the low fiber amount and the combination of steel fibers applied here, the hook-ended macrofiber L had a slightly more beneficial effect on increasing the maximum load-bearing capacity rather than on improving the post-cracking ductility. A similar tendency was also observed for the low area ratio of 4 (Figure A.8 , Appendix A).

The positive effect of L fiber on the overall load-bearing capacity was more distinct for a fiber content of 80 kg/m³ at the area ratio of 9 (Figure 4.30). As mentioned previously, due to the difficulties in the mixing process, for SFRCs with high fiber contents ≥ 80 kg/m³, the long hook-ended macrofibers L were partially substituted by other types of steel fibers with small dimension (i.e. M and S fiber). It can be seen that the curve courses of the SFRCs with hybrid reinforcement L40S40 and L40M20S20 were parallel to that of the SFRC with L80 monofiber reinforcement in the post-cracking zone. At the area ratio of 4, the curve shapes of the SFRCs with hybrid reinforcement approached more closely to that of the SFRC with monofiber reinforcement after the peak load (Figure A.9, Appendix A).

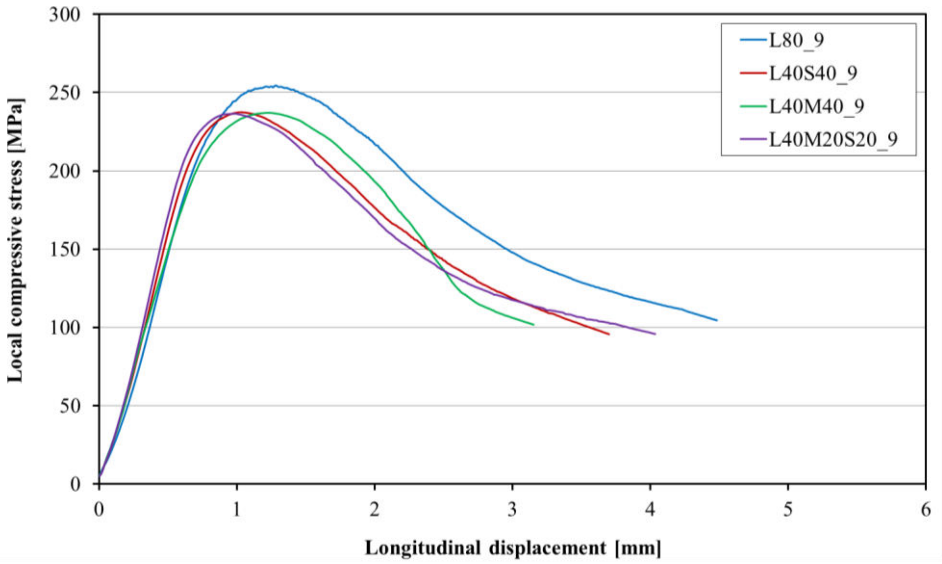


*Figure 4.30: Average local compressive stress versus longitudinal displacement curves of various SFRCs with a fiber content of 80 kg/m³ at the area ratio of 9*

The effect of fiber reinforcement with three different fiber types was depicted in Figure 4.31 for the area ratio of 9. Expectedly, the SFRC with the highest fiber amount of 120 kg/m³ (L40M40S40_9) exhibited the best overall load-bearing behavior. An additional fiber incorporation of 20 kg/m³ had a larger influence on the load-bearing response of the SFRC with a base fiber concentration of 100 kg/m³ than the SFRC with a base fiber content of 80 kg/m³. For a fiber content of 100 kg/m³, a slightly higher $q_{max}$ was observed by the SFRC with high proportion of S fibers (L40M20S40_9), compared to the SFRC with high proportion of M fibers (L40M40S20_9). Noticeably, the curve courses of all the SFRCs with hybrid fiber reinforcement were more or less parallel to each other after the peak stage.

The main purpose of using hybrid fiber reinforcement, besides the facilitation of the mixing process, was to utilize the advantages of the individual steel fibers, i.e. to control cracks at different size levels. According to Bentur and Mindess (1990), the short fibers serve primarily to arrest the cracks at a micro level once they are initiated, which is generally associated with an increase in the strength of concrete matrix. And the long fibers contribute mainly to retard the crack opening and propagating at a macro level, resulting in a substantial improvement in the toughness of concrete matrix, i.e. the post-cracking ductility. Therefore, when simultaneously incorporating various types of steel fibers into concrete, a so-called synergistic effect, namely a significant improvement in both load-bearing capacity and post-cracking ductility could be expected. However, for the various concentrations and combinations of steel fiber investigated above, effect of this kind was not achieved.

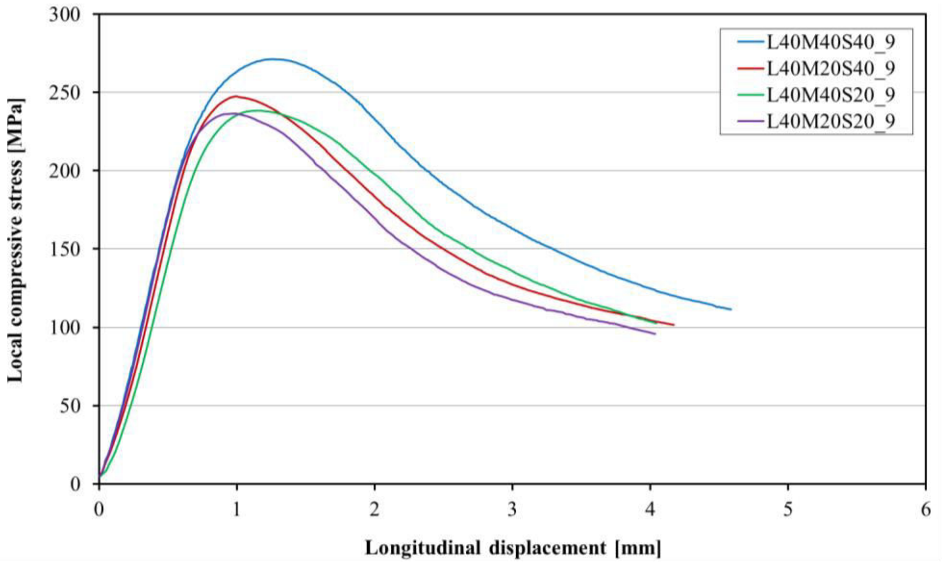


*Figure 4.31: Average local compressive stress versus longitudinal displacement curves of various SFRCs with three different fiber types at the area ratio of 9*

The synergy effect of hybrid fiber reinforcement was only observed by SFRCs with a base content of 60 kg/m³ hook-ended macrofibers L and comparatively high contents of additional straight microfibers S (≥ 40 kg/m³), as illustrated in Figure 4.32. With growing amount of additional S fibers, not only the load-bearing capacity but also the post-cracking ductility continued to increase substantially (e.g. L60S60_9 vs. L60_9 vs. S60_9). As shown in Figure 4.33, compared to the SFRCs with hybrid reinforcement L40M40S40 (with the same fiber content of 120 kg/m³), the SFRCs with L60S60 reinforcement distinguished itself mainly by a much more ductile material behavior in the post-cracking stage, especially at the high area ratio of 9.

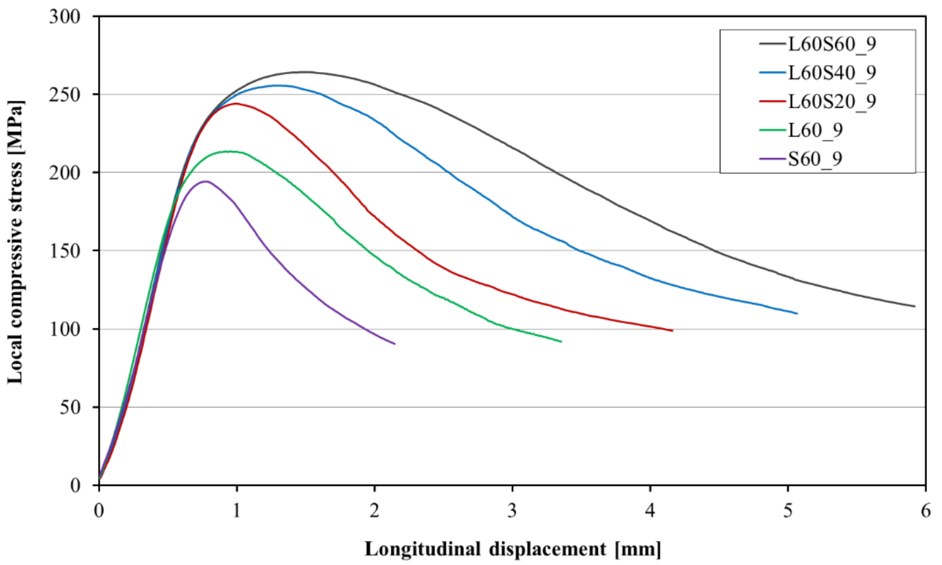


*Figure 4.32: Average local compressive stress versus longitudinal displacement curves of various SFRCs at the area ratio of 9*

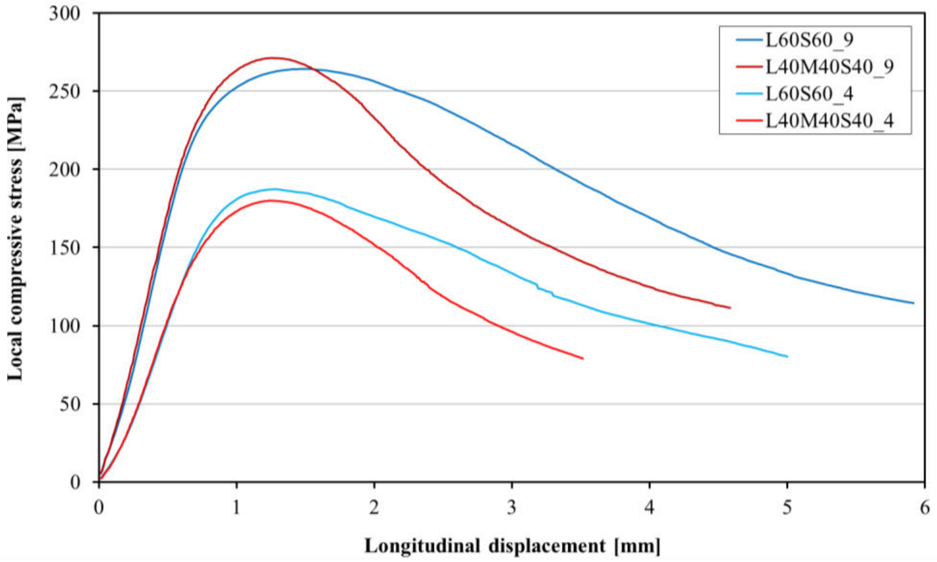


*Figure 4.33: Average local compressive stress versus longitudinal displacement curves of SFRCs with hybrid fiber reinforcement with a fiber content of 120 kg/m³ at the area ratios of 9 and 4*

The average stress versus lateral deformation curves of the various SFRCs exhibited essentially the similar characteristics as observed by the stress versus longitudinal displacement curves. Basically, the higher the $q_{max}$ was, the higher the stress level for the initial cracking was (Figure 4.34). The nature of the curve courses in the post-cracking zone was principally consistent with that of the stress-displacement curves. Some other representative curves are summarized in Appendix A.

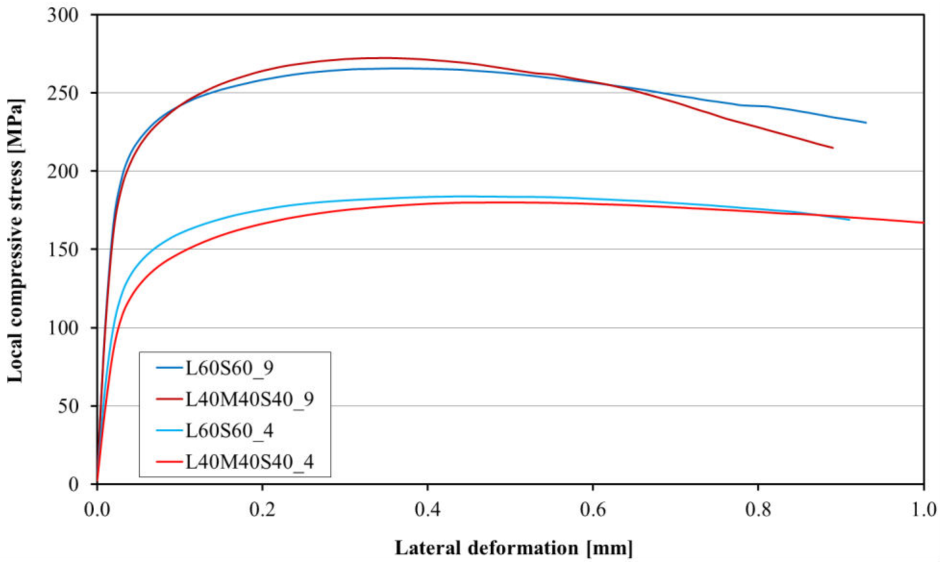


*Figure 4.34: Average local compressive stress versus lateral deformation curves of SFRCs with a fiber content of 120 kg/m³ at the area ratios of 9 and 4*

Regarding the average midpoint longitudinal compressive deformations at $q_{max}$, no clear correlation was found among the SFRCs with various types of fiber reinforcement, even at the same fiber concentration (Table B.6, Appendix B).

**Failure and crack characteristics**

Figure 4.35 and Figure 4.36 demonstrate some typical samples of the tested SFRC prisms (d150) produced with various types of fiber reinforcement. As expected, all the SFRC prisms exhibited a ductile failure behavior to varying degrees. However, the crack pattern differed among each other to a certain extent, greatly depending on the fiber content. In general, concrete damages in the form of cracking and spalling tended to deteriorate with decreasing area ratio.

For SFRC samples strengthened with 40 kg/m³ of L fibers, one major longitudinal crack was clearly to observe which spread almost through the lateral surface (Figure 4.35, L40_9), indicating an insufficient reinforcing effectiveness due to a low fiber concentration. This effect was more pronounced at the low area ratio of 4 (L40_4). By comparison, for a fiber content of 60 kg/m³, the cracks on the lateral surfaces propagated only to the half-height of specimen (Figure 4.11, L60_9). For prisms reinforced with 80 kg/m³ of L fibers, the crack pattern was similar to that of specimens produced with 60 kg/m³ of L fibers (Figure 4.11, L60_9 vs. Figure 4.35, L80_9). However, due to the increased fiber amount, the concrete damages in the lower half of specimen were confined comparatively in a smaller scale, in particular in the case of low area ratio of 4 (Figure 4.11, L60_4 vs. Figure 4.35, L80_4).

*L40_9* *L40_4* *L80_9* *L80_4*

*Figure 4.35: Typical failure patterns of SFRC specimens produced only with L fibers, but various fiber contents at the area ratios of 9 and 4*

In terms of the crack pattern of SFRC specimens produced with hybrid fiber reinforcement with a fiber content of 60 kg/m³, no notable difference was found between the prisms manufactured with L40S20 and L40M20 reinforcements. Compared to the samples cast only with L40 reinforcement, in the most cases the propagation of the longitudinal cracks did not completely extend to the bottom edge of prism due to the additional crack-bridging effect provided by the secondary fiber (e.g. Figure 4.35, L40_9 vs. Figure 4.36, L40S20_9). However, the length of the main longitudinal crack on the lateral surface was modestly longer than that of specimens produced with monofiber reinforcement L60, indicating a better crack-bridging response of L fiber. A similar trend was also observed among prisms reinforced with a uniform fiber content of 80 kg/m³, however, various types of fiber reinforcements (e.g. Figure 4.35, L80_9 vs. Figure 4.36, L40S20M20_9).

With growing fiber concentration (> 80 kg/m³), the SFRC prisms were more capable of withstanding the concentrated load in the post-cracking stage, resulting in a more ductile fracture behavior associated with more severe concrete damages at the predefined test end. However, for a certain fiber content, the crack patterns of the SFRC specimens produced with various types of fiber reinforcements did not make a noticeable distinction. It means that the different crack-bridging responses of various types of steel fiber can hardly be optically recognized on the failed specimens (e.g. Figure 4.36, L60S60_9 vs. L40M40S40_9).

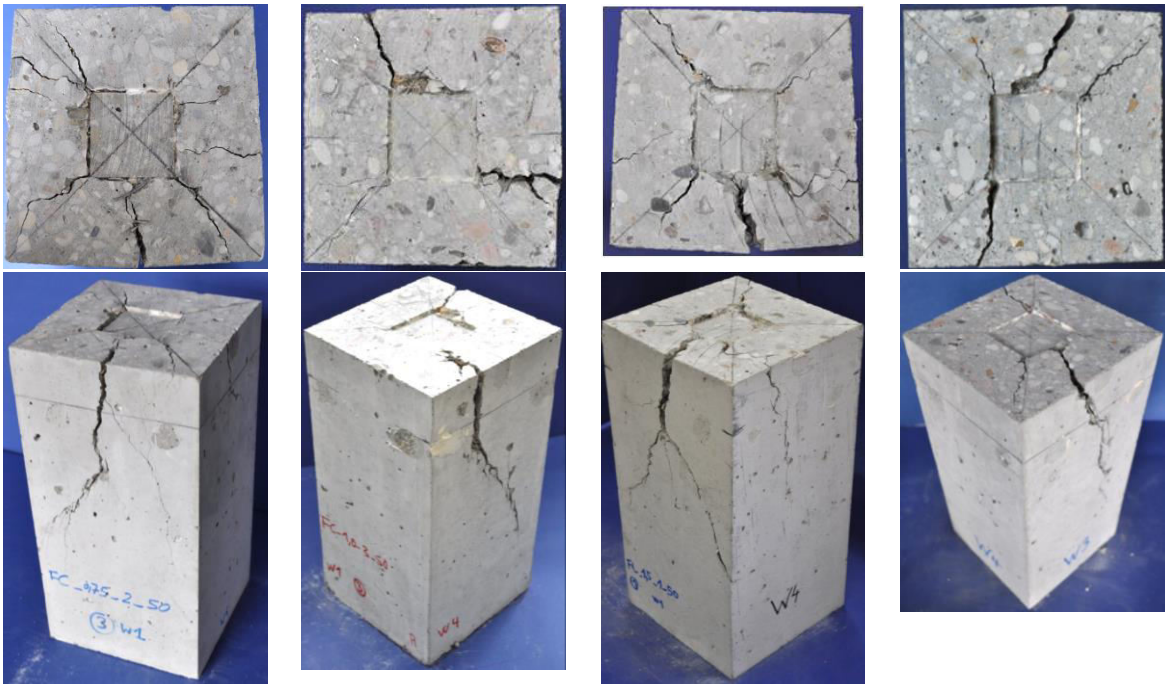

*L40S20_9* *L40M20S20_9* *L60S60_9* *L40M40S40_9*

*Figure 4.36: Typical failure patterns of SFRC specimens with hybrid fiber reinforcement at the area ratio of 9*

The average values of crack number and maximum crack width of the SFRCs produced with various fiber reinforcements were evaluated after the test end for the area ratios of 9 and 4 (Table B.7, Appendix B). Except for the specimens cast with L80 fiber reinforcement, no large variation in the average crack number on the testing surface was observed and the mean crack number varied from 6.8 to 10.8. Furthermore, no clear correlation was established between the crack number and fiber content. Except for a fiber content of 80 kg/m³, a marginal increase in the crack number with increasing proportion of the L fiber was found for both area ratios of 9 and 4. In terms of crack width, the SFRC samples manufactured with high fiber concentrations ≥ 100 kg/m³ exhibited generally higher values primarily due to the significantly long test duration. For a given fiber content, the influences of various fiber types on the crack width can hardly be determined for the cases studied here.

**Summary**

In this sub-section, the results of concentrated loading tests on concrete prisms reinforced with various fiber concentrations consisting of one or two, or even three different types of steel fibers have been presented. These high-strength SFRC prisms (d150: 150 x 150 x 300-mm) were loaded concentrically with two area ratios of 9 and 4.

On the basis of the experimental data obtained, the following relevant conclusions can be drawn:

- The maximum local compressive stress increased gradually with increasing fiber content, showing an increment from 27% to 80% on going from a fiber concentration of 40 kg/m³ to 120 kg/m³ in comparison with the plain concrete.

- The individual effect of different fiber types appeared to highly depend upon the total fiber content.
  - For a fiber content ≤ 80 kg/m³, the SFRCs with solely or high proportion of long hook-ended macrofibers (primary fiber L) generally showed modestly higher maximum stress (up to 12%); with a given fraction of primary fiber, the variation in the type of the secondary fiber M or the tertiary fiber S had insignificant influence.

  - For a fiber amount ≥ 100 kg/m³, the beneficial effect of the primary fiber L tended to be less evident and the SFRCs with high proportions of the secondary and/or tertiary fibers (M and S) exhibited even slightly higher maximum stress.

- For both area ratios investigated (R = 9 and 4), the stress ratio and the difference of stress ratios between the plain and fiber concretes increased progressively with the increase of fiber content. Basically, for a given fiber amount, the variation in the fiber type exerted no considerable effect.

- For a certain area ratio, the fiber concentration and combination had no impact on the stiffness of the stress-longitudinal displacement curves in the pre-peak stage; however, it had great influence on the post-cracking ductility.
  - Despite the increase in the maximum load-bearing capacity, the post-cracking ductility of SFRC could hardly be improved to an appreciable extent either by simply increasing the fraction of long end-hooked macrofibers L (rather impossible due to the workability and compactability problems) or by even using fiber reinforcement with three different fiber types without any consideration of adjusting and tailoring the concentration and combination of steel fibers as well as their individual crack bridging abilities to the properties of the concrete matrix.

  - Through an optimization process, a so-called synergistic effect of hybrid fiber reinforcement was achieved by the SFRCs with relatively high fiber contents (≥100 kg/m³) containing both long hook-ended macrofibers L with a base content of 60 kg/m³ and straight microfibers S with a minimum concentration of 40 kg/m³.

- The fiber concentration and combination influenced the failure pattern of SFRC to varying degrees.
  - At a low fiber content (40 kg/m³), the crack pattern was characterized by continuous cracking, while with further fiber incorporation (≥ 60 kg/m³), the downward crack propagation was effectively inhibited, and particularly effective when adding high proportions of long end-hooked macrofibers L.

  - From a fiber amount of 100 kg/m³, increased concrete damages were observed principally due to the superior post-cracking ductility till the predefined test end. However, for a given fiber concentration, the variations in the fiber type did not make a noticeable difference in the crack patterns.

### 4.2.5 Influence of fiber orientation

As has been extensively discussed in the previous sections, the orientation of steel fibers in concrete, which can be influenced by a variety of factors, has great impact on the mechanical properties of SFRC under various loading situations. In this test series, the orientation of steel fibers has been intentionally manipulated through varying the type of mold (lying or standing mold), the method of vibrating (vibrating table or internal vibrator) and the direction of sampling (parallel or perpendicular to casting direction), as explicitly described in Table 3.12 in Section 3.5. Besides the monofiber reinforcement (L60), a hybrid fiber reinforcement (L60S60) was also applied to produce the high-strength SFRC prisms (d150: 150 x 150 x 300-mm). These SFRC specimens were loaded concentrically with two area ratios of 9 and 4. The SFRC prisms produced in the standing molds and compacted with vibrating table were regarded as the standard prisms (e.g. test groups L60_9, L60_4 and L60S60_9, L60S60_4).

**Fiber orientation and concentration**

The orientation and concentration of steel fibers in the SFRC prisms strengthened with the monofiber reinforcement L60 were determined with the BSM100 device. The fiber content was uniformly 60 kg/m³ (L fiber: RC-80/60-BN). The measurements were consistently conducted on the sawed 150-mm cube corresponding to the half of the tested prism adjacent to the load introduction point. The results of fiber concentration are demonstrated in Figure 4.37. The data for fiber orientation are presented by percentage values with respect to the load direction in Figure 4.38.

As can be seen in Figure 4.37, the mean values of fiber content in the SFRC specimens produced with various methods differentiated insignificantly to each other, implying a proper mixing, placing and compacting of the SFRC mixtures throughout the experiments. Hence, the fiber orientation should be the only predominant factor influencing the load-bearing and fracture behavior of the SFRCs.

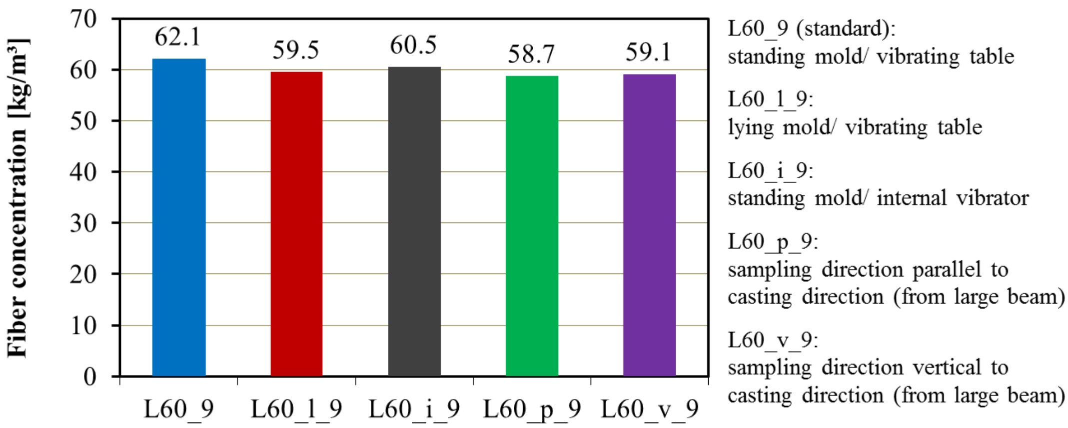


*Figure 4.37: Fiber concentration in the SFRC prisms manufactured with various production processes*

In terms of fiber orientation, for the prisms produced in the lying molds (Figure 4.38, L60_l_9), 45.8% of the steel fibers were oriented parallel to the loading direction, i.e. 20.7% more than the corresponding value of the prisms cast in the standing molds (L60_9, 25.1%). Thus, fewer fibers (L60_l_9, 37% + 17.2% = 54.2%) were aligned to the directions of the tensile stresses (i.e. perpendicular to the loading direction), compared to the prisms cast in the standing molds (L60_9, 38.7% + 36.2% = 74.9%). Note that, in the first case the fiber orientation was highly non-uniform in the vertical directions.

Changing the vibration type did not result in a notable difference in the fiber orientation, as clearly shown in Figure 4.38 (L60_9, vibrating table vs. L60_i_9, internal vibrator). It may be due to the relatively small cross-section of the molds (150 x 150-mm) compared with the fiber length (60 mm).

The SFRC prisms sampled parallel to the casting direction from the large beams (L60_p_9) exhibited comparable values of fiber orientation in the three spatial directions with those of the standard prisms (L60_9). A maximum difference of only 4.8% was observed in the load direction (L60_p_9, 20.3% vs. L60_9, 25.1%) or in the directions of the tensile stresses. It implied that the enlarged mold size along with a compaction with internal vibrator did not necessarily lead to a remarkable change in the fiber orientation for the cases investigated here. The fiber orientation in the prisms sampled perpendicular to the casting direction was rather more non-uniform. Although the fiber orientation aligned to the loading direction was similar to that of the test group L60_9 (L60_9, 25.1% vs. L60_v_9, 30.8%) or the total fiber orientation perpendicular to the loading direction (L60_9, 38.7% + 36.2% = 74.9% vs. L60_v_9, 48% + 21.2% = 69.2%), a large difference of about 27% was recorded between the two vertical directions. In this case, the higher value in vertical-1 direction might be caused by a softer consistency of the fresh mixture in conjunction with a possible excessive vibration.

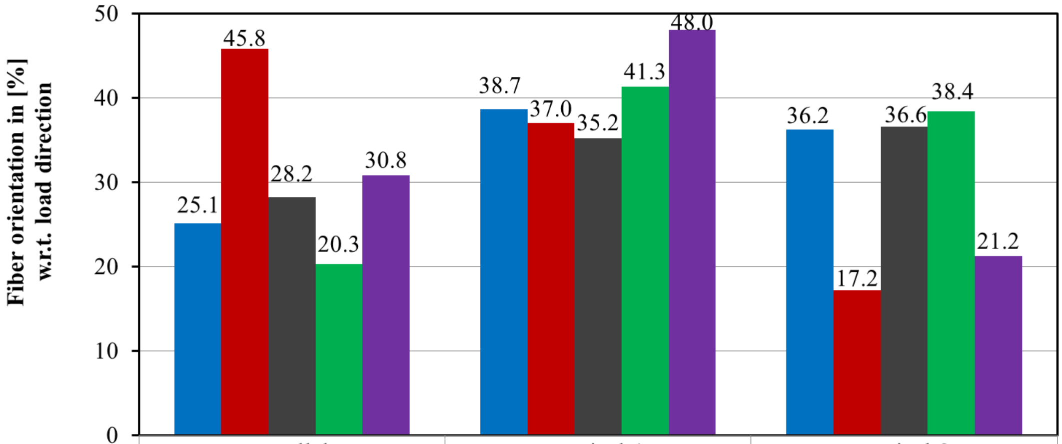


| | parallel | vertical-1 | vertical-2 |
|---|---|---|---|
| L60_9 | 25.1 | 38.7 | 36.2 |
| L60_l_9 | 45.8 | 37.0 | 17.2 |
| L60_i_9 | 28.2 | 35.2 | 36.6 |
| L60_p_9 | 20.3 | 41.3 | 38.4 |
| L60_v_9 | 30.8 | 48.0 | 21.2 |

*Figure 4.38: Fiber orientation with respect to load direction in the SFRC prisms manufactured with various production processes*

**Maximum local compressive stress**

As listed in Table 4.8, the various production processes of the SFRC prisms had obviously marked effect on the maximum load-bearing capacity.

Regarding the influence of mold type (i.e. casting direction), SFRC prisms produced in the lying molds exhibited considerably lower values of $q_{max}$. This phenomenon was independent of the type of fiber reinforcement used, indicating a similar fiber orientation in the prisms produced with the hybrid fiber reinforcement L60S60. Compared to the standing production, an average decrease in $q_{max}$ of about 21% was observed by the lying production with both types of fiber reinforcement (Table 4.8, L60_l vs. L60 and L60S60_l vs. L60S60). The reduction in $q_{max}$ was induced by a preferable fiber orientation with respect to the load direction, in other words, by reduced number of fibers oriented to the directions of the tensile stresses (Figure 4.38).

Varying the type of vibration did not seem to cause any appreciable influence on the $q_{max}$. A maximum reduction in $q_{max}$ of only 3% was documented by using internal vibrator, compared to the use of vibrating table (Table 4.8, L60_i_4 vs. L60_4). This was essentially due to the nearly identical fiber orientation in the three spatial directions.

Compared to the standard prisms (L60), the SFRC prisms sampled parallel (L60_p) or perpendicular (L60_v) to the casting direction from the large beams showed interestingly a nearly same average reduction in $q_{max}$ of about 9%. Between the sampled and standard specimens, the total values of fiber orientation in the directions of the tensile stresses did not differ noticeable with a maximum difference of 5.7% (L60_p_9 = 79.7% vs. L60_9 = 74.9% vs. L60_v_9 = 69.2%). Therefore, the somewhat lower values of $q_{max}$ for the sampled prisms shall be chiefly attributed to the reduced crack-bridging capacity of the cut fibers in the surface-near regions. This may also explain the almost same values of maximum bearing stress between the sampled SFRC prisms, despite a 10.5% difference of fiber orientation in the directions of the tensile stresses (L60_p_9 = 79.7% vs. L60_v_9 = 69.2%).

*Table 4.8: Influence of fiber orientation on the maximum stress $q_{max}$ and stress ratio n*

| **Index** | **Term** | **Area ratio R** | |
|---|---|---|---|
| | | 9 | 4 |
| L60 | $q_{max}$ [MPa] | 214 | 153 |
| | n | 2.45 | 1.75 |
| L60_l | $q_{max}$ [MPa] | 173 | 118 |
| | n | 1.98 | 1.35 |
| | $q_{max}/q_{max,\,L60}$ | 81% | 77% |
| | $\Delta(n-n_{L60})$ | -0.47 | -0.4 |
| L60S60 | $q_{max}$ [MPa] | 266 | 174 |
| | n | 2.82 | 1.95 |
| L60S60_l | $q_{max}$ [MPa] | 201 | 145 |
| | n | 2.13 | 1.54 |
| | $q_{max}/q_{max,\,L60S60}$ | 76% | 83% |
| | $\Delta(n-n_{L60S60})$ | -0.69 | -0.41 |
| L60_i | $q_{max}$ [MPa] | 212 | 149 |
| | n | 2.42 | 1.71 |
| | $q_{max}/q_{max,\,L60}$ | 99% | 97% |
| | $\Delta(n-n_{L60})$ | -0.03 | -0.04 |
| L60_p | $q_{max}$ [MPa] | 200 | 136 |
| | n | 2.28 | 1.56 |
| | $q_{max}/q_{max,\,L60}$ | 93% | 89% |
| | $\Delta(n-n_{L60})$ | -0.17 | -0.19 |
| L60_v | $q_{max}$ [MPa] | 195 | 140 |
| | n | 2.23 | 1.6 |
| | $q_{max}/q_{max,\,L60}$ | 91% | 92% |
| | $\Delta(n-n_{L60})$ | -0.22 | -0.15 |

Noticeably, no distinct correlation between the stress reduction rate $q_{max}/q_{max,\,L60}$ or $q_{max}/q_{max,\,L60S60}$ and area ratio n was observed. In spite of the influence of fiber orientation on the $q_{max}$, the stress ratio n decreased with the decrease of area ratio (Figure 4.39). Regarding the difference of stress ratios $\Delta(n-n_{L60})$ or $\Delta(n-n_{L60S60})$, for a given area ratio a large variation was only found for SFRC specimens cast with different mold types (L60_l vs. L60 and L60S60_l vs. L60S60). Changing the vibration type (L60_i vs. L60) or the sampling direction (L60_p vs. L60_v) did not affect the corresponding values notably (Figure 4.39).

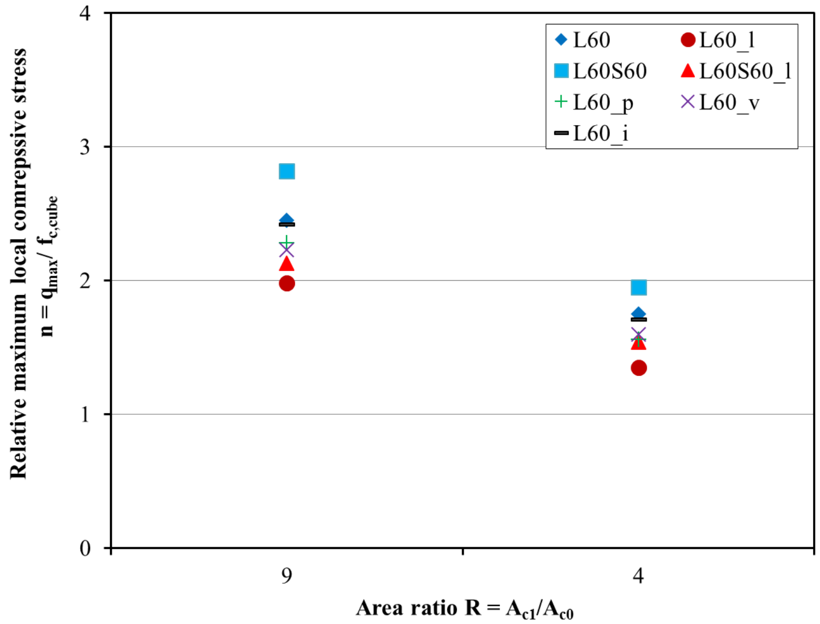


*Figure 4.39: Influence of fiber orientation on the stress ratio n at the area ratios of 9 and 4*

**Stress versus displacement response**

The stress versus longitudinal displacement responses of the SFRC prisms manufactured with various production methods are depicted in Figure 4.40 - Figure 4.43 for both area ratios of 9 and 4. For a given area ratio, the stiffness in the pre-peak branch of the curves was nearly identical amongst the SFRC specimens, independent of the production processes applied.

As is well known, steel fibers aligned to the acting direction of the tensile stresses have the best crack-bridging capacity. For the cases studied here, the tensile stresses were along directions perpendicular to the loading direction. As previously stated, a preferential fiber orientation towards the loading direction was observed by the lying production.

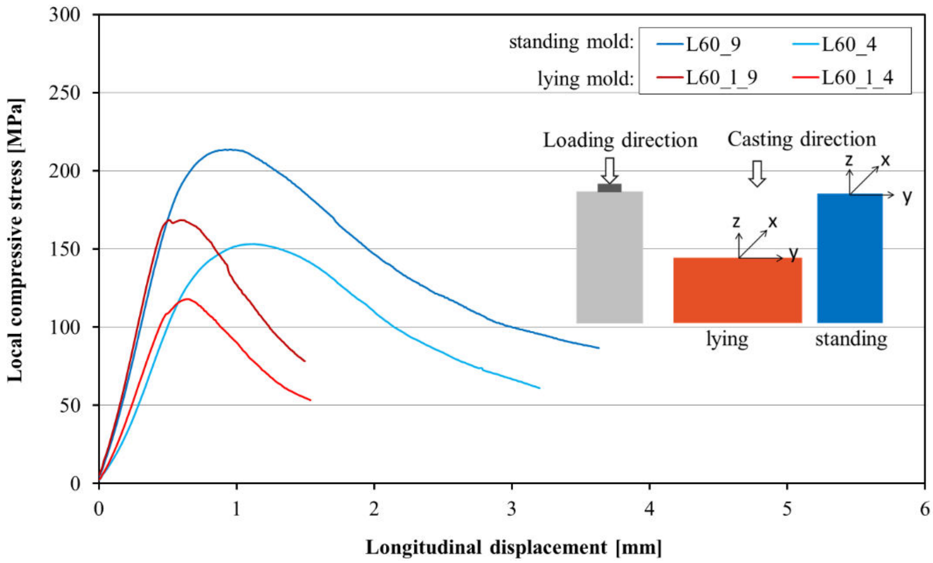


*Figure 4.40: Average local compressive stress versus longitudinal displacement curves of SFRC prisms with reinforcement L60 in the standing and lying (l) molds loaded at the area ratios of 9 and 4*

Thus, from the curves in Figure 4.40, it is evident that the specimens produced in the lying molds (L60_l_9 and L60_l_4) exhibited, as expected, significantly lower overall load-bearing capacity, compared to the prisms cast in the standing molds (L60_9 and L60_4). Beyond the elastic behavior stage of the curves (i.e. linear ascending branch), the stress reached its maximum value quite rapidly indicating a very short stress transmission period (i.e. plastic behavior stage), in which the microcracks initiated and the fibers were activated. Moreover, soon after the peak stage, a remarkably steep stress drop was clearly to see, implying a much less ductile post-cracking behavior. And this adverse effect was independent of the area ratios used. Apparently, the low load-bearing capacity and the inferior post-cracking ductility of the SFRC prisms produced in the lying molds were essentially attributed to the fewer number of fibers aligned to the acting direction of the tensile stresses and the highly non-uniform fiber orientation (Figure 4.38). The initial cracking shall occur on the plane (i.e. specimen surfaces) that contained insufficient number of fibers oriented towards the directions of the tensile stresses.

A similar phenomenon was also found for the specimens produced with the hybrid fiber reinforcement L60S60 (Figure 4.41). As above mentioned, in this case the stress reduction rate due to varied mold type was similar with that of SFRC prisms produced with the monofiber reinforcement L60. However, the stress decline after the peak stage due to the preferable fiber orientation was much more pronounced, in particular distinct at the high area ratio of 9 (L60S60_l_9 vs. L60S60_9). This may be due to the joint effect induced by using two types of steel fiber both exhibiting a preferential fiber orientation in the concrete prism.

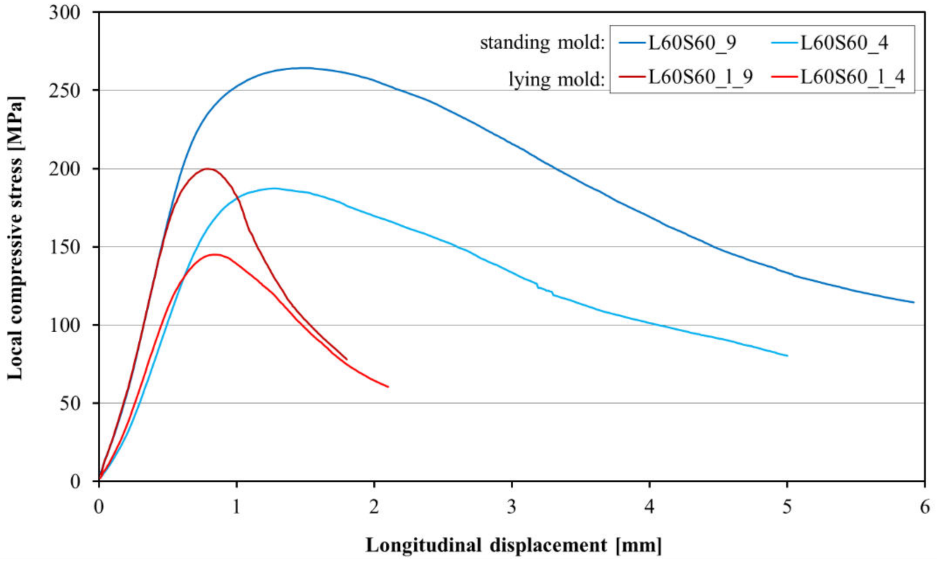


*Figure 4.41: Average local compressive stress versus longitudinal displacement curves of SFRC prisms with reinforcement L60S60 in the standing and lying (l) molds loaded at the area ratios of 9 and 4*

As illustrated in Figure 4.42, the shape of the average stress versus displacement curves of the SFRC samples compacted by various vibrating methods did not differ noticeably from each other, especially at the area ratio of 9 (L60_i_9, internal vibrator vs. L60_9, vibrating table). In both cases, the casting direction was aligned to the loading direction. As noted before, this effect was principally attributed to the nearly identical orientation of steel fibers in the three spatial directions in the SFRC prisms.

Despite the relatively lower values of $q_{max}$, the SFRC prisms sampled parallel to the casting direction showed somewhat comparable shapes of the average stress versus displacement curves with the standard SFRC prisms at both area ratios tested (e.g. Figure 4.43, L60_p_9 vs. L60_9). In both cases, the casting direction or sampling direction was constantly aligned to the loading direction. The similar curve courses, especially beyond the peak stage, were essentially due to the nearly identical orientation of steel fibers in the three spatial directions, as presented in Figure 4.38.

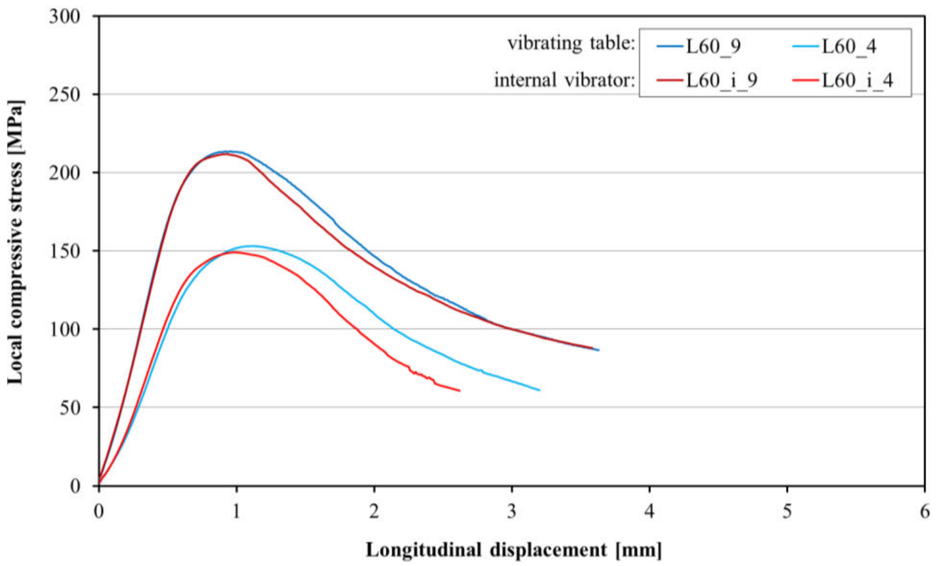


*Figure 4.42: Average local compressive stress versus longitudinal displacement curves of SFRC prisms compacted with vibrating table and internal vibrator (i) loaded at the area ratios of 9 and 4*

Interestingly, the prisms sampled perpendicular to the casting direction exhibited a sharp stress fall shortly after the peak stage (Figure 4.43, L60_v_9 and L60_v_4), although the values of $q_{max}$ were almost same with those of the prisms sawed parallel to the casting direction (L60_p_9 and L60_p_4) and only modestly lower (8.5%) than those of the standard prisms (L60_9 and L60_4). In this test group, the casting direction was perpendicular to the loading direction (i.e. sampling direction). As stated above, the total percentage values of fiber orientation in the directions of the tensile stresses were similar with those in the standard prisms. Therefore, the steep stress drop observed here in the post-cracking stage shall be accounted for by the large difference in the fiber orientation between the two vertical directions (Figure 4.38, L60_v_9, vertical-1: 48% vs. vertical-2: 21.2%).

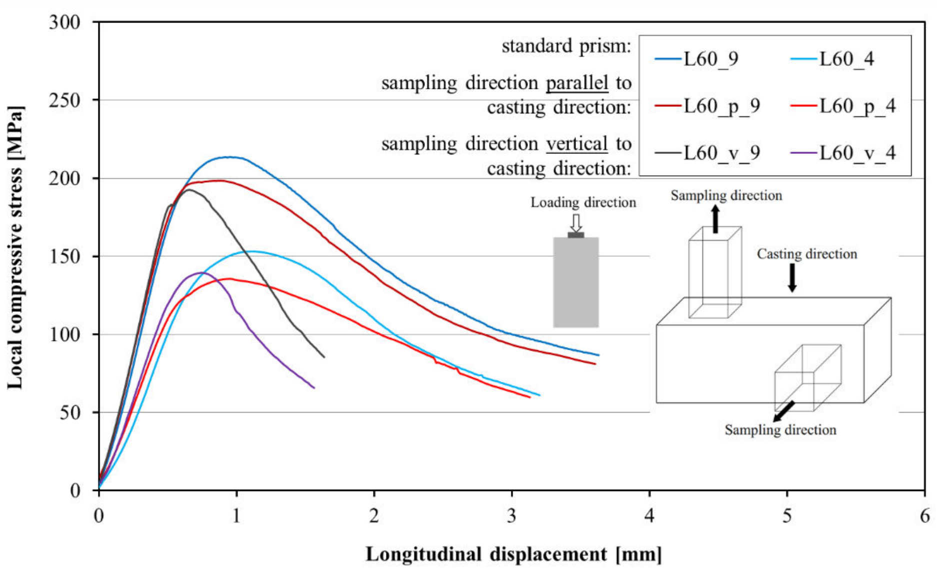


*Figure 4.43: Average local compressive stress versus longitudinal displacement curves of SFRC prisms (reinforcement L60) sampled parallel (p) and vertical (v) to the casting direction loaded at the area ratios of 9 and 4, compared with the standard SFRC prisms*

The average stress versus lateral deformation curves of the SFRCs produced with various production processes reflected basically the similar characteristics as observed by the stress versus longitudinal displacement curves. In general, the SFRC prisms produced in the lying molds or sampled perpendicular to the casting direction exhibited significantly low stress level at the initial cracking. Moreover, with growing crack width (i.e. lateral deformation) the stress fell more sharply, especially in the case of high area ratio and/or hybrid fiber reinforcement (Figure 4.44). Some representative curves are summarized in Appendix A.

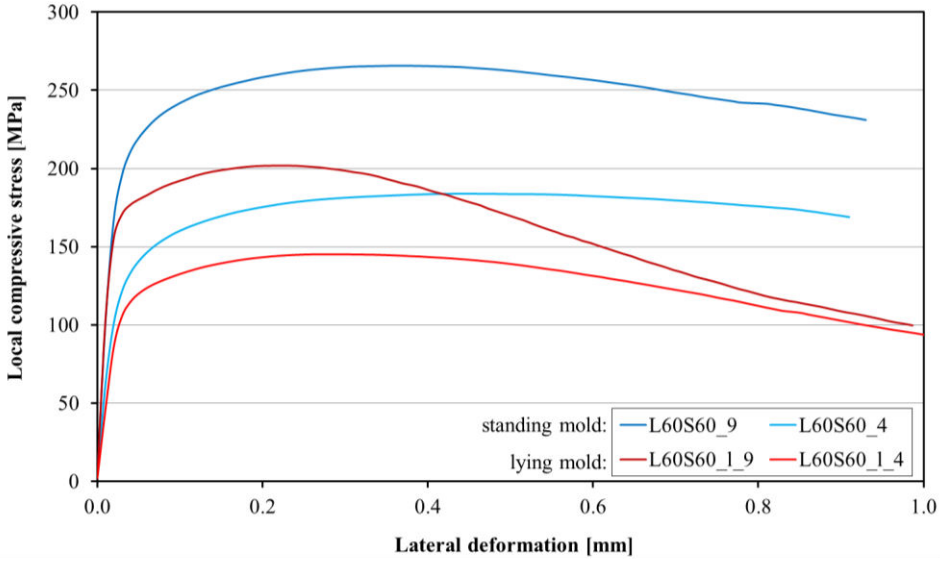


*Figure 4.44: Average local compressive stress versus lateral deformation curves of SFRC prisms produced with reinforcement L60S60 in the standing and lying (l) molds at the area ratios of 9 and 4*

In terms of the average midpoint longitudinal compressive deformations at $q_{max}$, the prisms cast in the lying molds or sampled perpendicular to the casting direction exhibited comparatively slightly lower values, indicating a somewhat weak deformability under localized compression (Table B.8, Appendix B).

**Failure and crack characteristics**

Some representative samples of the tested SFRC prisms manufactured with various production methods are shown in Figure 4.45 and Figure 4.46. As expected, all the SFRC specimens showed a more or less ductile fracture behavior; however, the crack pattern differed among each other considerably.

In the case of standing production (with vibrating table), the formation of cracks on the testing surface was random. Generally, the cracks spread approximately to the half-height of specimen at the area ratio of 9 (Figure 4.11, L60_9). With decreasing area ratio, concrete damages (i.e. cracking and spalling) tended to increase and propagate downwards to the lower half of specimen. A similar crack pattern was also observed by the specimens compacted with internal vibrator in the standing molds and the prisms sampled parallel to the casting direction from the large beams (Figure 4.45, L60_p_9 and L60_p_4).

For the specimens cast in the lying molds (Figure 4.46), the crack pattern was basically characterized by two main cracks spreading through the loaded surface along the x-axis and the lateral surfaces parallel to y-z plane, where fewer fibers were aligned to the directions of the tensile stresses (i.e. along z-direction = casting direction). For the cases investigated here, this typical crack pattern was evidently independent of the area ratio and the type of fiber reinforcement. Furthermore, the concrete damages did not seem to essentially deteriorate with the decrease of area ratio. A similar crack pattern was also found for the prisms sampled perpendicular to the casting direction from the large beams (Figure 4.45, L60_v_9 and L60_v_4).

*L60_p_9 L60_p_4 L60_v_9 L60_v_4*

*Figure 4.45: Typical failure patterns of SFRC specimens sampled parallel (p) and vertical (v) towards the casting direction from the large beams loaded at the area ratios of 9 and 4*

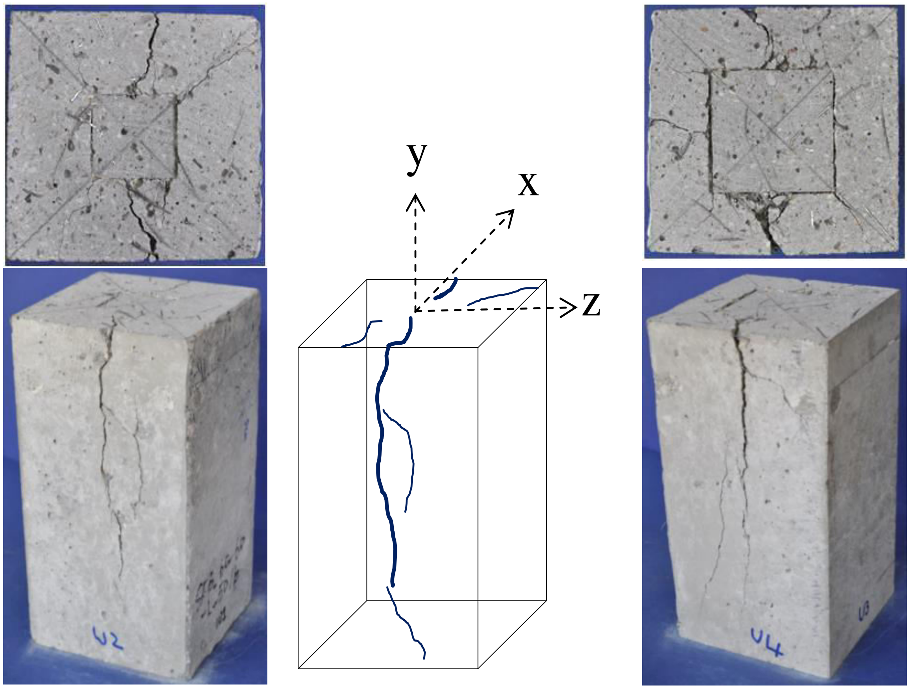


*L60_l_9 crack distribution L60_l_4*

*Figure 4.46: Typical failure patterns of SFRC specimens produced in the lying (l) mold loaded at the area ratios of 9 and 4*

For a certain area ratio the average crack number of the SFRCs manufactured with various production processes differed from each other unnoticeably (Table B.9, Appendix B). The mean values of crack number were in the range from 7.0 to 10.7. And no direct correlation can be established amongst the test groups. Concerning the average values of maximum crack width, the SFRCs produced in the lying molds (L60_l) or sampled perpendicular to the casting direction (L60_v) exhibited a relatively smaller crack opening mainly due to the premature failure induced by the unfavorable fiber orientation, as above pointed out.

**Summary**

In this sub-section, the concentration and orientation of steel fibers in the SFRC prisms (d150: 150 x 150 x 300-mm) manufactured with various production processes have been determined. The influence of fiber orientation on the load-bearing and fracture behavior of SFRC loaded concentrically with two different area ratios of 9 and 4 has been discussed.

On the basis of the experimental data obtained, the following relevant conclusions can be drawn:

- The methods applied here for the production of test prisms had inappreciable impact on the fiber content (or distribution) in the SFRC prisms, indicating a proper mixing, placing and compacting of the SFRC mixtures throughout the experiments; however, it had different influences on the fiber orientation.
  - Varying the mold type (i.e. casting direction, 150 x 150 x 300-mm) led to a preferential fiber orientation with respect to the loading direction as observed by the SFRC prisms cast in the lying molds (L60_l_9, 45.8% : 37.0% : 17.2% = load direction : transverse direction-1 : transverse direction-2), compared to the samples produced in the standing molds (standard prism, L60_9, 25.1% : 38.7% : 36.2%). In other words, fewer number of fibers (-20.7%) oriented in the directions of the tensile stresses and rather highly non-uniformly with a difference of 19.8%.

  - For the cases studied here, the enlarged dimension of specimen mold (300 x 300 x 800-mm) did not necessarily result in a noticeably different fiber orientation in the sawed SFRC specimens (150 x 150 x 300-mm, for a sampling direction parallel to the casting direction, L60_p_9, 20.3% : 41.3% : 38.4%) in comparison with the standard prisms (L60_9, 25.1% : 38.7% : 36.2%), when the casting and loading directions were consistent. However, if the sampling direction was perpendicular to the casting direction, a remarkably inhomogeneous fiber orientation in the two transverse directions of the tensile stresses occurred with a difference of 26.8% (L60_v_9, 30.8% : 48.0% : 21.2%).

- The production processes used here exerted quite diverse effects on the maximum local compressive stress $q_{max}$ and the stress ratio n; however, it had no influence on the decreasing tendency of maximum stress as a result of reducing area ratio.
  - Due to the reduced number of fibers towards the directions of the tensile stresses (-20.7%), the SFRC prisms cast in the lying molds exhibited considerably lower maximum load-bearing capacity with an average stress reduction of 21% than the specimens produced in the standing molds. The value of the stress reduction rate was independent of the type of fiber reinforcement (L60 or L60S60) and the area ratio (9 or 4).

  - Compared to the standard prisms, owing to the similar total amount of fibers aligned to the directions of the tensile stresses (L60_p_9 = 79.7% vs. L60_9 = 74.9% vs. L60_v_9 = 69.2%), the SFRC prisms sampled parallel or perpendicular to the casting direction showed an almost same slight decrease in the maximum stress of about 9%. The somewhat reduced ultimate load-bearing capacity may be primarily attributed to the reduced crack-bridging capacity of the cut fibers in the surface-near zones.

- The various production processes had no influence on the stiffness of the stress-longitudinal displacement curves in the pre-peak zone; however, it had great impact on the post-cracking ductility.
  - In contrast to the SFRC prisms cast in the standing molds, the SFRC specimens produced in the lying molds showed a remarkably inferior ductility characterized by a steep stress drop beyond the peak stage at both area ratios of 9 and 4.

  - Despite the slightly lower maximum stress, the SFRC prisms sampled parallel to the casting direction exhibited comparable stress-displacement responses with the standard prisms at both area ratios tested (R = 9 and 4). This was essentially due to the similar fiber orientation in the three spatial directions. The SFRC prisms sampled perpendicular to the casting direction showed a sharp stress fall beyond the peak stage basically due to the highly non-uniform fiber orientation in the two transverse directions of the tensile stresses.

- Changing the vibration type did not cause appreciable effects on fiber orientation, maximum local compressive stress and stress-displacement response for the small SFRC specimens tested here.

- Depending on the method of specimen production (consequently fiber orientation), the SFRC prisms exhibited varying failure patterns.
  - The SFRC samples compacted with internal vibrator in the standing molds or taken parallel to the casting direction shared generally the same failure patterns of the standard prisms due to a similar fiber orientation in the three spatial directions.

  - For the prisms cast in the lying molds or sampled perpendicular to the casting direction, the crack pattern was basically characterized by continuous longitudinal propagation of two individual major cracks on the lateral surfaces, where fewer fibers were aligned to the directions of the tensile stresses. Moreover, the concrete damages did not seem to deteriorate with the decrease of area ratio. Crack pattern of this kind was evidently independent of the area ratio and the type of fiber reinforcement used.

### 4.2.6 Influence of eccentricity of load

As stated previously, the eccentricity of load is one of the most principal factors influencing the load-bearing behavior of concrete under concentrated load. In the past, a great number of tests have been conducted to study the behavior of concrete under concentric load introduction. Only few attentions have been paid to the case of eccentric load introduction (e.g. Hawkins 1968 and Niyogi 1973 for plain concrete). However, from the practical point of view, the concentric load introduction is rather a special case, since the uniaxial or biaxial eccentric load introduction is more common. Hence, in this test series, the standard fibrous and non-fibrous high-strength concrete prisms (d150) have been tested under various eccentricities of load with two different area ratios of 9 and 4. In addition to the monofiber reinforcement L60, two types of hybrid fiber reinforcement (L60S60 and L40M40S40) were used to study the effect of the variations of fiber reinforcement.

**Maximum local compressive stress**

For comparison purposes, the mean values of $q_{max}$ of the concentric loading cases are listed with the results of eccentric loading tests in Table 4.9 and Table 4.10. As can be seen from the tables, both plain and fiber concrete samples tested under concentric load exhibited the highest values of $q_{max}$ for a given area ratio. With increasing eccentricity of load, the $q_{max}$ of both concretes decreased progressively. This effect was also reported by Hawkins (1968) and Niyogi (1973) for plain concrete.

*Table 4.9: Influence of eccentricity of load on the maximum stress $q_{max}$ and stress ratio n for the area ratio of 9*

| Index | Term | Eccentricity of load | | | | |
|---|---|---|---|---|---|---|
| | | concentric | e = 15 mm (e15) | e = 30 mm (e30) | edge loading (E) | corner loading (C) |
| | | Area ratio R | | | | |
| | | 9 | | | | |
| PC | $q_{max}$ [MPa] | 152 | 144 | 135 | 113 | 83 |
| | $q_{max, con.}/q_{max, ecc.}$ | 100% | 95% | 89% | 74% | 55% |
| | n | 1.8 | 1.7 | 1.6 | 1.34 | 0.98 |
| L60 | $q_{max}$ [MPa] | 214 | 204 | 185 | 141 | 110 |
| | $q_{max, con.}/q_{max, ecc.}$ | 100% | 95% | 86% | 66% | 51% |
| | $q_{max, fiber}/q_{max, plain}$ | 141% | 142% | 137% | 125% | 133% |
| | n | 2.45 | 2.33 | 2.11 | 1.61 | 1.26 |
| | $\Delta(n_{fiber}-n_{plain})$ | 0.65 | 0.63 | 0.51 | 0.27 | 0.28 |
| L60S60 | $q_{max}$ [MPa] | 266 | 234 | 193 | 161 | 110 |
| | $q_{max, con.}/q_{max, ecc.}$ | 100% | 88% | 73% | 61% | 41% |
| | $q_{max, fiber}/q_{max, plain}$ | 175% | 163% | 143% | 142% | 133% |
| | n | 2.82 | 2.48 | 2.04 | 1.7 | 1.17 |
| | $\Delta(n_{fiber}-n_{plain})$ | 1.02 | 0.78 | 0.44 | 0.36 | 0.19 |
| L40M40S40 | $q_{max}$ [MPa] | 273 | | | 172 | 117 |
| | $q_{max, con.}/q_{max, ecc.}$ | 100% | | | 63% | 43% |
| | $q_{max, fiber}/q_{max, plain}$ | 180% | | | 152% | 141% |
| | n | 2.89 | | | 1.82 | 1.27 |
| | $\Delta(n_{fiber}-n_{plain})$ | 1.09 | | | 0.48 | 0.29 |

It should be noted that the stress reduction was particularly evident at extremely large eccentricities (i.e. edge or corner loading), indicating a drastic decrease in the confining effect of the surrounding non-loaded concrete. And this phenomenon was more pronounced at the large area ratio of 9. For example, under edge loading (E) with the area ratio of 9, a reduction in $q_{max}$ of 34% was recorded by the test group L60_9_E and 26% by PC_9_E (Table 4.9), while at the area ratio of 4 the corresponding values were 23% by L60_4_E and 12% by PC_4_E (Table 4.10).

The SFRCs, especially strengthened with hybrid fiber reinforcement, exhibited considerably higher ultimate load-bearing capacity in all the cases of eccentricity. Depending on the test parameters, the increment in $q_{max}$ due to fiber incorporation ($q_{max, fiber}$/ $q_{max, plain}$) varied from 25% (Table 4.9, L60_9_E) to 63% (Table 4.9, L60S60_9_e15). However, compared to the plain concrete, the fiber concretes, particularly reinforced with hybrid fiber reinforcement, showed a somewhat sharper decline of stress ($q_{max, con.}$/ $q_{max, ecc.}$) with the increase of eccentricity. And this effect became distinct at extremely large eccentricities. For the small eccentricity of 15 mm (e15), a stress decrease of about 5% was observed by PC and L60 for R = 9 and 4, whereas the corresponding values were 12% for R = 9 and 16% for R = 4 by L60S60. Under extremely large eccentricities (i.e. edge or corner loading), the specimens produced with hybrid fiber reinforcement exhibited usually at least 10% higher percentage values of stress reduction, compared to the test groups of plain concrete PC and monofiber reinforcement L60 (Table 4.9, stress reduction under corner loading: PC_9_C = 45% vs. L60_9_C = 49% vs. L60S60_9_C = 59% and Table 4.10, stress reduction under edge loading: PC_4_E = 12% vs. L60_4_E = 23% vs. L60S60_4_E = 32%).

In other words, the effectiveness of fiber reinforcement reduced steadily with growing eccentricity of load. Again, this effect was particularly pronounced at the large area ratio of 9 (e.g. $q_{max, con.}$/ $q_{max, ecc}$ for edge loading in Table 4.9 and Table 4.10). Finally, the reinforcing effect of steel fibers reached the lowest level under corner loading, whereby the variations of fiber reinforcement appeared to exert insignificant influence on the $q_{max}$. This implied that the extreme eccentricity had more predominant influence on the load-bearing capacity of concrete than the variations in the types of fiber reinforcement.

*Table 4.10: Influence of eccentricity of load on the maximum stress $q_{max}$ and stress ratio n for the area ratio of 4*

| **Index** | **Term** | **Eccentricity of load** | | |
|---|---|---|---|---|
| | | concentric | e = 15 mm (e15) | edge loading (E) |
| | | **Area ratio R** | | |
| | | 4 | | |
| PC | $q_{max}$ [MPa] | 104 | 100 | 92 |
| | $q_{max, con.}$/ $q_{max, ecc.}$ | 100% | 96% | 88% |
| | n | 1.23 | 1.18 | 1.09 |
| L60 | $q_{max}$ [MPa] | 153 | 146 | 118 |
| | $q_{max, con.}$/ $q_{max, ecc.}$ | 100% | 95% | 77% |
| | $q_{max, fiber}$/ $q_{max, plain}$ | 147% | 146% | 128% |
| | n | 1.75 | 1.67 | 1.35 |
| | $\Delta(n_{fiber}-n_{plain})$ | 0.52 | 0.49 | 0.26 |
| L60S60 | $q_{max}$ [MPa] | 184 | 154 | 125 |
| | $q_{max, con.}$/ $q_{max, ecc.}$ | 100% | 84% | 68% |
| | $q_{max, fiber}$/ $q_{max, plain}$ | 177% | 154% | 136% |
| | n | 1.95 | 1.32 | 1.17 |
| | $\Delta(n_{fiber}-n_{plain})$ | 0.72 | 0.14 | 0.08 |

The aforementioned joint effects of fiber reinforcement and eccentricity of load on the ultimate load-bearing capacity of the SFRCs can also be observed when analyzing the stress ratio n and the difference of stress ratios $\Delta(n_{fiber}-n_{plain})$ in Table 4.9 and Table 4.10. For a better understanding, the stress ratio n as a function of eccentricity of load is graphically demonstrated in Figure 4.47 and Figure 4.48 for the area ratios of 9 and 4, respectively.

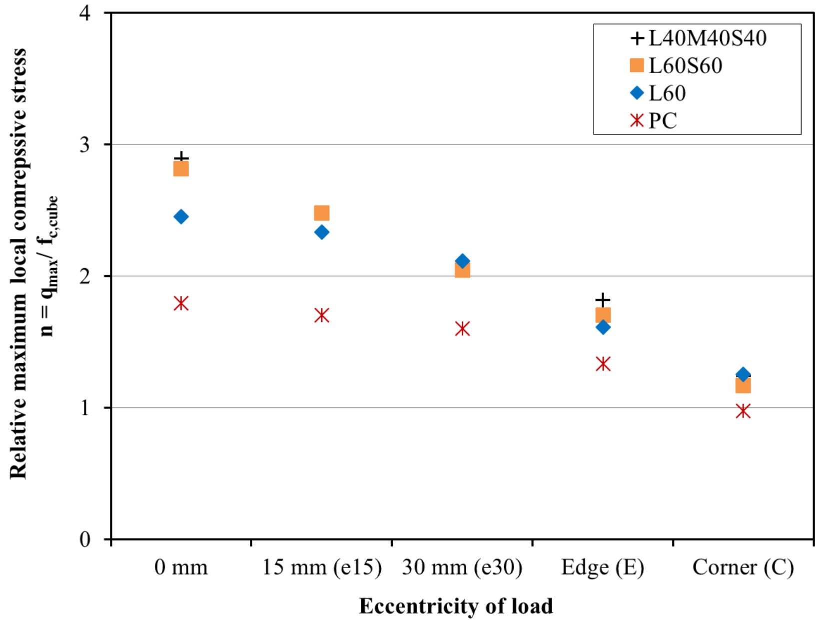


*Figure 4.47: Influence of eccentricity of load on the stress ratio n at the area ratio of 9*

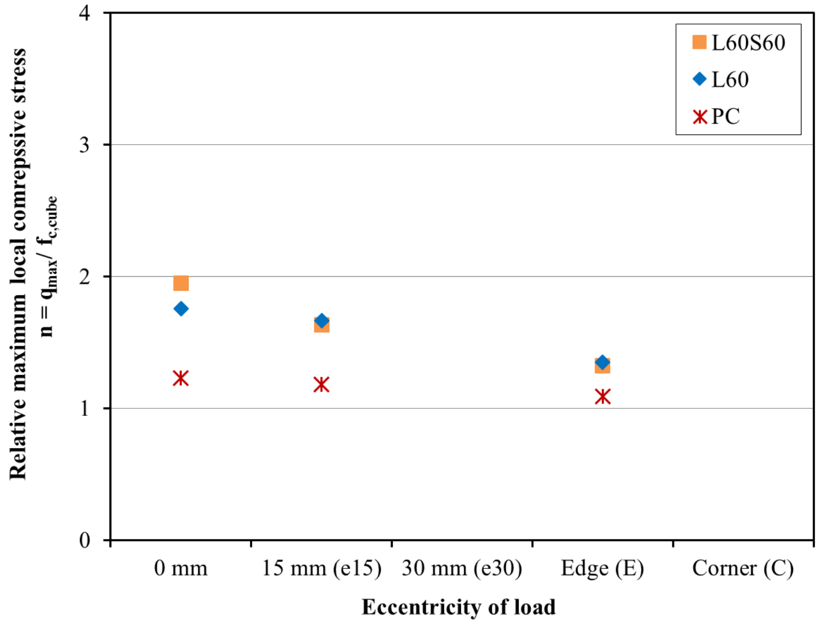


*Figure 4.48: Influence of eccentricity of load on the stress ratio n at the area ratio of 4*

**Stress versus displacement response**

The average stress versus longitudinal displacement curves of the plain and fiber concretes under concentric and eccentric loading are demonstrated in Figure 4.49 - Figure 4.53, showing a decreasing tendency of the stiffness and the load-bearing capacity with the increase of eccentricity of load. Similar to the case of load-bearing capacity, the reduction in stiffness was particularly evident at extremely large eccentricities (i.e. edge and corner loading). For a certain eccentricity of load, the stiffness was nearly identical among the various types of SFRC loaded with the same area ratio.

For small eccentricities up to 30 mm (e30), the curve slope in the pre-peak phase was nearly identical between the plain and fiber concretes at the area ratio of 9 (Figure 4.49). In the case of large eccentricities, the SFRC showed a remarkable stiffer curve slope (i.e. higher stiffness) than the plain concrete (e.g. Figure 4.50, L60_9_C vs. PC_9_C). A similar trend was also found at the area ratio of 4 (Figure 4.51). Shortly after the ultimate stress, the plain concrete, as expected, showed a steep stress drop in all the cases of eccentricity, whereas the fiber concrete (reinforcement L60) exhibited a ductile post-cracking behavior characterized by a gradual stress decline. In the latter case, the stress decreased more noticeably under edge or corner loading, especially at the large area ratio of 9. This marked deterioration in the post-cracking ductility was predominantly due to the strongly decreased confining effect of the non-loaded surrounding concrete at the extreme eccentricities associated with the heavily reduced number of steel fibers bridging across the cracks in the relatively small loaded boundary areas at the high area ratio of 9 (i.e. small bearing plate). In contrast, for the low area ratio of 4 (i.e. large bearing plate), such a remarkable reduction in the post-cracking ductility was not observed under edge loading (Figure 4.51).

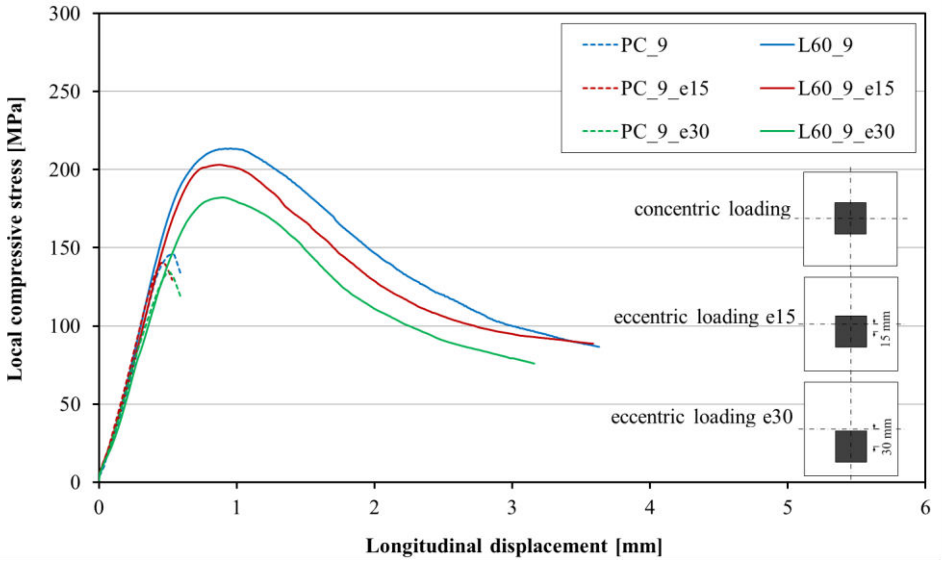


*Figure 4.49: Average local compressive stress versus longitudinal displacement curves of plain concrete (PC) and fiber concrete (reinforcement L60) loaded with small eccentricities at the area ratio of 9*

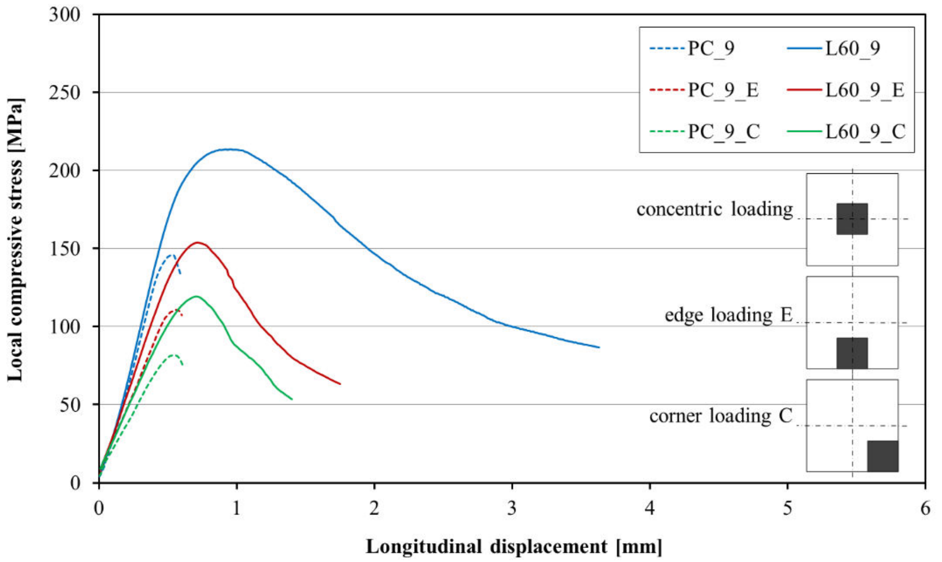


*Figure 4.50: Average local compressive stress versus longitudinal displacement curves of plain concrete (PC) and fiber concrete (reinforcement L60) loaded with large eccentricities at the area ratio of 9*

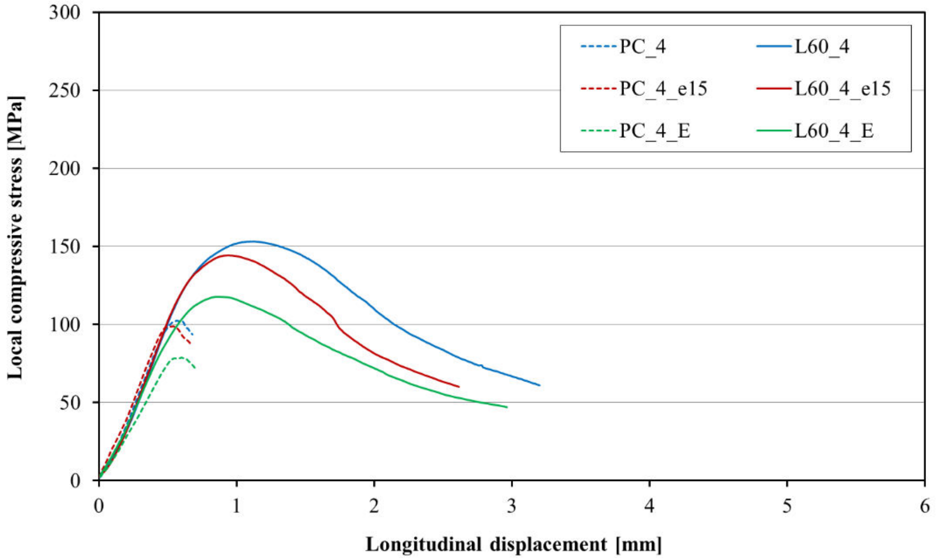


*Figure 4.51: Average local compressive stress versus longitudinal displacement curves of plain concrete (PC) and fiber concrete (reinforcement L60) loaded with various eccentricities at the area ratio of 4*

As discussed in the previous sections, under concentric loading not only the load-bearing capacity but also the post-cracking ductility can be substantially enhanced by using hybrid fiber reinforcement with high volume fraction. As expected, under eccentric loading the concrete prisms produced with hybrid fiber reinforcement (in particular with L60S60) exhibited a much better post-cracking ductility than the specimens reinforced with the monofiber reinforcement L60 (Figure 4.52, Figure 4.53 and Figure A.23, Figure A.24 in Appendix A). Even at extreme eccentricities (i.e. edge or corner loading), the hybrid fiber reinforcement still retained a sufficient post-cracking ductility. Yet, the increase in maximum bearing stress was quite marginal, as observed under corner loading at the area ratio of 9. Noticeably, at the area ratio of 4 no appreciable difference concerning both load-bearing capacity and ductility was found under edge loading (Figure 4.54).

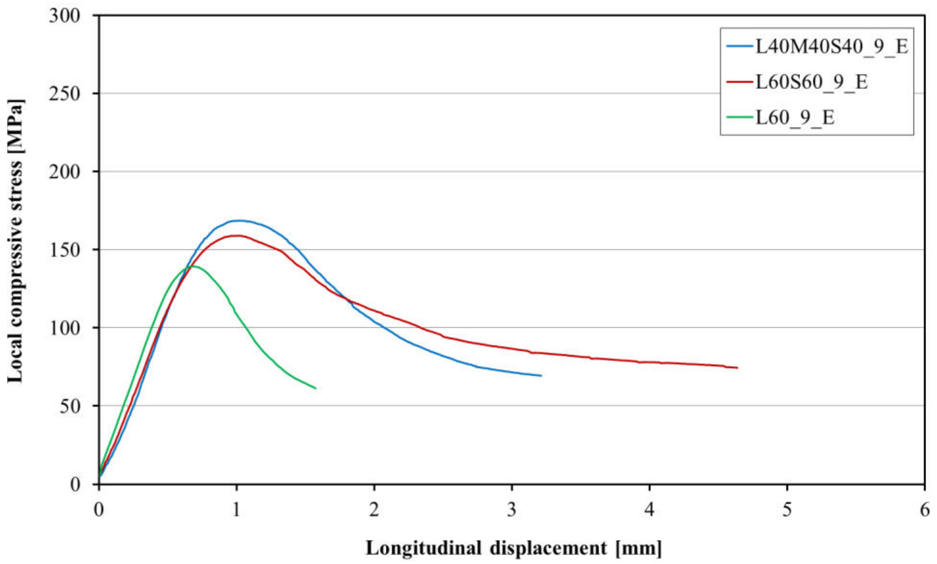


*Figure 4.52: Average local compressive stress versus longitudinal displacement curves of various types of SFRC under edge loading at the area ratio of 9*

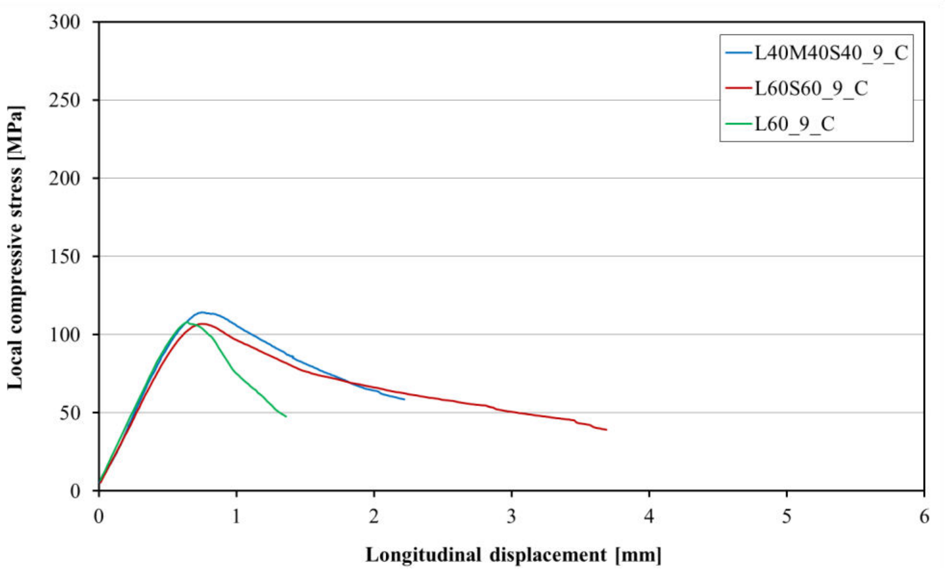


*Figure 4.53: Average local compressive stress versus longitudinal displacement curves of various types of SFRC under corner loading at the area ratio of 9*

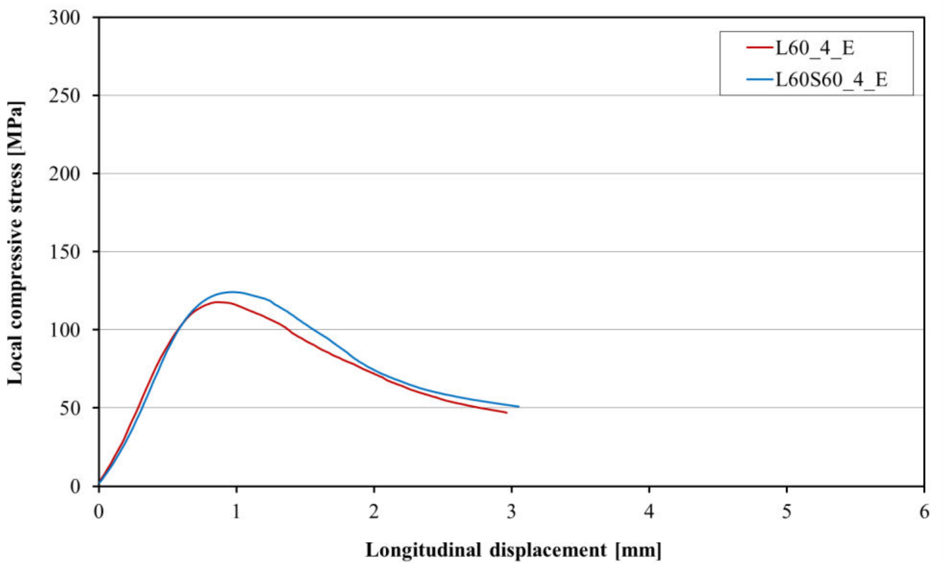


*Figure 4.54: Average local compressive stress versus longitudinal displacement curves of various types of SFRC under edge loading at the area ratio of 4*

In terms of the stress versus lateral deformation responses, the stress level at which the crack initiated basically tended to decrease with the increase of eccentricity of load. However, with growing crack width (i.e. lateral deformation), for both plain and fiber concretes, no evident correlation was observed between the stress decline rate and eccentricity of load. Nonetheless, at the high area ratio of 9, the hybrid fiber reinforcement exhibited a somewhat more gradual stress decline than the monofiber reinforcement under a given eccentricity of load. Some representative curves are given in Appendix A.

**Failure and crack characteristics**

Some representative samples of the failed plain and fiber concrete specimens under eccentric loading are demonstrated in Figure 4.55 - Figure 4.57. Similar to the case of concentric loading, for both plain and fiber concretes, no visible cracking or spalling was observed until shortly before reaching the peak load. Soon afterwards, all the plain concrete specimens failed in a brittle manner in all the cases of eccentricity, whereas the fiber concrete samples exhibited a ductile failure behavior. Under concentric loading the initial cracks developed and spread randomly through either side of the unloaded surface of specimen, while under eccentric loading the cracks developed preferably in the regions closest to the loaded area. Depending on the area ratio and eccentricity, the failure patterns differed significantly.

For the plain concrete specimens loaded eccentrically with the area ratio of 9, severe concrete spalling combined with continuous cracks on the lateral surface adjacent to the load did not appear to occur until reaching an eccentricity of 30 mm (Figure 4.55, PC_9_e30). Under edge loading, in addition to wide continuous cracks, the concrete in the edge zones adjacent to the load was often one-sidedly chipped away almost downwards to the specimen bottom (Figure 4.55, PC_9_E), while under corner loading the prisms remained their integrity and presented a failure pattern with several relatively fine cracks mostly on the lateral surfaces closest to the loaded area (Figure 4.55, PC_9_C).

The severe concrete damages observed on the plain concrete prisms loaded under edge loading can be explained as follows: With increasing eccentricity of load, the bursting tensile stresses in the edge zones adjacent to the load tended to increase (as pointed out previously in Section 2.2), which may lead to concrete damages preferably in these edge regions. Compared to the case of corner loading, due to the comparatively higher tensile stresses in the case of edge loading, the relatively thinner unloaded concrete in the edge zones adjacent to the load was more likely to be damaged.

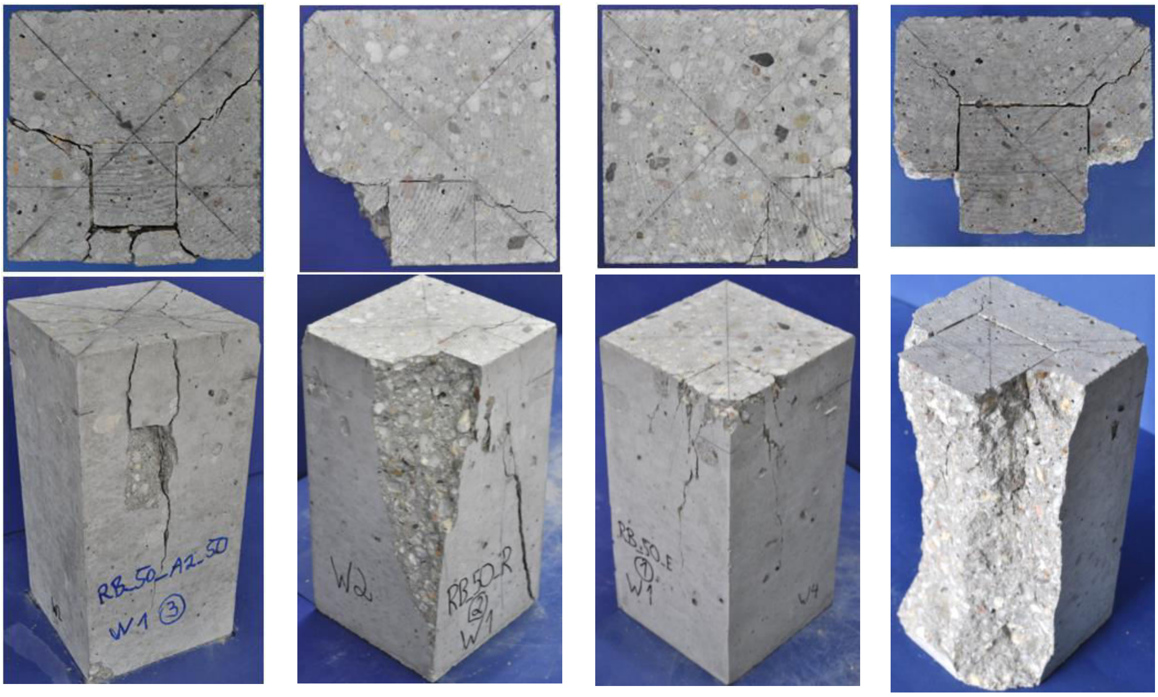


*PC_9_e30* *PC_9_E* *PC_9_C* *PC_4_e15*

*Figure 4.55: Typical failure patterns of high-strength plain concrete specimens loaded eccentrically with the area ratios of 9 and 4*

In the case of low area ratio of 4, a large mass of concrete in the zones closest to the loaded area was punched away completely downwards to the specimen bottom even at the small eccentricity of 15 mm (Figure 4.55, PC_4_e15). This was primarily attributed to the relatively high energy release at failure at low area ratio and the asymmetric stress distributions under eccentric loading (i.e. increased tensile stresses in the zones adjacent to the load).

For the specimens reinforced with the monofiber reinforcement L60, no noticeable difference in failure pattern was observed at the area ratio of 9 between the prisms loaded concentrically and the prisms loaded with the eccentricity of 15 mm (e15). Appreciable concrete damages were found mostly either from an eccentricity of 30 mm (e30) at the area ratio of 9 or at the low area ratio of 4, demonstrating either wide continuous cracks or increased concrete spalling on the lateral surfaces nearest to the load. For specimens loaded on the edge or one corner with the area ratio of 9, relatively fine cracks and minor concrete spalling appeared solely in the region directly beneath the loaded area and no crack propagation through the lateral surface was observed. In these two cases, concrete damages tended to translocate from the testing surface to the lateral surfaces adjacent to the load, typically in the form of increased concrete spalling. As explained above, the relocation of concrete damages should be accounted for by the increased tensile stresses in the edge zones adjacent to the loaded area under extreme eccentric loading. Due to the crack-bridging effect of steel fibers, no serve concrete damages occurred in spite of higher increased tensile stresses, compared to the case of plain concrete.

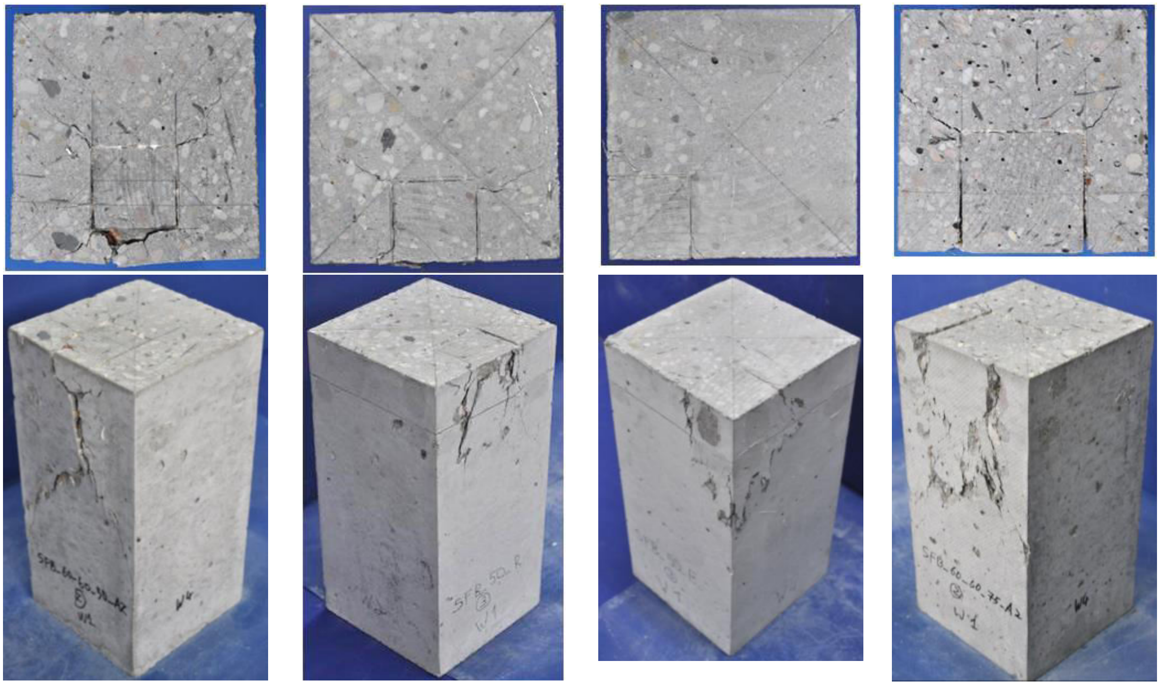

*L60_9_e30* *L60_9_E* *L60_9_C* *L60_4_E*

*Figure 4.56: Typical failure patterns of high-strength SFRC specimens (fiber reinforcement L60) loaded eccentrically with the area ratios of 9 and 4*

In terms of the effect of hybrid fiber reinforcement, despite a much longer test duration (basically due to a superior ductile failure behavior), the failure patterns of specimens tested here were quite similar with those of the prisms manufactured with the monofiber reinforcement L60, however, presented slightly increased crack width and concrete spalling (Figure 4.57).

For both plain and fiber concretes, the average values of crack number on the testing surface decreased steadily with the increase of eccentricity (Table B.10, Appendix B). This effect was independent of the area ratio and the type of fiber reinforcement. A similar tendency was also observed by the mean values of maximum crack width. For a given area ratio and eccentricity of load, concrete prisms made of hybrid fiber reinforcement exhibited few cracks, however, larger crack width, compared to the specimens produced with monofiber reinforcement. Nonetheless, it should be noted that the extent of concrete damages on the lateral surfaces tended to drastically increase with increasing eccentricity.

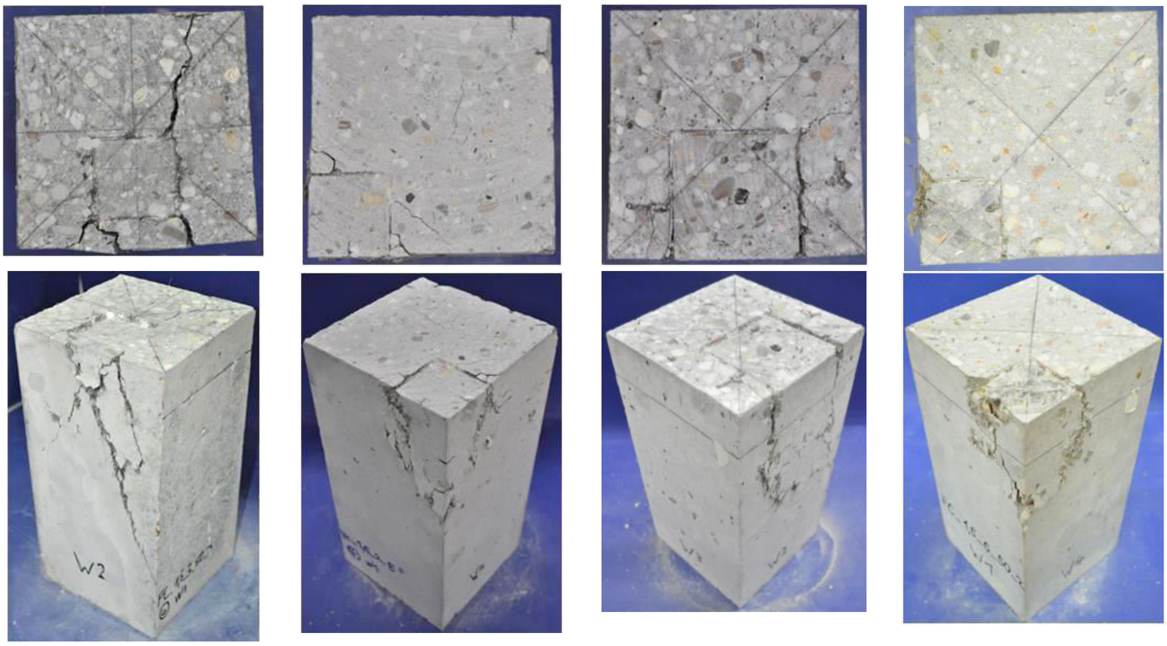

*L60S60_9_e30* *L60S60_9_C* *L60S60_4_E* *L40M40S40_9_C*

*Figure 4.57: Typical failure patterns of high-strength SFRC prisms (fiber reinforcement L60S60 and L40M40S40) loaded eccentrically at the area ratios of 9 and 4*

**Summary**

In this sub-section, the high-strength plain and fiber concrete prisms (d150: 150 x 150 x 300-mm) have been tested under various eccentricities of load with two different area ratios of 9 and 4. The results have been presented and compared with the results obtained from the tests under concentric load introduction.

On the basis of the experimental data obtained, the following conclusions can be drawn:

- With increasing eccentricity of load, for both plain and fiber concretes, the maximum local compressive stress $q_{max}$ and the stress ratio n decreased significantly. At the high area ratio of 9, the stress reduction was more evident and reached its highest level under corner loading with decreases ranging from 45% to 59%, compared to the values obtained from the cases of concentric loading.

- Compared to the plain concrete, the SFRCs generally exhibited larger stress reduction especially under extreme eccentricities. This effect became more pronounced when using hybrid fiber reinforcement. For instance, under edge or corner loading the hybrid fiber reinforcement L60S60 exhibited a maximum 9% higher stress reduction than the monofiber reinforcement L60, and 14-20% higher stress reduction than the plain concrete.

- In all the cases of eccentricity the addition of fibers (60 kg/m³ as monofiber reinforcement and 120 kg/m³ as hybrid fiber reinforcement) improved the maximum load-bearing capacity of concrete markedly with increases varying from 25% to 63%. However, with the increase of eccentricity the reinforcing effectiveness of steel fibers tended to considerably reduce and reached its lowest level under corner loading. Under corner loading, the variations of fiber reinforcement type affected the $q_{max}$ insignificantly, indicating that in this extreme case the load introduction had an overriding influence on the load-bearing capacity of concrete than the type of fiber reinforcement.

- For both plain and fiber concretes, with growing eccentricity the stiffness of the stress-longitudinal displacement curves in the pre-peak stage decreased noticeably. For a given area ratio, the SFRCs showed a remarkable higher stiffness than the plain concrete under large eccentricities (i.e. edge or corner loading), however, no difference amongst each other.

- Under edge or corner loading, the SFRCs produced with the monofiber reinforcement L60 exhibited a marked reduction in the post-cracking ductility, while the hybrid fiber reinforcement (especially L60S60) still remained a superior post-cracking behavior. However, this phenomenon was only observed at the high area ratio of 9. At the low area ratio of 4 the monofiber and hybrid fiber reinforcements showed a similar stress versus displacement response in the post-cracking zone under edge loading.

- Basically, under eccentric loading the initial crack formation and the subsequent crack propagation occurred preferably in the regions closest to the loaded area, while under concentric loading the initial cracks developed and spread randomly through either side of the unloaded surface of specimen.

- The failure pattern of plain concrete depended greatly on the eccentricity of load and area ratio.
  - At the high area ratio of 9, with increasing eccentricity of load concrete damages generally tended to deteriorate from concrete cracking and spalling in a small scale to chipping of concrete in a large scale.

  - At the low area ratio of 4, complete collapse of specimen appeared already at very small eccentricity of 15 mm.

- Through incorporating steel fibers, the magnitude of concrete damages was less influenced by the eccentricity of load.
  - Cracking and spalling of concrete were confined mostly in the small regions directly beneath the loaded area in a small scale.

  - Nonetheless, slightly increased concrete damages were found at the low area ratio of 4 or by specimens reinforced with hybrid fiber reinforcement due to the superior post-cracking ductility.

### 4.2.7 Hybrid concrete system

As previously pointed out, the critical tensile stresses (i.e. bursting stresses) developed in a concrete member subjected to concentrated load distribute in the St. Venant disturbance zone (i.e. in the upper half of the prisms for the cases investigated here) and spread along directions perpendicular to the load. For a given area ratio the variations in the properties of concrete and the types of reinforcement in this region exert certain influence on the magnitude and distribution of the tensile stresses as well as the load-bearing and fracture behavior of concrete, as reported by Schmidt and Fiedler (1993) and Empelmann and Wichers (2009).

The basic concept of this test series was to partially strengthen the concrete specimen with steel fibers in its upper half, instead of a full range of fiber reinforcement. Therefore, hybrid concrete prisms (d150: 150 x 150 x 300-mm) containing both high-strength plain and fiber concretes were cast either in the standing or in the lying (l) wooden molds by means of a “fresh in fresh” concreting technique. Two sorts of fiber reinforcement (L60 and L60S60) with three different thicknesses (z50 = 50 mm, z100 = 100 mm and z150 = 150 mm) were used. These hybrid concrete prisms were loaded either concentrically with two area ratios of 9 and 4 or eccentrically with one area ratio of 9 under the same testing conditions applied for the plain and fully reinforced concrete prisms (with reinforcement thickness of 300 mm).

**Maximum local compressive stress**

The mean values of ultimate local compressive stress $q_{max}$ of hybrid concrete prisms are summarized in Table 4.11 - Table 4.13 for the concentric and eccentric loading cases. As a comparison, the results of the plain and fully reinforced concrete specimens are also listed in the tables.

*Table 4.11: Influence of incorporation of fiber reinforcement on the maximum stress $q_{max}$ for the case of concentric load introduction*

| Index | Thickness of fiber reinforcement [mm] | Area ratio R | | | | | |
|---|---|---|---|---|---|---|---|
| | | 9 | | | 4 | | |
| | | $q_{max}$ | $\Delta q_{max}$ | $\Delta q_{max}/z_{FR}$ [MPa/ cm] | $q_{max}$ | $\Delta q_{max}$ | $\Delta q_{max}/z_{FR}$ [MPa/ cm] |
| PC | 0 | 152 | - | - | 104 | - | - |
| L60_z50_l | 50 | 160 | 5.3% | 1.6 | | | |
| L60_z100_l | 100 | 165 | 8.6% | 1.3 | | | |
| L60_z150_l | 150 | 168 | 10.5% | 1.1 | | | |
| L60_l | 300 | 173 | 13.8% | 0.7 | | | |
| L60_z50 | 50 | 157 | 3.3% | 1 | | | |
| L60_z100 | 100 | 194 | 27.6% | 4.2 | 129 | 24% | 2.5 |
| L60_z150 | 150 | 215 | 41.4% | 4.2 | | | |
| L60 | 300 | 214 | 40.8% | 2.1 | 153 | 47.1% | 1.6 |
| L60S60_z50_l | 50 | 158 | 3.9% | 1.2 | | | |
| L60S60_z100_l | 100 | 181 | 19.1% | 2.9 | | | |
| L60S60_z150_l | 150 | 188 | 23.7% | 2.4 | | | |
| L60S60_l | 300 | 201 | 32.2% | 1.6 | | | |
| L60S60_z50 | 50 | 197 | 29.6% | 9 | | | |
| L60S60_z100 | 100 | 247 | 62.5% | 9.5 | 152 | 46.2% | 4.8 |
| L60S60_z150 | 150 | 270 | 77.6% | 7.9 | | | |
| L60S60 | 300 | 266 | 75.0% | 3.8 | 184 | 76.9% | 2.7 |

For the hybrid concrete prisms produced in the standing molds under concentric loading (Table 4.11), the $q_{max}$ increased progressively with increasing reinforcement thickness with increases ($\Delta q_{max}$, relative to the plain concrete) from 3.3% to 77.6% on going from 50 mm to 150 mm thick of fiber reinforcement. The improvement in $q_{max}$ was especially distinct when using optimized hybrid fiber reinforcement (L60S60). In this case, by incorporating a reinforcement layer of merely 50 mm (i.e. 1/6 of the total specimen height), an increase in $q_{max}$ of 29.6% was documented (Table 4.11, L60S60_z50_9 vs. PC_9), implying its significantly high effectiveness in enhancing the ultimate load-bearing capacity. With a reinforcement thickness of 150 mm (i.e. 1/2 of the specimen height), all the hybrid concrete samples exhibited slightly higher mean values of $q_{max}$ than the fully reinforced prisms (Table 4.11, L60_z150_9 vs. L60_9 and L60S60_z150_9 vs. L60S60_9). It indicated that when only considering the ultimate load-bearing capacity, a full range of fiber reinforcement in the entire specimen is not necessary. In terms of the influence of area ratio, the increment in $q_{max}$ due to fiber addition was relatively lower at the low area ratio of 4 than at the high area ratio of 9. This effect was particularly evident when using hybrid fiber reinforcement (Table 4.11, L60S60_z100_9, $\Delta q_{max}$ = 62.5% vs. L60S60_z100_4, $\Delta q_{max}$ = 46.2%).

For the hybrid concrete samples cast in the lying molds, the increase in $q_{max}$ due to fiber incorporation was considerably insignificant ($\Delta q_{max}$ from 5.3% to 23.7%, Table 4.11) compared to that obtained in the standing production. This effect was more distinct for hybrid fiber reinforcement and/or reinforcement thickness ≥ 100 mm. For example, for a fiber reinforcement thickness of 100 mm, the difference of $\Delta q_{max}$ between the standing and lying production was 19% for the monofiber reinforcement L60 (Table 4.11, L60_z100_9 vs. L60_z100_l_9) and drastically increased by 43.4% for the hybrid reinforcement L60S60 (Table 4.11, L60S60_z100_9 vs. L60S60_z100_l_9). As pointed out in Section 4.2.5, this marginal growth in $q_{max}$ was primarily attributed to the preferred fiber orientation with respect to the load direction in the samples cast in the lying molds. Placing the steel fibers (maximum 60 mm in length) in a 50 mm thick layer in the lying molds did not seem to effectively facilitate a preferred fiber orientation perpendicular to the load direction. With a reinforcement thickness of 50 mm, the increase in $q_{max}$ between the standing and lying production was comparable for the monofiber reinforcement L60 (Table 4.11, L60_z50_9 vs. L60_z50_l_9). However, for the hybrid reinforcement L60S60 the value of $\Delta q_{max}$ of prisms cast in the lying molds was 25.7% lower than that of samples cast in the standing molds, primarily due to the joint effect of hybrid fiber reinforcement on the fiber orientation.

A graphic description of the influence of type and thickness of fiber reinforcement as well as mold type (i.e. casting direction) on the $q_{max}$ is given in Figure 4.58. The tendencies above-mentioned can also be clearly seen in the diagram. The effectiveness of fiber reinforcement relative to thickness ($z_{FR}$ in cm) was further analyzed and is depicted in Figure 4.59. For the high area ratio of 9, the effectiveness of fiber reinforcement generally reached its maximum value at 100 mm and tended to decrease with the increase of reinforcement thickness. Apparently, the standing production exhibited marked advantage over the lying production. It is also evident that the hybrid fiber reinforcement L60S60 showed higher effectiveness in improving the $q_{max}$ at all the thickness than the monofiber reinforcement L60, especially for a reinforcement thickness of 50 mm in the standing production.

As discussed in Section 2.2.2, the magnitude and distribution of the bursting tensile stresses (or force) in a concrete member subjected to concentrated load depend essentially upon the area ratio for a given specimen geometry. In not a few literatures (e.g. Mörsch 1924, Grasser & Thielen 1991, Nguyen 2002), the position of the resulting tensile force (i.e. the maximum tensile force), which is commonly used for design of the lateral reinforcement, was roughly determined at a distance approximately equal to the half of specimen width (0.4-0.5d) away from the loaded surface. In the spatial case of concentrated loading (i.e. point loading), the maximum bursting stresses locate closer to the loaded surface than in the plane case. And this tendency becomes more evident with increasing area ratio (Yettram & Robbins

1969, Hiltscher & Florin 1972). Theoretically, the magnitude and position of the maximum tensile stresses (or force) can be calculated using the curves in Figure 2.30 for various area ratios. For the cases studied here, the maximum tensile stresses located approximately at a distance of 4.8 mm (≈ 0.32d, for d = 150 mm) away from the loaded surface for the area ratio of 9. However, the incorporation of a surface-near reinforcement certainly led to a change in the distribution of the tensile stresses and consequently in the position and magnitude of the maximum tensile stresses. Thus, the optimal thickness of fiber reinforcement should be determined individually for every specific case to effectively resist the bursting tensile stresses.

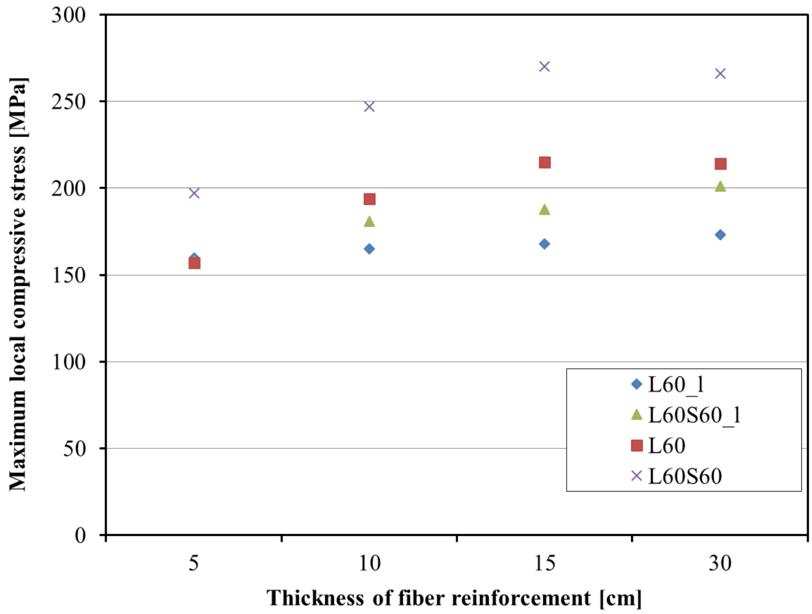


*Figure 4.58: Influence of thickness of fiber reinforcement on the maximum stress $q_{max}$ for the case of concentric load introduction at the area ratio of 9*

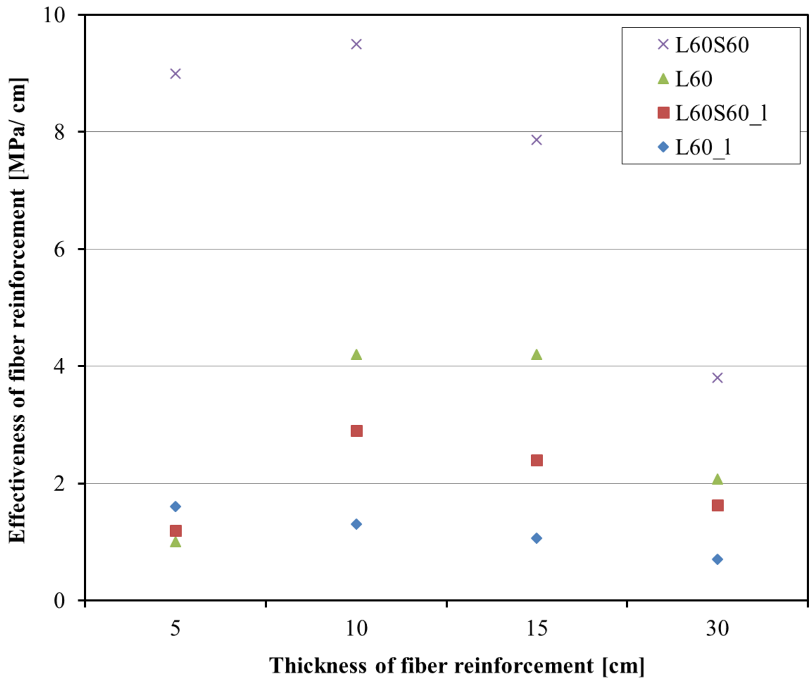


*Figure 4.59: Effectiveness of fiber reinforcement relative to thickness in cm ($\Delta q_{max}/z_{FR}$) for the case of concentric load introduction at the area ratio of 9*

In general, concrete specimens loaded eccentrically showed lower values of $q_{max}$ than specimens loaded concentrically due to the reduction in confining effect of the surrounding unloaded concrete. The load-bearing behavior of the hybrid concrete prisms with a reinforcement thickness of 100 mm (produced in the standing molds) was also consistent with this trend (Table 4.12). The stress reduction rate of the hybrid concrete prisms due to increasing eccentricity ($q_{max, con.}$/ $q_{max, ecc.}$) corresponded well to that of the specimens fully strengthened with the same type of fiber reinforcement (e.g. Table 4.12, L60_z100_9 vs. L60_9 ). For a given eccentricity, hybrid specimens with hybrid fiber reinforcement (L60S60) exhibited a slightly higher reduction rate in comparison with hybrid concrete prisms with monofiber reinforcement (L60).

Compared to the plain concrete, the incorporation of fiber reinforcement layer, in particular with the hybrid fiber reinforcement L60S60, resulted in a remarkable improvement in $q_{max}$ from 14.2% up to 32.5% under edge or corner loading (Table 4.13). Compared to the fully reinforced prisms, the reduction in $q_{max}$ ($q_{max, hyb.}$/ $q_{max, ful.}$) was only up to 11.8% (Table 4.12, L60S60_z100_9_E vs. L60S60_9_E). Furthermore, under corner loading the prisms partially reinforced with the hybrid fiber reinforcement L60S60 had interestingly the same value of $q_{max}$ as those of the fully reinforced samples (Table 4.13, L60S60_z100_9_C vs. L60S60_9_C vs. L60_9_C). The observations made here reflected again the predominant influence of extreme eccentricity on the load-bearing capacity of concrete specimen.

*Table 4.12: Influence of incorporation of fiber reinforcement layer on the maximum stress $q_{max}$ for the case of eccentric load introduction at the area ratio of 9*

| **Index** | **Thickness of fiber reinforcement** [mm] | **Term** | **Eccentricity of load** | | |
|---|---|---|---|---|---|
| | | | concentric | edge loading (E) | corner loading (C) |
| PC_9 | 0 | $q_{max}$ [MPa] | 152 | 113 | 83 |
| | | $q_{max, con.}$/ $q_{max, ecc.}$ | 100% | 74% | 55% |
| L60_z100_9 | 100 | $q_{max}$ [MPa] | 194 | 129 | 100 |
| | | $q_{max, con.}$/ $q_{max, ecc.}$ | 100% | 66% | 51% |
| L60_9 | 300 | $q_{max}$ [MPa] | 214 | 141 | 110 |
| | | $q_{max, con.}$/ $q_{max, ecc.}$ | 100% | 66% | 51% |
| | | $q_{max, hyb.}$/ $q_{max, ful.}$ | 90.7% | 91.5% | 90.9% |
| L60S60_z100_9 | 100 | $q_{max}$ [MPa] | 247 | 142 | 110 |
| | | $q_{max, con.}$/ $q_{max, ecc.}$ | 100% | 58% | 44% |
| L60S60_9 | 300 | $q_{max}$ [MPa] | 266 | 161 | 110 |
| | | $q_{max, con.}$/ $q_{max, ecc.}$ | 100% | 61% | 41% |
| | | $q_{max, hyb.}$/ $q_{max, ful.}$ | 92.9% | 88.2% | 100% |

*Table 4.13: Influence of eccentricity of load on the maximum stress $q_{max}$ of hybrid concrete samples relative to the plain concrete specimens at the area ratio of 9*

| **Index** | **Thickness of fiber reinforcement** [mm] | **Eccentricity of load** | | | | | |
|---|---|---|---|---|---|---|---|
| | | edge loading (E) | | | corner loading (C) | | |
| | | $q_{max}$ | $\Delta q_{max}$ | $\Delta q_{max}$/ $z_{FR}$ [MPa/ cm] | $q_{max}$ | $\Delta q_{max}$ | $\Delta q_{max}$/ $z_{FR}$ [MPa/ cm] |
| PC_9 | 0 | 113 | - | | 83 | - | |
| L60_z100_9 | 100 | 129 | 14.2% | 1.6 | 100 | 20.5% | 1.7 |
| L60_9 | 300 | 141 | 24.8% | 0.9 | 110 | 32.5% | 0.9 |
| L60S60_z100_9 | 100 | 142 | 25.7% | 2.9 | 110 | 32.5% | 1.7 |
| L60S60_9 | 300 | 161 | 42.5% | 1.6 | 110 | 32.5% | 0.9 |

**Stress versus displacement response**

Figure 4.60 - Figure 4.65 illustrate the effects of diverse testing parameters on the stress versus longitudinal displacement responses of the hybrid concrete prisms under concentric and eccentric loading, respectively. For comparison purposes, the corresponding curves of the plain concrete and fully reinforced concrete specimens are plotted in the corresponding diagrams as well. In general, the slope of the curves (i.e. stiffness) in the pre-peak branch was nearly identical for the concrete specimens tested with the same area ratio or eccentricity of load. And it was independent of the type and thickness of fiber reinforcement and the mold type (i.e. casting direction) applied. Beyond the peak stage, compared to the plain concrete samples, the hybrid concrete prisms, even with a thin reinforcement layer of 50 mm, presented a more or less ductile post-cracking behavior.

For the prisms produced in the standing molds, the casting and loading directions were identical. Based on the test results from Section 4.2.5, the steel fibers in these samples oriented preferentially along the directions of the tensile stresses, indicating a better crack-bridging capacity. Compared to the plain concrete samples, with growing reinforcement thickness, the hybrid concrete prisms showed not only a great increase in the load-bearing capacity but also a remarkable improvement in the post-cracking ductility (Figure 4.60 and Figure 4.61). This kind of enhancement was particularly evident when using hybrid fiber reinforcement (L60S60). Compared to the fully reinforced prisms, the hybrid concrete specimens reinforced with the monofiber reinforcement L60 of 150 mm in thickness exhibited, besides an almost identical $q_{max}$, a similar stress-displacement response in the post-cracking zone (Figure 4.60, L60_z150_9 vs. L60_9). The hybrid specimens strengthened with the hybrid fiber reinforcement L60S60 of an identical thickness showed a quite steep stress decline beyond the peak stage despite a slightly higher $q_{max}$ (Figure 4.61, L60S60_z150_9 vs. L60S60_9).

This phenomenon can be explained as follows: For the monofiber reinforcement, the stresses retained after the peak stage was not high enough so that the steel fibers in the upper half of specimen may be capable of withstanding the main fraction of the load. In other words, the fibers in the lower half of the fully reinforced specimen did not contribute to the load transfer to a large extent. For the hybrid fiber reinforcement, the stresses were considerably higher so that the steel fibers in the upper region may not be able to resist the load alone. Thus, with the further introduction of load, a great number of the fibers in the lower half of the fully reinforced prism were activated, leading to a more ductile fracture behavior.

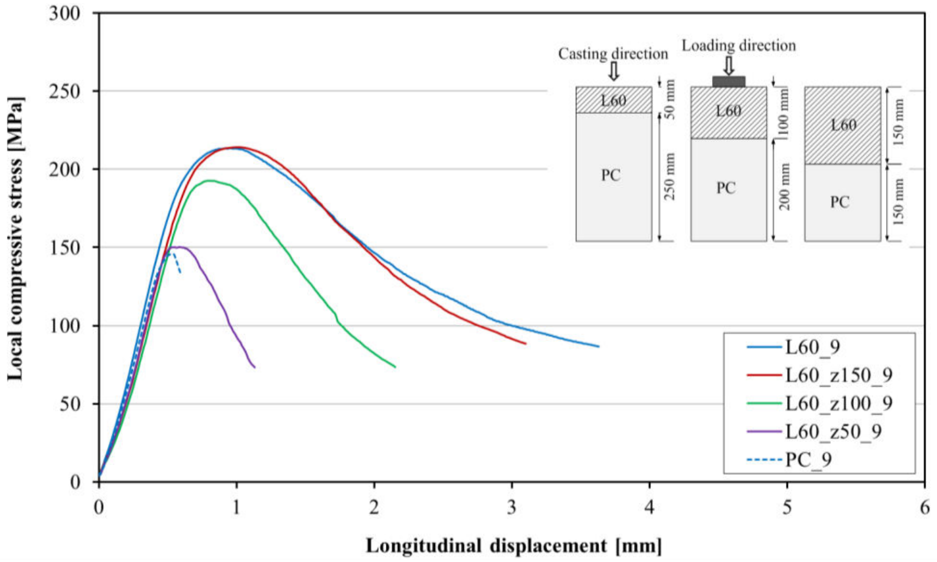


*Figure 4.60: Average local compressive stress versus longitudinal displacement curves of hybrid concrete prisms (reinforcement L60) cast in the standing molds under concentric loading at the area ratio of 9*

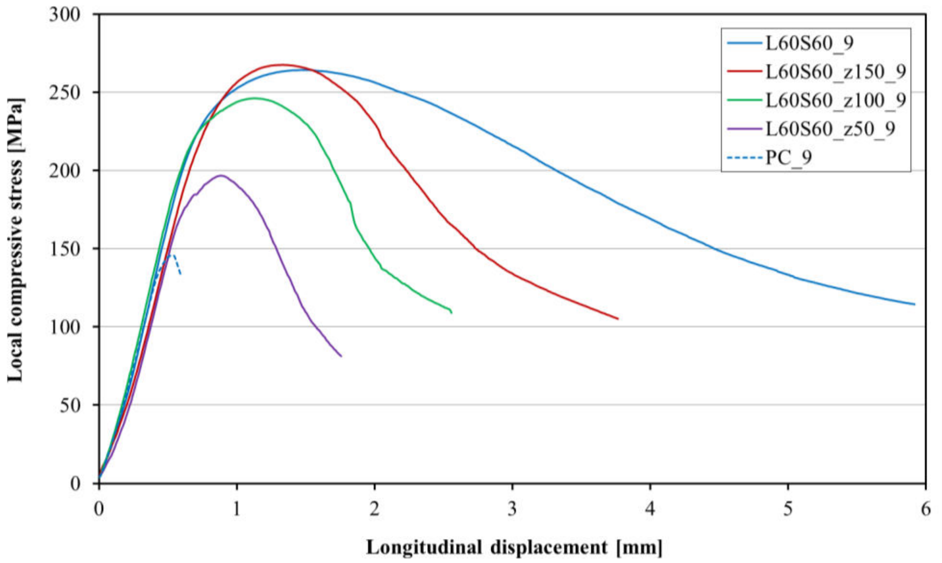


*Figure 4.61: Average local compressive stress versus longitudinal displacement curves of hybrid concrete prisms (reinforcement L60S60) cast in the standing molds under concentric loading at the area ratio of 9*

In the lying production, the casting direction was perpendicular to the loading direction. Compared to the plain concrete samples, the hybrid specimens with the monofiber reinforcement L60 showed only a slightly improved load-bearing behavior (Figure 4.62). With growing reinforcement thickness, the increase in $q_{max}$ was rather unnoticeable. After the peak stage, the stress drop was significantly sharper than that of the specimens cast in the standing molds. And no notable difference was observed in the curve shapes in the post-cracking stage between the hybrid prisms with a reinforcement thicknesses ≥ 100 mm and the fully reinforced concrete samples. Although for the hybrid specimens reinforced with the hybrid reinforcement L60S60 the increase in $q_{max}$ was slightly more evident (Figure 4.63), this enhancement was still even not comparable with that of the prisms cast in the standing molds. The unsatisfactory improvement in load-bearing capacity and ductility observed here was basically due to the insufficient number of steel fibers oriented towards the directions of the tensile stresses.

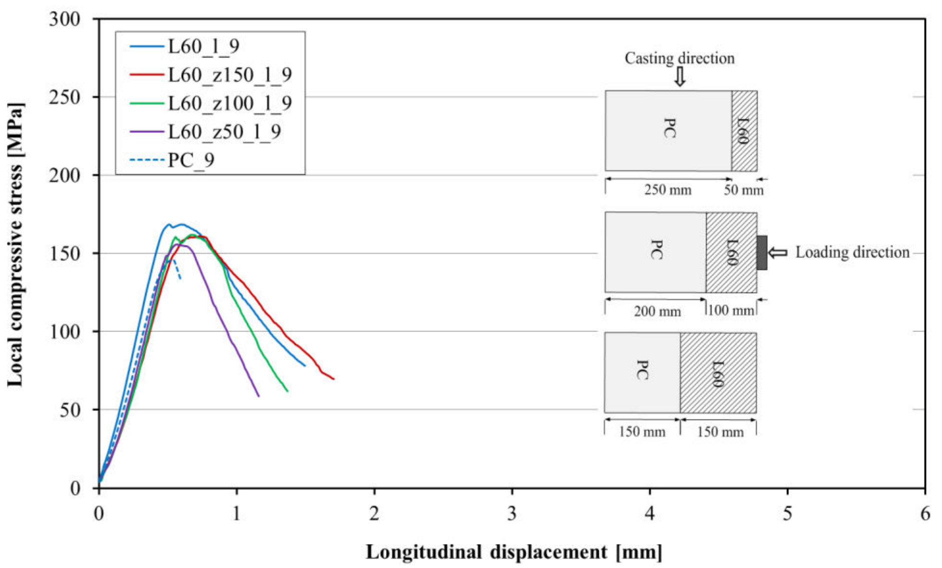


*Figure 4.62: Average local compressive stress versus longitudinal displacement curves of hybrid concrete prisms (reinforcement L60) cast in the lying (l) molds under concentric loading at the area ratio of 9*

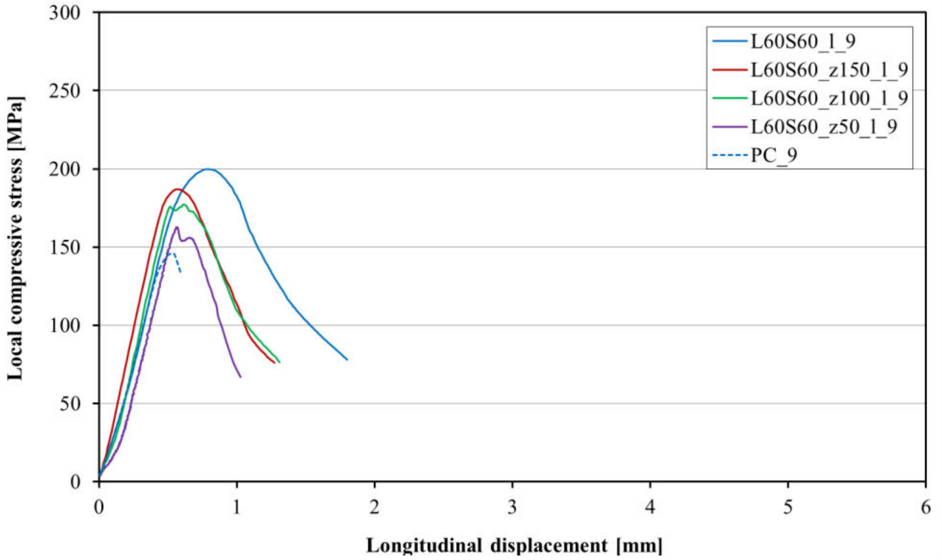


*Figure 4.63: Average local compressive stress versus longitudinal displacement curves of hybrid concrete prisms (reinforcement L60S60) cast in the lying (l) molds under concentric loading at the area ratio of 9*

By incorporating a fiber reinforcement layer of 100 mm in thickness, a ductile post-cracking behavior can be readily imparted to the concrete subjected to extremely eccentric load introduction (Figure 4.64 and Figure 4.65). It should be noted that the hybrid concrete specimens with the hybrid reinforcement L60S60 exhibited a comparable post-cracking ductility than the specimens fully reinforced with the monofiber reinforcement L60.

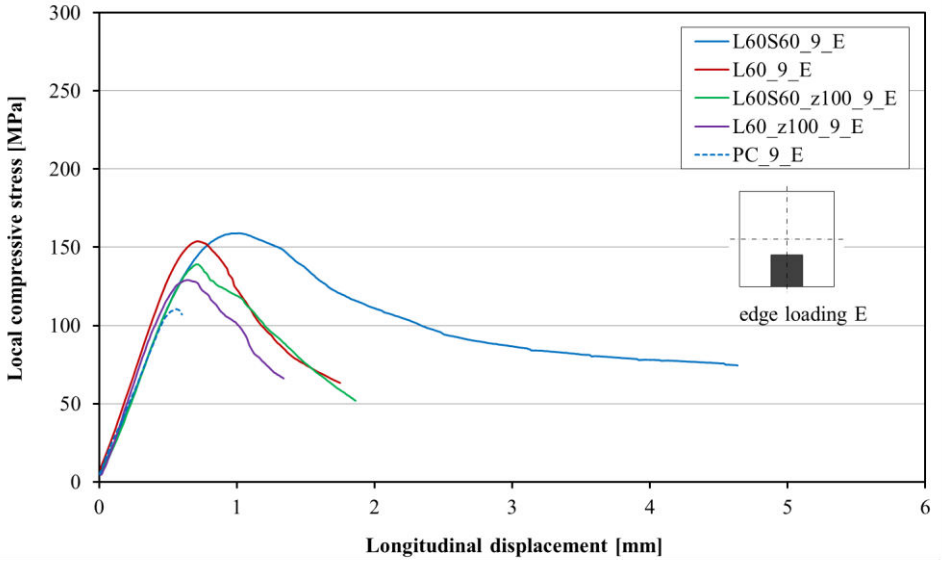


*Figure 4.64: Average local compressive stress versus longitudinal displacement curves of various hybrid concrete prisms produced in the standing molds under edge loading at the area ratio of 9*

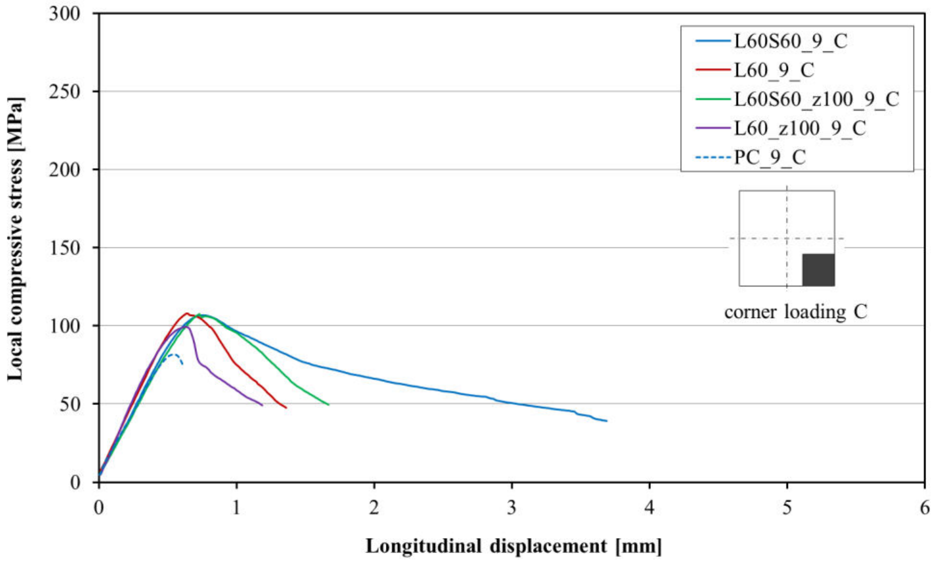


*Figure 4.65: Average local compressive stress versus longitudinal displacement curves of various hybrid concrete prisms produced in the standing molds under corner loading at the area ratio of 9*

Basically, the average stress versus lateral deformation curves of the hybrid prisms exhibited the similar features as observed by the average stress versus longitudinal displacement curves. Generally, the hybrid samples produced in the lying molds exhibited significantly lower stress level at the initial cracking than the hybrid prisms cast in the standing molds. Moreover, with growing crack width (i.e. lateral deformation), the stress fell more quickly. In the standing production, the stress level at the initial crack formation increased with increasing reinforcement thickness. The hybrid reinforcement L60S60 distinguished itself by a more gradual stress decline with growing deformation. Some representative curves are summarized in Appendix A.

In terms of the average midpoint longitudinal compressive deformation at $q_{max}$ (under concentric loading at the area ratio of 9), only an increasing trend with the increase of reinforcement thickness was observed in the standing production, implying a growing deformability of specimen (Table B.11, Appendix B). In the case of lying production under the same testing conditions, no direct relationship between the reinforcement thickness and the compressive deformation can be established.

**Failure and crack characteristics**

Some representative samples of the failed hybrid concrete prisms are demonstrated in Figure 4.66 - Figure 4.68 for the cases of concentric and eccentric loading, respectively. Similar to the fully reinforced prisms, no visible cracking or spalling was observed by the hybrid concrete specimens until shortly before reaching the ultimate load. Soon afterwards, all the hybrid concrete prisms, even with a fiber reinforcement of 50 mm in thickness, showed a ductile fracture behavior. However, the crack patterns differed remarkably amongst each other.

Under concentric loading at the area ratio of 9, the hybrid concrete prisms produced in the standing molds shared a roughly similar crack pattern with that of the fully reinforced samples, which was characterized by random multi-crack distribution on the testing surface and longitudinal crack propagation on the lateral surfaces (e.g. Figure 4.11, L60_9 vs. Figure 4.66, L60_z100_9 and Figure 4.36, L60S60_9 vs. Figure 4.66, L60S60_z100_9). Nevertheless, for the hybrid concrete samples, the cracks on the lateral surfaces spread continuously downwards to the bottom edges of specimen essentially due to the absence of steel fibers in the zone beneath the reinforced concrete layer. This typical crack pattern of the hybrid concrete specimens was independent of the thickness and type of fiber reinforcement used. In the case of hybrid fiber reinforcement L60S60, along with the continuous longitudinal cracks, several horizontal cracks were observed, propagating along the borderline of the plain and fiber concrete layer on the lateral surfaces (Figure 4.66, L60S60_z100_9).

With growing reinforcement thickness, concrete damages in terms of the number and width of cracks and the extent of concrete spalling tended to increase, in particular when incorporating hybrid fiber reinforcement. This was chiefly due to the strongly improved post-cracking ductility with increasing reinforcement thickness. With decreasing area ratio, fine longitudinal cracks increasingly developed on the lateral surfaces, along with several horizontal ones (e.g. Figure 4.66, L60_z100_4). In contrast to the fully reinforced samples (e.g. Figure 4.11, L60_4), the extent of concrete damages on the surfaces did not appear to increase with decreasing area ratio, mainly due to the comparatively inferior post-cracking ductility resulting in a premature failure.

For the production in the lying molds, the crack patterns of the partially and fully reinforced specimens under concentric loading were almost identical and characterized by two main cracks starting from the testing surface and spreading through the lateral surfaces (e.g. Figure 4.46, L60_l_9 vs. Figure 4.66, L60_z100_l_9). This typical crack pattern was basically caused by the preferential fiber orientation towards the loading direction in conjunction with the non-uniform fiber orientation in the directions of the tensile stresses, as explicitly discussed in Section 4.2.5. In the case of hybrid concrete specimens, crack pattern of this kind was found to be independent of the type and thickness of fiber reinforcement adopted. Furthermore, with growing reinforcement thickness, no considerable increase in the number and width of cracks as well as the extent of concrete spalling was observed by both types of fiber reinforcement (L60 and L60S60) investigated here.

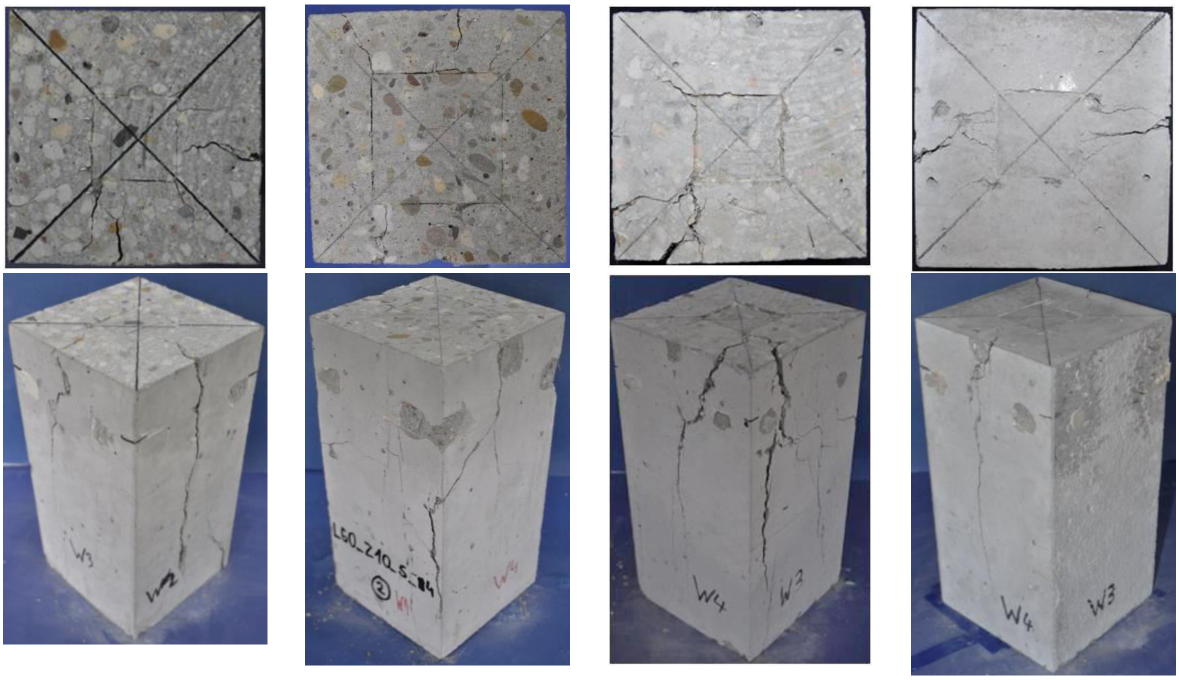


*L60_z100_9* *L60_z100_4* *L60S60_z100_9* *L60_z100_l_9*

*Figure 4.66: Typical failure patterns of hybrid concrete prisms loaded concentrically with the area ratios of 9 and 4*

Some failed hybrid concrete samples were sawed through along the central axis in order to observe the internal concrete damages (Figure 4.67). Compared to the modest surficial concrete damages (Figure 4.66), the internal damages were much more severe in the form of increased concrete crushing and crumbling in the border region of the plain and fiber concretes. It may be primarily accounted for by the penetration of the inverted fiber concrete cone into the plain concrete. This phenomenon was particularly pronounced in the case of specimens produced in the standing molds with the hybrid fiber reinforcement L60S60 and loaded with the high area ratio of 9 (Figure 4.67, L60S60_z100_9). Additionally, the extent of the internal damages observed by the hybrid concrete specimens was larger than that of the samples fully reinforced with the same type of fiber reinforcement (e.g. Figure 4.67, L60_z100_9 vs. Figure 4.13, L60_9).

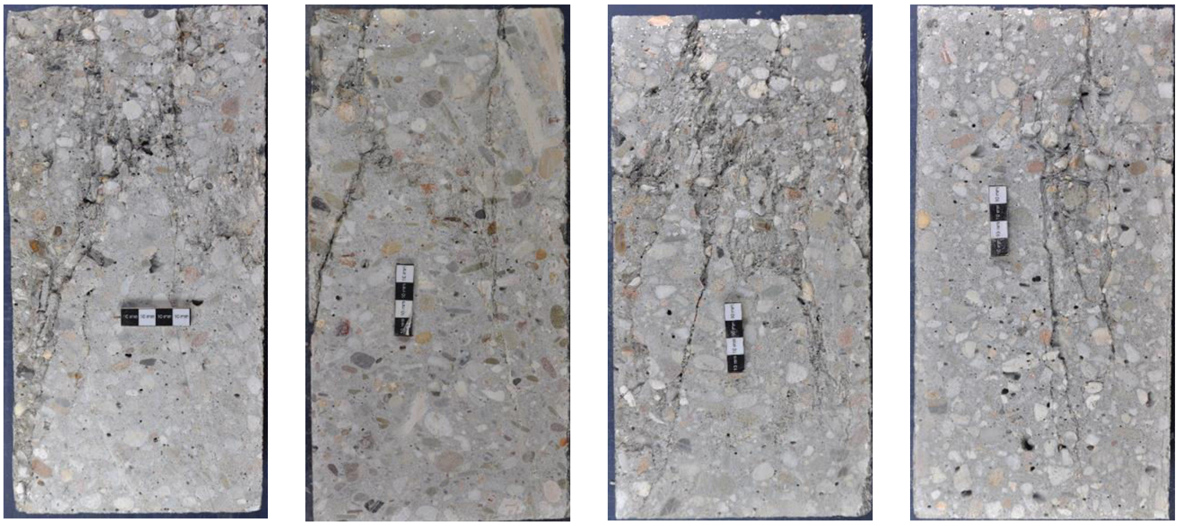

*L60_z100_9* *L60_z100_4* *L60S60_z100_9* *L60_z100_l_9*

*Figure 4.67: Sawed samples of failed hybrid concrete prisms loaded concentrically at the area ratios of 9 and 4*

For the hybrid concrete specimens tested under extreme eccentricity of load, analog to the case of fully strengthened specimens, the concrete damages occurred mainly on the lateral surfaces rather than on the testing surface. Under corner loading, the hybrid concrete samples strengthened with a 100 mm thick fiber reinforcement layer (with L60 or L60S60 reinforcement) showed a nearly similar failure pattern with that of the corresponding fully reinforced concrete specimens (e.g. Figure 4.56, L60_9_C vs. Figure 4.68, L60_z100_9_C). Except for a slightly more downward propagation of the two major cracks, no other severe concrete damages were found. Although under edge loading the hybrid concrete specimens remained their integrity after the test, two major continuous cracks were observed that started from the outer edge of the loaded area and diagonally spread through the lateral surface downward to the bottom edge of specimen. For the hybrid fiber reinforcement L60S60, due to the superior ductile failure behavior, the downward propagation of cracks was associated with severe concrete spalling occurred mostly in the plain concrete region closest to the specimen bottom (Figure 4.68, L60S60_z100_9_E). On the contrary, for the fully reinforced specimens the concrete damages in the form of cracking and minor concrete spalling were restricted to the local region adjacent to the loaded area (e.g. Figure 4.56, L60_9_E).

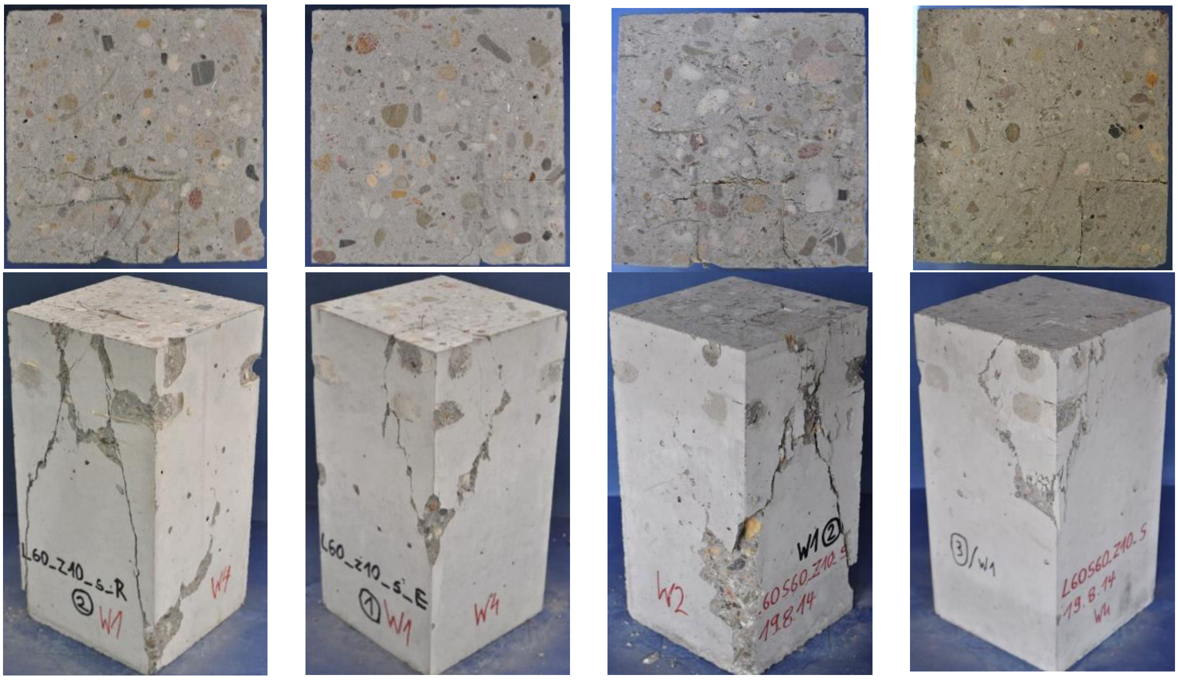

*L60_z100_9_E* *L60_z100_9_C* *L60S60_z100_9_E* *L60S60_z100_9_C*

*Figure 4.68: Typical failure patterns of hybrid concrete prisms loaded eccentrically at the area ratio of 9*

Under concentric loading, due to a better ductile facture behavior, the hybrid specimens produced in the standing molds showed modestly higher mean values of crack number and maximum crack width than the hybrid samples cast in the lying molds (Table B.12, Appendix B). An evident growing trend of crack width with increasing reinforcement thickness was only observed by the samples manufactured in the standing molds. The aforementioned tendencies were independent of the type of fiber reinforcement. At the low area ratio of 4, no noticeable difference in crack number and width was found between the partially and fully reinforced prisms with the monofiber reinforcement L60, whereas the specimens fully strengthened with the hybrid fiber reinforcement L60S60 showed much higher mean values of crack width than the partially reinforced prisms. Under eccentric loading (Table B.13, Appendix B), the partially and fully reinforced samples exhibited comparable mean values of crack width and number for a given eccentricity on the testing surface. Only in the case of hybrid fiber reinforcement under edge loading, the fully reinforced concrete prisms showed a slight increase in crack width.

**Summary**

In this sub-section, the hybrid concrete prisms (d150: 150 x 150 x 300-mm) containing both high-strength plain and fiber concretes were produced in either standing or lying molds using a "fresh in fresh" concreting technique and later loaded either concentrically or eccentrically with different area ratios. The results have been presented and compared with those obtained from the plain or fully reinforced fiber concrete samples.

On the basis of the experimental data obtained, the following relevant conclusions can be drawn:

- Under concentric load introduction, the mold type (i.e. casting direction), along with the type and thickness of fiber reinforcement, had great influence on the load-bearing capacity of the hybrid concrete prisms.
  - In the standing production, the maximum bearing stress $q_{max}$ of hybrid concrete prisms increased progressively with growing thickness of fiber reinforcement. Compared to the plain concrete prism, at the high area ratio of 9 the stress increment was from 3.3% to 41.4% for the monofiber reinforcement L60 on going a reinforcement thickness from 50 mm to 150 mm, and much more

pronounced for the hybrid fiber reinforcement L60S60 from 29.6% to 77.6%. In the latter case, a 50 mm thick fiber reinforcement showed already a significant increase in the maximum bearing stress (29.6%), while for the monofiber reinforcement at least 100 mm thick reinforcement layer was required to reach the similar improvement (27.6%).

- With a reinforcement thickness of 150 mm (i.e. 1/2 prism height), the hybrid concrete samples (with L60S60 or L60 reinforcement) exhibited even slightly higher maximum bearing stress than the fully reinforced prisms at the area ratio of 9. This implied that when only considering the ultimate load-bearing capacity, a full range of fiber reinforcement is not necessary.

- At the low area ratio of 4, the stress increase was less distinct especially for the hybrid fiber reinforcement L60S60, showing a 16.3% lower increment than the value obtained at the high area ratio of 9 for a reinforcement thickness of 100 mm.

- In the lying production, the increases in maximum stress as a result of growing reinforcement thickness were considerably low. Compared to the plain concrete prism, at the high area ratio of 9 the stress increment was from 5.3% to 10.5% for the monofiber reinforcement L60 on going a reinforcement thickness from 50 mm to 150 mm, and modestly higher for the hybrid fiber reinforcement L60S60 from 3.9% to 23.7%. In comparison with the values obtained in the standing production, the improvement was rather inappreciable, in particular in the case of hybrid fiber reinforcement.

- As explicitly discussed in Section 4.2.5, the inferior performance of fiber reinforcement in the lying production was primarily due to the preferential fiber orientation towards the loading direction. Even placing the steel fibers (with a maximum fiber length of 60 mm) in a 50 mm thick layer in the lying molds did not seem to effectively facilitate a preferable orientation of steel fibers perpendicular to the load direction (i.e. parallel to the directions of the tensile stresses) for the cases studied here.

- At the area ratio of 9, the effectiveness of fiber reinforcement relative to its thickness reached the highest level at a fiber reinforcement thickness of 100 mm (i.e. 1/3 specimen height) and afterwards decreased with increasing reinforcement thickness. Since the magnitude and distribution of tensile stresses depend not only upon the area ratio and specimen geometry, but also upon the type of reinforcement incorporated, the optimal thickness of fiber reinforcement should be determined individually for every specific case to resist the bursting tensile stresses more effectively.

- Even under extremely eccentric loading (i.e. edge and corner loading), the incorporation of a 100 mm thick fiber reinforcement layer readily led to a marked increase in maximum stress from 14.2% to 32.5%, compared to the plain concrete. Under corner loading, the hybrid concrete elements with the hybrid fiber reinforcement L60S60 showed the same maximum load-bearing capacity of the fully reinforced samples.

- For the hybrid specimens loaded concentrically, for a given area ratio or eccentricity of load, the casting direction or the type and thickness of fiber reinforcement had no influence on the stiffness of the stress versus longitudinal displacement curves in the pre-peak branch, however, large impact on the post-cracking ductility.
  - In the standing production, the post-cracking ductility increased considerably with increasing reinforcement thickness. Depending on the magnitude of the residual stress beyond the peak

stage, the half reinforced prisms (i.e. with 150 mm thick fiber reinforcement) exhibited either a similar stress versus displacement response of the fully strengthened specimens (for L60 monofiber system, relatively low residual stress) or a relatively less ductile post-cracking behavior (for L60S60 hybrid fiber system, relatively high residual stress).

- In the lying production, with growing reinforcement thickness, the post-cracking ductility was only marginally improved for both types of fiber reinforcement. It implied that for a given area ratio the casting direction (i.e. fiber orientation) exerted a more predominant influence on the load-bearing behavior than the type and thickness of fiber reinforcement.

- Even at extreme eccentricities (i.e. edge or corner loading), a ductile post-cracking behavior can be readily introduced to the concrete through incorporating a 100 mm thick fiber reinforcement layer. This phenomenon was in particular evident when using optimized hybrid fiber reinforcement L60S60 that showed a similar post-cracking ductility of the prisms fully strengthened with the monofiber reinforcement L60.

- Similar to the fully reinforced prisms, no visible cracking or spalling was observed by the hybrid concrete samples until shortly before reaching the maximum load. All the hybrid concrete prisms showed a more or less ductile fracture behavior, however, the failure pattern differed remarkably amongst each other.
  - Under concentric loading at the high area ratio of 9, the failure pattern of the hybrid concrete prisms cast in the standing molds were roughly similar to that of the fully reinforced samples, however, characterized by continuous longitudinal cracks and additional horizontal cracks on the lateral surfaces when using hybrid fiber reinforcement (L60S60).

  - In the lying production, the crack pattern of the partially and fully reinforced prisms was almost identical and characterized by continuous longitudinal propagation of two individual major cracks on the lateral surfaces. Crack pattern of this kind was basically independent of the type and thickness of fiber reinforcement used.

  - Compared to the surficial concrete damages, the internal damages of the hybrid concrete prisms were much more severe. Moreover, the extent of the internal damages was noticeably larger than that of the corresponding fully reinforced samples.

  - Under extremely large eccentric loading, the concrete damages of the hybrid concrete samples occurred mainly in the edge zones adjacent to the loaded area, analog to the fully strengthened specimens. Under corner loading, the hybrid samples showed a nearly similar failure pattern with that of the fully reinforced specimens, while under edge loading the hybrid specimens, especially with the hybrid fiber reinforcement L60S60, presented more severe damages in the form of continuous wide cracks and large-scaled spalling of concrete.

# 5 Conclusions and future perspectives

## 5.1 Conclusions

In practice, the problem of heavy compressive load transmitted onto limited area of concrete member occurs frequently in a variety of industrial and engineering structures. Numerous researches have been done in the last decades to investigate the structural behavior of concrete under such loading situation; however, the majority of them dealt with the performance of plain and conventionally reinforced concretes. With the increasingly widespread use of steel fibers in diverse structural applications, it became essential to intensively study the behavior of steel fiber reinforced concrete (SFRC) subjected to concentrated load for the purpose of constructive design and practical application of this material.

The research work presented here was designed to characterize the load-bearing and fracture behavior of SFRC under concentrated loading (i.e. point loading) by means of experimental approach under laboratory conditions. In the scope of the comprehensive parametric study (Figure 1.1), not only the non-fiber-related variables generally governing the structural behavior of plain concrete, but also the fiber-related factors specifically affecting the mechanical properties of SFRC have been systematically studied. Additionally, hybrid concrete elements containing both plain and fiber concretes have been produced using a “fresh in fresh” concreting technique and tested under the same conditions. In some test series the parameters were investigated in a combined way to better study their joint effects. The influence of various variables on the maximum load-bearing capacity, the stress versus displacement (or deformation) response, and the failure and crack characteristics of concrete specimen has been intensively discussed and compared with each other in the corresponding sub-sections.

Based on the test results obtained, the following conclusions that shall expand the understanding of the load-bearing and fracture behavior of SFRC under concentrated loading can be drawn:

In general, the non-fiber-related variables had qualitatively similar influence on the maximum load-bearing capacity of plain and fiber concretes under concentrated load: Increasing the concrete strength and area ratio led to an increase in the maximum local compressive stress $q_{max}$ (i.e. bearing stress), while increasing the specimen dimension and eccentricity of load resulted in a reduction of $q_{max}$. Nevertheless, due to the presence of steel fibers, the extent of increase or decrease in the maximum value of bearing stress was not always similar between the plain and fiber concretes.
Basically, the **addition of steel fibers** had a remarkably positive effect on improving the load-bearing behavior of concrete and changed the failure mode of concrete from a brittle to a ductile one under various situations of concentrated loading. The magnitude of these effects was controlled not only by the fiber-related parameters but also by the non-fiber-related variables. In some cases, the non-fiber-related factors exerted a more overriding impact than the fiber-related ones. For instance, the stiffness of SFRC under concentrated load was hardly affected by the fiber-related factors, but rather significantly by the non-fiber-related variables. More specifically, it increased with increasing area ratio and concrete strength, but decreased with increasing eccentricity of load and specimen dimension. Similarly, the maximum bearing stress $q_{max}$ and the stress ratio n showed a gradually decaying tendency with the decrease of **area ratio** R, whereby the stress reduction rate corresponded well to the square-root of area ratio $\sqrt{R}$. Through analyzing the difference of stress ratios between the plain and fiber concretes, it can be ascertained that the reinforcing effectiveness of steel fibers were more evident at high area ratio (R = 16 and 9, i.e. severe stress concentration) than at low area ratio (R = 4 and 2.25).

A qualitative evaluation of the influence of individual testing parameters on the maximum load-bearing capacity, post-cracking ductility and crack characteristics of the partially or fully reinforced concrete specimens exposed to concentrated load is given in Figure 5.1.

| | Maximum load-bearing capacity | Post-cracking ductility | Crack characteristics |
|---|---|---|---|
| Area ratio | +++ | ++ | +++ |
| Concrete strength | +++ | ++ | ++ |
| Specimen size | ++ | ++ | ++ |
| Eccentricity of load | | | |
| Small eccentricity | + | + | ++ |
| Large eccentricity | +++ | +++ | +++ |
| Fiber property | | | |
| Tensile strength | ++ | +++ | ++ |
| Aspect ratio | + | o | o |
| Geometry | + | ++ | ++ |
| Dimension | + | + | ++ |
| Fiber concentration | +++ | +++ | +++ |
| Fiber combination | | | |
| Low concentration | ++ | + | ++ |
| High concentration | + | ++ | + |
| Fiber orientation | | | |
| Mold type | +++ | +++ | +++ |
| Vibration type | o | o | o |
| Sampling direction | + | +++ | +++ |
| Thickness of fiber reinforcement | | | |
| Lying production | + | + | + |
| Standing production | +++ | +++ | ++ |

+++ large influence
++ moderate influence
+ small influence
o negligible influence

*Figure 5.1: Qualitative evaluation of the influence of the individual testing parameters on the maximum load-bearing capacity, post-cracking ductility and crack characteristics of the partially or fully reinforced concrete specimens at the predefined test end*

In the following, the effect of the individual variables on the load-bearing and fracture behavior of SFRC will be summarized in details.

A higher **concrete compressive strength** led to significantly higher maximum bearing stress, however, modestly lower stress ratio and less ductile post-cracking behavior of SFRC. Interestingly, the average increase in the maximum bearing stress due to the improvement in concrete strength was identical (55%) between the plain and fiber concretes. The variation in concrete strength hardly affected the mean stress increase induced by fiber addition (60 kg/m³ of hook-ended normal-strength macrofiber L), showing nearly the same average value (about 42%) between the normal-strength and high-strength SFRCs. The lower stress ratios of the high-strength concretes were essentially due to the disproportionate increase of tensile strength; however, this phenomenon was less pronounced for the SFRCs and even negligible when loaded at low area ratio ($R = 4$ and 2.25). The relatively less ductile stress-displacement response observed by the high-strength SFRCs was mainly accounted for by the more accelerating pullout process of fibers induced by the more explosive fracture behavior of the high-strength composite. Nonetheless, the crack-bridging capacity of fibers was utilized to a higher extent in the high-strength concrete matrix, since the fibers successfully prevented the explosive collapse of concrete specimens and maintained their integrity especially at low area ratio (R = 4 and 2.25).

The **specimen dimension** affected the load-bearing capacity of SFRC more noticeably than that of plain concrete. With increasing specimen size, SFRC showed a slightly higher average reduction of $q_{max}$ (14.5%) than the plain concrete (10%), and particularly evident at high area ratio (17%, for R = 9). Meanwhile, the large-sized SFRC prisms exhibited a slightly lower average stress increase (36%) as a result of fiber addition (60 kg/m³ of macrofiber L) than the small-sized SFRC specimens (44%). These effects indicated that the reinforcing effectiveness of fibers was rather size-sensitive and slightly lower in large-sized concrete element. Apart from a more smooth stress transition across the peak stage, the external failure pattern of the large-sized SFRC samples was less susceptible to the area ratio than that of the small-sized SFRC prisms, which deteriorated progressively with decreasing area ratio.

The **property of steel fiber** had higher impact on the post-cracking ductility and fracture behavior of SFRC than on the maximum bearing stress (or stress ratio). Although the maximum bearing stress of plain concrete was markedly improved (from 28% to 58%) by adding different types of steel fibers (with the same content of 60 kg/m³), amongst the various fiber types the variation in peak stress was comparatively modest (~ 15.4%). Increasing the fiber dimension and/or strength was found to be very effective in improving the stress-displacement response of SFRC in the post-cracking stage. Besides the highest maximum bearing stress, the specimen made of high-strength hook-ended macrofiber (Lh) exhibited the most ductile post-cracking behavior, however, the failure pattern was afflicted with significantly increased cracking and spalling of concrete. Varying the aspect ratio of hook-ended macrofiber (Lt vs. L) had marginal influence on the load-bearing and facture behavior. As expected, the hook-ended mesofiber (M) and the straight microfiber (S) demonstrated a considerably less ductile post-cracking behavior combined with continuous crack propagation induced by insufficient crack-bridging capacity of the fibers. Nonetheless, the microfibers are capable of arresting the microcracks and retarding the coalescence of microcracks into macrocracks at earlier stages of loading. Additionally, for a given content the fiber number can be drastically increased due to the much smaller dimension. Thus, in addition to macrofibers that primarily prevent the propagation of macrocracks after the peak stage, these fibers can be applied as secondary reinforcement to increase the overall load-bearing capacity and post-cracking ductility of SFRC.

With increasing **fiber concentration** (40 kg/m³ - 120 kg/m³), a progressive improvement in the maximum bearing stress (27% - 80%), stress ratio and post-cracking ductility was observed. However, a high fiber content containing only long hook-ended macrofiber L (≥ 80 kg/m³) caused difficulties in the dispersion of fibers and the workability of fresh SFRC mix, which can be to a large extent overcome by means of **combination of different fiber types** with various dimensions (i.e. hybrid fiber reinforcement).
For the cases studied here, the individual effects of the various fibers in a hybrid reinforcement system on the maximum load-bearing capacity appeared to depend greatly upon the total fiber amount. For fiber contents ≤ 80 kg/m³, the proportion of the primary fiber (long hook-ended macrofiber L) was generally more crucial than that of the secondary or tertiary fiber (hook-ended mesofiber M or straight microfiber S), while for fiber amounts ≥ 100 kg/m³, the beneficial effect of the primary fiber on improving the maximum bearing stress tended to be less evident.
A synergistic effect of hybrid fiber reinforcement can only be achieved by simultaneously adjusting and tailoring the fiber concentration and the combination of different fiber types to the properties of the concrete matrix. For the high-strength concrete applied here, the synergy effect was attained by SFRCs with relatively high fiber contents (≥ 100 kg/m³) that consisted of both long end-hooked macrofibers L

(60 kg/m³) and straight microfibers S (≥ 40 kg/m³). Moreover, the synergistic effect became more distinct with growing fraction of microfibers.
With growing fiber content, the continuous longitudinal crack propagation on the lateral surfaces due to insufficient number of fibers intersecting the cracks was effectively inhibited. At high fiber contents (≥ 100 kg/m³), the variations in fiber type did not make a noticeable distinction in the crack pattern.

The **fiber orientation** in the SFRC specimens was considerably influenced by the production processes and further exerted an impact on the load-bearing and fracture behavior of SFRC. For the cases studied here, the mold type (i.e. casting direction) and the sampling direction (relative to the casting direction) affected the orientation of steel fibers most significantly. In contrast, varying the specimen dimension, the vibration type and the reinforcement type (i.e. fiber type and combination of steel fibers) did not lead to a noticeable difference of fiber orientation in the SFRC samples.
Compared to the standing production (i.e. standard prism), a preferential fiber alignment towards the load direction as observed in the lying production (+20.7%, for monofiber reinforcement L60) led to a considerably lower maximum bearing stress (the same average stress reduction of 21% for both fiber reinforcements L60 and L60S60). As long as the fiber orientation towards the load direction was similar as observed between the standard and sampled prisms ($\Delta_{max}$ = 5.7%), a comparable maximum load-bearing capacity can still be expected. The nearly same average stress decrease (about 9%) obtained by the sampled prisms was primarily due to the reduced crack-bridging capacity of the cut fibers in the surface-near zones of specimen.
If the fibers oriented highly anisotropically in the directions of the tensile stresses, a drastic deterioration of the post-cracking ductility occurred inevitably after the peak stress. It was associated with continuous longitudinal crack propagation on the lateral surfaces, on which fewer fibers were aligned to the direction of the tensile stresses. The high inhomogeneity of fiber orientation in the two transverse directions of tensile stresses was observed by the SFRC prisms produced in the lying molds (Δ = 17.8%) and those sampled perpendicular to the casting direction from large beams (Δ = 26.8%).
The phenomena mentioned above were independent of the area ratio (R = 9 or 4) and the type of fiber reinforcement used (L60 or L60S60). It should be noted that the post-cracking ductility of hybrid fiber reinforcement (L60S60) was found to be more sensitive to the casting direction (i.e. fiber orientation), and particularly pronounced when loaded at high area ratio (R = 9). This was chiefly due to the joint effect induced by simultaneously using two types of steel fiber.

Under all the situations of **eccentric load introduction** the incorporation of steel fibers considerably improved the maximum load-bearing capacity of concrete (25% - 63%) and introduced a ductile load-bearing and failure behavior to concrete. Through adding steel fibers the extent of concrete cracking and spalling was less influenced by the eccentricity of load and the concrete damages were confined mostly in the small regions directly beneath the loaded area in a small scale.
The maximum bearing stress (and stress ratio) decreased gradually with increasing eccentricity and the stress reduction reached its highest value under corner loading (~ 59%, for R = 9). In other words, the reinforcing effectiveness of steel fibers arrived at its lowest level under corner loading. In this case, the variations of reinforcement type marginally affected the maximum stress, indicating an overriding influence of eccentricity of load. Compared to the plain concrete, the SFRCs generally showed a larger stress reduction ($\Delta_{max}$ = 20%) as a result of the increasing eccentricity especially under extreme situations (i.e. edge or corner loading). This effect was more pronounced when using hybrid fiber reinforcement (e.g. L60S60) at high area ratio (R = 9).
At small eccentricities ($e \leq 30$ mm), the stress-displacement behavior of SFRC in the post-cracking stage did not change appreciably, while under extreme eccentricities (i.e. edge or corner loading) the SFRCs produced with monofiber reinforcement (L60) exhibited a drastic reduction in the post-cracking ductility, however, only at high area ratio (R = 9). Compared to the monofiber reinforcement (L60), the advantage

of using hybrid fiber reinforcement (e.g. L60S60) was rather to effectively retain the post-cracking ductility even at extremely large eccentricities and high stress concentration (i.e. high area ratio) than to increase the maximum bearing stress.

**Hybrid concrete element** exhibited basically higher maximum load-bearing capacity, more ductile post-cracking behavior and much more limited concrete damages than unreinforced concrete member, even under extremely eccentric loading. These performances were further substantially improved by increasing reinforcement thickness and/or using optimized hybrid fiber reinforcement and eventually approached to those of the fully reinforced specimen. However, it can only be achieved under the condition that no preferable fiber alignment with respect to the load direction and a uniform fiber orientation in the directions of the tensile stresses are guaranteed, as observed in the case of standing production.

In the standing production, the hybrid fiber reinforcement (L60S60) distinguished itself again by the superior reinforcing effectiveness under concentric loading, even with a thin reinforcement layer of 50 mm (stress increment of 29.6%). With 150 mm thick fiber reinforcement (i.e. 1/2 prism height), the hybrid samples (partially strengthened with L60 or L60S60) exhibited even a slightly higher stress increase (41.4% or 77.6%, R = 9) than the corresponding fully reinforced prisms (40.8% or 75.0%, R = 9). This indicated that when only considering the maximum load-bearing capacity, a full range of fiber reinforcement is not necessary. Depending on the magnitude of bearing stress after the peak stage, the half-reinforced hybrid prisms exhibited either a similar stress-displacement response to the fully strengthened samples (L60 monofiber system, relatively low residual stress) or a comparatively less ductile post-cracking behavior (L60S60 hybrid fiber system, relatively high residual stress).

Even under edge or corner loading, the incorporation of thin fiber reinforcement layer (100 mm, with L60 or L60S60) readily led to a remarkable stress increase (14.2% or 32.5%) and a ductile post-cracking behavior. The hybrid specimens partially reinforced with hybrid fiber reinforcement (L60S60) exhibited a similar post-cracking ductility to the prisms fully strengthened with monofiber reinforcement (L60).

Compared to the fully reinforced specimens, the hybrid elements produced in the standing molds showed increased cracking under concentric loading and relatively severe concrete spalling in the regions of plain concrete under eccentric loading. Therefore, additional vertical thin fiber reinforcement layers extending to the specimen bottom in the edge zones adjacent to the load shall be useful to effectively control concrete damages of this kind.

The optimal thickness of the horizontal fiber reinforcement with which the maximum tensile stresses can be most effectively resisted depends not only upon the type of fiber reinforcement but also upon the magnitude of stress concentration (i.e. area ratio) and the position of load introduction. Thus, it should be determined individually for every specific case so as to utilize the reinforcement material and to sufficiently improve the load-bearing capacity of concrete structure member.

In the lying production, the improvement in maximum bearing stress and post-cracking ductility due to growing reinforcement thickness were rather inappreciable compared to that in the standing production. This was primarily due to the preferential fiber orientation towards the load direction. Even placing the fibers (with a maximum fiber length of 60 mm) in a 50 mm thick layer in the lying molds did not effectively facilitate a favorable fiber orientation, indicating again the predominant influence of casting direction (i.e. mold type) over the type and thickness of fiber reinforcement for the cases investigated here. The crack patterns of the partially and fully reinforced prisms were almost identical in the lying production.

## 5.2 Future perspectives and practical recommendations

**Future perspectives**

In the present work, the experimental investigations focused primarily on the load-bearing behavior of high-strength SFRC with conventional concrete composition and fiber concentrations in the normal range (< 2% by volume). With the further exploration of concrete technologies and production processes, new types of SFRCs with high performance and high ductility (e.g. with a strain-hardening behavior in tension) have been currently developed and increasingly used in diverse structural applications. SFRCs of this kind possess highly modified compositions of base concrete mixture regarding w/b-ratio, quantity of cement and additive, maximum grain size and packing density of aggregates. Meanwhile, the steel fibers incorporated are usually greater than about 2% by volume or even much higher, and often added in combined way as hybrid reinforcement. Furthermore, new types of fibers such as twisted or multiply end-hooked have been recently developed and applied in such SFRC composites. Consequently, these SFRCs differed significantly in the material and mechanical properties with the SFRC studied here, which should be intensively investigated when exposed to localized force.

The SFRC samples tested here were mostly small-sized prisms with dimensions of 150 x 150 x 300-mm and only few of them were with large dimensions (300 x 300 x 600-mm). Under considerations of reproducibility and transferability of the experimental results for the practical applications, a number of tests should be conducted on large-sized SFRC specimens with varying dimensions and shapes under concentric or eccentric concentrated load. The base concrete can be composed either as conventional concrete composite or as aforementioned modified concrete mixture. These large-sized specimens can be produced with various types of reinforcement such as combined reinforcement of rebars and steel fibers, or optimized hybrid fiber reinforcement, or even manufactured with the concept of hybrid system consisting of both high performance and high ductility SFRC (as thin reinforcement layer) and conventional SFRC (or ferroconcrete).

**Practical recommendations**

In order to improve the load-bearing capacity and the post-cracking ductility of SFRC under concentrated loading more effectively and economically, the following aspects should be particularly considered when formulating the SFRC mixtures and producing the SFRC structural elements for the practical applications.

- To ensure a favorable and uniform fiber orientation with respect to the acting directions of the tensile stresses

Amongst all the fiber-related parameters, the fiber orientation which can be most effectively affected by the mold type (i.e. casting direction) has the highest impact, and in some cases it is even more influential than the non-fiber-related parameters (e.g. area ratio).

- To adjust and tailor the properties, concentration and combination of steel fibers to the properties of concrete matrix

Without a careful and thoughtful optimization process, the reinforcing effectiveness of the (individual) steel fibers in either monofiber or hybrid fiber system cannot be utilized to a satisfactory level. In the latter case, the synergy effect of different fibers cannot be achieved.

- To apply optimized hybrid fiber reinforcement for extremely eccentric load introduction

Hybrid fiber reinforcement with optimized fiber content and combination distinguishes itself not only in the appreciable increase of maximum load-bearing capacity but also in the substantial improvement of post-cracking ductility especially under extremely large eccentricity of load and high stress concentration.

- To use hybrid concrete system when economic costs and static requirements are both concerned.

When economic costs and static requirements are both concerned, hybrid concrete system containing both conventional SFRC (or ferroconcrete) and high-performance SFRC is feasible. Moreover, a multi-lateral fiber reinforcement in the near-surface regions adjacent to the load should be taken into account.

# References


ACI 544.1R-96 (1996). State-of-the-art report on fiber reinforced concrete. Technical report (reapproved 2002). American Concrete Institute.

ACI 544.3R-93 (1993). Guide for specifying, proportioning, mixing, placing, and finishing steel fiber reinforced concrete. Technical report (reapproved 1998). American Concrete Institute.

ASTM A820/ A820M-11 (2011). Standard specification for steel fibers for fiber-reinforced concrete. ASTM International, West Conshohocken, PA, USA.

DAfStb-Guideline (1995). DAfStb-Richtlinie für hochfesten Beton. Deutscher Ausschuss für Stahlbetonbau (DAfStb). Berlin, Germany: Beuth. (in German).

DIN 1045 (1988). Beton und Stahlbeton, Bemessung und Ausführung. (in German).

DIN 1045-1 (2008). Concrete, reinforced and prestressed concrete structures - Part 1: Design and construction (in German).

DIN 1045-2 (2008). Concrete, reinforced and prestressed concrete structures - Part 2: Concrete - Specification, properties, production and conformity - Application rules for DIN EN 206-1. (in German).

DIN 1048-5 (1991). Testing methods for concrete: hardened concrete, specially prepared specimens. (in German).

DIN EN 12350-5 (2009). Testing fresh concrete - Part 5: Flow table test. German version EN 12350-5: 2009.

DIN EN 12350-6 (2011). Testing fresh concrete - Part 6: Density. German version EN 12350-6: 2009.

DIN EN 12350-7 (2009). Testing fresh concrete - Part 7: Air content Pressure methods. German version EN 12350-7: 2009.

DIN EN 12390-2 (2009). Testing hardened concrete - Part 2: Making and curing specimens for strength tests. German Version EN 12390-2: 2009.

DIN EN 12390-3 (2009). Testing hardened concrete - Part 3: Compressive strength of test specimens. German version EN 12390-3: 2009.

DIN EN 12390-6 (2010). Testing hardened concrete - Part 6: Tensile splitting strength of test specimens. German version EN 12390-6: 2009.

DIN EN 14721 (2007). Test method for metallic fibre concrete - Measuring the fibre content in fresh and hardened concrete. German version EN 14721: 2005 + A1: 2007.

DIN EN 14889-1 (2006). Fibres for concrete - Part 1: steel fibres - definitions, specifications and conformity. German version EN 14889-1: 2006.

Eurocode 2 (2004). Design of concrete structures, Part 1-1: General rules and rules for buildings. German version EN 1992-1-1: 2004.

Eurocode 2 (2011). Design of concrete structures, Part 1-1: General rules and rules for buildings. German version EN 1992-1-1:2004 + AC: 2010.

Abu-Lebdeh, T., Hamoush, S. & Zornig, B. (2010). Rate effect on pullout behavior of steel fibers embedded in very-high strength concrete. *American Journal of Engineering and Applied Sciences*, 3(2), 454-463.

Adeghe, L. N. (1986). A finite element model for studying reinforced concrete detailing problems. Ph.D. thesis, Department of Civil Engineering, University of Toronto, Toronto, Canada.

Al-Taan, S. A. & Al-Hamdony, J. A. (2005). Bearing capacity of steel fibrous concrete. *Al-Rafidain Engineering*, 14(1), 1-11.

Alwan, J. M., Naaman, A. E. & Guerrero, P. (1999). Effect of mechanical clamping on the pull-out response of hooked steel fibers embedded in cementitious matrices. *Concrete Science and Engineering Journal*, 1(1), 15-25.

Alwan, J. M., Naaman, A. E. & Hansen, W. (1991). Pull-out work of steel fibers from cementitious composites: analytical investigation. *Cement and Concrete Composites*, 13(4), 247-255.

Au, T. & Baird, D. L. (1960). Bearing capacity of concrete blocks. *ACI Journal Proceedings*, 56(3), 869-880.

Balaguru, P. & Ramakrishnan, V. (1988). Properties of fiber reinforced concrete: workability, behavior under long-term loading, and air-void characteristics. *ACI Materials Journal*, 85(3), 189-196.

Banthia, N & Trottier, J. F. (1994). Concrete reinforced with deformed steel fibers, Part I: bond-slip mechanisms. *ACI Materials Journal*, 91(5), 435-446.

Banthia, N. & Trottier J. F. (1991). Deformed steel fiber - cementitious matrix under impact. *Cement and Concrete Research*, 21(1), 158-168.

Banthia, N. (1991). Temperature sensitivity of steel fibre pull-out from cement-based matrices. *Journal of Materials Science Letters*. 10(8), 448-450.

Barnett, S. J., Lataste, J. F., Parry, T., Millard, S. G., & Soutsos, M. (2010). Assessment of fibre orientation in ultra-high performance fibre reinforced concrete and its effect on flexural strength. *Materials and Structures*, 43(7), 1009-1023.

Barr, B. (1987). The fracture characteristics of FRC materials in shear. In *Fiber Reinforced Concrete Properties and Applications* (SP-105, pp. 27-53). Detroit, USA: American Concrete Institute.

Barragan, B. E. (2003). Failure and toughness of steel fiber reinforced concrete under tension and shear. Ph.D. thesis, University of Politecnica De Catalunya, Barcelona, Spain.

Bartos, P. J. M. & Duris, M. (1994). Inclined tensile strength of steel fibres in a cement-based composite. *Composites*, 25(10), 945-952.

Batson, G., Ball. C., Bailey, L., Landers, E. & Hooks, J. (1972). Flexural fatigue strength of steel fiber reinforced concrete beams. *ACI Journal Proceedings*, 69(11), 673-677.

Bauschinger, J. (1876). Versuche mit Quadern aus Naturstein. In Mitteilungen des Mechanischen und Technischen Laboratoriums der Kgl. Technischen Hochschule München, No. 6. (in German).

Bentur, A. & Mindess, S. (1990). Fibre reinforced cementitious composites (1st ed.). London and New York: Elsevier Applied Science.

Bentur, A. & Mindess, S. (2007). Fibre reinforced cementitious composites (2nd ed.). London and New York: Taylor & Francis.

Bentur, A. (1998). Durability of fiber reinforced cementitious composites. In J. P. Skalny & S. Mindess (Eds.), *Materials Science of Concrete-V* (pp. 513-536). Westerville, USA: The American Ceramic Society.

Bentur, A., Diamond, S. & Mindess, S. (1985). The microstructure of the steel fibre-cement interface. *Journal of Materials Science*, 20(10), 3610-3620.

Bernasconi, A., Cosmi, F. & Hine, P. J. (2012). Analysis of fibre orientation distribution in short fibre reinforced polymers: a comparison between optical and tomographic methods. *Composites Science and Technology*, 72(16), 2002-2008.

Billig, K. (1948). A proposal for a draft code of practice for prestressed concrete (P. R. C.) (2nd ed.). New York, USA: F. F. Billig.

Bindiganavile, V., Banthia, N. & Aarup, B. (2002). Impact response of ultra-high-strength fiber-reinforced cement composite. *ACI Materials Journal*, 99(6), 543-548.

Böhme, T., Empelmann, M. & Wichers, M. (2009). Emsquerung für die Erdgasleitung A660 : Einsatz von stahlfaserbewehrten Tübbingen. *Beton- und Stahlbetonbau*, 104(12), 882-889. (in Germany).

Bonzel, J. & Dahms, J. (1981). Schlagfestigkeit von faserbewehrten Beton. *beton*, 31(3), 97-101 and 31(4), 136-142. (in German).

Breen, J. E., Burdet, O., Roberts, C., Sanders, D. & Wollmann, G. (1994). Anchorage zone reinforcement for post-tensioned concrete girders. National Cooperative Highway Research Program, Report No. 356. Washington, D. C., USA: National Academy Press.

Breitenbücher, R. & Rahm, H. (2009). Zerstörungsfreie Bestimmung des Stahlfasergehalts und der Stahlfaserorientierung im Frisch- und Festbeton. *beton*, 59(3), 88-93. (in German).

Breitenbücher, R. & Song, F. (2014). Experimentelle Untersuchungen zum Auszugsverhalten von Stahlfasern in höherfesten Betonen. *Beton- und Stahlbetonbau*, 109(1), 43-52. (in German).

Breitenbücher, R. (2012). Herstellung und Eigenschaften von Stahlfaserbeton. In Festschrift zum 60. Geburtstag von Univ.-Prof. Dr.-Ing. Manfred W. Keuser, *Berichte aus dem Konstruktiven Ingenieurbau*. Universität der Bundeswehr München, München, Germany. (in German).

Breitenbücher, R., Meschke, G., Song, F. & Zhan, Y. (2014). Experimental, analytical und numerical analysis of the pullout behavior of steel fibres considering fiber types, inclination angles and concrete strengths. *Structural Concrete*, 15(2), 126-135.

Breitenbücher, R., Meschke, G., Song, F., Hofmann, M. & Zhan, Y. (2014). Experimental and numerical study on the load-bearing behavior of steel fiber reinforced concrete for precast tunnel lining segments under concentrated loads. In B. Massicotte, B. Mobasher, G. Plizzari & J.-P. Charron (Eds.), Proceedings of Joint ACI-fib International Workshop: *Fibre Reinforced Concrete: from Design to Structural Applications* (FRC 2014, pp. 431-443). Montreal, Canada.

BSM100 (2008). Guidebook for the BSM100 device. Hertz Systemtechnik GmbH, Delmenhorst, Germany (in German).

Buchhardt, F. (1978). Anmerkungen zum räumlichen Problem der Lasteinleitung. *Beton- und Stahlbetonbau*, 73(6), 140-145. (in German).

Chan, Y. -W. & Chu, S. -H. (2004). Effect of silica fume on steel fibre bond characteristics in reactive powder concrete. *Cement and Concrete Research*, 34(7), 1167-1172.

Chanvillard, G. & Rigaud, S. (2003). Complete characterization of tensile properties of DUCTAL® UHPFRC according to the French recommendations. In A. E. Naaman & H. W. Reinhardt (Eds.), *High Performance Fiber Reinforced Cement Composites* (HPFRCC 4, pp. 21-34), RILEM Proceedings PRO 30. Bagneux, French: RILEM Publications SARL.

Chen, W. F. & Drucker, D. C. (1969). Bearing capacity of concrete blocks or rock. *Journal of the Engineering Mechanics Division*, 95(4), 955-978.

Chen, W. F., & Carson, J. L. (1974). Bearing capacity of fiber reinforced concrete. *ACI Special Publication*, SP-44, 209-220.

Chern, J. -C. & Young, C. -H. (1990). Factors influencing the drying shrinkage of steel fiber reinforced concrete. *ACI Materials Journal*, 87(2), 123-139.

Christodoulides, S. P. (1956). A photoelastic investigation of prestressed concrete anchorage. *Civil Engineering and Public Review*, 51(63), 994-997.

Cunha, V. (2010). Steel fibre reinforced self-compacting concrete (from micro-mechanics to composite behaviour). Ph.D. thesis, School of Engineering, University of Minho, Minho, Portugal.

Drucker, D. C., Greenberg, H. J. & Prager, W. (1952). Extended limit design theorems for continuous media. *Quarterly Journal of Applied Mathematics*, 9(4), 381-389.

Edgington, J., Hannant, D. J. & Williams, R. I. T. (1974). Steel fibre reinforced concrete. Current Paper CP69/74. Garston, UK: Building Research Establishment.

Empelmann, M. & Wichers, M. (2008). Untersuchungen von Betonbauteilen unter Teilflächenbelastung. Technical report. Institute for Building Materials, Concrete Construction and Fire Protection, Technical University of Braunschweig, Braunschweig, Germany. (in German).

Empelmann, M. & Wichers, M. (2009). Stabwerke und Teilflächenbelastung nach DIN 1045-1 und Eurocode 2 - Modelle und Anwendungen. *Beton- und Stahlbetonbau*, 104(4), 226-235. (in German).

Fanella, D. & Krajcinovic, D. (1985). Continuum damage mechanics of fiber reinforced concrete. *Journal of Engineering Mechanics*, 111(8), 995-1009.

Fanella, D. & Naaman, A. E. (1985). Stress-strain properties of fiber reinforced concrete in compression. *ACI Journal Proceedings*, 82(4), 475-483.

Fenwick, R. C & Lee, S. C. (1986). Anchorage zones in prestressed concrete members. *Magazine of Concrete Research*, 38(135), 77-89.

Feyerabend, B. (1995). Zum Einfluss verschiedener Stahlfasern auf das Verformungs- und Rissverhalten von Stahlfaserbeton unter den Belastungsbedingungen einer Tunnelschale. Technical report No. 95-8, Ruhr-University Bochum, Bochum, Germany. (in German).

Granju, J. -L. & Baluch, S. U. (2005). Corrosion of steel fibre reinforced concrete from the cracks. *Cement and Concrete Research*, 35(3), 572-577.

Grasser, E. & Thielen, G. (1976). Hilfsmittel zur Berechnung der Schnittgrößen und Formänderungen von Stahlbetontragwerken nach DIN 1045. Deutscher Ausschuss für Stahlbeton (DAfStb), Technical report No. 240. Berlin, Germany: Wilhelm Ernst & Sohn. (in German).

Grasser, E. & Thielen, G.(1991). Hilfsmittel zur Berechnung der Schnittgrößen und Formänderungen von Stahlbetontragwerken nach DIN 1045 (3. Auflage). Deutscher Ausschuss für Stahlbeton (DAfStb), Technical report No. 240. Berlin, Germany: Beuth. (in German).

Groth, P. (2000). Fibre Reinforced Concrete. Ph.D. Thesis, Department for Construction Technology, Lulea University of Technology, Lulea, Sweden.

Grünewald, S. (2004). Performance-based design of self-compacting fibre reinforced concrete. Ph.D. thesis, Technical University of Delft, Delft, Netherlands.

Guererro, P. & Naaman A. E. (2000). Effect of mortar fineness and adhesive agents on pullout response of steel fibres. *ACI Materials Journal*, 97(1), 12-20.

Guyon, Y. (1953). Prestressed concrete. New York, USA: John Wiley and Sons, Inc..

Guyon, Y. (1958). Béton précontraint: Etude théorique et expérimentale (Tome 1). Paris, France: Editions Eyrolles. (in French).

Hamoush, S. A., Abu-Lebdeh, T., Cummins, T. & Zornig, B. (2010). Pullout characterizations of various steel fibers embedded in very high-strength concrete. *American Journal of Engineering and Applied Sciences*, 3(2), 418-426.

Hannant, D. J. (1975). Additional data on fibre corrosion in cracked beams and theoretical treatment of the effect of fibre corrosion on beam load capacity. In A. Neville (Ed.), *Fibre Reinforced Cement and Concrete* (pp. 533-538), Proceedings RILEM Symposium. Lancaster, UK: The Construction Press.

Hannant, D. J. (1978). *Fibre Cements and Fibre Concretes*, New York, USA: John Wiley & Sons.

Hawkins, N. M. (1968a). The bearing strength of concrete loaded through rigid plates. *Magazine of Concrete Research*, 20(62), 31-40.

Hawkins, N. M. (1968b). The bearing strength of concrete loaded through flexible plates. *Magazine of Concrete Research,* 20(63), 95-102.

Hawkins, N. M. (1970). The bearing strength of concrete loaded for strip loading. *Magazine of Concrete Research*, 22(71), 87-98.

Hayland M. W. & Chen, W. F. (1970). Bearing capacity of concrete blocks. *ACI Journal*, 67(3), 228-236.

Hemmy, O. (2003). Zum Gebrauchs- und Tragverhalten von Tunnelschalen aus Stahlfaserbeton und stahlfaserverstärktem Stahlbeton. Ph.D. thesis, IBMB, Technical University of Braunschweig, Braunschweig, Germany. (in German).

Hiltscher, R. & Florin, G. (1962). Die Spaltzugkraft in einseitig eingespannten, am gegenüberliegenden Rand belasteten rechteckigen Scheiben. *Bautechnik*, 39(10), 325-328.(in German).

Hiltscher, R. & Florin, G. (1968). Darstellung der Spaltzugspannungen unter einer konzentrierten Last (Druckplatte) nach Guyon-Iyengar und nach Hiltscher und Florin. *Bautechnik*, 6(45), 196-200. (in German).

Hiltscher, R. & Florin, G. (1972). Spaltzugspannungen in kreiszylindrischen Säulen, die durch kreisförmige Flächenlast zentrisch-axial belastet sind. *Bautechnik*, 3(49), 90-94. (in German).

Hiltscher, R.& Florin, G.(1963). Spalt- und Abreißzugspannungen in rechteckigen Scheiben, die durch eine Last in verschiedenem Abstand von einer Scheibenecke belastet sind. *Bautechnik*, 40(12), 401-408. (in German).

Holschemacher, K., Dehn, F. & Klug, Y. (2011). Grundlagen des Faserbetons. In K. Bergmeister, F. Fingerlos & J. -D. Wörner (Eds.), *Beton-Kalender 2011: Kraftwerke, Faserbeton* (pp. 19-88). Berlin, Germany: Ernst & Sohn. (in German).

Houde, J., Prezeau, A. & Roux, R. (1987). Creep of concrete containing fibres and silica fume. In S. P. Shah & G. B. Batson (Eds.), In *Fiber Reinforced Concrete - Properties and Application* (SP-105, pp. 101-108), Farmington Hills, USA: American Concrete Institute.

Ibell, T. J. & Burgoyne, C. J. (1993). Experimental investigation of behaviour of anchorage zones. *Magazine of Concrete Research*, 45(165), 281-291.

Ibell, T. J. & Burgoyne, C. J. (1994a). A plasticity analysis of anchorage zones. *Magazine of Concrete Research*, 46(166), 39-48.

Ibell, T. J. & Burgoyne, C. J. (1994b). A generalized lower-bound analysis of anchorage zones. *Magazine of Concrete Research*, 46(167), 133-143.

Ince, R. & Arici, E. (2005). Size effect in concrete blocks under local pressure. *Structural Engineering and Mechanics*, 19(5), 567-580.

Iyengar, K. T. S. R. & Yogananda, C. V. (1966). A three-dimensional stress distribution problem in the anchorage zone of a post-tensioned concrete beam. *Magazine of Concrete Research*, 18(55), 75-84.

Iyengar, K. T. S. R. (1960). Der Spannungszustand in einem elastischen Halbstreifen und seine technische Anwendung. Ph.D. Thesis, Institute for Concrete Construction, Technical University of Hannover, Hannover, Germany. (in German).

Jähring, A. (2005). Zur Einleitung konzentrierter Kräfte in den Betongurt durch Verbundmittel. In Festschrift zum 60. Geburtstag von Univ.-Prof. Dr.-Ing. Konrad Zilch, *Massivbau in ganzer Breite* (pp. 393-399). Berlin Heidelberg, Germany: Springer. (in German).

Johnston, C. D. & Coleman, R. A. (1974). Strength and deformation of steel fiber reinforced mortar in uniaxial tension. In *Fiber Reinforced Concrete* (SP-44, pp. 177-193). Farmington Hills, USA: American Concrete Institute.

Johnston, C. D. & Zemp, R. W. (1991). Flexural fatigue performance of steel fiber reinforced concrete - influence of fiber content, aspect ratio and type. *ACI Materials Journal*, 88(4), 374-383.

Johnston, C. D. (1974). Steel fibre reinforced mortar and concrete - a review of mechanical properties. In *Fiber Reinforced Concrete* (SP-44, pp. 127-142). Detroit, USA: American Concrete Institute.

Johnston, C. D. (1996). Proportioning, mixing and placement of fibre-reinforced cements and concretes. In P. J. M. Bartos, D. J. Cleland & D.L. Marrs (Eds.), *Production Methods and Workability of Concrete* (pp. 155-179). London, UK: E&FN Spon.

Kim, D. J., El-Tawil, S. & Naaman, A. E. (2008). Loading rate effect on pullout behavior of deformed steel fibers. *ACI Materials Journal*, 105(6), 576-584.

Klotz, S. (2008). Ultrahochfester Beton unter Teilflächenbelastung. Ph.D. thesis, Department of Economy and Science, Technical University of Leipzig, Leipzig, Germany. (in German).

Komendant, A. (1952). Prestressed concrete structure (1st ed.). New York, USA: McGraw-Hill Book.

König, G., Tue, N. V. & Zink, M. (2001). Hochleistungsbeton - Bemessung, Herstellung und Anwendung. Berlin, Germany: Ernst & Sohn. (in German).

Kooiman, A. G. (2000). Modelling steel fibre reinforced concrete for structural design. Ph.D. thesis, Technical University of Delft, Delft, Netherlands.

Kotsovos, M. D. & Newman, J. B. (1981). Effect of boundary conditions on the behaviour of concrete under concentrations of load. *Magazine of Concrete Research*, 33(116), 161-170.

Kotsovos, M. D. (1981). An analytical investigation of the behaviour of concrete under concentrations of load. *Materials and Structures*, 14(83), 341-348.

Kriz, L. B. & Raths, C. H. (1963). Connections in precast concrete structures - bearing strength of columns heads. *Journal of the Prestressed Concrete Institute*, 8(6), 45-75.

Kupfer, H. (2005). Theorie der Druckfestigkeit des Betons bei Teilflächenbelastung. In Festschrift zum 60. Geburtstag von Univ.-Prof. Dr.-Ing. Konrad Zilch, *Massivbau in ganzer Breite* (pp. 401-411). Berlin Heidelberg, Germany: Springer. (in German).

Kützing, L. (2000). Tragfähigkeitsermittlung stahlfaserverstärkter Betone. Ph.D. thesis, Leipzig University, Leipzig, Germany. (in German).

Lee, M. K. & Barr, B. I. G. (2004). An overview of the fatigue behaviour of plain and fibre reinforced concrete. *Cement & Concrete Composites*, 26(4), 299-305.

Leonhardt, F. & Mönnig, E. (1986). Vorlesungen über Massivbau: Teil 2: Sonderfälle der Bemessung im Stahlbetonbau (3. Auflage). Berlin Heidelberg, Germany: Springer.(in German).

Leung, C. K. Y. & Cheung, A. K. F. (2009). Some recent findings on concrete members under localised compression. *International Journal of Structural Engineering*, 1(1), 59-70.

Leung, C. K. Y. & Geng, Y. P. (1998). Micromechanical modeling of softening behaviour in steel fibre reinforced cementitious composites. *International Journal of Solids and Structures*, 35(32), 4205-4222.

Li, V. C. & Stang, H. (1997). Interface property characterisation and strengthening mechanisms in fibre reinforced cement based composites. *Advanced Cement Based Composites*, 6(1), 1-20.

Lieberum, K. -H. (1987). Das Tragverhalten von Beton bei extremer Teilflächenbelastung. Ph.D. thesis. Department of Constructive Engineering, Technical University of Darmstadt, Darmstadt, Germany. (in German).

Lieberum, K. -H., Reinhardt H. -W. & Weigler, H. (1989). Das Tragverhalten von Beton bei extremer Teilflächenbelastung. *Beton- und Stahlbetonbau*, 84(1), 1-5. (in German).

Lin, Y. (1999). Tragverhalten von Stahlfaserbeton. Deutsche Ausschuss für Stahlbeton (DAfStb), Technical report No. 494. Berlin, Germany: Beuth. (in German).

Magnel, G. (1954). Prestressed concrete (3rd ed.). New York, USA: McGraw-Hill Book Co..

Maibaum, C. & Hüttl, R. (2004). Neuer Zusatzstoff für Hochleistungsbetone. *beton*, 3, 132-133. (in German).

Maidl, B. (1991). Stahlfaserbeton. Berlin, Germany: Ernst & Sohn. (in German).

Malmberg, B. & Skarendahl, A. (1978). Method of studying the cracking of fibre concrete under restrained shrinkage. In R. N. Swamy (Ed.), *Testing and Test methods of Fibre Cement Composites* (pp. 173-179). Lancaster, UK: The Construction Press.

Mandel, J., Wei, S. & Said, S. (1987). Studies of the properties of the fiber-matrix interface in steel fiber reinforced mortar. *ACI Materials Journal*, 84(2), 101-109.

Mangat, P. S. & Gurusamy, K. (1987). Permissible crack widths in steel fibre reinforced marine concrete. *Materials and Structures,* 20(5), 338-347.

Mangat, P. S. & Gurusamy, K. (1988). Corrosion resistance of steel fibres in concrete under marine exposure. *Cement and Concrete Research*, 18(1), 44-54.

Markovic, I. (2006). High-performance hybrid-fibre concrete - development and utilization. Ph.D. thesis, Technical University of Delft, Delft, Netherlands.

Meyerhof, G. G. (1953). The bearing capacity of concrete and rock. *Magazine of Concrete Research*, 4(12), 107–116.

Middendorf, K. H. (1960). Anchorage bearing stresses in post-tensioned concrete. *ACI Journal*, 580-584.

Middendorf, K. H. (1963). Practical aspects of end zone bearing of post-tensioning tendons. *Journal of the Prestressed Concrete Institute*, 8(4), 57-62.

Mörsch, E. (1924). Über die Berechnung der Gelenkquader. *Beton und Eisen*, 23(12), 156-161. (in German).

Naaman, A. E. & Najm, H. (1991). Bond-slip mechanisms of steel fibers in concrete. *ACI Materials Journal*, 88(2), 135-145.

Naaman, A. E. & Shah, S. (1976). Pullout mechanism in steel fibre reinforced concrete. *Journal of the Structural Division*, 102(8), 1537-1548.

Naaman, A. E. (2000). Fasern mit verbesserter Haftung. *Beton- und Stahlbetonbau*, 95(4), 232-238. (in German).

Naaman, A. E. (2003). Engineered steel fibers with optimal properties for reinforcement of cement composites. *Journal of Advanced Concrete Technology*, 1(3), 241-252.

Naaman, A. E. (2004). Evaluation of steel fibers for applications in structural concrete. In M. di Prisco, R. Felicetti & G.A. Plizzari (Eds.), 6th International RILEM Symposium on *Fibre Reinforced Concretes* (pp. 389-400). Bagneux, French: RILEM Publications SARL.

Naaman, A. E., Argon, A. S. & Moavenzadeh, R. (1973). Fracture model for fiber reinforced cementitious materials. *Cement and Concrete Research*, 3(4), 397-411.

Nguyen, D. T. (2002). Räumliche Stabwerkmodelle zur Bemessung von Betontragwerken. Ph.D. thesis, Department of Civil Engineering and Surveying, University of Stuttgart, Stuttgart, Germany. (in German).

Niyogi, S. K. (1973). Bearing strength of concrete: geometric variations. *Journal of the Structural Division*, 99(7), 1471-1490.

Niyogi, S. K. (1974). Concrete bearing strength: support, mix, size effect. *Journal of the Structural Division*, 100(8) 1685-1702.

Niyogi, S. K. (1975). Bearing strength of reinforced concrete blocks. *Journal of the Structural Division*, 101(5), 1125-1137.

Ouyang, C., Palacios, A. & Shah, S. P. (1994). Pullout of inclined fibers from cementitious matrix. *Journal of Engineering Mechanics*, 120(12), 2641-2659.

Ozyurt, N., Mason, T. O. & Shah, S. P. (2006). Non-destructive monitoring of fiber orientation using AC-IS: an industrial-scale application. *Cement and Concrete Research*, 36(9), 1653-1660.

Papworth, F. (1997). Use of steel fibres in concrete. Presented at The Concrete Institute of Australia, NSW Branch, Australia.

Ramakrishnan, V., Oberling, G. & Tatnall, P. (1987). Flexural fatigue strength of steel fiber reinforced concrete. In *Fiber Reinforced Concrete Properties and Applications* (SP-105, pp. 225-245). Detroit, USA: American Concrete Institute.

Reinhardt, H. -W. & Koch, R. (1997). Untersuchungen zum Einfluss von Bauteilgröße und Betonzusammensetzung auf die Tragfähigkeit von hochfestem Beton unter Teilflächenbelastung. Research report No. V 362. Institute for Materials in Civil Engineering, Technical University of Stuttgart, Stuttgart, Germany. (in German).

Reinhardt, H. -W. & Koch, R. (1998). Hochfester Beton unter Teilflächenbelastung. *Beton- und Stahlbetonbau*, 93(7), 182-188. (in German).

Richard, P. & Cheyrezy, M. H. (1994). Reactive powder concrete with high ductility and 200-800 MPa compressive strength. In P. K. Mehta (Ed.), *Concrete Technology Past, Present and Future* (SP-144, pp. 507-518). Farmington Hills, USA: American Concrete Institute.

Robins, P. J., Austin, S. A. & Jones, P. A. (2003). Spatial distribution of steel fibres in sprayed and cast concrete. *Magazine of Concrete Research*, 55(3), 225-235.

Robins, P., Austin, S. & Jones, P. (2002). Pull-out behaviour of hooked steel fibres. *Materials and Structures,* 35(7), 434-442.

Rosenbusch, J. (2004). Einfluss der Faserorientierung auf die Beanspruchbarkeit von Bauteilen aus Stahlfaserbeton. *Beton- und Stahlbetonbau*, 99(5), 372-377. (in German).

Rümmelin, A. T. (2005). Entwicklung, Bemessung, Konstruktion und Anwendung von ultrahochfesten Betonen. Master Thesis. University of Applied Sciences, Stuttgart, Germany. (in Germany).

Samkari, M. (1987). Vorspannkrafteintragung im Spannbeton. Ph.D. thesis, Department of Civil Engineering, University of Kassel, Kassel, Germany. (in German).

Sargious, M. (1960). Beitrag zur Ermittlung der Hauptzugspannungen am Endauflager vorgespannter Betonbalken. Ph.D. thesis, Technical University of Stuttgart, Stuttgart, Germany. (in German).

Schlaich, J. & Schäfer, K. (2001). Konstruieren im Stahlbetonbau. In *Beton-Kalender 2001* (pp. 311-492). Berlin, Germany: Ernst & Sohn. (in German).

Schmidt, H. & Fiedler, M. (1993). Versuche zur Teilflächenbelastung von stahlfaserverstärktem Stahlbeton. *Bauzeitung*, 47(4), 64-66. (in German).

Schnell, J. & Ackermann, F. P. (2009). Innovative Verbunddeckensysteme mit stahlfaserbewehrten Betonen. Research report No. F 2531. Stuttgart, Germany: Fraunhofer IRB. (in German).

Schön, A. & Reinhardt, H. -W. (1994). Teilflächenbelastung von hochfestem Beton. Research report No. T 2654. Institute for Materials in Civil Engineering, Technical University of Stuttgart, Stuttgart, Germany. (in German).

Schuler, F. & Sych, T. (2009). Analyse der Faserorientierung in Betonen mit Hilfe der Computer-Tomographie. Deutsches Institut für Bautechnik (DIBt), Research report No. T-3218. Berlin, Germany: Fraunhofer IRB.

Schulz. M. (2000). Stahlfasern: Eigenschaften und Wirkungsweisen. *beton*, 7, 382-387. (in German).

Schupack, M. (1986). Durability of SFRC exposed to severe environments. In *Steel Fiber Concrete* (pp. 479-496). New York, USA: Elsevier Applied Science.

Shelson, W. (1957). Bearing capacity of concrete. *ACI Journal*, 29(5), 405-414.

Soroushian, P. & Lee, C. -D. (1990). Distribution and orientation of fibers in steel fiber reinforced concrete. *ACI Materials Journal*, 87(5), 433-439.

Spieth, H. -P. (1959). Das Verhalten von Beton unter hoher örtlicher Pressung und Teilbelastung unter besonderer Berücksichtigung von Spannbetonverankerungen. Ph.D. thesis, Technical University of Stuttgart, Stuttgart, Germany. (in German).

Spieth, H. -P. (1961). Das Verhalten von Beton unter hoher örtlicher Pressung. *Beton- und Stahlbetonbau*, 56(11), 257-263. (in German).

Spitz, H. M. (1977). Beitrag zur Untersuchung von Krafteinleitungsproblemen des Stahlbetonbaus im Zustand II mit Hilfe finiter Elemente. Ph.D. thesis, Technical University of Aachen, Aachen, Germany. (in German).

Stähli, P., Custer, R. & van Mier, J. G. M. (2008). On flow properties, fibre distribution, fibre orientation and flexural behaviour of FRC. *Materials and Structures*, 41(1), 189-196.

Stangenberg. F. (1986). Stahlfaserbeton als hervorragender Baustoff für stoßbeanspruchte Bauteile. *Bauingenieur*, 61, 339-345. (in German).

Stengel, T. (2009). Effect of surface roughness on the steel fibre bonding in ultra-high performance concrete (UHPC). In *Nanotechnology in Construction 3* (pp. 371-376), Proceedings of the NICOM3. Berlin, Germany: Springer.

Strack, M. (2007). Modellbildung zum rissbreitenabhängigen Tragverhalten von Stahlfaserbeton unter Biegebeanspruchung. Ph.D. thesis. Ruhr-University Bochum, Germany. (in German).

Stroeven, P. (1986). Stereology of concrete reinforced with short steel fibres. *Heron-Fracture mechanics and structural aspects of concrete*, 31(2), 15-28.

Sun, W., Pan, G., Yan, H., Qi, C. & Chen H. (1999). Study on the anti-exploding characteristics of fiber reinforced cement based composite. In H. W. Reinhardt & A. E. Naaman (Eds.), *High Performance Fiber Reinforced Cement Composites*, (HPFRCC 3, pp. 565-574), RILEM Proceedings PRO 6. Bagneux, French: RILEM Publications SARL.

Swamy, R. N. & Stavrides, H. (1979). Influence of fiber reinforcement in restrained shrinkage and cracking. *ACI Journal*, 76 (21), 443-460.

Taerwe, L., van Gysel, A., de Schutter, G., Vyncke, J. & Schaerlaekens, S. (1999). Quantification of variations in the steel fibre content of fresh and hardened concrete. In H. W. Reinhardt & A. E. Naaman (Eds.), *High Performance Fiber Reinforced Cement Composites* (HPFRCC 3, pp. 213-222), RILEM Proceedings PRO 6, Bagneux, French: RILEM Publications SARL.

Torrents, J. M., Blanco, A., Pujadas, P., Aguado, A. & Juan-García, P. (2012). Inductive method for assessing the amount and orientation of steel fibers in concrete. *Materials and Structures*, 45(10), 1577-1592.

Ukhagbe, J. (1990). Ausgewählte Probleme zur Vorspannkrafteinleitung im Spannbeton. Ph.D. thesis, Department of Civil Engineering, University of Kassel, Kassel, Germany. (in German).

Valle, M. & Buyukozturk, O. (1993). Behavior of fiber reinforced high-strength concrete under direct shear. *ACI Materials Journal*, 90(2), 122-133.

van Gysel, A. (1999). A pullout model for hooked end steel fibres. In H. W. Reinhardt & A. E. Naaman (Eds.), *High Performance Fiber Reinforced Cement Composites*, (HPFRCC 3, pp. 351-359), RILEM Proceedings PRO 6. Bagneux, French: RILEM Publications SARL.

Vandewalle, L., Heriman, G. & van Rickstal, F. (2008). Fibre orientation in self-compacting fibre reinforced concrete. In R. Gettu (Ed.), Proceedings of the 7th RILEM International Symposium on Fibre Reinforced Concrete (BEFIB 2008, pp. 719-728). Bagneux, French: RILEM Publications SARL.

Vitt, G., Schulz, M. & Nell, W. (2009). Herstellung und Prüfung von Biegebalken nach DAfStb-Richtlinie Stahlfaserbeton. *Beton- und Stahlbetonbau*, 104(8), 543-549. (in German).

Vodicka, J., Spura, D. & Kratky, J. (2004). Homogeneity of steel fiber reinforced concrete (SFRC). In M. di Prisco, R. Felicetti & G.A. Plizzari (Eds.), *Fibre-Reinforced Concretes* (BEFIB 2004, pp. 537-544), RILEM Proceedings. Bagneux, French: RILEM Publications SARL.

Wei, S., Mandel, J. & Said, S. (1986). Study of the interface strength of steel fibre reinforced cement based composites. *ACI Journal Proceedings*, 83(4), 597-605.

Wichers, M. (2013). Bemessung von bewehrten Betonbauteilen bei Teilflächenbelastung unter Berücksichtigung der Rissbildung. Ph.D. thesis, Technical University of Braunschweig, Braunschweig, Germany. (in German).

Wichmann, H.-J. (2009). Ein neues Messsystem zur Bestimmung des Gehaltes an Stahlfasern im Beton. Betonbodenfachtagung, BetonMarketing Nord. Braunschweig, Germany. (in German).

Woo, L. Y., Wansom, S., Ozyurt, N., Mu, B., Shah, S. P. & Mason, T. O. (2005). Characterizing fiber dispersion in cement composites using AC-Impedance Spectroscopy. *Cement and Concrete Composites*, 27(6), 627-636.

Wurm, P. & Daschner, F. (1977). Versuche über Teilflächenbelastung von Normalbeton. Deutscher Ausschuss für Stahlbeton (DAfStb), Technical report No. 286. Berlin, Germany: Ernst & Sohn. (in German).

Wurm, P. & Daschner, F.(1983). Teilflächenbelastung von Normalbeton, Versuche an bewehrten Scheiben. Deutscher Ausschuss für Stahlbeton (DAfStb), Technical report No. 344. Berlin, Germany: Ernst & Sohn. (in German).

Yettram, A. L. & Robbins, K. (1969). Anchorage zone stresses in axially post-tensioned members of uniform rectangular section. *Magazine of Concrete Research*, 21(67), 103-112.

Zielinski, J. & Rowe, R. E. (1960). An investigation of the stress distribution in the anchorage zones of post-tensioned concrete members. Research report No. 9. London, UK: Cement and Concrete Association.

# Appendix A

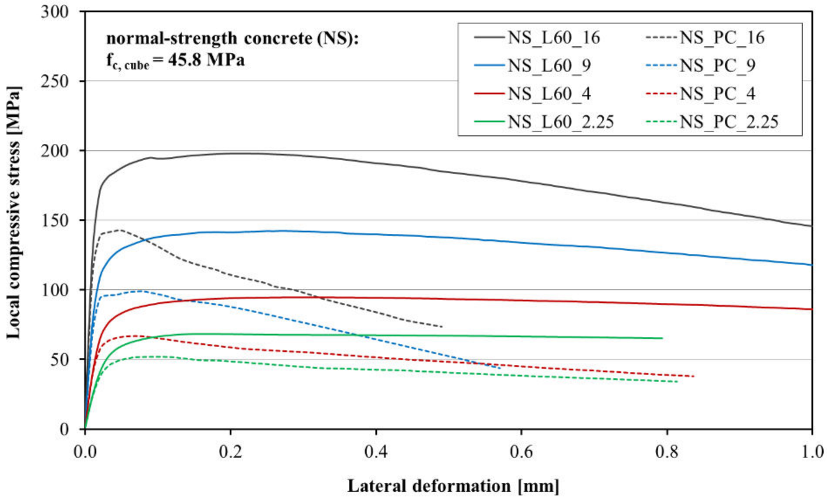


*Figure A.1: Average local compressive stress versus lateral deformation curves of the normal-strength concrete prisms (NS_PC and NS_L60) loaded at the area ratios of 16, 9, 4 and 2.25*

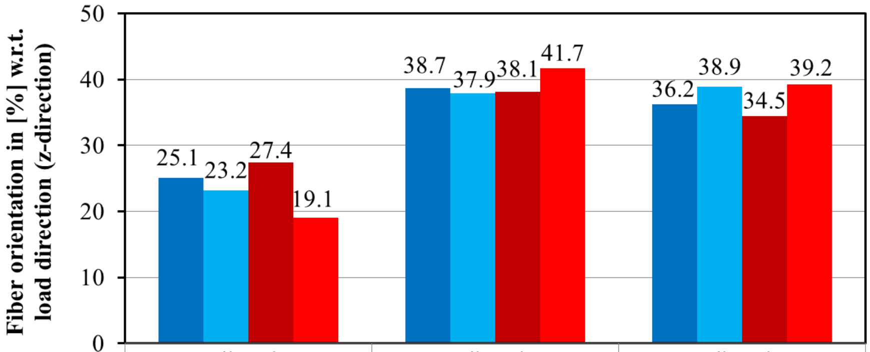


| | z-direction | x-direction | y-direction |
|---|---|---|---|
| L60_9 | 25.1 | 38.7 | 36.2 |
| L60_4 | 23.2 | 37.9 | 38.9 |
| L60_9_d300 | 27.4 | 38.1 | 34.5 |
| L60_4_d300 | 19.1 | 41.7 | 39.2 |

*Figure A.2: Fiber orientation (z-direction = casting direction) in the upper half of SFRC specimens with different dimensions (d150: L60_9 and L60_4; d300: L60_9_300 and L60_4_d300)*

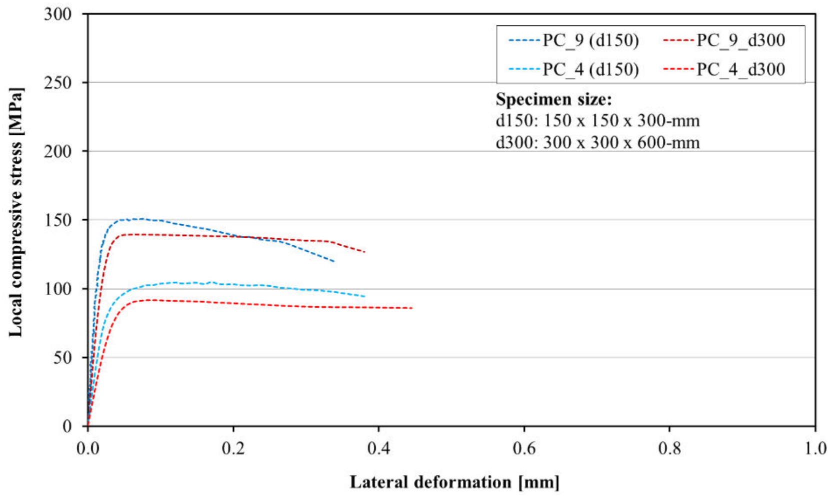


*Figure A.3: Average local compressive stress versus lateral deformation curves of the high-strength plain concrete prisms with various sizes loaded at the area ratios of 9 and 4 (d150: PC_9 and PC_4; d300: PC_9_d300 and PC_4_d300)*

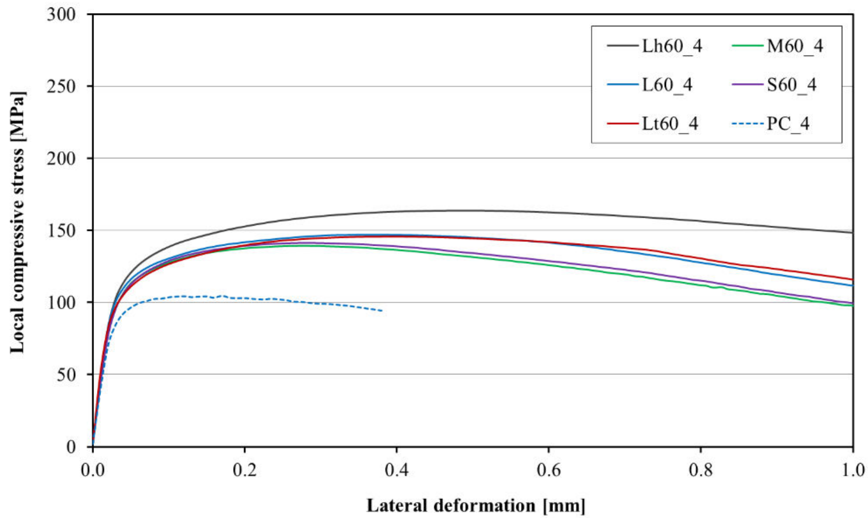


*Figure A.4: Average local compressive stress versus lateral deformation curves of the high-strength SFRC prisms produced with various fiber types and loaded at the area ratio of 4*

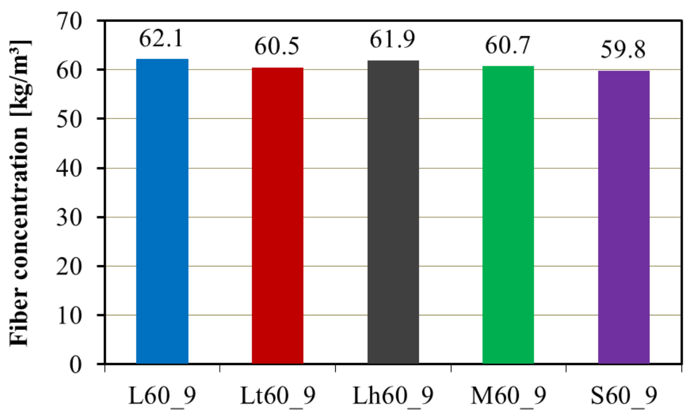


*Figure A.5: Fiber concentration in the upper half of SFRC prisms produced with various fiber types*

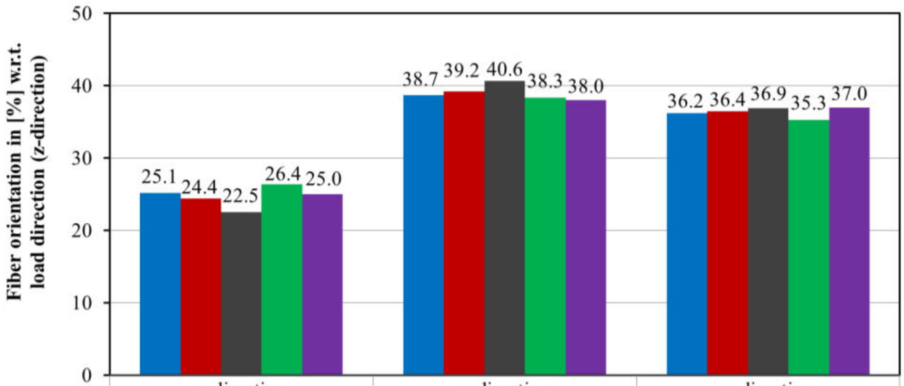


| | z-direction | x-direction | y-direction |
|---|---|---|---|
| L60_9 | 25.1 | 38.7 | 36.2 |
| Lt60_9 | 24.4 | 39.2 | 36.4 |
| Lh60_9 | 22.5 | 40.6 | 36.9 |
| M60_9 | 26.4 | 38.3 | 35.3 |
| S60_9 | 25.0 | 38.0 | 37.0 |

*Figure A.6: Fiber orientation (z-direction = casting direction) in the upper half of SFRC prisms produced with various fiber types*

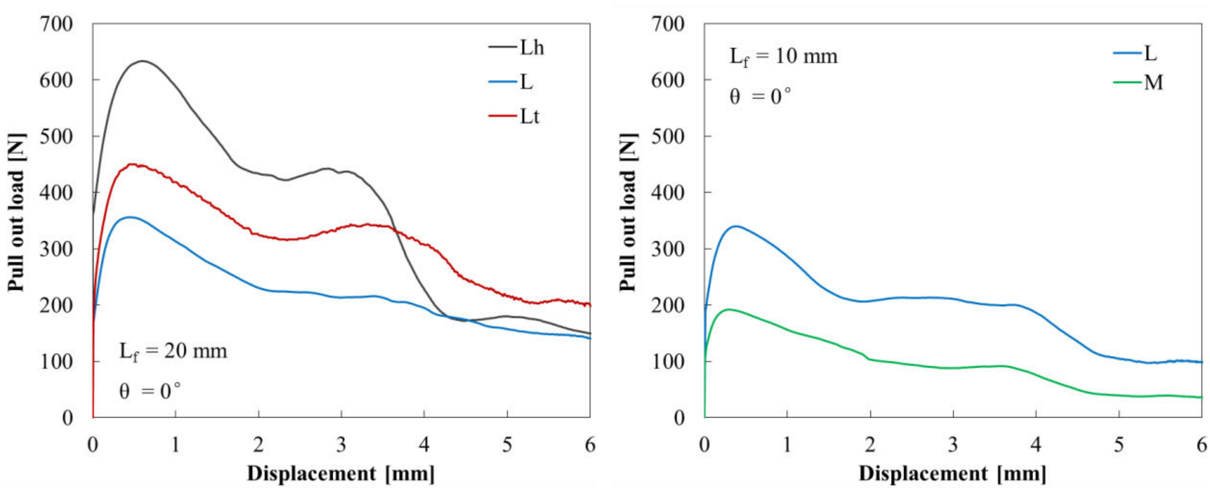


*Figure A.7: Pullout load versus displacement behavior of various types of steel fiber embedded in high-strength concrete ($f_{c,cube}$ = 84 MPa)*

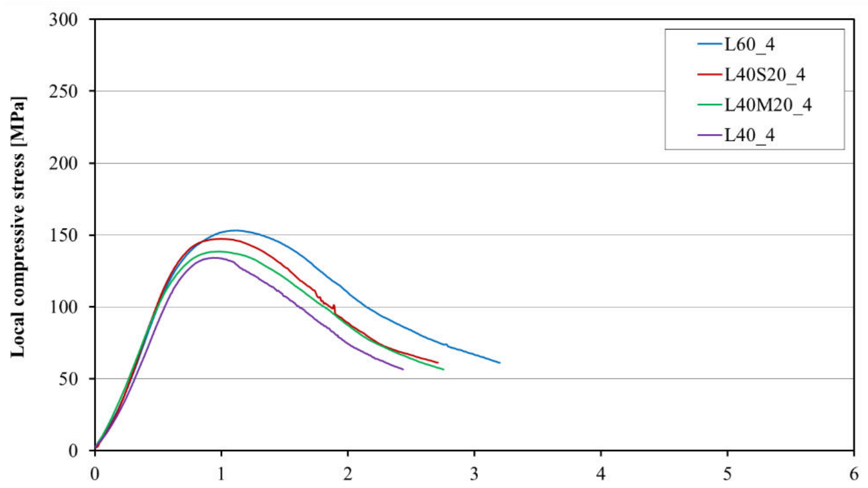


*Figure A.8: Average local compressive stress versus longitudinal displacement curves of various SFRCs produced with a fiber content of 60 kg/m³ and loaded at the area ratio of 4*

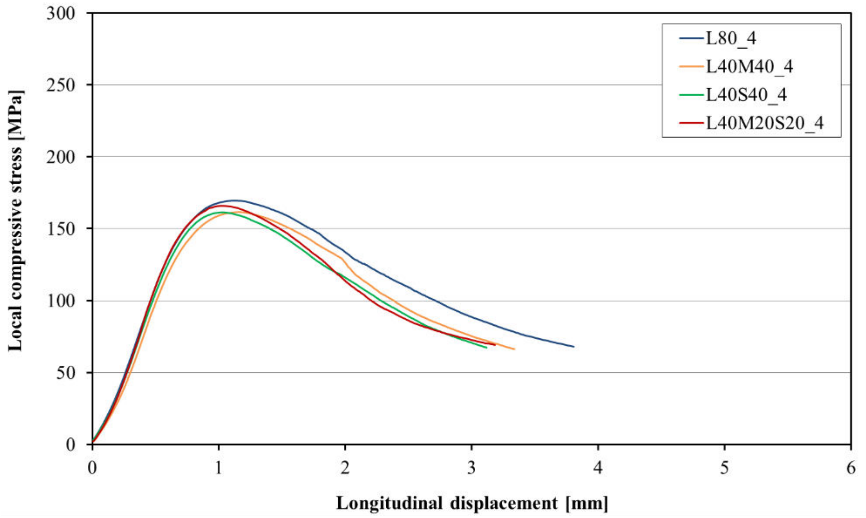


*Figure A.9: Average local compressive stress versus longitudinal displacement curves of various SFRCs produced with a fiber content of 80 kg/m³ and loaded at the area ratio of 4*

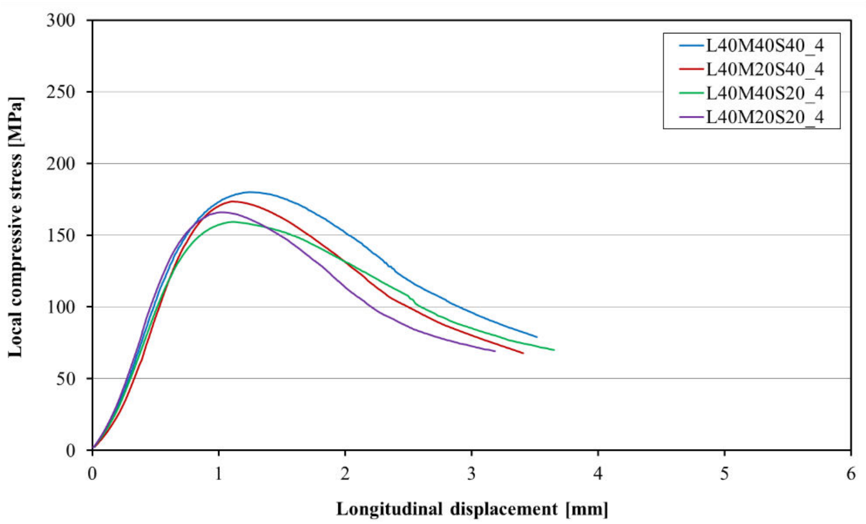


*Figure A.10: Average local compressive stress versus longitudinal displacement curves of various SFRCs produced with three different fiber types and loaded at the area ratio of 4*

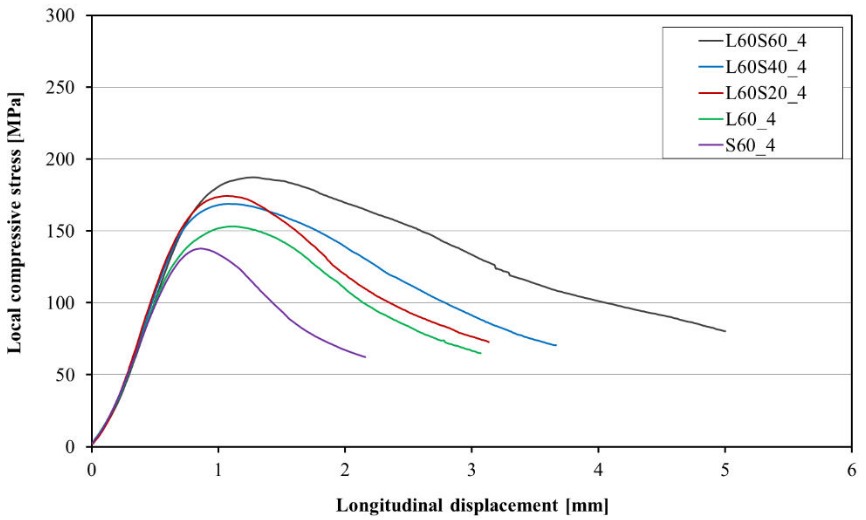


*Figure A.11: Average local compressive stress versus longitudinal displacement curves of various SFRCs loaded at the area ratio of 4*

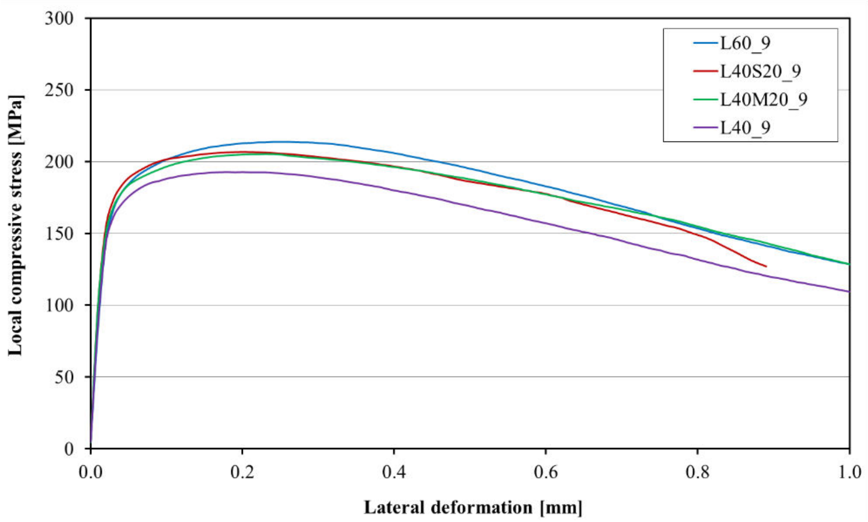


*Figure A.12: Average local compressive stress versus lateral deformation curves of various SFRCs produced with a fiber content of 60 kg/m³ and loaded at the area ratio of 9*

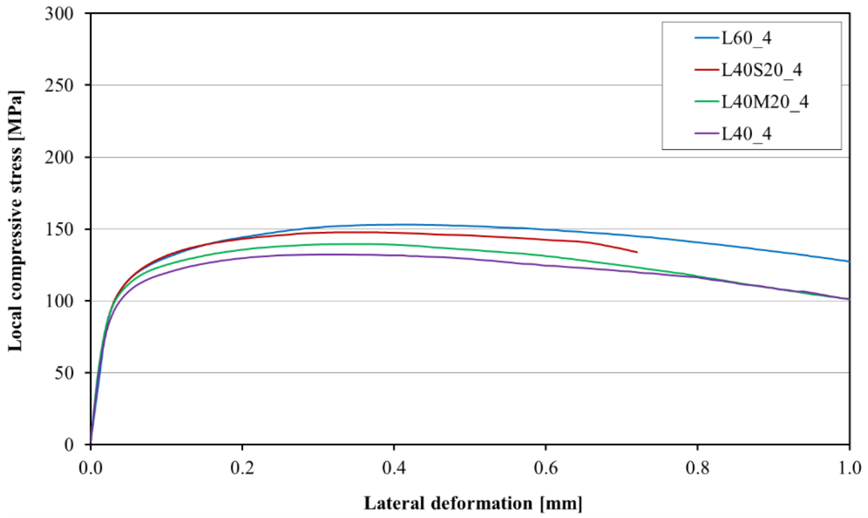


*Figure A.13: Average local compressive stress versus lateral deformation curves of various SFRCs produced with a fiber content of 60 kg/m³ and loaded at the area ratio of 4*

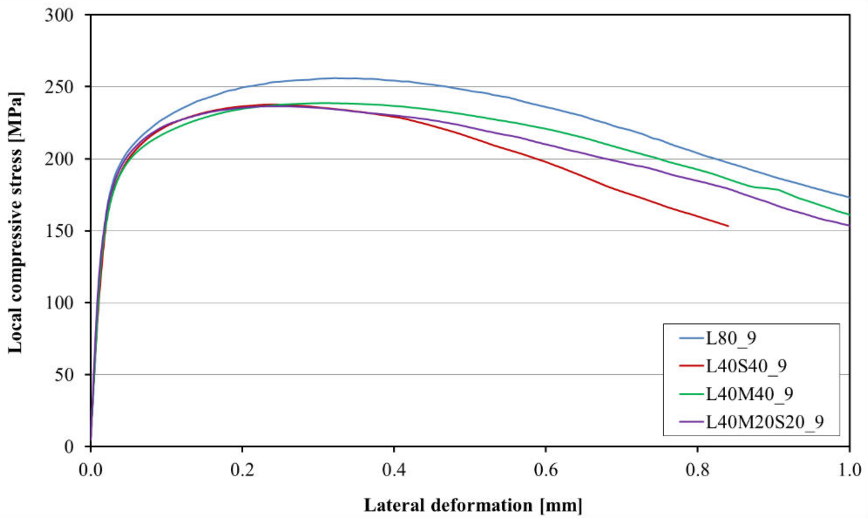


*Figure A.14: Average local compressive stress versus lateral deformation curves of various SFRCs produced with a fiber content of 80 kg/m³ and loaded at the area ratio of 9*

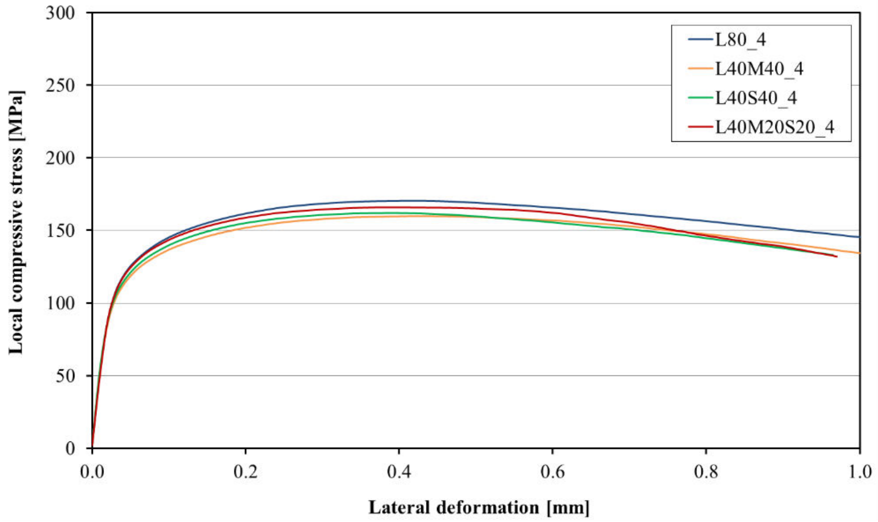


*Figure A.15: Average local compressive stress versus lateral deformation curves of various SFRCs produced with a fiber content of 80 kg/m³ and loaded at the area ratio of 4*

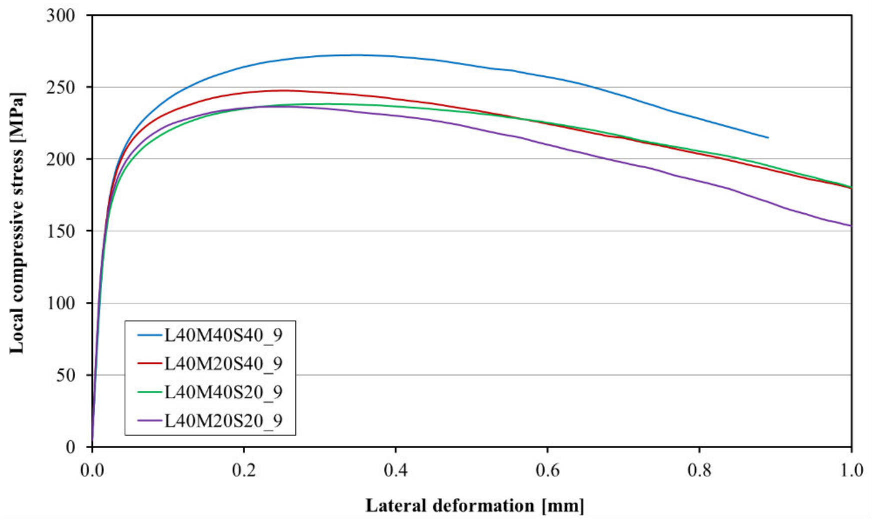


*Figure A.16: Average local compressive stress versus lateral deformation curves of various SFRCs produced with three different fiber types and loaded at the area ratio of 9*

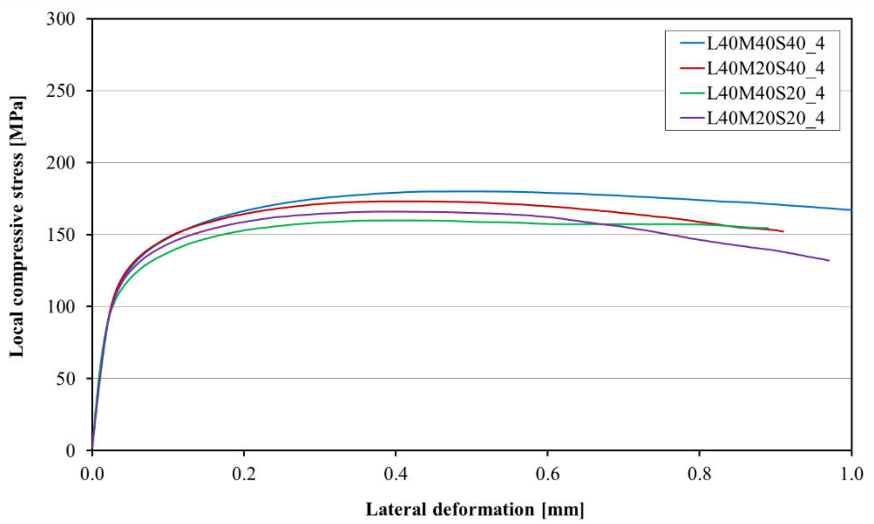


*Figure A.17: Average local compressive stress versus lateral deformation curves of various SFRCs produced with three different fiber types and loaded at the area ratio of 4*

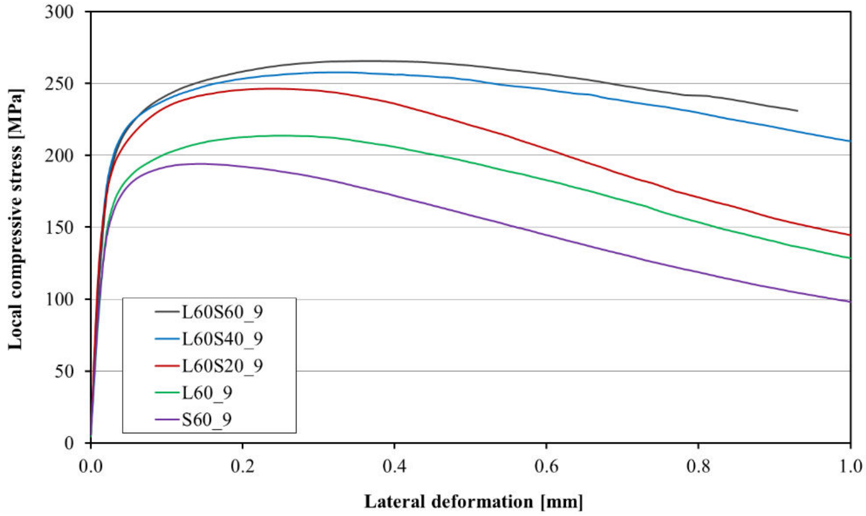


*Figure A.18: Average local compressive stress versus lateral deformation curves of various SFRCs loaded at the area ratio of 9*

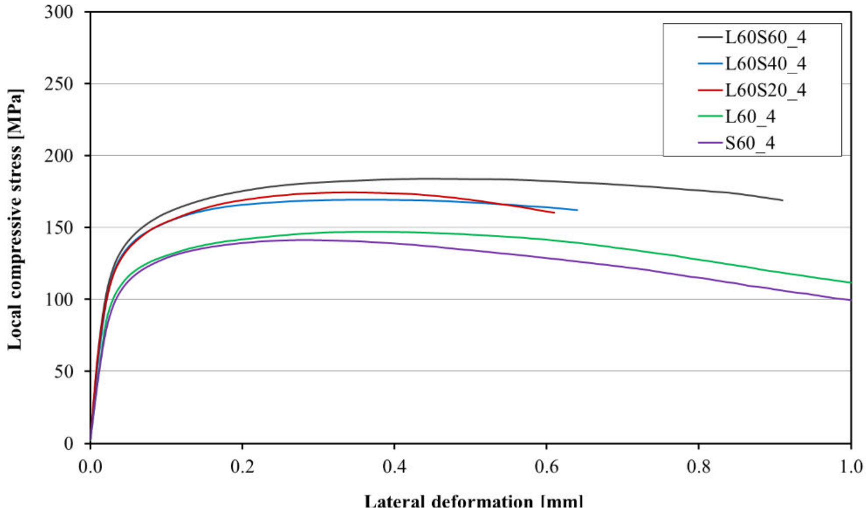


*Figure A.19: Average local compressive stress versus lateral deformation curves of various SFRCs loaded at the area ratio of 4*

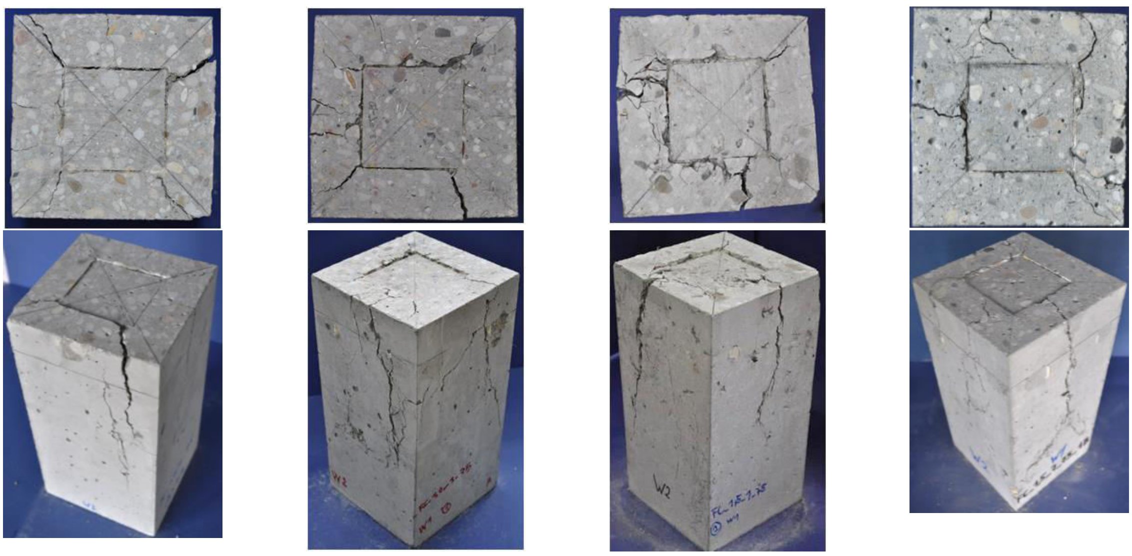

*L40S20_4* *L40M20S20_4* *L60S60_4* *L40M40S40_4*

*Figure A.20: Typical failure patterns of SFRC prisms produced with hybrid reinforcement and loaded at the area ratio of 4*

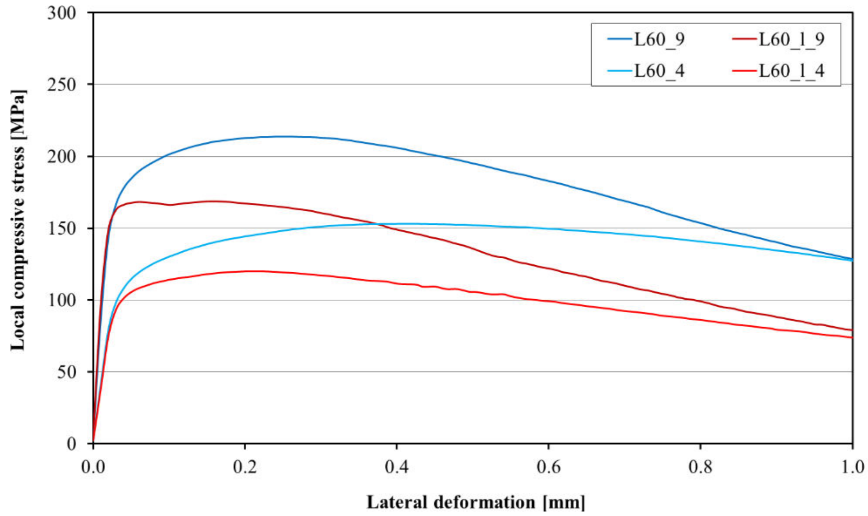


*Figure A.21: Average local compressive stress versus lateral deformation curves of SFRC prisms (L60) produced in the standing and lying molds and loaded concentrically at the area ratios of 9 and 4*

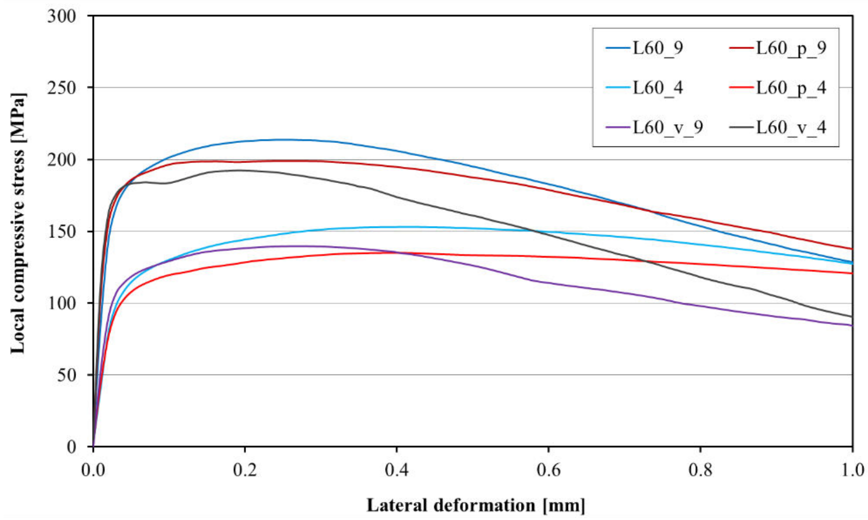


*Figure A.22: Average local compressive stress versus lateral deformation curves of SFRC prisms (L60) sampled parallel and perpendicular to the casting direction and loaded at the area ratios of 9 and 4, in comparison with the standard SFRC prisms (L60_9 and L60_4)*

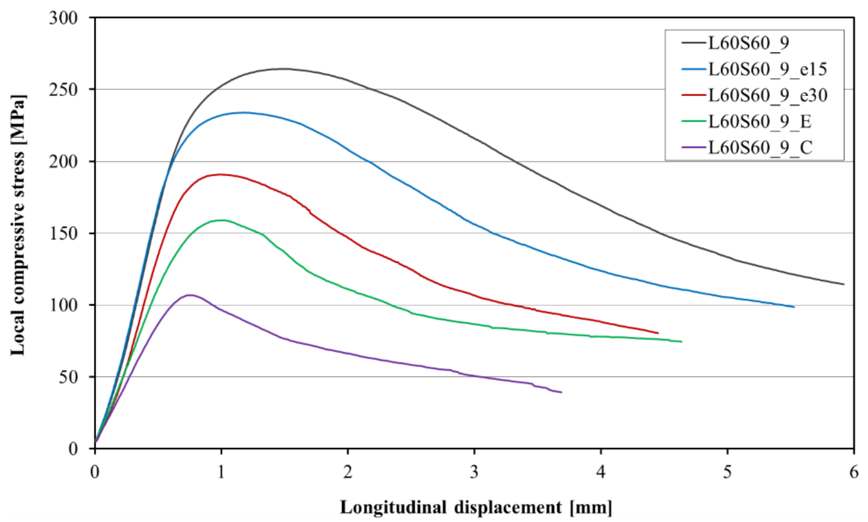


*Figure A.23: Average local compressive stress versus longitudinal displacement curves of SFRC prisms (L60S60) loaded under various eccentricities at the area ratio of 9*

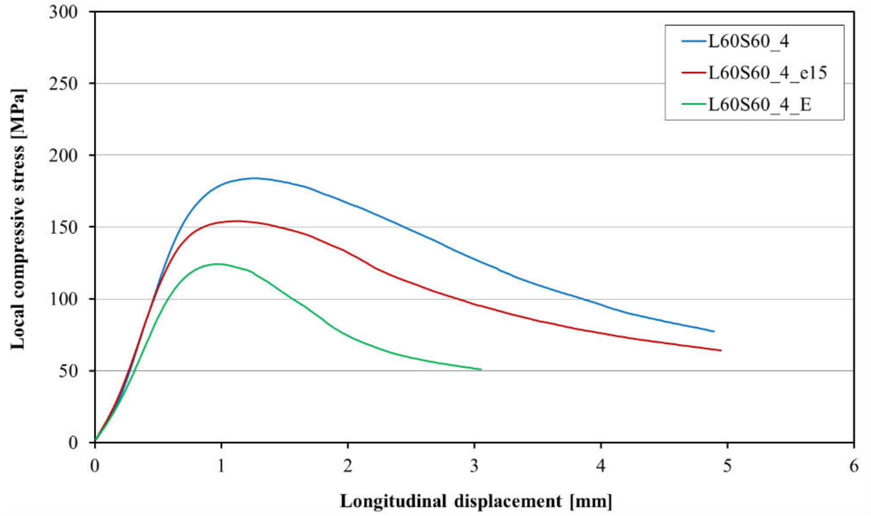


*Figure A.24: Average local compressive stress versus longitudinal displacement curves of SFRC prisms (L60S60) loaded under various eccentricities at the area ratio of 4*

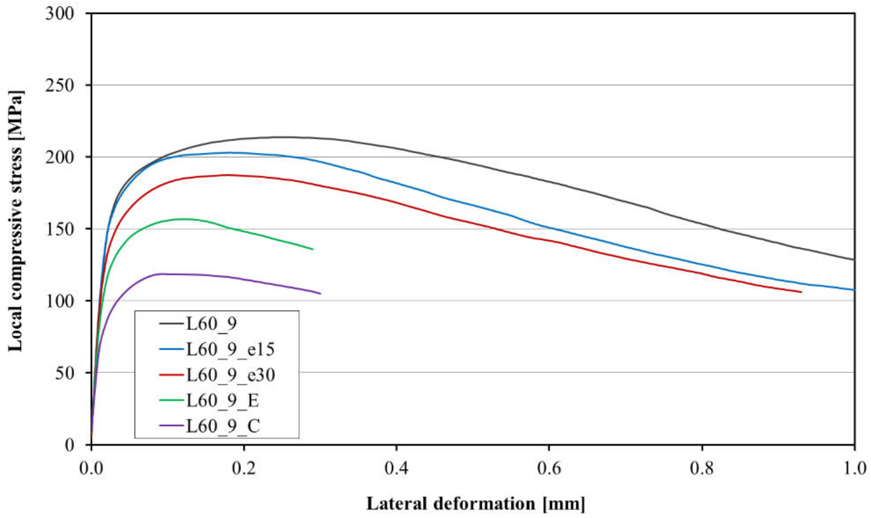


*Figure A.25: Average local compressive stress versus lateral deformation curves of SFRC prisms (L60) loaded under various eccentricities at the area ratio of 9*

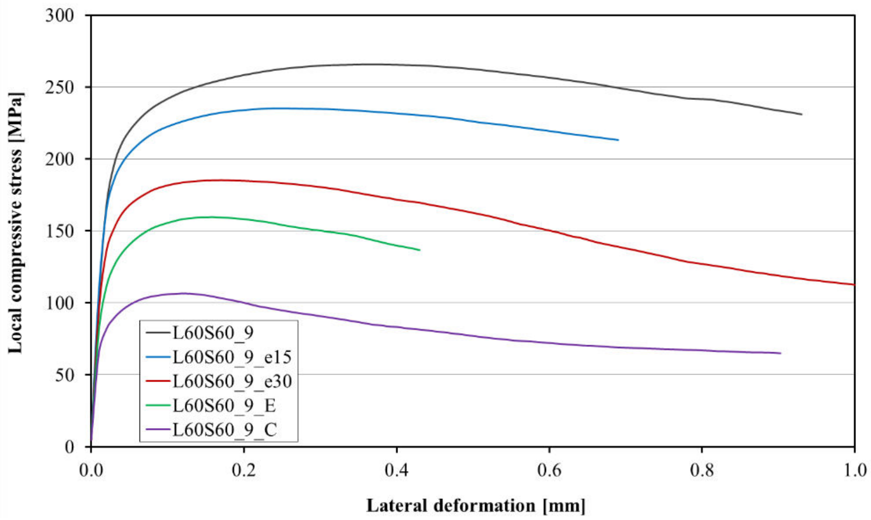


*Figure A.26: Average local compressive stress versus lateral deformation curves of SFRC prisms (L60S60) loaded under various eccentricities at the area ratio of 9*

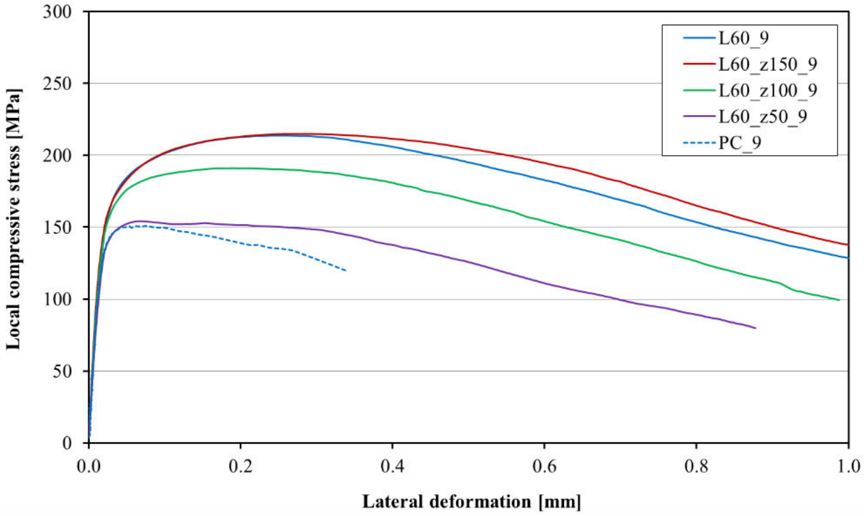


*Figure A.27: Average local compressive stress versus lateral deformation curves of hybrid concrete prisms (reinforcement L60) cast in the standing molds and loaded concentrically at the area ratio of 9*

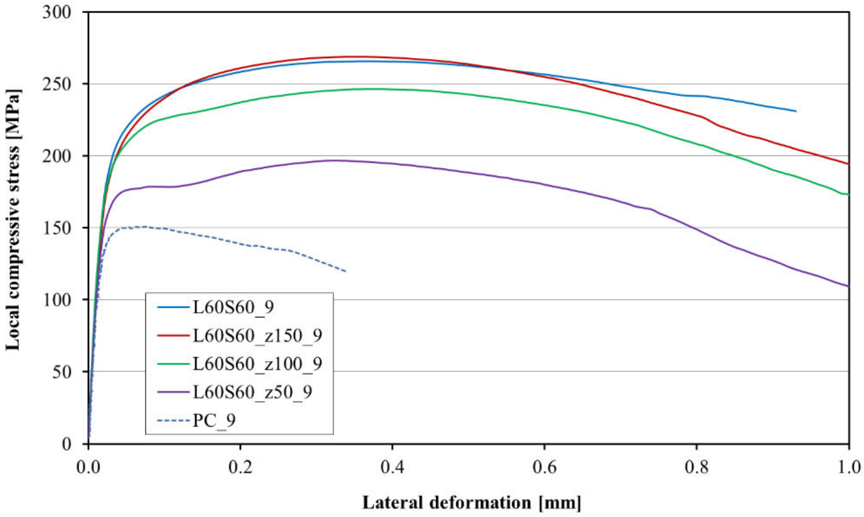


*Figure A.28: Average local compressive stress versus lateral deformation curves of hybrid concrete prisms (reinforcement L60S60) cast in the standing molds and loaded concentrically at the area ratio of 9*

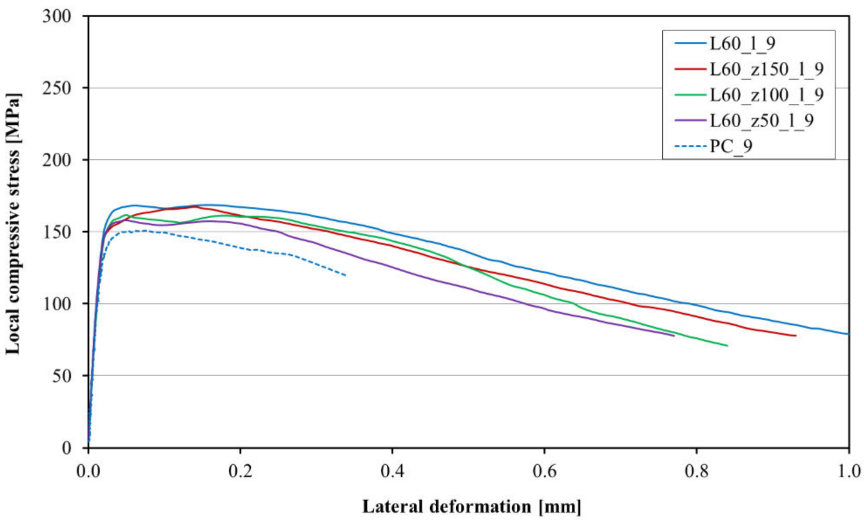


*Figure A.29: Local compressive stress versus lateral deformation curves of hybrid concrete prisms (reinforcement L60) cast in the lying molds and loaded concentrically at the area ratio of 9*

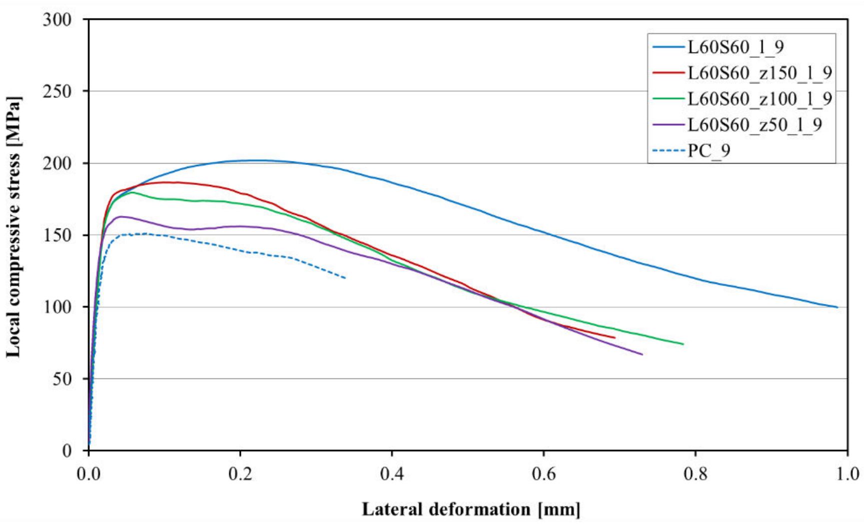


*Figure A.30: Local compressive stress versus lateral deformation curves of hybrid concrete prisms (reinforcement L60S60) cast in the lying molds and loaded concentrically at the area ratio of 9*

# Appendix B

*Table B.1: Properties of the fresh plain and fiber concretes*

| Index | Superplasticizer [kg/m³] | Flow consistency [cm] | Air void content [%] | Bulk density [kg/m³] |
|---|---|---|---|---|
| NS_PC | 0.75 | 45 | 1.9 | 2370 |
| NS_L60 | 1.40 | 43 | 1.0 | 2430 |
| PC | 1.30 | 42 | 3.0 | 2360 |
| L40 | 1.60 | 41 | 2.4 | 2360 |
| L60 | 1.98 | 43 | 1.9 | 2440 |
| L80 | 2.11 | 41 | 1.7 | 2460 |
| Lt60 | 1.98 | 42 | 2.2 | 2380 |
| Lh60 | 2.10 | 40 | 2.1 | 2430 |
| S60 | 1.98 | 42 | 3.4 | 2390 |
| M60 | 1.75 | 45 | 2.8 | 2380 |
| L40S20 | 1.98 | 43 | 1.7 | 2420 |
| L40M20 | 1.98 | 40 | 1.9 | 2410 |
| L40S40 | 2.23 | 38 | 2.2 | 2420 |
| L40M40 | 1.98 | 39 | 1.9 | 2440 |
| L40M20S20 | 2.64 | 42 | 1.8 | 2450 |
| L40M20S40 | 3.30 | 36 | 2.0 | 2460 |
| L40M40S20 | 2.64 | 36 | 2.7 | 2440 |
| L40M40S40 | 2.64 | 37 | 2.0 | 2480 |
| L60S20 | 2.64 | 34 | 2.5 | 2460 |
| L60S40 | 1.98 | 38 | 1.9 | 2440 |
| L60S60 | 1.98 | 37 | 1.3 | 2470 |

*Table B.2: Properties of the hardened plain and fiber concretes*

| Index | Compressive strength [MPa] | Splitting tensile strength [MPa] | Young's modulus [GPa] |
|---|---|---|---|
| NS_PC | 45.8 | 3.2 | 28.1 |
| NS_L60 | 53.1 | 5.1 | 29.2 |
| PC | 84.5 | 4.0 | 36.9 |
| L40 | 85.5 | 5.3 | 35.9 |
| L60 | 87.4 | 6.7 | 35.4 |
| L80 | 94.5 | 7.4 | 36.6 |
| Lt60 | 77.7 | 6.5 | 38.7 |
| Lh60 | 89 | 6.3 | 34.6 |
| S60 | 88.5 | 5.1 | 40.7 |
| M60 | 81.4 | 6 | 35.6 |
| L40S20 | 87 | 6.6 | - |
| L40M20 | 87.3 | 6.5 | - |
| L40S40 | 91.6 | 7.3 | - |
| L40M40 | 91.3 | 6.3 | - |
| L40M20S20 | 93.9 | 7.7 | - |
| L40M20S40 | 100.7 | 7.4 | - |
| L40M40S20 | 93.3 | 7.6 | - |
| L40M40S40 | 98.7 | 8.6 | - |
| L60S20 | 100.6 | 9.6 | - |
| L60S40 | 95.1 | 7.8 | - |
| L60S60 | 94.4 | 7.5 | - |

*Table B.3: Average values of crack number and maximum crack width on the testing surface for test series 1 (area ratio and concrete strength)*

| Index | Area ratio | Crack number | Maximum crack width [mm] |
|---|---|---|---|
| PC | 16 | 5 | 3.25 |
| | 9 | 6.7 | 3.5 |
| | 4 | - | |
| | 2.25 | - | |
| NS_PC | 16 | 3 | 1 |
| | 9 | 5 | 1 |
| | 4 | 7.3 | 2.53 |
| | 2.25 | 9 | 2.88 |
| L60 | 16 | 7.7 | 4.75 |
| | 9 | 10.7 | 3.4 |
| | 4 | 9 | 2.83 |
| | 2.25 | 7 | 2.23 |
| NS_L60 | 16 | 9 | 3.25 |
| | 9 | 9 | 3.58 |
| | 4 | 7.7 | 4.33 |
| | 2.25 | 9.7 | 4.83 |

*Table B.4: Average values of crack number and maximum crack width on the testing surface for test series 2 (specimen dimension)*

| Index | Area ratio | Crack number | Maximum crack width [mm] |
|---|---|---|---|
| L60 (d150) | 9 | 10.7 | 3.4 |
| | 4 | 9 | 2.83 |
| L60_d300 | 9 | 7.7 | 6.33 |
| | 4 | 8 | 6.13 |

*Table B.5: Average values of crack number and maximum crack width on the testing surface for test series 3 (fiber property)*

| Index | Area ratio | Crack number | Maximum crack width [mm] |
|---|---|---|---|
| L60 | 9 | 10.7 | 3.4 |
| | 4 | 9 | 2.83 |
| | 2.25 | 7 | 2.23 |
| Lt60 | 9 | 10 | 1.6 |
| | 4 | 11.3 | 2.6 |
| Lh60 | 9 | 9.3 | 4.33 |
| | 4 | 8.3 | 4.03 |
| M60 | 9 | 9 | 1.9 |
| | 4 | 9 | 1.47 |
| | 2.25 | 10.7 | 2.4 |
| S60 | 9 | 7.7 | 3 |
| | 4 | 8.3 | 2.6 |

*Table B.6: Midpoint longitudinal compressive deformations at $q_{max}$ of various SFRC prisms for test series 4 (fiber concentration and combination)*

| Index | Fiber content [kg/m³] | Compressive deformation at $q_{max}$ [mm] | |
|---|---|---|---|
| | | Area ratio | |
| | | 9 | 4 |
| L40 | 40 | 0.23 | 0.32 |
| L40S20 | 60 | 0.21 | 0.44 |
| L40M20 | | 0.22 | 0.36 |
| L60 | | 0.26 | 0.34 |
| L40S40 | 80 | 0.16 | 0.23 |
| L40M40 | | 0.21 | 0.24 |
| L40M20S20 | | 0.20 | 0.24 |
| L60S20 | | 0.23 | 0.27 |
| L80 | | 0.21 | 0.22 |
| L40M20S40 | 100 | 0.22 | 0.23 |
| L40M40S20 | | 0.21 | 0.25 |
| L60S40 | | 0.23 | 0.28 |
| L40M40S40 | 120 | 0.16 | 0.20 |
| L60S60 | | 0.22 | 0.28 |

*Table B.7: Average values of crack number and maximum crack width on the testing surface for test series 4 (fiber concentration and combination)*

| Index | Fiber content [kg/m³] | Area ratio | crack number | Maximum crack width [mm] |
|---|---|---|---|---|
| L40 | 40 | 9 | 8.3 | 3.5 |
| | | 4 | 7.7 | 3.17 |
| L40S20 | 60 | 9 | 8.7 | 4 |
| | | 4 | 8.3 | 3.33 |
| L40M20 | | 9 | 9 | 3.27 |
| | | 4 | 10.8 | 3.63 |
| L60 | | 9 | 10.7 | 3.4 |
| | | 4 | 9 | 2.83 |
| L40S40 | 80 | 9 | 8.2 | 4.02 |
| | | 4 | 7.5 | 4.13 |
| L40M40 | | 9 | 8.3 | 2.05 |
| | | 4 | 8.7 | 3.24 |
| L40M20S20 | | 9 | 6.8 | 4.5 |
| | | 4 | 9.5 | 3.05 |
| L60S20 | | 9 | 7.7 | 6 |
| | | 4 | 7.3 | 4.5 |
| L80 | | 9 | 5.5 | 3.13 |
| | | 4 | 3.7 | 2.37 |
| L40M20S40 | 100 | 9 | 7.3 | 4.63 |
| | | 4 | 7 | 2.55 |
| L40M40S20 | | 9 | 6.8 | 4.88 |
| | | 4 | 7.3 | 4.25 |
| L60S40 | | 9 | 8 | 8.13 |
| | | 4 | 9 | 4.5 |
| L40M40S40 | 120 | 9 | 8.5 | 5.63 |
| | | 4 | 7 | 3.38 |
| L60S60 | | 9 | 9.3 | 5.13 |
| | | 4 | 8.3 | 8.5 |

*Table B.8: Midpoint longitudinal compressive deformations at $q_{max}$ of various SFRC prisms for test series 5 (fiber orientation)*

| Index | Code | Area ratio | Compressive deformation at $q_{max}$ [mm] |
|---|---|---|---|
| L60 | L60_9 | 9 | 0.21 |
| | L60_4 | 4 | 0.22 |
| | L60_l_9 | 9 | 0.13 |
| | L60_l_4 | 4 | 0.17 |
| | L60_i_9 | 9 | 0.22 |
| | L60_i_4 | 4 | 0.25 |
| | L60_p_9 | 9 | 0.20 |
| | L60_p_4 | 4 | 0.22 |
| | L60_v_9 | 9 | 0.10 |
| | L60_v_4 | 4 | 0.20 |
| L60S60 | L60S60_9 | 9 | 0.22 |
| | L60S60_4 | 4 | 0.28 |
| | L60S60_l_9 | 9 | 0.20 |
| | L60S60_l_4 | 4 | 0.20 |

*Table B.9: Average values of crack number and maximum crack width on the testing surface for test series 5 (fiber orientation)*

| Index | Area ratio | Crack number | Maximum crack width [mm] |
|---|---|---|---|
| L60 | 9 | 10.7 | 4.75 |
| | 4 | 9 | 3.4 |
| L60_l | 9 | 7.7 | 2.23 |
| | 4 | 8.7 | 2.33 |
| L60_i | 9 | 8.3 | 3.5 |
| | 4 | 9 | 2.2 |
| L60_p | 9 | 7 | 3.97 |
| | 4 | 7.3 | 5.17 |
| L60_v | 9 | 8.7 | 2.07 |
| | 4 | 8.7 | 1.93 |

*Table B.10: Average values of crack number and maximum crack width on the testing surface for test series 6 (eccentricity of load)*

| Index | Eccentricity | Area ratio | Crack number | Maximum crack width [mm] |
|---|---|---|---|---|
| PC | concentric | 9 | 6.7 | 3.5 |
| | e15 (e = 15 mm) | 9 | 5.7 | 1.83 |
| | e30 (e = 30 mm) | 9 | 4.5 | 3.6 |
| | E (edge loading) | 9 | - | - |
| | C (corner loading) | 9 | 3.7 | 0.3 |
| L60 | concentric | 9 | 10.7 | 3.4 |
| | | 4 | 9 | 2.8 |
| | e15 | 9 | 9 | 4.33 |
| | | 4 | 8 | 2.7 |
| | e30 | 9 | 8.3 | 2.3 |
| | E | 9 | 5.7 | 0.65 |
| | | 4 | 5.3 | 1.87 |
| | C | 9 | 4.3 | 0.62 |
| L60S60 | concentric | 9 | 9.3 | 5.13 |
| | | 4 | 8.3 | 8.5 |
| | e15 | 9 | 7 | 6.9 |
| | | 4 | 7.5 | 4.5 |
| | e30 | 9 | 6.8 | 6 |
| | E | 9 | 4 | 1.16 |
| | | 4 | 3 | 1.2 |
| | C | 9 | 2 | 0.5 |
| L40M40S40 | E | 9 | 4.5 | 0.79 |
| | C | 9 | 2.5 | 0.29 |

*Table B.11: Midpoint longitudinal compressive deformations at $q_{max}$ of various SFRC prisms for test series 7 (hybrid concrete system, under concentric loading at the area ratio of 9)*

| Index | Code | Thickness of fiber reinforcement [mm] | Compressive deformation at $q_{max}$ [mm] |
|---|---|---|---|
| L60 | L60_z50_l_9 | 50 | 0.19 |
| | L60_z100_l_9 | 100 | 0.19 |
| | L60_z150_l_9 | 150 | 0.22 |
| | L60_l_9 | 300 | 0.13 |
| | L60_z50_9 | 50 | 0.15 |
| | L60_z100_9 | 100 | 0.18 |
| | L60_z150_9 | 150 | 0.19 |
| | L60_9 | 300 | 0.21 |
| L60S60 | L60S60_z50_l_9 | 50 | 0.31 |
| | L60S60_z100_l_9 | 100 | 0.22 |
| | L60S60_z150_l_9 | 150 | 0.17 |
| | L60S60_l_9 | 300 | 0.20 |
| | L60S60_z50_9 | 50 | 0.11 |
| | L60S60_z100_9 | 100 | 0.13 |
| | L60S60_z150_9 | 150 | 0.22 |
| | L60S60_9 | 300 | 0.22 |

*Table B.12: Average values of crack number and maximum crack width on the testing surface for the case of concentric loading for test series 7 (hybrid concrete system)*

| Index | Area ratio | Crack number | Maximum crack width [mm] |
|---|---|---|---|
| PC | 9 | 6.7 | 3.5 |
| L60_z50_l | | 6 | 0.78 |
| L60_z100_l | | 7 | 2.23 |
| L60_z150_l | | 7.3 | 1.97 |
| L60_l | | 7.7 | 2.23 |
| L60_z50 | | 7.3 | 1.4 |
| L60_z100 | | 8 | 1.78 |
| L60_z150 | | 8 | 3 |
| L60 | | 10.7 | 3.4 |
| L60S60_z50_l | | 4.7 | 2.07 |
| L60S60_z100_l | | 4.3 | 1.4 |
| L60S60_z150_l | | 5 | 1.63 |
| L60S60_l | | 7 | 2.8 |
| L60S60_z50 | | 8.7 | 2.28 |
| L60S60_z100 | | 7.7 | 3.13 |
| L60S60_z150 | | 9.7 | 3.38 |
| L60S60 | | 9.3 | 5.13 |
| PC | 4 | - | - |
| L60_z100 | | 9 | 2.67 |
| L60 | | 9 | 2.83 |
| L60S60_z100 | | 9.7 | 1.63 |
| L60S60 | | 8.3 | 8.5 |

*Table B.13: Average values of crack number and maximum crack width on the testing surface for the case of eccentric loading for test series 7 (hybrid concrete system)*

| Index | Area ratio | Crack number | Maximum crack width [mm] |
|---|---|---|---|
| PC_E | 9 | - | - |
| L60_z100_E | | 2.7 | 0.54 |
| L60_E | | 5.7 | 0.65 |
| L60S60_z100_E | | 4.3 | 0.74 |
| L60S60_E | | 4 | 1.16 |
| PC_C | | 3.7 | 0.3 |
| L60_z100_C | | 5.7 | 0.53 |
| L60_C | | 4.3 | 0.62 |
| L60S60_z100_C | | 6.3 | 0.59 |
| L60S60_C | | 2 | 0.5 |

# Curriculum Vitae

## Personal Details

| | |
|---|---|
| Name: | Fanbing Song |
| Date of birth: | 04.06.1980 |
| Place of birth: | Shanghai, China |
| Nationality: | German |
| Cell: | 0152 0318 1945 |
| E-Mail: | Fanbing.Song@rub.de |

## Work Experience

| | |
|---|---|
| 09.2010 - present | Research Associate<br>Institute for Building Materials, Ruhr-University Bochum |
| 11.2005 - 08.2007 | Project Sales Manager<br>Caparol (Shanghai) Co., Ltd. |
| 02.2004 - 05.2005 | Product Manager<br>Dashöfer Management Consulting Co., Ltd. (Shanghai) |
| 03.2003 - 02.2004 | Construction Manager<br>Yongda Municipal Construction Co., Ltd. (Shanghai) |

## Education

| | |
|---|---|
| 10.2007 - 05.2010 | Master degree, Bauhaus-Weimar University<br>Faculty: Civil Engineering<br>Major: Building Materials and Rehabilitation<br>Master's thesis: Production of a gypsum plaster binder under laboratory conditions |
| 09.1998 - 07.2003 | Bachelor degree, Tongji University (Shanghai)<br>Faculty: Civil Engineering<br>Major: Underground Construction<br>Bachelor's thesis: Investigation on the durability of subway structures in Shanghai |
| 09.2001 - 07. 2002 | Intensive German course, Tongji University (Shanghai) |
| 09.1995 - 07.1998 | Abitur, Fengxian Senior High School (Shanghai) |